Structural analogues of complex magnetic phases

Emma H. Wolpert

Hertford College, Oxford



A thesis submitted to the University of Oxford for the degree

of Doctor of Philosophy

Inorganic Chemistry Laboratory

University of Oxford

Michaelmas 2020

The work presented in this thesis was carried out between October 2017 and December 2020 in the Inorganic Chemistry Laboratory, University of Oxford under the supervision of Prof. Andrew L. Goodwin. All of the work is my own unless otherwise stated, and has not been submitted previously for any degree at this or any other university.

Emma Helen Wolpert
December 2020

Summary of contents of thesis and key results

This thesis studies the phase behaviour of a variety of complex solid structures. The principal approach taken is to develop a suitable coarse graining of the degrees of freedom in order to allow a representation in terms of interaction models.

Chapter 3 concerns the polytypism of layered AB_2 compounds. We develop a simple interaction model that has at its ground states many of the key experimentally determined structural phases. At phase boundaries we identify complex disordered states that we show sometimes provide a more convincing descriptor of the polytypism than established models. These results allow us to question the existence of previously characterised phases and new undocumented phases are put forward as perhaps more chemically sensible alternatives.

Continuing on the theme of layered materials, Chapter 4 maps the stacking disorder present in the layered inorganic material $Ni(CN)_2$ onto a model containing continuous degrees of freedom. Moreover, the model can also take the form of the Heisenberg XXZ model used to describe interacting chains of quantum spins, and as such, we have identified a system realising the classical analogue of a 1D quantum chain.

Chapter 5 maps complex magnetic phases onto structural degrees of freedom by focusing on topological defects within chiral magnets. Here we show that these degrees of freedom can be related to quadrupolar orientations of molecules within a chiral framework, and can create analogous topological defects in chiral MOFs. This result expands the field of data storage by highlighting potential materials not

normally associated with emergent phenomena.

This thesis ends with two appendices containing experimental work carried out during the DPhil, which had to be put on hold due to constraints set up by the ongoing COVID-19 pandemic. Both these studies tie into the theme of statistical mechanical models and structural disorder, with the first centring on the extent to which ice like disorder manifests in the compositionally disordered cyanospinel $KRb[Zn(CN)_4]$. The second study focuses on the stacking disorder present in the solid solution $K[Ag_xAu_{1-x}(CN)_2]$ which varies as a function of composition and temperature. The larger aim of both these studies is to see how correlated disorder may selectively effect the phononic properties of materials.

Acknowledgements

I would like to start by thanking my supervisor, Professor Andrew Goodwin for his kindness and generosity, in trusting me with these projects, and for giving me free reign to explore many different avenues. It has been a wonderful journey, made much richer by his scientific guidance. I would also like to thank Professor FX Coudert for hosting my 4 month stay in Paris and patiently teaching me new computational techniques.

A big thank you to all members of the Goodwin group—past and present—for their help and company over the last five or so years: Ali without whom this journey would have never begun; Arkadiy for many insightful (and confusing) discussions and general physics help as well as constant motivation; Chloe for her kindness and friendship; Phil for his puns and niche knowledge—an excellent (and important) addition to cryptic crosswords; Harry for his always appreciated dad jokes; Emily R. for her continued support and enthusiasm; Adam for his constant stream of memes; Arianna and Ella for diffraction advice and commitment to social sec duties; as well as the numerous part IIs, visiting students, and summer students who have passed through the group over the last few years.

As a mainly computational chemist, I am indebted to many experimentalists in the group; Emily R., Chloe, Simon, and Emily M., who have taught me so much and answered my questions no matter how basic. Simon and Emily R. have both been instrumental to the data analysis within the appendix chapters of my thesis and I thank them for their help (and patience therein). I would also like to thank Harry,

Arianna, Arkadiy, Emily R., Ella, Jonny, Chloe, and Simon who each proofread parts of this thesis; as well as my mum for giving it the last final proof read.

On top of their scientific help, I am incredibly thankful to both Chloe and Emily R. for their endless support throughout the whole degree, even after leaving the group: Emily R. for always guiding me through a scientific crisis or otherwise, no matter how busy she may be, and Chloe for keeping me company on many London-Oxford journeys, helping me put everything into perspective, and always lending an ear to my DPhil worries and strifes.

Finally, I would also like to thank my wonderful friends and family. Although they may not share my love for all things diffuse, their friendship and laughter have been invaluable; Alex and Jonny who kept me entertained through my last days in Oxford; Rachel and Harriet for being constant pillars of support (and fun) throughout my life; mine (and Yoels) parents for their continued support, especially my dad who has answered many inane scientific questions and has managed to withhold his frustrations at least half the time, and finally Yoel for his endless encouragement who, particularly due to the ongoing pandemic, has had to put up with more than his fair share of complaints.

For mum & dad

Contents

1 Introduction **1**

1.1 Disorder 1

1.2 Microscopic models of complex systems 22

1.3 Emergence in complex systems 36

1.4 Mapping between structural and magnetic phases 48

1.5 Thesis outline 59

2 Methods **62**

2.1 Diffraction 62

2.2 Monte Carlo simulations 77

2.3 Density functional theory 84

2.4 Lattice dynamical calculations 89

2.5 Molecular dynamics 92

2.6 Overview 95

3 Polytypism in layered AB_2 solids **97**

3.1 Summary 97

3.2 Background 99

3.3 The model . . . 108
3.4 Hamiltonian . . . 113
3.5 Reinterpretation of exception phases . . . 117
3.6 Solid solutions . . . 127
3.7 Outlook . . . 129

4 Stacking disorder in $Ni(CN)_2$ 134

4.1 Summary . . . 134
4.2 Background . . . 136
4.3 The model . . . 140
4.4 Relation to magnetic models . . . 147
4.5 Outlook . . . 162

5 Skyrmion lattices in chiral metal organic frameworks 164

5.1 Summary . . . 164
5.2 Background . . . 165
5.3 The model . . . 171
5.4 Monte Carlo simulations . . . 177
5.5 *Ab initio* techniques . . . 183
5.6 Outlook . . . 191

6 Conclusions and future outlook 193

Bibliography 196

Appendix A: Ice-like disorder in $KRbZn(CN)_4$ 218

A.1 Summary . . . 219

A.2 Synthesis and experiment 220

A.3 Experimental results 222

A.4 Models 227

A.5 Outlook 231

Appendix B: Stacking disorder in $KAg_xAu_{1-x}(CN)_2$ **232**

B.1 Summary 233

B.2 Synthesis and experiment 234

B.3 Structural dependence on the composition of

$K[Ag_xAu_{1-x}(CN)_2]$ 236

B.4 Temperature dependence of the structure of $K[Ag_xAu_{1-x}(CN)_2]$ . . . 238

B.5 Model and phase behaviour 241

B.6 DFT 247

B.7 Outlook 249

Appendix C: Supplementary information for Chapter 3 **251**

C1 Simulated diffraction patterns of the limiting phases 252

Appendix D: Supplementary information for Chapter 4 **252**

D1 Lattice parameter data for pressure calculations 254

Appendix E: Supplementary information for Chapter 5 **254**

E1 Phase diagram for Monte Carlo simulations with constant A' 256

E2 DFT geometry optimised structure of $[Al(N_3)_3]\cdot C_6H_6$ 257

Appendix F: Contents of zip appendix **257**

F1 Contents of zip file 258

Publications

Part of this thesis is under consideration for publication and is listed below along with the chapter which contains the work. Other publications from work unrelated to this thesis, but pertaining to work carried out during my DPhil are also listed here.

- Hybrid local-order mechanism for inversion symmetry breaking
  E. H. Wolpert, A. R. Overy, P. M. M. Thygesen, A. Simonov, M. S. Senn, A. L, Goodwin, *Phys. Rev. B* **97**, 134106 (2018).
- Function from configurational degeneracy in disordered framework materials
  E. M. Reynolds, **E. H. Wolpert**, A. R. Overy, L. Mizzi, A. Simonov, J. N. Grima, S. Kaskel, A. L. Goodwin, *Faraday Discuss.*, Advance Article (2020).
- Skyrmion lattices in chiral metal-organic frameworks
  E. H. Wolpert, F. X. Coudert, AL Goodwin, *submitted*, chemrxiv.12515594.v1 (2020).
  Chapter 5

List of Figures

1.1 Types of disorder 5

1.2 Examples of compositional disorder 7

1.3 Examples of positional disorder 8

1.4 Examples of topological disorder 11

1.5 Square ice 16

1.6 Experimental examples of different probes of disorder 19

1.7 Experimental examples of direct imaging used to characterise disorder 21

1.8 Ising and ANNNI models 24

1.9 Triangular Ising antiferromagnet 26

1.10 Ice rule materials 29

1.11 Magnetic models 31

1.12 Skyrmion phases 35

1.13 Topological defects 37

1.14 Conditions for Coulomb phases 40

1.15 Magnetic monopoles 41

1.16 Liquid crystals 44

1.17 Schlieren textures 47

1.18 Spin ice physics in $Cd(CN)_2$ 50

1.19 Multipolar order in the cyanoelpasolite molecular perovskites 53

1.20 Stacking and magnetic models 55

1.21 Polytypes of transition metal dichalcogenides 57

2.1 Scattering of waves by atoms 63

2.2 Single crystal and powder diffraction patterns 71

2.3 PXRD and SCXRD evidencing the stacking disorder in Pigment Red 170 72

2.4 Preferred orientations 73

2.5 SANS 75

2.6 Monte Carlo example 79

2.7 Monte Carlo regime 80

2.8 Computational times of DFT functionals 87

2.9 Molecular dynamics equilibration 95

3.1 Universal building block of AB_2 100

3.2 $1T, 2H_c$ and $CdCl_2$ 102

3.3 Layered chalcogenides model 110

3.4 Equivalent phases 111

3.5 Layered chalcogenides phase diagram 112

3.6 Layered chalcogenides phases 114

3.7 Layered chalcogenides disordered phases 117

3.8 $4H_b$ diffraction patterns 119

3.9 $4H_b$ with mixed stacking 120

3.10 $6R$ experimental diffraction patterns 122

3.11 $6R$ simulated diffraction patterns 123

3.12 $4H_a$ from paper 124

3.13 $4H_a$ and $4H_c$ 125

3.14 Direct image comparison of $4H_a$ and a mixture of $\langle \pm, \pm \rangle$ and $\langle +, \pm \rangle$. 126

3.15 $Re_xTa_{1-x}Se_2$ and $Ru_xNb_{1-x}S_2$ diffraction patterns 129

3.16 Representative structure of intermediate phase 129

4.1 $Ag_{0.5}Au_{0.5}(CN)$ 138

4.2 Previous models of $Ni(CN)_2$ 139

4.3 $Ni(CN)_2$ structure 141

4.4 Crystallographic data on $Ni(CN)_2$ 141

4.5 Potential energy surface calculations 143

4.6 Topological mapping of periodic shapes 144

4.7 $Ni(CN)_2$ diffraction patterns 147

4.8 Mapping of $Ni(CN)_2$ layers onto a 1D quaternion chain 149

4.9 Stereographic projection 150

4.10 Fibration 151

4.11 Potential energy surfaces of $Ni(CN)_2$ layers with changing pressure . . 160

4.12 Variation of the interaction parameter between $Ni(CN)_2$ layers with pressure 161

5.1 Skyrmion phase diagram 167

5.2 Dipolar and quadrupolar skyrmions 167

5.3 Example of chiral MOFs 168

5.4 Molecular orientations within MOFs 169
5.5 Quadrupolar interactions 173
5.6 Phase diagram 178
5.7 Small-angle scattering of phases 180
5.8 Averaged small-angle scattering used for phase characterisation . . . 181
5.9 Scattering criteria for phase determination 182
5.10 Structure of $[Al(N_3)_3]\cdot C_6H_6$ determined by DFT 184
5.11 AIMD equilibration 187
5.12 AIMD orientation fluctuations 188
5.13 AIMD results 189

A.1 $K_2[Zn(CN)_4]$ structure 220
A.2 Solid solution 223
A.3 Pawley refinements for different members of the $Rb_xK_{2-x}[Zn(CN)_4]$ family 224
A.4 $KRb[Zn(CN)_4]$ SCXRD 225
A.5 Lattice parameters of the solid solution $Rb_xK_{2-x}[Zn(CN)_4]$ 226
A.6 $KRb[Zn(CN)_4]$ structure 227
A.7 $K_2[Hg(CN)_4]$ structure and kagome rigid unit modes 229
A.8 Simulated $KRb[Zn(CN)_4]$ SCXRD 230
A.9 $KRb[Zn(CN)_4]$ experimental and simulated diffraction patterns 231
B.1 Stacking in $K[Au(CN)_2]$ and $K[Ag(CN)_2]$ 234
B.2 Pawley refinements of low temperature structures of $K[Au(CN)_2]$ and $K[Ag(CN)_2]$ 237

B.3 Composition dependence on the structure of $K[Ag_xAu_{1-x}(CN)_2]$ . . . 238

B.4 Variable temperature diffraction patterns of $K[Au(CN)_2]$ 239

B.5 High and low temperature diffraction patterns of $K[Ag_xAu_{1-x}(CN)_2]$ 240

B.6 Variable temperature diffraction patterns of $K[Au(CN)_2]$ 243

B.7 Simulated diffraction patterns compared to experimental data of $K[Au(CN)_2]$ at 375 K and 450 K 244

B.8 Variable temperature diffraction patterns of $K[Ag_{0.5}Au_{0.5}(CN)_2]$ . . . 245

B.9 Simulated and experimental diffraction patterns of $K[Ag_{0.5}Au_{0.5}(CN)_2]$ at 125 K 246

B.10 Variable temperature diffraction patterns of $K[Ag(CN)_2]$ 247

B.11 Effects of expansion on the energy of the two different structures . . . 249

B.12 Overview of phase behaviour of $K[Ag_xAu_{1-x}(CN)_2]$ 250

C.1 Powder X-ray diffraction patterns of the limiting phases of the stacking model for layered dichalcogenides 253

E.1 Simulations at constant temperature and changing strain 256

Abbreviations

1D	One dimensional
2D	Two dimensional
3D	Three dimensional
2θ	Scattering angle (diffraction)
3D-ΔPDF	3D difference pair distribution function
a.u.	Atomic units
AIMD	*Ab initio* molecular dynamics
ANNNI	Axial next nearest neighbour Ising model
BFGS	Broden-Fletcher-Goldfarb-Shanno
BLBQ	Bilinear biquadratic
CIF	Crystallographic Information File
CCP	Cubic close packed
D	Dimensionality of spins
d	Dimensionality of lattice
DFT	Density functional theory
EXAFS	Extended X-ray absorption fine structure

GGA	Generalised gradient approximation
GPW	Gaussian plane waves
GULP	General utility lattice program
HCP	Hexagonal close packed
IR	Infared spectroscopy
LDA	Local density approximation
MC	Monte Carlo
MD	Molecular dynamics
MOF	Metal organic framework
NMR	Nuclear magnetic resonance
nn	Nearest neighbour
nnn	Next nearest neighbour
NTE	Negative thermal expansion
PBE	Perdew-Burke-Ernzerhof
PDF	Pair distribution function
PXRD	Powder X-ray diffraction
RMC	Reverse Monte Carlo
RUM	Rigid unit mode
SANS	Small angle neutron scattering
SCLD	Supercell lattice dynamical
SCXRD	Single crystal X-ray diffraction
TIA	Triangular Ising antiferromagnet
TSF	Translational shear faults

vDW	van der Waal

Chapter 1

Introduction

This thesis focuses on developing our understanding of complex phase behaviour, explored through two main aims. The first is to make use of magnetic models to understand the structural phase behaviour of various materials, and the second is to access experimentally inaccessible states by finding structural analogues of exotic magnetic phases. To accomplish the first, it is important to have an overview of the different statistical mechanical models and understanding of their degrees of freedom and how they may be mapped onto different materials. For the second, we look to what type of complex phases are found predominantly in magnetic materials and identify sets of materials with easy-to-manipulate degrees of freedom which may potentially harbour structural analogues of these complex phases. To begin with, we discuss a variety of types of disorder that arise in materials, with reference to examples in the literature, and the techniques employed to characterise disorder.

1.1 Disorder

From the earliest days of solid-state chemistry, the paradigm of structure and function has played a central role. Early crystallographic explorations of water and ice provided an explanation of the seemingly anomolous behaviour of ice—high dielectric constant and comparatively low density—through an understanding of the hydrogen bonded network within the structure [1, 2]. The physical properties of a

material often depend on structures at different length scales, ranging from local structure *e.g.* controlling the optical properties of ruby, to the microstructure *e.g.* governing the strengths of metals and ceramics [3]. By virtue of their translational periodicity, crystals are the most straightforward phases to describe structures [4]. Moreover, this same periodicity allows, *via* the Bloch Theorem, efficient calculations of the electronic and vibrational states, hence establishing links to functional properties [5].

Yet deviations from long-range order have been known to play a key role in fundamental properties since the 1950s [6]. These deviations lead to disordered arrangements where the atomistic structure cannot be fully described by the average structure alone. Disorder is known to exist in many functional materials and greatly influence materials' behaviour, even enhancing their properties. Examples include enhancing superconductivity as seen in $NbSe_2$ [7] and predicted in many other conventional and unconventional superconductors [8], improving electrocatalytic performance through eletrochemical oxygen evolution in missing-linker metal organic frameworks [9], and improving wave transport in photonic quasicrystals [10]. It is not only the existence of disorder that affects the properties, but the extent of disorder within a material which can have a pronounced effect on the behaviour [11]. This is especially true in materials where the disorder is far from random and contains a degree of correlation. Therefore the ability to characterise disorder and ultimately determine the extent of disorder correlations is key to understanding the effect of disorder on the properties of materials.

Characterising materials in the absence of periodicity, however, proves more

challenging as structural complexity increases when structural periodicity is lost. Although modern developments have lead to vastly improved crystallographic methods, studying disorder still remains more challenging than analysing ordered phases from theoretical, computational, and experimental perspectives [12]. Whilst periodic materials benefit from the application of routine methods, the sheer diversity of types of disorder and the granularity needed in the model to reproduce accurate reciprocal space data requires the use of powerful computational methods [13]. To overcome this, modelling techniques rely on coarse graining where groups of atoms or molecules are represented as a pseudo-atom, minimising computational expense [14]. This considerably reduces simulation times by decreasing the number of degrees of freedom needed to be modelled as the system is condensed to the most important components. Coarse graining is particularly useful when the chemical ingredients responsible for the property/structural motif of interest are well understood as it allows the model to be simplified to only contain features pertaining to the interactions of interest [15, 16].

By examining the literature, it is clear the effects of disorder have been known about for quite some time. The question then remains of why techniques to analyse disordered materials are not as routine as those for ordered materials [12]. Only relatively recently have advancements led to an increased ease of studying disordered states. There are two main reasons for this. Firstly, the increased availability of synchrotron radiation has resulted in less experimentally demanding and time consuming measurements of the comparatively weak diffuse scattering intensities [13]. Secondly, the advent of fast and inexpensive computers has led to increased compu-

tational method development which has informed the analysis of diffuse scattering. This has allowed for large supercells of coarse grained models to be modelled and scattering calculated with greater ease than ever before.

1.1.1 Correlated disorder

Disorder does not necessarily imply randomness and many phases exist which exhibit short-range order and long-range disorder. Such phases are described as containing correlated disorder [12] and may even be more common than crystalline phases in simple systems such as the dense packings of simple polyhedra [17]. The concept of strongly correlated disorder is well illustrated by the toy-model of square ice [18]. Square ice is a two-dimensional representation of H_2O molecules where the molecule is simplified to contain a 90° bond angle. The molecules are arranged on a square lattice where the mixture of covalent and hydrogen-bonding dictates the allowed orientation of water molecules such that all hydrogens point in the same direction along each row or column. There is no unique way of satisfying these rules, hence the system is disordered, even though the molecular orientations are far from random [Fig. 1.1(a)]. The rules leading to the correlated disorder present in square ice are not unique to molecular orientation and similar disorder is found in a multitude of other materials [Fig. 1.1(b)-(d)] [19, 20].

The origins of disorder may arise from one degree of freedom or from a combination of sources including electronic, magnetic, and structural [21]. The interplay of many degrees of freedom is central to forming complex phases with exotic phenomena that are widely studied today [22]. Central to this thesis is the idea of

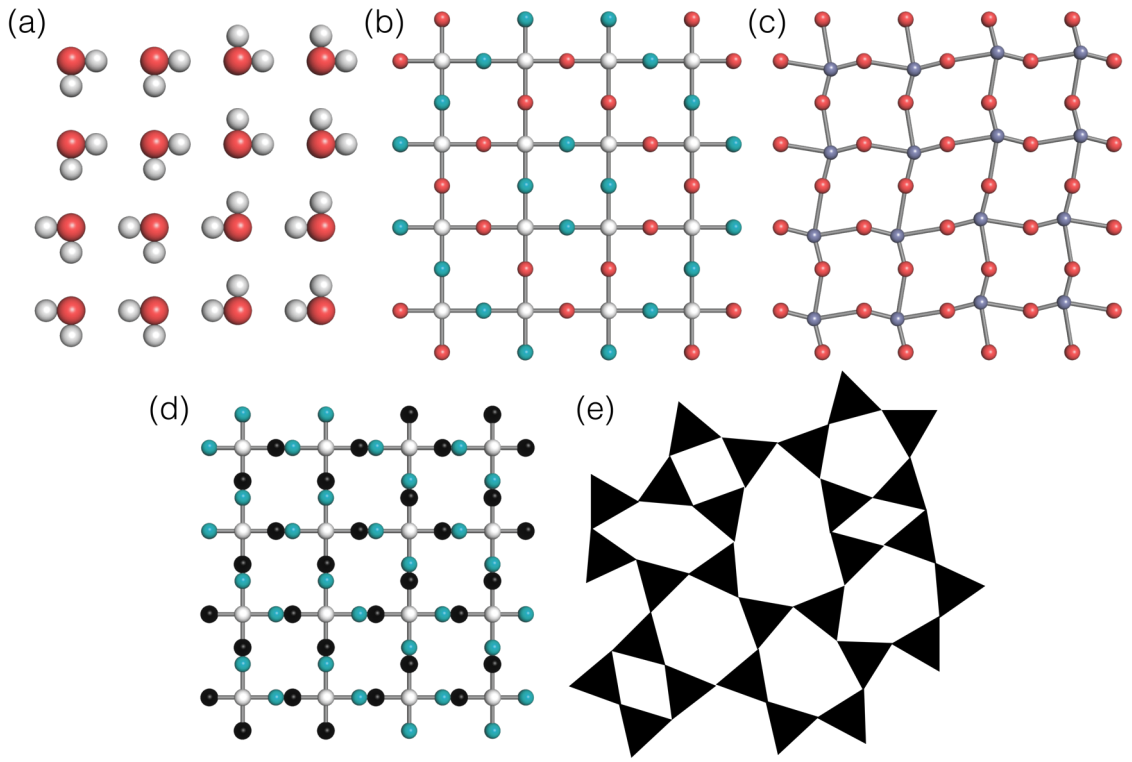

Figure 1.1: (a) Square ice where each water molecule has a bond angle of 90° and bonding rules dictate the directions of hydrogen atoms along each row or column. The disorder present in square ice can be mapped across systems containing (b) compositional disorder, shown here by the positions of oxygen and nitrogen atoms in oxynitrides, (c) positional disorder, in an MO_2 lattice where the metal ion off centres in a correlated fashion so each oxygen is surrounded by one long bond and one short bond, and (d) orientational disorder, represented in a square planar metal cyanide where the disorder comes from cyanide orientations. (e) Topological disorder as seen in a network of SiO_2 tetrahedra.

mapping different types of disorder across length scales and degrees of freedom from seemingly unrelated systems. Below we focus on types of structural disorder.

1.1.2 Compositional disorder

Compositional disorder occurs when different types of atoms can inhabit the same crystallographic site. The degree of correlation between atom types dictates the amount of order in the system. For example, for a binary alloy on a square lattice, correlations can range from fully ordered configurations with a preference for neigh-

bouring non-identical atoms, to completely random configurations in which atoms have no preference in neighbouring like or unlike atoms [21]. The relationship between the Ising model and binary alloys has been presented by many studies [23, 24]. Between the two limiting cases, differing degrees of correlated disorder emerge.

Crystals containing multiple sublattices also exhibit correlated compositional disorder where different atoms are located on the same sublattice. One such example is the case of oxynitride perovskites, where each metal centre is coordinated to two nitrogen and four oxygen atoms. There is a preference for the nitrogen atoms to be *cis* to one another, leading to correlated disorder analogous to that seen in square ice [Fig. 1.1(b)]. Although shown here in two dimensions, correlated compositional disorder can also propagate along three dimensions and in some materials, can change dimensionality by varying strain [Fig. 1.2(a)-(e)] [25]. Compositional disorder can also be caused by vacancy distribution as seen in metal substituted analogues of Prussian blue [Fig. 1.2(f)] [26]. The form of the disorder and extent to which it is correlated greatly effects the materials' properties and has been shown to change with composition, allowing for targeted design strategies for property manipulation [27].

1.1.3 Positional disorder

Positional disorder is present in every material as vibrational motion occurs at all non-zero temperatures, causing atomic displacements about their average site. In most cases, these displacements are uncorrelated and of finite timescale, but when the motion is correlated, it can have an important role in the function of materials

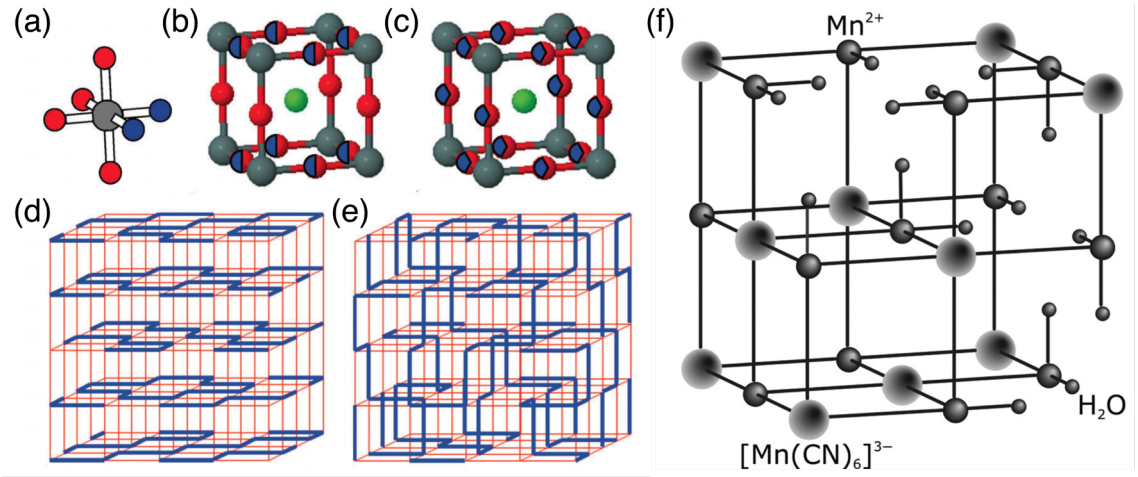

Figure 1.2: Compositional disorder seen in oxynitride pervoskites from connecting (a) *cis* coordination of N atoms in MO_4N_2 octahedra where the blue spheres represent the N atoms and the red spheres represent the O atoms. Average anion distribution in (b) 2D and (c) 3D oxynitride perovskites. View of *cis*-MN chains where the blue/red lines correspond to M–N–M/M–O–M connections respectively (d) confined to 2D as in (b) and Fig. 1.1(b), (e) propagating in 3D as in (c). Figure reproduced from Ref. [25]. (f) Compositional disorder in Prussian blue analogues due to vacancy distribution. Figure reproduced from Ref. [26].

as in the ferroelectric perovskites $PbTiO_3$ [28], $BaTiO_3$ [29], and $KNbO_3$ [30]. At low temperatures, they all contain correlated motion of the ions, resulting in off-centring of the Ti^{4+}/Nb^{5+} ions, lowering the symmetry of the material and causing a ferroelectric response. For $PbTiO_3$, at high temperautres the thermal motion is uncorrelated and the material is cubic. On decreasing temperature the Pb^{2+} and Ti^{4+} cations off-centre along [001] *via* a displacive phase transition, generating a ferroelectric state, evidenced by the soft phonon mode [Fig. 1.3(a)] [31].

Conversely, in $BaTiO_3$ and $KNbO_3$ off-centring occurs along the crystallographic $\langle 111 \rangle$ direction at all temperatures and contains a different degree of correlation as a function of temperature, characterised by single crystal diffraction experiments [Fig. 1.3(b)-(e)] [30]. On heating, both perovskites undergo three main phase transitions; at low temperatures the Ti^{4+}/Nb^{5+} ions off-centre along the crystallographic

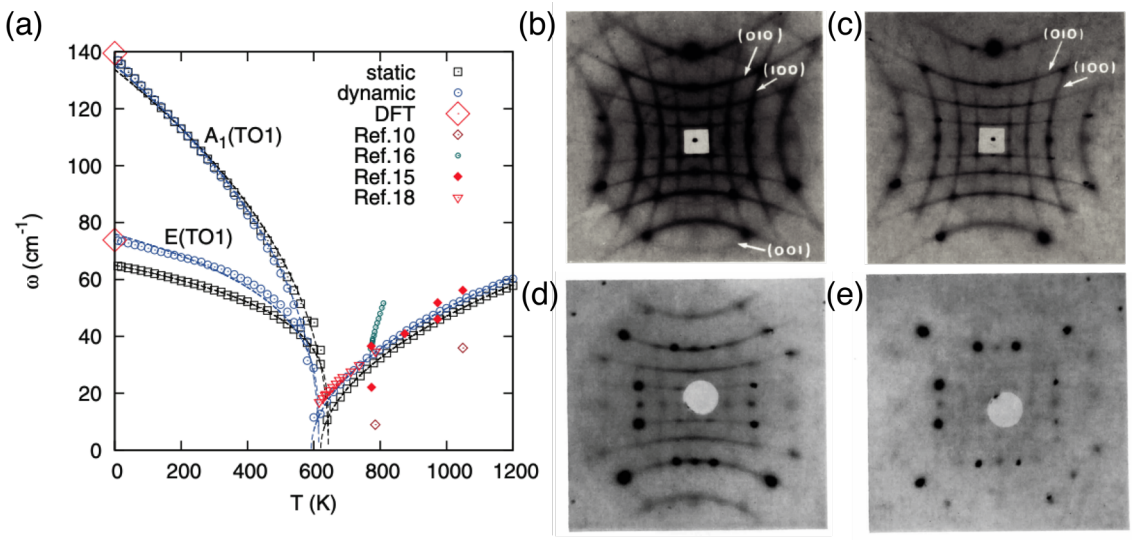

Figure 1.3: (a) Temperature dependence of the soft-mode frequencies of $PbTiO_3$, evidencing the instability of the high-symmetry phase with respect to distortion to the low symmetry phase at just above 600 K, leading to the ferroelectric phase transition. Figure from Ref. [32]. Reprinted with permission from the American Physical Society. Single crystal diffraction patterns of $KNbO_3$. In all phases, the Nb^{5+} ion off-centres towards a face of each NbO_6 octahedron along $\langle 111 \rangle$. The displacements are correlated in chains running along $\langle 100 \rangle$ but each chain is decoupled from neighbouring chains in the cubic phase, reflected in the diffuse scattering (b). The dimensionality of the diffuse scattering is reduced on cooling as the dimensionality of the correlations increases (c)-(e) resulting in a ferroelectric response. Figure adapted from Ref. [30].

$\langle 111 \rangle$ direction with rhombehedral symmetry; increasing temperatures leads to an orthorhombic phase where the ions appear to displace in the $\langle 110 \rangle$ direction; heating further drives a transition to a tetragonal phase where the average structure has the ions displacing along the $\langle 100 \rangle$ direction, and finally there is a transition to the cubic phase where the average position of the Ti^{4+}/Nb^{5+} ions is in the centre of the octahedra [33, 34]. These phase transitions appear, from an average structure perspective, to show the Ti^{4+}/Nb^{5+} displacing along different axes. However, local structure refinements of $BaTiO_3$ [35] show that each individual ion displaces along the $\langle 111 \rangle$ direction at all temperatures and the series of phase transitions on increasing temperature is seen as a disordering of these displacements over one, two,

four, and eight directions respectively [33, 36]. A two-dimensional example of this disorder is represented in Fig. 1.1(c).

Stacking disorder is a subclass of positional disorder which refers to psuedo one-dimensional materials that have strong intralayer interactions but weak interlayer interactions, resulting in disorder. Many materials exhibit stacking disorder: examples include transition-metal cyanides [37]; graphite [38–40]; batteries [41–43], and ice [44]. In each case, the disorder is known to have profound consequences on material properties. Qualitatively analysing the interactions responsible for stacking disorder in materials is a central theme of this thesis which is drawn on in Chapters 3 and 4 as well as studies mentioned in Appendix B.

1.1.4 Orientational disorder

Orientational disorder is a naturally occurring phenomenon in many molecular and inorganic materials with anisotropic components, as their orientation can act as a degree of freedom. The disorder tends to be dynamic at high temperatures where the molecules or molecular ions have enough thermal energy to rotate between molecular orientations [45], and can be frozen in at low temperatures into a correlated, or ordered, fashion [Fig. 1.1(d)]. Some materials such as metal cyanides show two types of orientational disorder [46]. For group-12 metal cyanides such as $Zn(CN)_2$ and $Cd(CN)_2$, the cyanides can be treated as electric dipoles which exhibit orientational disorder through the static orientation of the C and N ions [47, 48]. For alkali metal cyanides, the molecular ions have a more dynamic motion showing continuous rotational diffusion rather than static jump motions [49, 50]. Additionally,

orientational disorder is commonly present in higher symmetry molecules such as the orientation of polyatomic ions in metal-organic frameworks [51], and molecular perovskites [52]. High symmetry molecules containing three-dimensional positional order but orientational disorder are known as plastic crystals [21, 53, 54].

1.1.5 Topological disorder

The types of disorder explained above are all examples occurring in crystals, where the disorder leads to deviations from the average structure on the local scale. As the material maintains an underlying periodicity, the structure can still be described by a space group which greatly simplifies the material's characterisation [13]. Materials containing topological disorder cannot be described by a unit cell and as such are harder to classify [55, 56]. Topologically disordered materials are not considered in this thesis but are mentioned here briefly for completeness. Within topologically disordered materials, the local geometry of each atom is well defined, but fluctuations in bond length and angles lead to aperiodic connectivity, resulting in the loss of long-range order whilst short-range order is maintained [Fig. 1.1(e)]. Formally, topological disorder can be considered as positional disorder but is usually distinguished from positional disorder due to the loss of long-range structure [6].

Noncrystalline or amorphous systems are mostly considered equivalent to those classified as topologically disordered, as no remnants of crystalline structures are retained. These phases are thought to form due to the extra entropic stabilisation from the number of possible configurations relative to the crystalline phase [59]. Although hard to classify, this disorder is nonetheless important to their application

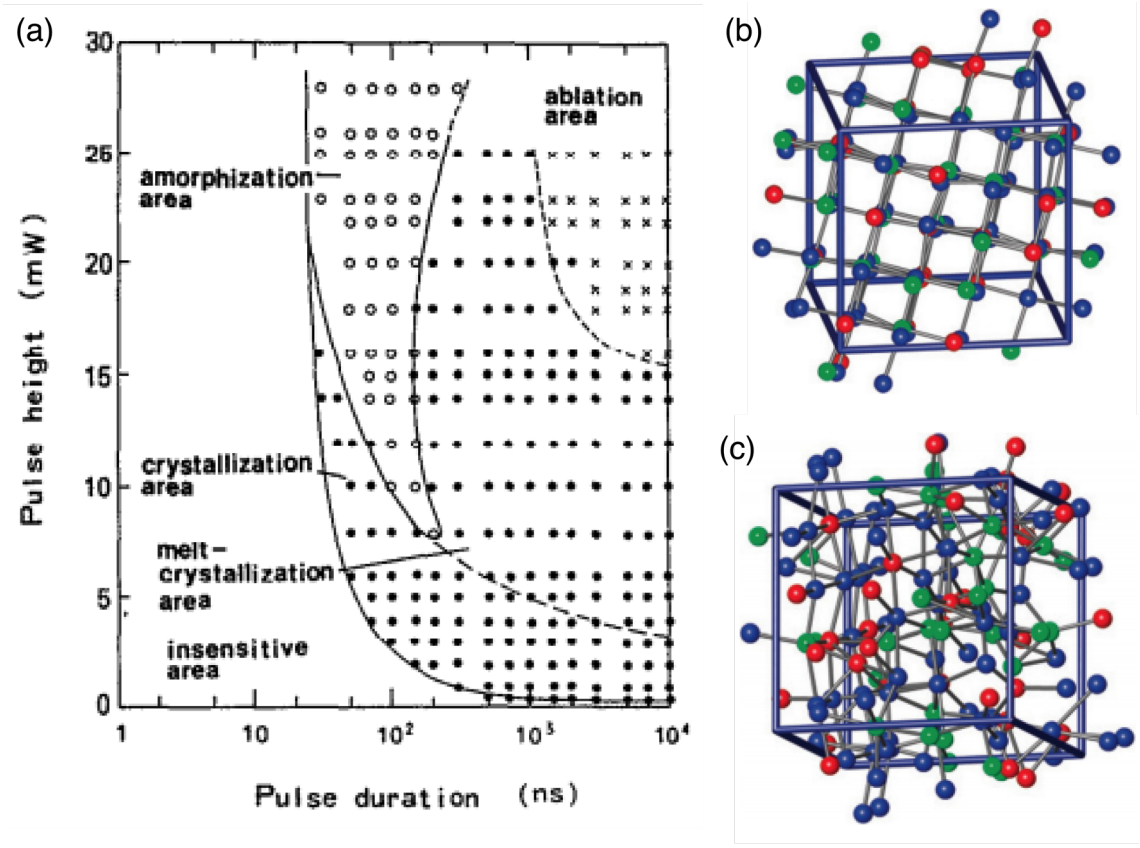

Figure 1.4: (a) Graph of laser pulse heights and durations required for amorphising and crystallizing $GeSb_2Te_4$, evidencing reversible phase changes between the amorphous and crystalline states produced by short laser irradiations. Representative configurations of (b) a crystalline and (c) amorphous phase of GeSbTe materials. Figures reproduced from Ref. [57] and Ref. [58]. Reprinted with permission from AIP Publishing and Springer Nature respectively.

as seen in the crystalline-amorphous phase transitions of GeSbTe materials used in memory technologies [57, 58]. Here the reversibility and short time period of the crystalline-amorphous phase transition on the application of lasers could be applicable to high-speed data recorders [Fig. 1.4] [57]. However, not all amorphous phases are topologically disordered as 'collapsed' MOFs can retain their crystalline topology but do not give Bragg peaks [60]. Conversely, not all topologically disorder phases are non crystalline; one such example is $ZrW_2O_8{\cdot}H_2O$ which forms a spaghetti phase which is topologically disordered but gives Bragg peaks [61].

1.1.6 Characterising disorder

Characterising the structure of materials has become an increasingly routine procedure since the discovery of X-ray diffraction 100 years ago. The underlying premise of crystallographic techniques is the existence of three-dimensional periodicity within materials [4]. However, real materials contain deviations from periodicity due to disorder, manifesting as diffuse scattering in the subsequent diffraction pattern. Although diffuse scattering has been understood and interpreted since the earliest days of crystallography [62], its analysis remains a specialised technique [63–66]. In recent years, characterising disorder is becoming an increasingly simpler task for two main reasons: (1) Vast improvements in experimental capability; (2) Increased access to high performance computing resources.

From an experimental perspective, with the marked improvement of diffraction techniques—including the advent of spallation neutron sources (time of flight), development of synchrotrons, and high sensitivity X-ray detectors—analysis of the relative low intensity diffuse scattering behaviour can be conducted with greater ease, leading to comparatively simpler exploration of disordered materials [67]. The increased sensitivity means weak diffuse scattering contribution (often 2000 times weaker than Bragg scattering) can be measured quantitatively [13].

Methods such as pair distribution function (PDF) have also had a notably increased prominence in the study of materials chemistry [68]. High energy X-ray sources (short λ) allow large $Q_{\max}$, which gives good resolution to PDF, making it a more routine technique. This is an essential development as it helps resolve one

of the fundamental challenges of structural science of combined local and average structural determination [68].

Not all techniques used to characterise disorder are only used due to recent improvements. Nuclear magnetic resonance (NMR), extended X-ray absorption fine structure (EXAFS) and other spectroscopic techniques, are local environment probes, providing a complementary signature of disordered structure to that obtained by scattering [69]. Due to the more widespread use of structural models, these techniques have had an increased prominence in characterising structural disorder. Using many experimental techniques in conjunction allows for individual structural models to be developed to qualitatively account simultaneously for all observations. Moreover, often multiple experimental techniques are employed to help probe and understand disorder over different length scales, for example in determining the defect distribution as in the metal organic framework (MOF) UiO-66 [70, 71] and helping classify transitions as in the semiconductor GeTe [72].

The improvement of experimental techniques for analysing diffuse scattering has led to advances in diffuse scattering analysis, which has coincided with drastically improved computational techniques to model disorder due to increased computing power. Moreover, with increased PDF data collection capabilities came the development of analytical tools through more user friendly software [73–75], allowing for more routine characterisation of local structure containing essential information of disordered materials. Whereas solving the average crystal structure of a material can be implemented systematically using powerful algorithms behind user friendly programs [76–78], analysing diffuse scattering requires a sensible model and therefore *a*

priori knowledge of the material [13]. Analytic models to describe diffuse scattering were first introduced in the early days of crystallography by Debye [79] and Laue [62] and have since been developed to describe a wide variety of systems [80–82]. Using models to help understand disorder has become more widespread in recent years as the computational cost of scattering calculations has vastly decreased, overcoming a key difficulty of using these models in the past [83].

Whilst currently there is no program or routine way to create a model for the disordered interactions within a material, once developed, using modelling techniques such as Monte Carlo (MC) simulations allows for accurate analysis of disordered structures and how they manifest in materials [84]. With the advent of reverse Monte Carlo (RMC) [85], the method eliminated the need of a model when constructing disordered configurations. Rather than minimising the energy of the overall structure with respect to a predefined Hamiltonian as in direct MC, RMC minimises the difference between observed and calculated diffuse scattering intensities as a function of known causes of disorder *i.e.* positional, orientational, and occupancies. In the remainder of Section. 1.1, we proceed by giving an overview of the main experimental techniques used to characterise disordered states, with a discussion for the types of disorder they are most useful for.

Diffuse scattering

In perfect crystalline materials, the long-range periodicity leads to diffraction patterns with characteristically sharp Bragg reflections [86]. Diffuse scattering describes all scattering from a crystal which is not Bragg scattering. Commonly, diffuse scattering is broad and at comparably low intensity, occurring when the crystal structure

is, in some form, aperiodic [63]. The form of diffuse scattering depends on the type of disorder and extent of correlation. In completely disordered phases, the diffraction pattern contains no Bragg peaks and consists only of continuous broad rings due to the incoherent nature of the materials interactions with the radiation source [87]. When the disorder contains some correlations, the diffuse scattering can be structured. Some forms of characteristic diffuse signatures from different structural motifs have been collected in a database [88].

The example of square ice makes clear the relationship between correlated disorder and diffraction patterns. If every water molecule has the same orientation, it leads to an ordered configuration with long-range periodicity and thus the diffraction pattern consists of only sharp Bragg peaks [Fig. 1.5(a)]. In Fig. 1.5(b), the water molecules are allowed to take any orientation but are confined to a square lattice, leading to a diffraction pattern consisting of Bragg peaks from the regular lattice, and broad unstructured diffuse scattering due to the random hydrogen atom orientations. However, when sensible hydrogen bonding rules are followed, the configuration becomes locally ordered but disordered in the long-range. Although these hydrogen positions are not periodic, the disorder correlations give rise to structured diffuse scattering which, in this case, appear as lines of diffuse scattering passing through the Bragg peaks [Fig. 1.5(c)] [12, 89].

Total scattering is one of the most used techniques when extracting information on correlated disordered systems as it gives an overview of both the average, through the Bragg scattering, and local structure, through the diffuse, and is sensitive to both static and dynamic ordering. Importantly, diffuse and Bragg scattering can both

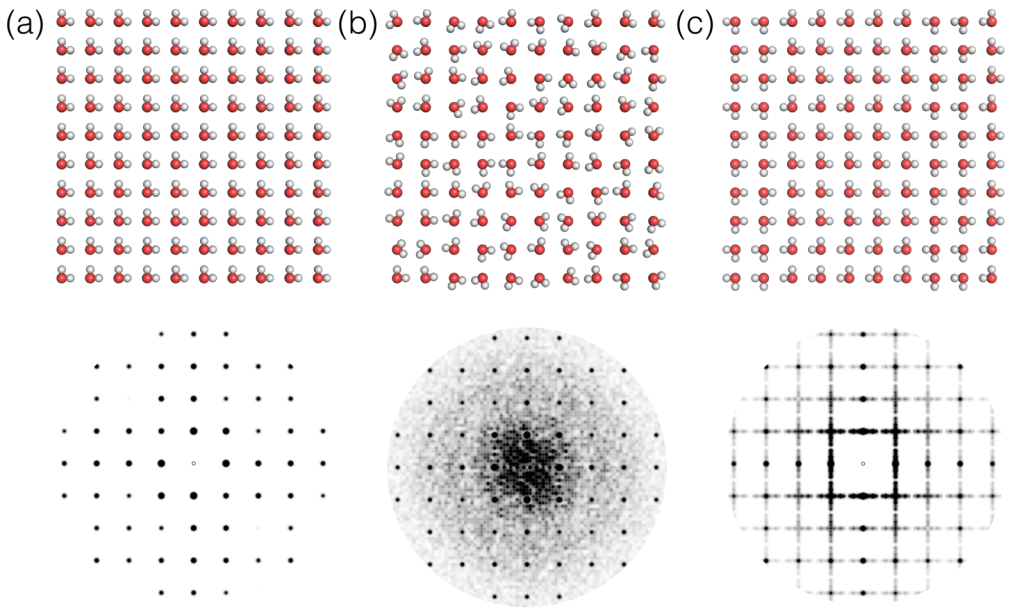

Figure 1.5: Square ice, a simplified two-dimensional representation of the three-dimensional structure of water ice with (a) ordered water molecules, (b) randomly oriented water molecules within the confines of a square lattice, and (c) correlated water molecules where each oxygen atom is covalently bonded to two protons, and hydrogen bonded to two protons, causing correlations of O—H bond directions along each row or column. Below are the corresponding single crystal diffraction patterns for each phase.

be calculated from an atomistic model whereas other local probes such as NMR or EXAFS may require extra information [90, 91].

If there is correlated disorder, careful analysis of the details of the structure can provide valuable information in explaining properties such as ferroelectricity [92] and ion-conductivity [93]. Understanding the local distortions is crucial to explain properties of materials. A key example is in the interpretation of conductive pathways in fast ion conductors where ions move through lattices with liquid-like diffusivities; such materials are commonly used in batteries and capacitors [94, 95]. Using total scattering measurements, the superionic conducting high-temperature δ-phase of Bi_2O_3 was shown to have structural motifs observed in both the α and β phases, which were found to be critical to the functionality [96]. Analysis of diffuse

scattering planes in $BaTiO_3$ evidenced different extents of correlation between chains of neighbouring ion displacements, paving the way for new routes in designing proper ferroelectrics [33, 97].

Computational techniques such as MC simulations are often implemented in conjunction with diffraction techniques where comparison between calculated and observed scattering is used to discriminate between different atomistic models, determining the microscopic interactions responsible for the underlying disorder [98]. Setting up MC simulations requires the user to have a degree of understanding of the interactions present in the material in order to create the initial model. Other modelling techniques are able to refine structures against data with no predefined interactions such as in the case of RMC modelling [85]; however, interpretation of the resulting structure can prove challenging [99]. Moreover, often there is not just one model that fits the experimental signature and a lack of suitable microscopic interactions may lead to what would be considered high energy configurations matching the data. For example, integrating the first peak of the pair distribution function of amorphous silicon can imply an average coordination number of 4, but having half the atoms with coordination number 3 and half with 5 is also consistent with the data [100]. Therefore extra conditions are needed to overcome what is known as the uniqueness problem.

Diffraction is a powerful technique to prove the existence of disorder but is not always able to provide information on the form of the disorder, details of which are particularly useful to know when dealing with correlated disorder. To address this, complementary techniques are available that provide details of the local behaviour

of the structures, which highlights correlations within the structure.

Pair distribution function

The pair distribution function (PDF) is a 1D function produced by taking the Fourier transformation of the total scattering, revealing information on the real space correlations from the local structure. In the case of materials which can be described with a space group, local structure probes along with diffraction techniques are sufficient in describing the structure of the material, and in fact, PDF techniques are able to do both simultaneously [Fig. 1.6(a)-(b)] [68, 101]. PDFs are well defined irrespective of the presence of long-range order as they essentially provide a 'histogram' of the interatomic distances weighted by the atomic scattering lengths, making it suitable for studies of disorder where long-range order is absent [73].

From single crystal data, 3D-PDFs can be used to produce directional information about correlations within the system, as opposed to their projections onto 1D. Since the correlations are dominated by the average structure, for studying disorder we remove the Bragg peaks before the Fourier transform so that all we see are deviations from average resulting in a spatial resolved map of the disorder correlations. This is known as 3D-ΔPDF [102, 103] which was developed for advanced characterisation of disorder types. Although diffuse scattering and 3D-ΔPDF maps contain the same information, the maps are more intuitive and allow for the classification of the disorder [Fig. 1.6(d)-(e)] [104, 105]. This is particularly fruitful when the disorder within the material emerges from multiple sources as it allows for categorisation into component parts.

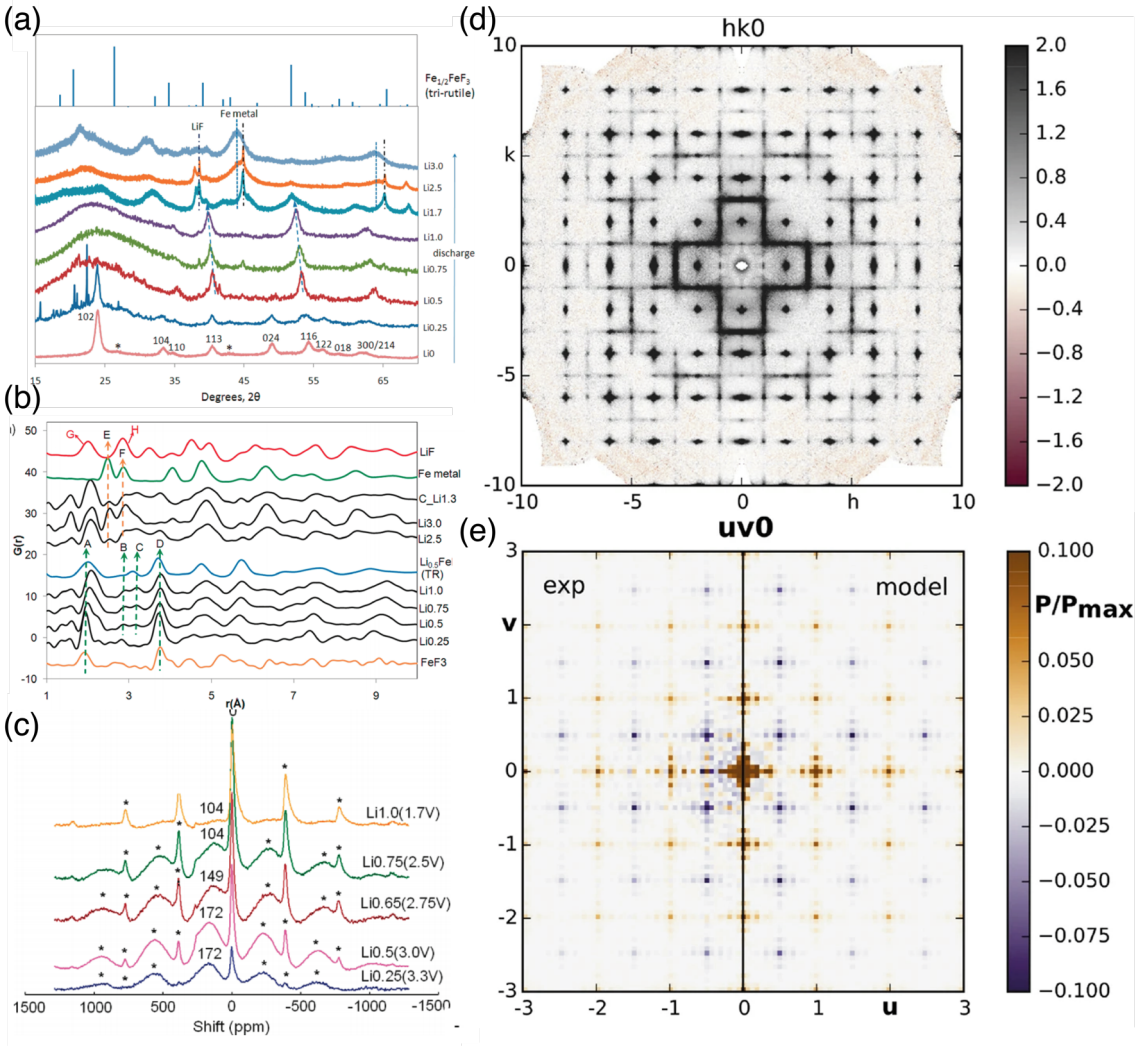

Figure 1.6: . (a) Powder X-ray diffraction, (b) PDF, and (c) ^{7}Li NMR spectra of Li_xFeF_3 with varying composition, x, used in conjunction to determine the local structure of the battery material on cycling. Figure reproduced from Ref. [101]. (d) $hk0$ section of experimental diffuse scattering from the Prussian blue analogue $Co[Co(CN)_6]$. (e) $uv0$ section of experimental and model 3D-ΔPDF map of the sample evidencing positive (red) and negative (blue) correlations indicative of substitutional disorder. Figure reproduced from Ref. [27]. Adapted with permission from Springer Nature.

Other local structure probes

Local structural probes do exactly that, probe the local structure, so many are unable to provide much useful information on the longer range structure of the material. In the case of materials which can be described with a space group, the underlying

periodicity issues a relatively easy starting point in the progression of studying and classifying these phases. However, many disordered phases cannot be defined by the average structure, and for these phases, other techniques are required. EXAFS, infrared (IR) and NMR are complementary as their sensitivity to short-range correlations is helpful for almost all disordered phases, and for topologically disordered phases, proves essential [106–109]. These techniques are often used in conjunction with average structure determination such as diffraction techniques [Fig. 1.6(a)-(c)] [42, 73].

The choice of local structure probe is heavily dependent on the material studied and the type of disorder present. NMR studies are particularly useful when looking at dynamic disorder as time-resolved measurements can be used to look at cation rearrangement [108], whereas IR absorption is best when the local feature of interest is sensitive to vibrational frequencies as in compositionally disordered hybrid perovskites [110]. For topologically disordered structures, although there is no long-range order, the intermediate structure may play an important role in the materials properties and to encapsulate this information, direct imagine techniques are particularly helpful.

Direct imaging

Imaging techniques—including electron microscopy—are powerful methods to view the projections of the network connectivity of a material directly. This proves particularly useful when studying two-dimensional materials where the absence of bulk material in three dimensions makes crystallographic investigation more challenging [112]. These procedures offer the spatial resolution for atomic- and nano- scale be-

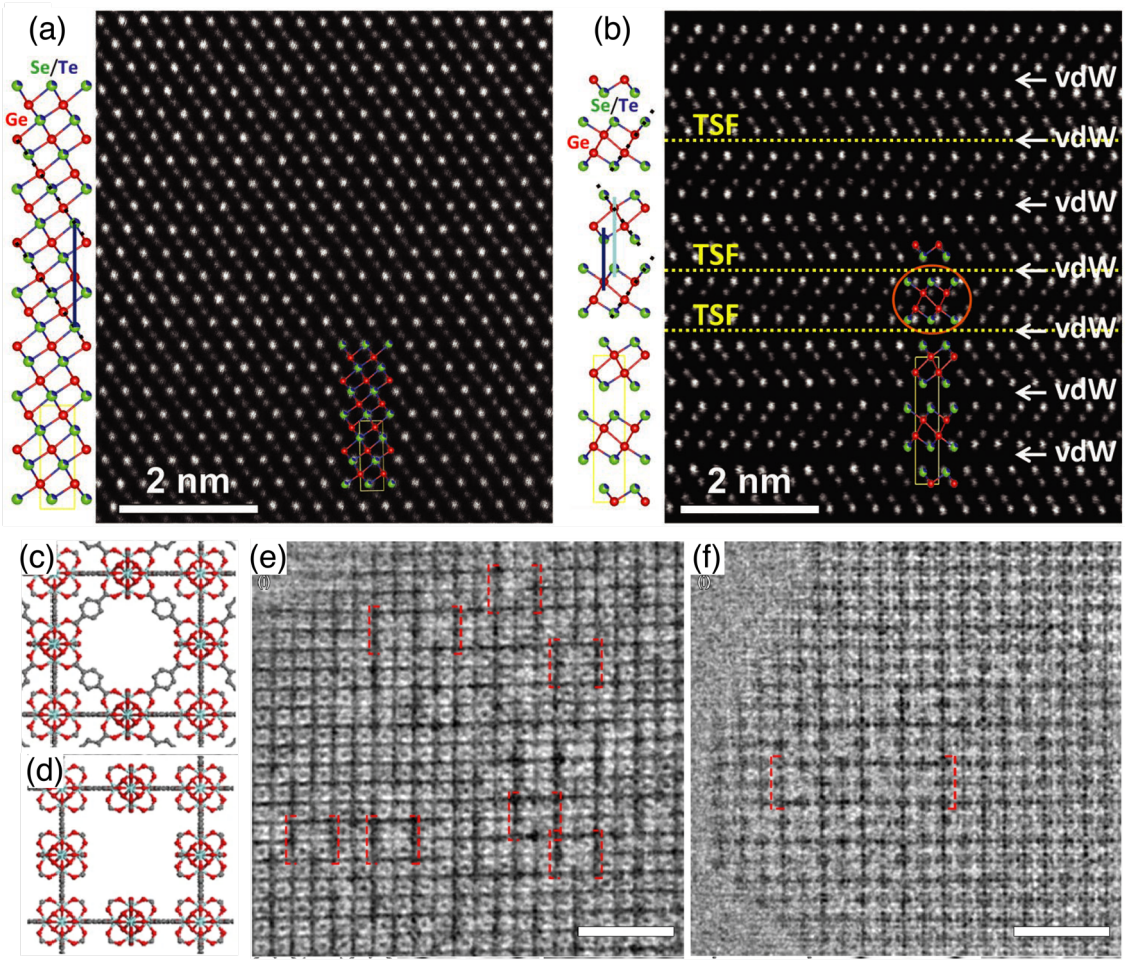

Figure 1.7: High angle annular dark field scanning transmission electron microscopy images of Ge_4Se_3Te along the [100] zone axis in the (a) metastable ordered structure, and (b) stable phase with translational shear faults (TSFs). Representative structures are shown to the left where the Ge, Se, and Te atoms are red, green, and blue, respectively. The yellow dotted lines indicate the translational shear faults occuring in the van der Waal (vdW) gaps. Reproduced from Ref. [111]. (c)-(f) High-resolution transmission electron microscopy images of defective UiO-66 in the [001] direction evidencing different types of missing-cluster defects. (c)/(d) Representative structural units with the missing cluster characterised from (e)/(f) respectively. Figure reproduced from Ref. [71]. Adapted with permission from Springer Nature.

haviour, revealing stacking faults in layered materials [Fig. 1.7(a)-(b)] [111] as well as allowing for defect characterisation as in MOF UiO–66 [Fig. 1.7(c)-(f)] [71]. As such, imaging can encapsulate many types of topological disorder and has been successful at determining both cation and structural disorder in materials [113, 114]. The benefits of this technique lie in the direct, real space, observation of disorder

and/or phase boundaries without having to interpret reciprocal space. However, a major drawback is that many materials undergo significant damage under a low cumulative electron dose [115]. This is the case for many of the materials considered within this thesis and so, with the exception of Chapter 3, direct imaging is not used. Instead this thesis principally relies on a combination of X-ray diffraction techniques and Monte Carlo simulations to characterise disorder.

1.2 Microscopic models of complex systems

Statistical mechanical models assume a particular importance in contemporary condensed matter physics because they establish a link between microscopic interactions in a system and its macroscopic properties (*e.g.* symmetry). Although seemingly simple, these models are able to correctly encapsulate the phase behaviour of materials with very few parameters. Particularly useful for complex systems, one of the key long-realised results is that simple interactions can give rise to complex phases [116, 117]. Often, statistical mechanical models are phrased in terms of spin models.

Spin models vary due to the dimensions and interactions involved in the material. It is important to note that the models contain two different types of dimensions: one referring to the dimensionality, D, of the spins; the other referring to the dimension, d, of the lattice on which the spins sit [118]. Throughout the thesis we explore materials with different dimensions, both in spin—D—and lattice—d—, starting from the simplest case where $D = 1, d = 1$ and increasing D as we progress through the chapters. To begin with, we explore spin models interacting through only exchange energy in systems with increasing number of dimensions, D. Magnetism is inher-

ently a quantum phenomena as it arises from the behaviour of electrons, however, in materials where the spin quantum number $S > 1$, spins can be approximated as classical vectors; this is the case for most models considered throughout the thesis. We include a discussion of implications where this assumption might not hold true in Chapter 4. For the models described below, all spins are assumed to be classical.

1.2.1 Ising model

The simplest model for interacting spins is when $D = 1$, *i.e.* a spin can be oriented in either an 'up' or 'down' state [Fig. 1.8(a)]. This is known as the Ising model which is used in magnetism to explore ferromagnetic and antiferromagnetic behaviour [119]. For classical cases, the model works by defining a variable, S_i, with a discrete value of ± 1 that represents the spin state of the magnetic ions. The Hamiltonian for the exchange interaction between Ising spins is

$$H = -\sum_{ij} J_{ij} S_i S_j, \tag{1.1}$$

over sites i, j. When $J_{ij} > 0$, the energy of the system is minimised in the ferromagnetic regime (neighbouring spins align) and when $J_{ij} < 0$ the antiferromagnetic regime (neighbouring spins anti-aligning) is preferred. Although this model accounts for the pairwise interactions of all spins in the material, the strength of J_{ij} drops off drastically with the distance between spins and thus it is usually sufficient to a first approximation to account only for the nearest neighbour interactions, J_1. Where this is insufficient, including a second and third nearest neighbour term with smaller exchange energies tends to account for the energetics.

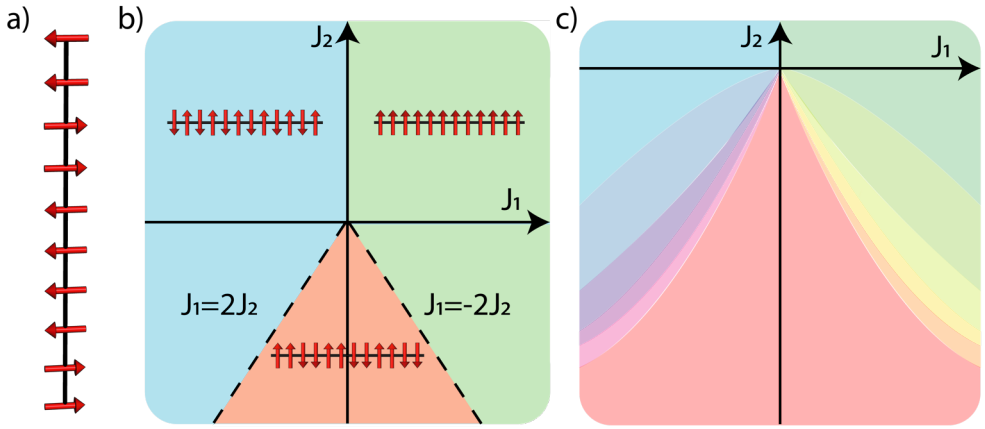

Figure 1.8: (a) A chain of Ising spins whose energetics can be described by the Ising model [Eqn. 1.1] (b) Schematic ground state phase diagram for the ANNNI model described in Eqn. 1.2 with different interaction strengths resulting in three phases; antiferromagnetic (blue), ferromagnetic (green), and a frustrated phases described as $\langle 2 \rangle$ (red). (c) Schematic phase diagram of the ANNNI model at finite temperature. Each colour represents a different modulation of spin structures. Clockwise from top right the phases are, ferromagnetic $\langle \infty \rangle$, $\langle 3 \rangle$, $\langle 23 \rangle$, $\langle 2^2 3 \rangle$, $\langle 2^3 3 \rangle$, $\langle 2 \rangle$, $\langle 12^4 \rangle$, $\langle 12^3 \rangle$, $\langle 12^2 \rangle$, $\langle 12 \rangle$, and antiferromagnetic $\langle 1 \rangle$.

Axial next-nearest neighbour model

For one-dimensional, d, systems, if extra terms are required, commonly the model is only extended to next-nearest neighbour interactions, forming the axial (or anisotropic) next-nearest neighbour Ising model (ANNNI) [120, 121],

$$H = -J_1 \sum_{ij \in nn} S_i S_j - J_2 \sum_{ij \in nnn} S_i S_j. \tag{1.2}$$

At 0 K, the model forms three ground states: an antiferromagnetic ground state when $J_1 < 0$ and $J_1 < 2J_2$; a ferromagnetic ground state when $J_1 > 0$ and $J_1 > -2J_2$; and a frustrated ground state of alternating two 'up' spins and two 'down' spins between the two cases [Fig. 1.8(b)]. Commonly, phases formulated by the ANNNI model are described by the number of spins in each domain using the

Zhdanov notation [122, 123]. For example the antiferromagnetic phase with alternating up and down spins has one spin in each domain (... ↑↓↑↓↑↓ ...) so is denoted as $\langle 1 \rangle$, whereas the ferromagnetic phase has an infinite number of spins in its domain (... ↑↑↑↑↑↑ ...) and is therefore denoted as $\langle \infty \rangle$. The frustrated modulated ground state has two spins in each domain (... ↑↑↓↓↑↑↓↓↑↑↓↓ ...) and is denoted by $\langle 2 \rangle$. This allows for a quickhand notation of more complex modulated states with a mix of domains such as $\langle 12^4 \rangle$(... ↑↓↓↑↑↓↓↑↑↓↑↑↓↓↑↑↓↓ ...) where the superscript represents the number of domains which contain the same number spins.

Although there are only three states in the low temperature limit, the interest in the ANNNI model stems from the seemingly endless number of thermodynamically stable modulated phases that are formed at finite temperatures around the phase boundaries [Fig. 1.8(c)]. Through its simplicity, this model contains a wealth of different phases exhibiting sophisticated behaviour with just the combination of two pairwise interactions [117], and proved pivotal in interpreting incommensurate phenomena in condensed phases [116]. The ANNNI model can predict and rationalise an assortment of distinct commensurate modulated phases [117]. Hence, given the right chemical ingredients, simple models can lead to incredibly complex phases, largely due to frustration from constraints on the degrees of freedom set out by the interactions (*e.g.* geometric or magnetic) [22].

1.2.2 Frustration

Frustration in classical materials can arise from several different sources. The first occurs when Hamiltonians contain competing interactions, as described above, which

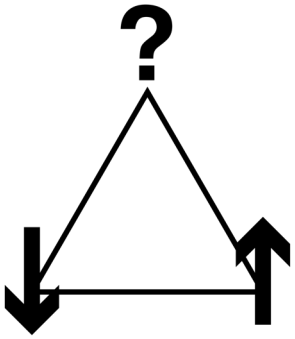

Figure 1.9: Triangular Ising antiferromagnet where Ising spins on the vertices couple antiferromagnetically. The first two spins are able to sit antiparallel to one another but the third spin must be parallel to one of the first two spins, leading to a frustrated interaction.

cannot simultaneously be minimised [124]. The second arises in ground states of materials where there is a mismatch between the degrees of freedom in question and the underlying lattice. This mismatch causes the interacting components to either be under-constrained or over-constrained, both resulting in disordered phases but with different root causes. For under-constrained degrees of freedom, the structure has energetically indistinguishable arrangements of the states, leading to degenerate ground states much like the formation of the correlated disorder seen in square ice [Fig. 1.1(c)]. For over-constrained states, the degrees of freedom are frustrated from unsatisfied interactions.

An exemplary case of over-constrained degrees of freedom is the triangular Ising antiferromagnet (TIA) where Ising spins decorate the vertices of a triangle and couple antiferromagnetically [125]. The first two spins can be placed antiparallel, satisfying the antiferromagnetic interactions, but the third spin has no choice but to lie parallel to one of the two spins and cannot completely satisfy the interactions [Fig. 1.9]. Analogues to the TIA are well characterised and map across degrees of freedom and length scales, including the resonating valence bond model used

to describe the electronic structure of graphene and its analogues [126], stacking disorder in supramolecular systems [127], and geometrically frustrated orbital order in $Ba_3CuSb_2O_9$ [128]. For under-constrained disorder, the example of square ice and its analogues [Fig. 1.1(a)-(e)] highlight the numerous length scales and degrees of freedom that can be spanned.

Although they descend from different causes, there are many parallels to be made between under-constrained disorder and frustration. From an experimental viewpoint, it is almost impossible to distinguish between the two. Both lead to long-range disorder and scattering that diverges from well-understood Bragg scattering, both have residual entropy at 0 K, and both show anomalous behaviour in their specific heat [12]. Therefore, in order to determine the cause of the disorder, an understanding of the degrees of freedom within the material and their interactions is essential for correct characterisation.

1.2.3 Ices

One of the best studied examples of frustration is the group of compounds known as ices. Although many different lattices can be categorised as ices, we focus on those whose degrees of freedom are arranged on a lattice comprised of corner sharing tetrahedra (called a pyrochlore lattice) such that they abide by a 'two-in-two-out' rule, first named by Pauling when studying the atomic arrangement of ice [2]. The interest in these materials lies in their physics associated with excitations out of the local order [129].

The namesake of the so-called 'ice rules' is due to the discovery of the rule in

water ice [1]. Water ice was key in identifying the need for both average and local experimental probes. It was initially thought that the position of the hydrogens were halfway between the oxygens [130–132]. Both Raman spectra [1]—suggesting the retention of the molecular nature of H_2O—and heat capacity measurements [133]—evidencing residual entropy at 0 K—lead to the reasoning that this was not the case. Theoretically, the seemingly anomalous behaviour was rationalised using the Bernal-Fowler 'ice rules' [1] and quantified by Pauling [2]. Much like in the analogous square ice, the local rules which form the ice rules are set out by the bonding interactions between the oxygen and hydrogens. Each oxygen sits in the centre of the tetrahedra and is surrounded by four hydrogens which lie along the four $\langle 111 \rangle$ axes, two that are covalently bonded, and two which are hydrogen bonded. Each tetrahedra contains two covalently bonded hydrogens pointing 'in' and two hydrogen bonded hydrogens pointing 'out' [Fig. 1.10(a)]. Frustration ensues as there are six configurations of protons around an oxygen in any tetrahedron which satisfy the ice rules. The local order imposed by the ice rules impacts both the structure and dynamics of water ice, affecting its elastic, electrical, and optical properties [134].

Water ice was the first material identified as following these rules, but mappings of the degrees of freedom to other compounds have been well established and used to explain anomalous behaviour [89]. The equivalence of ice rules originating from other degrees of freedom was first noted by Anderson in 1956 [137]. He suggested that the degeneracy in water ice was also seen in the charge ordering in the inverse spinel Fe_3O_4 [Fig. 1.10(b)] [137]. In the same seminal paper, Anderson also predicted that perhaps spins sitting on a pyrochlore lattice may also show similar degeneracy

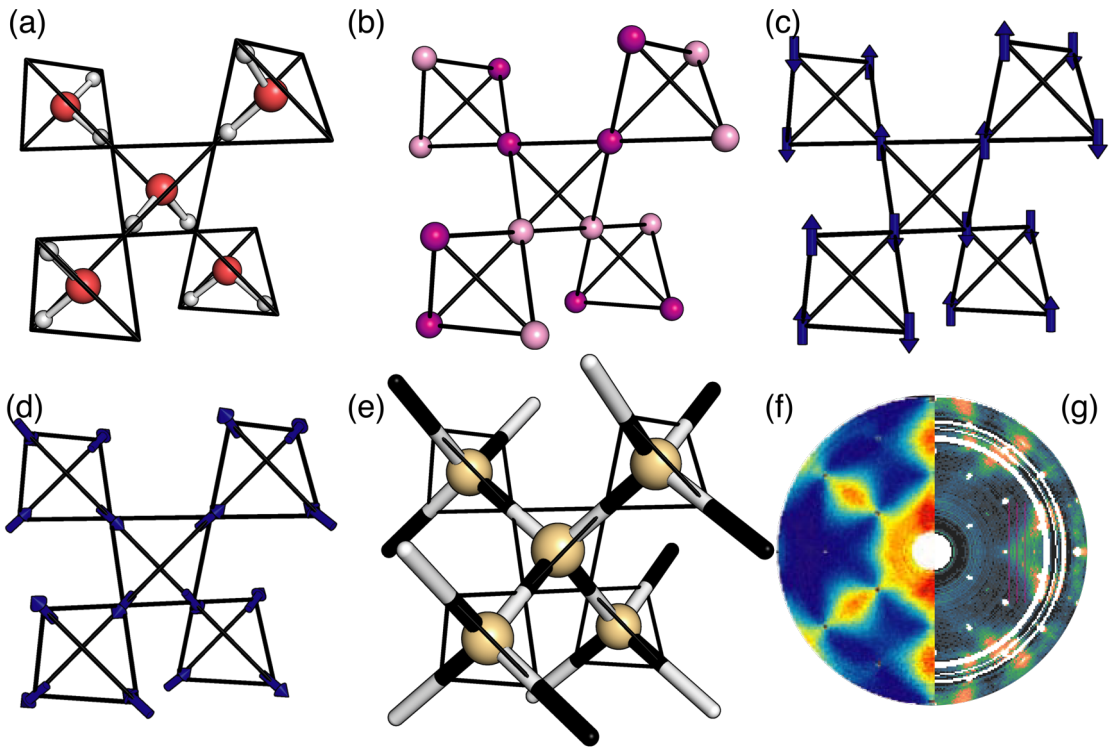

Figure 1.10: Ice mappings which abide by the 'two-in-two-out' rule. Ice rules in (a) cubic ice VII, (b) compositional order or charge ordering of ions, for example in inverse spinels, (c) antiferromagnetic Ising spins coupled along the [001] axis, (d) ferromagnetic interactions between ⟨111⟩ Ising spins in spin ices *e.g.* $Ho_2Ti_2O_7$, and (e) cyanide orientations in $Cd(CN)_2$. The characteristic pinch points in reciprocal space for (f) the spin ice $Ho_2Ti_2O_7$ from magnetic diffuse scattering measurements (reproduced from Ref. [135]) and (g) the ordering of Ni^{2+} and Cr^{3+} in $CsNiCrF_6$ from structural diffuse scattering measurements (reproduced from Ref. [136]). Adapted with permission from Springer Nature.

to that of water ice where antiferromagnetic Ising spins coupled along one of the ⟨100⟩ axes [Fig. 1.10(c)]. In a cubic material however, there is no reason for one axis to be preferred and, unsurprisingly, no state has been observed experimentally [89]. Perhaps the example that has caused the most excitement within the field is spin ice, first evidenced in $Ho_2Ti_2O_7$ [138]. In these materials, rare earth magnetic ions sit on the corners of the tetrahedra and behave as Ising spins pointing along the ⟨111⟩ axes—towards or away from the tetrahedra. The ferromagnetic coupling between spins causes two spins to point into the tetrahedra and two spins to point

out [Fig. 1.10(d)].

More recently, other degrees of freedom have been mapped onto ice rules including orbital ices where the orbital ordering of the spin glass $Y_2Mo_2O_7$ distributes Mo^{4+}—Mo^{4+} dimers according to the ice rules [139], and dipole ices through the orientation of cyanides within the framework $Cd(CN)_2$ [48]. $Cd(CN)_2$ consists of two interpenetrating diamondoid frameworks with tetrahedrally coordinated Cd atoms [140]. The position/orientation of the cadmium/cyanide ions can be mapped onto the position/bonding of the oxygen/protons such that there are two carbons and two nitrogens surrounding each cadmium in a two-in-two-out fashion [Fig. 1.10(e)] [48]. This structure has a substantial effect on the properties of the material which are discussed in more detail in section 1.4.1 [20].

1.2.4 Potts model

So far in this section, all models used to describe interactions have interacted by (or been analagous to) Ising spins [Fig. 1.11(a)]. Ising spins can describe the behaviour of magnetic systems with high single-ion anisotropy; causing the spins to preferentially lie along one axis. Depending on the dimensionality of the lattice, Ising interactions occur in multiple directions and as evidenced from Section. 1.2.3, are not limited to a one-dimensional, d, chain. Similarly, spins can have increased dimensionality. Two-dimensional, D, interactions can either contain continuous degrees of freedom as in the XY model, or discrete degrees of freedom such as in the Potts model [141, 142]. In the Potts model, the Hamiltonian is such that,

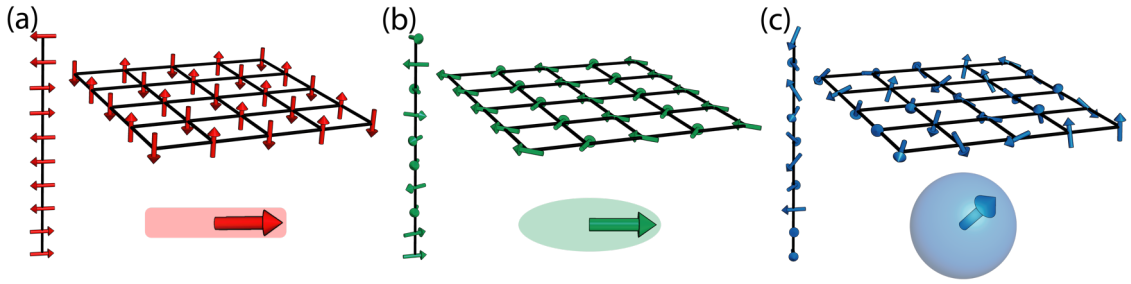

Figure 1.11: Magnetic models with (a) one degree of freedom (Ising), (b) two degrees of freedom (XY model), and (c) three degrees of freedom (Heisenberg model). Each of these models are shown for a one-dimensional chain (left), and a two-dimensional plane (right). Diagrams below represent the degrees of freedom navigated by each spin.

$$H = -J \sum_{ij \in nn} \delta(S_i S_j), \tag{1.3}$$

where the Kronecker delta function is defined as

$$\delta(S_i S_j) = \begin{cases} 1, & \text{if } S_i = S_j, \\ 0, & \text{if } S_i \neq S_j. \end{cases} \tag{1.4}$$

The variable $S_i = 1, 2, ..., N$, depending on the number of states in the Potts model, N. Potts models have wide-reaching applications in many complex systems [143, 144] for modelling multidimensional order such as the multipolar order seen in cyanoelpasolite molecular perovskites discussed in section 1.4.2 [52], magnetic phase transitions [145], and structural phase transitions as shown in the perovskite $SrTiO_3$ [146]. In the limit where $N \to \infty$, the model contains continuous degrees of freedom and becomes the XY model.

1.2.5 XY model

The degrees of freedom in a magnetic system need not be discrete and the simplest model with continuous degree of freedom arises when spins are confined to lie in a plane, known as the XY model [Fig. 1.11(b)] [147]. The Hamiltonian has the form

$$H = \sum_{ij} (J_x S_i^x S_j^x + J_y S_i^y S_j^y), \tag{1.5}$$

where the interactions strengths can differ between directions and, in the classical case, $\mathbf{S}_i = (S_i^x, S_i^y) = S(\cos\theta_i, \sin\theta_i)$ with arbitrary magnitude S and phase θ_i. Materials exhibiting this behaviour are of particular interest to the condensed matter physics community due to the onset of topological order explained in more detail in section 1.3.3 [148, 149]. Materials which interact *via* the XY model must contain large xy anisotropy [150]. Therefore target systems mostly consist of layered materials. For example, $CoCl_2$ is a layered structure consisting of hexagonal layers of Co^{2+} in a triangular net separated by two hexagonal layers of Cl^- and was found to interact *via* the 2D XY model [151]. The XY model is not only used to describe magnetic degrees of freedom. Mapping magnetic spins to the phase angle between polymer chains led to the surprising discovery of topological order within supramolecular assembly of inorganic polymers, discussed in more detail in Section 4.2 [152].

1.2.6 Heisenberg model

For materials with no constraints on their degrees of freedom, D, the spins can propagate in all three dimensions and the interactions follow the Heisenberg Hamiltonian

[Fig. 1.11(c)] [153]:

$$H = \sum_i (J_x S_i^x S_{i+1}^x + J_y S_i^y S_{i+1}^y + J_z S_i^z S_{i+1}^z), \tag{1.6}$$

where, in the classical limit, $\mathbf{S}_i$ represents a three-dimensional vector that can be split into its three components $\mathbf{S}_i = (S_i^x, S_i^y, S_i^z)$. A variety of different ground states form depending on the relative interaction strengths and signs of J_x, J_y, and J_z [150]. Of particular importance to this thesis is the case where $J_x = J_y$, known as the Heisenberg XXZ model [150]. Many magnetic systems can be modelled using the Heisenberg model, and some Fe^{2+} and Ni^{2+} compounds such as $FeCl_2{\cdot}2H_2O$ and $Ni(CN)_2NH_3C_6H_6$ transition from Heisenberg spins at high temperature to being strongly anisotropic at lower temperatures and are often thought of as Ising-like spins [154]. Care has to be taken when studying these materials as their behaviour may differ from theoretical models due to the change in spin degrees of freedom with temperature [154].

Most real magnetic materials have exchange interactions between neighbouring spins to some extent, but other interactions may come into play from the local or global environment. These interactions are usually smaller in magnitude than the exchange interactions but have important effects on the magnetic ground states of the materials and can lead to the formation of complex phases. This is especially true in frustrated materials, as the lattice geometry means there is a lack of long-range magnetic order from exchange alone [155]. There are several possible interactions that exist in magnetic materials that can be included in the Hamiltonian such as a dipolar coupling [156, 157], biquadratic exchange ($\propto (\mathbf{S}_i \cdot \mathbf{S}_j)^2$) [158], and, of

particular relevance to this thesis, the Dzyaloshinsky-Moriya interaction [159, 160].

1.2.7 Antisymmetric interactions

Certain magnetic spins that reside in chiral magnets are subject to the Dzyaloshinsky-Moriya interaction, also known as antisymmetric exchange which, when combined with a ferromagnetic interaction, lead to the emergence of phases on the mesoscopic scale due to the competing interactions [161]. Introducing a magnetic field causes the spins to couple to the field. The combination of the three interactions leads to exotic magnetic phases, the most studied of which is the non-trivial topological texture known as a Skyrmion [162]. These textures are of scientific curiosity due to their stability, small size, and potential capacity in the development of new materials such as storage and low-energy spintronic devices [163–165]. A schematic phase diagram for a skyrmionic system is given in Fig. 1.12(a) and can be theoretically reproduced using the Hamiltonian

$$H = J\sum_{ij}\mathbf{S}_i\cdot\mathbf{S}_j + K\sum_{ij}(\mathbf{S}_i\times\mathbf{S}_j)\cdot\mathbf{r}_{ij} + \mathbf{B}\cdot\sum_i\mathbf{S}_i. \tag{1.7}$$

The variables $\mathbf{S}_{i,j}$ are the spins on the atomic sites i, j, $\mathbf{r}_{ij}$ is known as the Dzyaloshinskii vector—the vector between the magnetic ions—and $\mathbf{B}$ is the magnetic field. These interactions, when combined, give rise to three different textures: helical, conical, and skyrmionic [Fig. 1.12(b)-(d)] [161, 166–168].

Accessing the area of the phase diagram responsible for skyrmions proves tricky

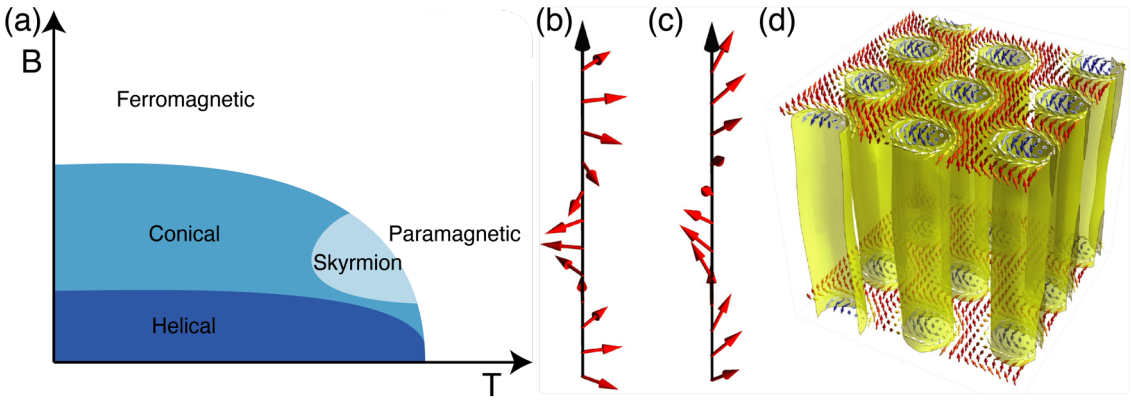

Figure 1.12: (a) Schematic phase diagram for a typical skyrmionc system showing three mesoscopic phases with representative configurations (b) helical, (c) conical, and (d) skyrmion phases adapted from Ref. [167] with permission from the American Physical Society.

as there are very few candidates that are driven by the three interactions and even fewer with the required relative strengths to produce a skyrmion [166, 169]. Since their experimental discovery in 2009 [165], there have been increased efforts to find materials that fit the criteria with varying success [168, 170, 171]. Recently, skyrmions were theoretically predicted to arise in non-chiral magnetic materials with frustrated interactions [172] and similar vortex-like states have been evidenced in frustrated A-site spinels [173].

Skyrmions are certainly the most studied, but not the sole topological defect known to form in magnetic materials. Similar vortex-like states such as merons, antimerons, and antiskyrmions are evidenced and can even exist within the same material under different physical conditions [174]. Moreover, vortices are not the only source of topological defects in magnetic materials and magnetic excitations out of the ground state can also form topological defects such as monopoles [175].

1.3 Emergence in complex systems

The formation of mesoscopic skyrmionic states comes from the underlying competition between the microscopic interactions outlined in Eqn. 1.7 [176]. Likewise, many other disordered states support emergent phenomena operating on much larger length scales than their underlying degrees of freedom [27]. Often the emergent behaviour has interesting physics associated with it, potentially leading to properties that could be utilised in industrial applications. For example, vortices which form in materials whose degrees of freedom are described by the XY model have potential application in data storage [177], and excitations out of spin ice—monopoles—are thought to have applications in magnetronic devices [178–180]. In this section we shall give an overview of different emergent behaviour through topological states of matter, before discussing relevant emergent phases in a range of materials.

1.3.1 Topological states

Topological defects occur in a wide variety of systems such as soft matter [181], superfluid liquids [182], thin magnetic films [164], and cosmology [183]. Commonly, topological defects are defined by a point singularity where the degrees of freedom (such as spins or molecule orientation) cannot be continuous at a specific point within the defined dimensions of the material [184]. In most magnetic materials, defects can be removed through continuous distortions, restoring alignment of the spins [Fig. 1.13(a)]. However, in some it is impossible to align all the spins without tampering with spins an arbitrary distance from the core [Fig. 1.13(b)]. Thus the discontinuity is deemed topologically stable [184]. For example, vortex formation in

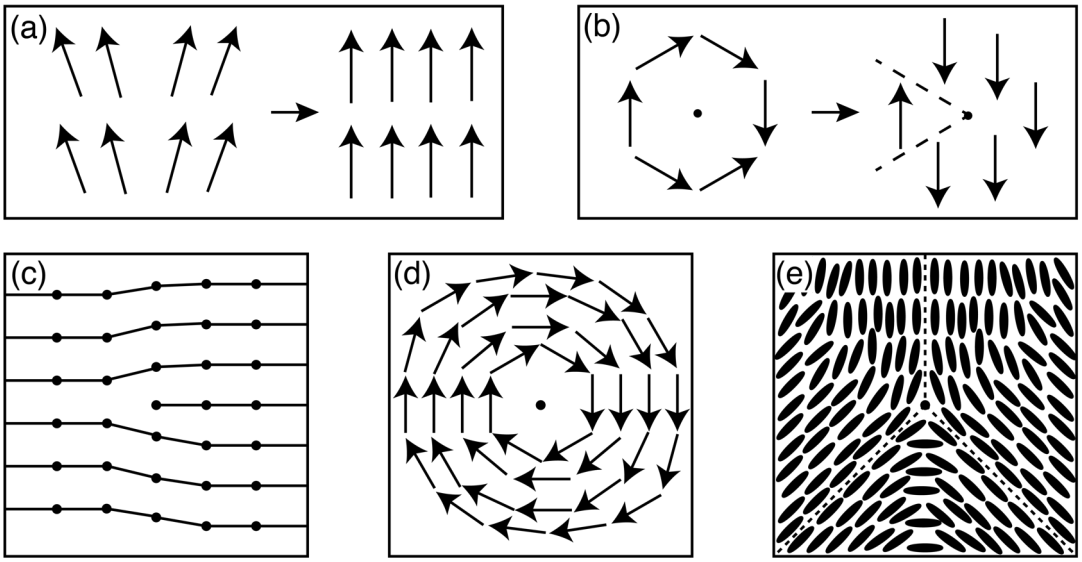

Figure 1.13: (a) A non topological defect that can be distorted continuously from the singularity free state to a state of total alignment. (b) A topological defect that can not be aligned by a contninuous distortion. When the spins attempt to align, boundaries appear (dashed lines) where the spin changes rapidly from up to down. Examples of topological defects in three materials (c) dislocations in crystalline solids, (d) vortex in magnetic spins, and (e) disclinations in nematic liquid crystals.

some materials leads to disordered or metastable states [185], whereas other materials form topologically protected textures such as skyrmions which persist and are stabilised [168].

For the topologically protected states examined in this thesis, the formation of topological defects occurs due to broken symmetry. The type of symmetry broken determines the nomenclature surrounding the defect resulting in different classes of defects depending on the degrees of freedom involved [184]. Periodic crystals form dislocations, XY models form vortices (as in the formation of skyrmions), and disclinations are produced in nematic liquid crystals [Fig. 1.13(c)-(e)]. Topological defects can be characterised experimentally; the specific technique for visualisation highly depends on the form of the defect itself [184]. To view dislocations within

periodic crystals, directing imaging techniques are utilised [186]. For vortex states, these are characterised through small angle scattering and more specifically, in the case of magnetic materials, through small angle neutron scattering (SANS) [187]. Small angle scattering is particularly useful due to the mesoscopic nature of vortex formation where the periodicity of the topological defect (vortex) is on a larger scale than the interspin distance [188]. For disclinations in liquid crystals, the topological defects are characterised through the observation of Schlieren textures when viewed between crossed polarisers in a polarising microscope [189]. Much like with vortex formation, these textures are defined by an integer, s, which represents the strength of the Schlieren texture, corresponding to how much the director rotates around the singularity point.

Topological defects are known to have a profound effect on the properties of materials. Dislocations are responsible to a large degree for the mechanical properties of materials [5], vortex states are thought to be able to store memory and have application to spintronics [165], and liquid crystals may have applications in optical memories when the type and position of defects can be precisely controlled [190]. Thus, finding materials which can harbour topological defects can unlock a wealth of physics [191].

1.3.2 Coulomb phases

The frustrated interactions leading to ice phases belong to the group known as Coulomb phases, so-called as the energetics of excitations interact *via* a Coulomb potential. This group comprises of any materials whose deviations from the local

constraints lead to effective charges with Coulombic interactions. Although many lattices can form Coulomb phases [129], we focus on those within pyrochlore lattices.

For a system to be described as a Coulomb phase it has to follow three conditions [129]: (i) Each degree of freedom can be mapped to a flux $\mathbf{P}_i$ running along bond i. For example in the case of spin ices such as $Dy_2Ti_2O_7$, the flux is the spin represented as an Ising variable $\sigma = \pm 1$ running along the bond O—Dy—O as shown in Fig. 1.14. (ii) The variables obey constraints so that the sum of incoming fluxes for each tetrahedra is zero; *i.e.* $\Sigma\mathbf{P}_i = \underline{0}$. Taking the example of $Dy_2Ti_2O_7$ again, there are two spins going in $(+1)$ and two spins going out (-1) of each tetrahedra, summing to 0. (iii) The system must be in a highly disordered phase with no long-range order and is 'liquid-like'. For spins on a pyrochlore lattice, there are many degenerate ground states formed by the 'two-in-two-out' configuration, resulting in long-range disorder.

All materials that can be described as a Coulomb phase on a pyrochlore lattice have the same signature of pinch points in their diffraction pattern [129]. These pinch points in reciprocal space are due to the correlations in real space having power-law behaviour, in contrast to exponential correlations expected in liquid-like systems. Experimentally, they have been observed in magnetic diffuse scattering as in the spin ice system $Ho_2Ti_2O_7$ [Fig. 1.10(f)] [135], and structural diffuse scattering as in the compositional order of $CsNiCrF_6$ [Fig. 1.10(g)] [136] and have been widely reproduced by computation [135, 192, 193].

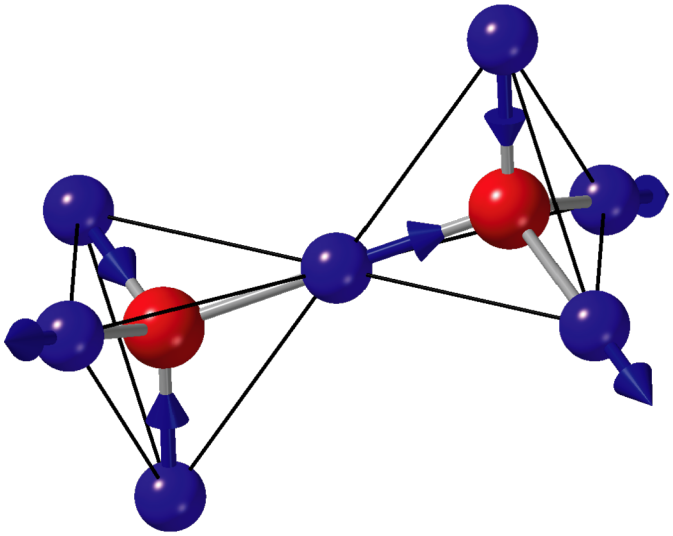

Figure 1.14: Two tetrahedra (black lines) formed by Dy atoms within the pyrochlore lattice of $Dy_2Ti_2O_7$. The Ising spins running along the O—Dy—O bond (grey) obey the 'two-in-two-out' rule ensuring each tetrahedra has a net flux of $\underline{0}$. Here the Dy and O atoms are represented in blue and red respectively.

Monopoles

Coulomb phases are of particular interest as a result of their low energy excitations out of the ground state. In the case of spin ices, these manifest as magnetic monopoles which are hypothetical elementary particles (quasiparticles) that carry an effective magnetic charge [194]. Spin ices are thought to form magnetic monopoles through a spin flip resulting in two defected tetrahedra with a 'three-in-one-out' and 'one-in-three-out' configuration [Fig. 1.15(a)-(d)]. The two tetrahedra then have a negative and positive 'charge' associated with them respectively which interact *via* Coulomb's law [175]. Flipping a subsequent spin in the defected tetrahedra reconstructs the ice rules within the tetrahedra, moving the defect and associated charge around [Fig. 1.15(e)]. This results in deconfined 'north' and 'south' poles of magnets which are able to propagate around the structure freely, with no global

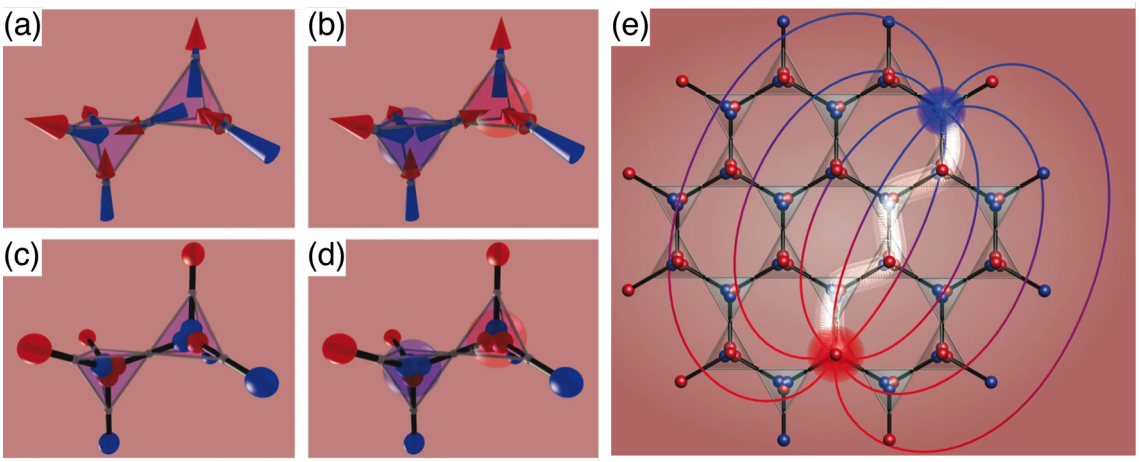

Figure 1.15: (a) Two tetrahedra of spin ice obeying the ice rule. (b) A spin flip between the two tetrahedra leads to two defected tetrahedra with a 'one-in-three-out' and 'three-in-one-out' configuration. (c)-(d) Each spin in (a) and (b) is replaced with a pair of opposite charges. (e) A pair of monopoles that has been moved by subsequent spin flips, (Dirac string) highlighted in white. Magnetic field lines are sketched between the two deconfined poles. Figure adapted from Ref. [175] with permission from Springer Nature.

energy change. The intrigue in monopoles stems from their potential application in magnetronic devices as the monopoles may be manipulated with external fields [178–180].

If monopoles are generated from a configuration obeying the ice rules, their separation is uniquely defined by a path of inverted spins known as a Dirac string [194] [Fig. 1.15(e)]. Dirac strings can be detected in the scattering function where instead of pinch point, cone-like scattering emanates from the position the pinch point originates from through sheets of scattering, and the scattering is shown to be sensitive to monopole populations [195].

The main barrier in using these excitations in applications comes from the external conditions needed for them to form. The temperature scales on which the excitations are produced exist on the order of mK which means reproducing them

can be experimentally demanding. For Coulomb phases, the ice correlations tend to emerge at extremely low temperatures such as in the spin ice $Dy_2Ti_2O_7$ where the correlations are frozen in at $T_c \approx 0.7\,K$ with excitations out of the phase occurring marginally above T_c ($\approx 1.3\,K$) [89, 196].

1.3.3 XY vortices

Another source of emergent phenomena occurs in materials subject to the XY model. Here the degrees of freedom involve the orientation of spin vectors lying within a plane [147]. Under the right conditions, the XY model is known to be unstable to the formation of vortex-antivortex pairs where the orientation of the degrees of freedom rotate continuously around a point [177]. Whether the orientations rotate in the same or opposite sense determines whether they are a vortex or antivortex, and each is assigned a charge (+1/-1) and thus have potential application in data storage [177]. Forming vortex/antivortex pairs requires a significant amount of energy and is only achievable at high temperatures. Heating a 2D XY system leads to cumulatively more vortex-antivortex pairs forming until the density of the pairs is so high that they unbind. This is known as the Kosterlitz-Thouless Transition [177].

Although commonly associated with magnetism the relevance of this transition is not just confined to magnetic thin films as the degrees of freedom described by the XY model exist in many other materials. The spin vector orientation can also be described by a phase angle, θ, which can map on to the orientation of molecules in a rotator phase [197]. A less obvious mapping can be found onto collective tilt distortions [198], vertical shifts in columnar phases [152], and most notably, thin

films of superconductive materials [199, 200].

1.3.4 Nematic phases/Schlieren textures

Liquid crystals is the name given to materials whose properties are between conventional isotropic liquids and crystalline materials. They are usually comprised of large organic molecules whose intermolecular interactions drive them to organise into collective phases. The phases formed are dictated by the temperature and structural behaviour of the individual molecular unit, many of which are anisotropic, and the properties of the collective behaviour vary with the alignment of the molecules [201]. Director alignment can cause highly anisotropic macroscopic properties, whereas when there is no driving force to align liquid crystals are isotropic. Due to their collective nature, there are a number of parallels between liquid crystals and other mesoscopic materials such as magnetic textures. This makes them attractive candidates for topological defect formation at less demanding experimental conditions [202], so much so that liquid crystals have already been exploited in studying topologically defected systems which are difficult to access experimentally [203, 204]. Owing to the broad definition of liquid crystals, there are a number of phases which can be formed. We summarise these phases briefly here.

Nematic phases

Nematic phases are one of the most common forms of liquid crystals, and are of most relevance to this thesis. These occur when molecules align, ordering their orientations, but have complete translational degrees of freedom such that they are orientationally ordered but positionally disordered [Fig. 1.16(a)] [201]. These tend

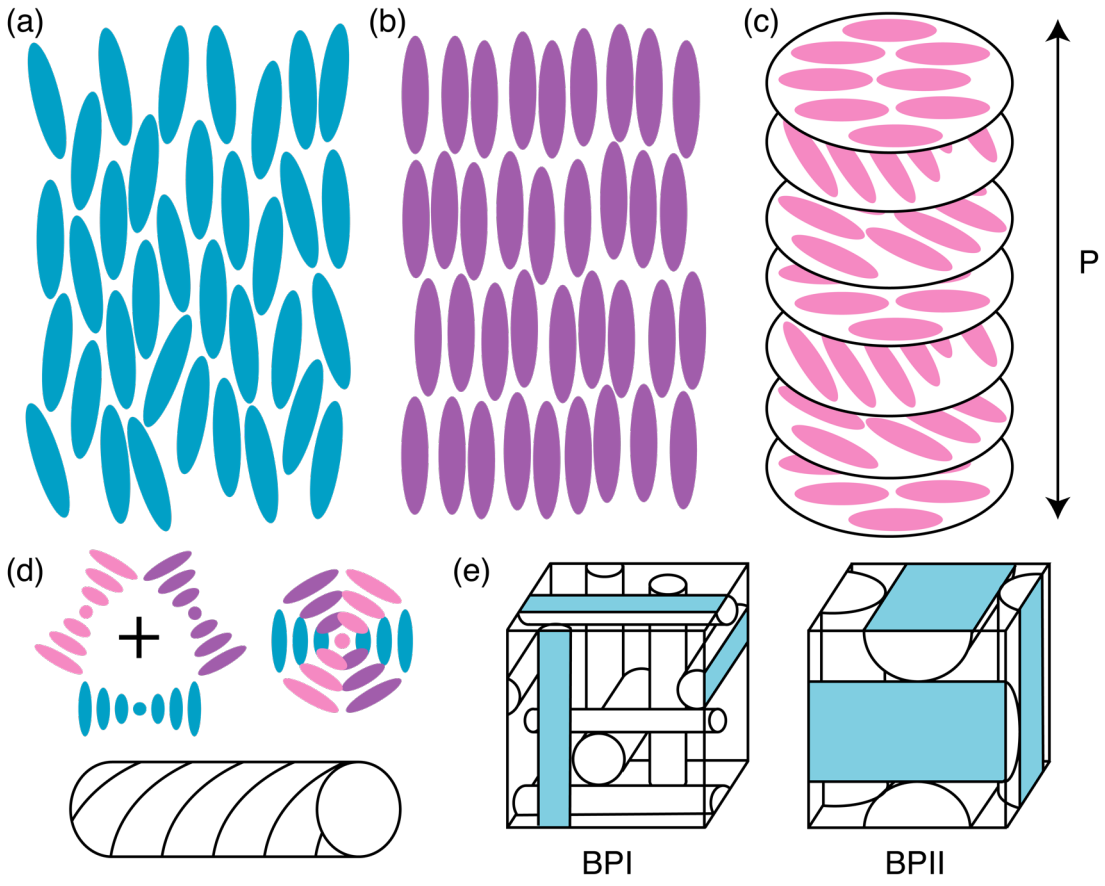

Figure 1.16: Liquid crystal phases formed from organic rod molecules represented as ellipses. Representative (a) nematic, (b) smectic, and (c) cholesteric phases where the rods preferentially align in planes. Each plane is rotated by a characteristic angle yielding a well defined pitch length, P. (d) Cholesteric phases can align at different orientations (here 120° to one another) forming a cylinder of molecules. (e) These cylinders can pack together forming blue phases, when the rod stacking is ordered they either form blue phase I (BPI) or blue phase II (BPII).

to form from large anisotropic rod-like macromolecules [191]. The local orientational order of each molecule is specified by a director, $\mathbf{n}$, which represents a unit vector without a distinction between a head or tail. Nematic liquid crystals are known to form defects (disclinations) which can have different winding numbers and are therefore topologically distinct [189]. Optical microscopes can uncover the states of the defects and highlight their use in potential applications [189, 191].

Smectic phases

Smectic phases show a degree of translational order which is absent in the nematic phases [Fig. 1.16(b)] [205]. Molecules within the smectic phase are orientationally ordered, as in the nematic phase, but align in layers or planes, restricting motion within these planes [201]. This increased order makes the smectic phase more solid-like than the nematic. The orientation of the directors define the subclass of smectic phases and some smectic phases show signs of three-dimensional order as the molecules are affected by the surrounding layers [205]. Molecules constructing liquid crystals are often able to form multiple liquid crystal phases as a function of temperature and tend to transition through isotropic liquid, nematic, smectic, and crystal phases with decreasing temperature [206]. Depending on the molecules' structure, not all phases are spanned and many form the first three phases but never fully crystallise [206].

Cholesteric phases

The cholesteric (or chiral nematic) phase is formed when molecular units contain a chiral centre. The two-dimensional nematic layers then have a preferential direction of alignment between the layers, forming a helical pattern in the direction normal to the layers. As with any helical structure, the phase has an associated pitch, P, which is the distance it takes for the director to rotate one full turn in the helix [Fig. 1.16(c)]. The angle between the directors of different layers is highly dependent on the temperature of the material and as such, the length of this pitch can change as a function of temperature [207]. Chiral nematic phases can then selectively reflect

light of equal wavelengths to the pitch length [207]. Consequently, the cholesteric phases have applications in thermometers and sensors as the colour given out reflects the temperature of the environment [208, 209].

Blue phases

Blue phases exist at the transition between cholesteric and isotropic liquid phases. They form cylinders out of superimposing cholesteric phases [Fig. 1.16(d)]. These cylinders can stack into three different phases. The phases BPI and BPII [Fig. 1.16(e)] pack the cylinders into cubic lattices which have a periodicity on the scale of several hundred nanometers and closely resemble close-packed structures of rods corresponding to the Π^+ and Π^* assemblies, respectively [210]. BPIII, however, has a similar structure to the isotropic phase [211].

All types of liquid crystal phases mentioned are able to form topological defects. Both nematic and smectic phases show singularities in their Schlieren textures, however the defects in the smectic phases are more disturbed than the nematic counterparts [Fig. 1.17] [191]. Cholesteric phases form monopoles as well as singularities [212] which only hold when the pitch length is much less than the characteristic sample size. The formation of rod-packed phases in blue phases form ordered cubic arrangements of topological defects. However in practice, these phases are polycrystalline with random domains leading to limitations in their applications [213]. Forming single crystals of the blue phases could lead to the enhancement of their topological properties which could have applications in sensing as the defects length scale is of the same order as visible light [213].

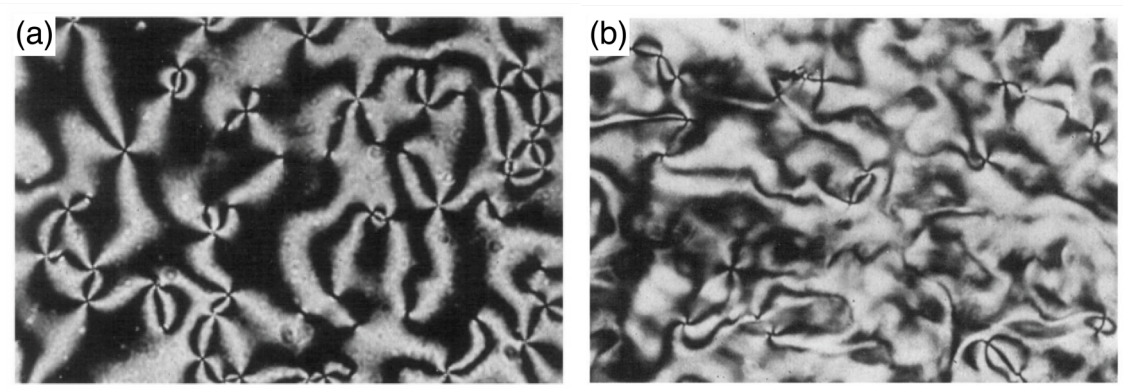

Figure 1.17: Cross polarising images of liquid crystals evidencing Schlieren textures of (a) a nematic and (b) smectic-C phase. The Schlieran texture of the smectic phase is more disturbed than the nematic phase. Reproduced from Ref. [191] with permission from the Royal Society of Chemistry.

Liquid crystals can form many topological defects with various degrees of application. Of most relevance to this thesis is the prediction and subsequent evidence of nematic phases forming skyrmionic-like textures and other topologically protected phases [202, 214–216]. Whilst skyrmions are associated with magnetism, they are purely topological in nature. Finding other materials that harbour skyrmionic textures can open up a new field of opportunities for applications to data storage. Although skyrmionic textures have been found in liquid crystals, they come with the added caveat that the translational degrees of freedom lead to unconfined defects, causing difficulties in applications [217]. Therefore the question remains of what happens to the skyrmionic textures when the nematic liquid crystals lose their translational degrees of freedom as if anchored to an underlying lattice, much like in the analogous case for chiral magnets. Moreover, can anchored nematic skyrmionic textures be synthesised and if so, in what types of materials? This idea will be developed in Chapter 5 where we explore the propensity for skyrmions to be found in non-magnetic materials. The hope here is that, as with many mappings between

structural and magnetic phases, we can decrease the experimental complexity whilst also mapping the well-characterised behaviour of skyrmionic materials.

1.4 Mapping between structural and magnetic phases

Finding mathematical mappings between magnetic phases and structural analogues is useful as it helps address three challenges:

(i) Phase instability: Exotic magnetic phases tend to manifest at low temperatures and can therefore be experimentally expensive to probe. Structural analogues demonstrate equivalent phenomena but may be stable over much larger temperature ranges.

(ii) Tuning interaction strengths: Interaction strengths in magnetic materials are difficult to vary as they are inherent properties of the material. In seeking to design materials with specific interaction strengths—for example to access topologically non-trivial phases—there is much greater potential control in structural analogues than magnetic phases themselves.

(iii) Rationalising complex phase behaviour: Understanding complex structural phase formation requires robust models of the interacting degrees of freedom. The theory behind magnetic models has been well established and drawing on analogous magnetic models can help rationalise seemingly unexpected structural phase behaviour.

Looking at each challenge in turn with relevant examples, we examine how mapping the behaviour between magnetic and structural phases can simplify and help solve each issue.

1.4.1 Phase instability

For some frustrated ground states, such is the case for lanthanide based magnetic behaviour as seen in spin ice, the magnetic phase transitions tend to occur at temperatures down to a few K or mK [89, 196]. Therefore, physically realising ground state magnetic phases can be experimentally laborious and becomes problematic when applying materials to industrial processes. Structural phases transitions, however, tend to occur at higher temperatures and can even be less experimentally time-consuming to characterise [48]. X-rays which are used for structural determination are substantially more difficult for magnetic phase determination due to the small magnetic cross sections and neutrons are required for magnetic structure investigation [218]. This leads to more time-demanding experiments and also the inability to perform in house characterisation due to the reliance on synchrotron and spallation facilities for neutron generation.

If exotic magnetic phases can be mathematically mapped onto structural phases, the results are two fold. Firstly, the phase behaviour can be replicated and further studied at less experimentally demanding temperatures, allowing for easier determination of the states behaviour and dynamics. Secondly, finding analogues to these materials at higher (ambient) temperatures accelerates the development of utilising such states in potential applications.

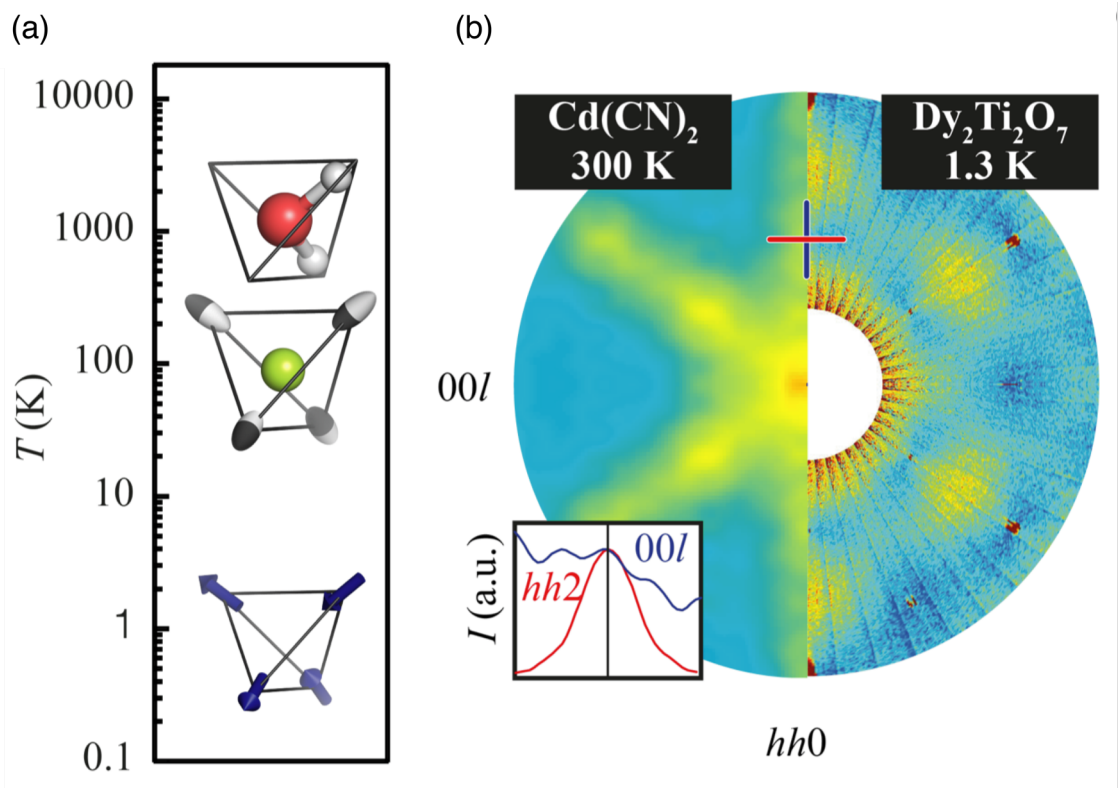

Figure 1.18: (a) A schematic representation of the relative energy scales of different degrees of freedom (magnetic spins in spin ice, cyanide orientations in $Cd(CN)_2$, and O—H bonds in water ice) ordering into the ice rules. Figure reproduced from Ref. [219]. (b) Left, effective magnetic diffuse scattering pattern ((hhl) plane) from Monte Carlo simulations at 300 K. Here CN^- orientations are interpreted as classical spin vectors when calculating the magnetic scattering. Right, experimental magnetic diffuse scattering pattern measured for spin ice $Dy_2Ti_2O_7$ at 1.3 K [220]. Broadened pinch-points are characteristic of the population of monopole defects which is further evidenced by the longitudinal and transverse intensity cuts (blue and red lines in inset). Figure reproduced from Ref. [48].

A successful example of mapping spin dynamics to a higher temperature structural phase is apparent in the relationship between $Cd(CN)_2$ and spin ices [48]. The interest in spin ices lies in their dynamical behaviour outside the ground state [221]. However, the ice rules are only satisfied at low temperatures (around 1 K) [89] [Fig. 1.10(e)] with spin excitations in the form of monopoles occuring just above the transition temperature making practical applications virtually impossible. On the other hand, $Cd(CN)_2$ transitions to a phase where the cyanide orientations obey

the ice rules at a temperature nearly two orders of magnitude higher (about sixty times) than that of spin ice [48] and similar dynamics have been observed through flipping of the analogous CN^- ions [Fig. 1.18]. Thus the link between spin ice and $Cd(CN)_2$ allows for spin ice physics to be probed at less experimentally demanding temperatures, overcoming the issue of the low temperature formations of the exotic magnetic phase by increasing the scale of the interaction parameters from $J_{\text{eff}} = 3.3\,\text{K}$ to $J_{\text{eff}} = 191\,\text{K}$ [48]. Additionally, mapping the degrees of freedom helped explain the anomalous negative thermal expansion (NTE) seen in $Cd(CN)_2$ as diffuse scattering calculations show that the cyanide flipping contributed to approximately a third of the NTE seen in $Cd(CN)_2$ [222]. This result has helped justify why materials with the same structure, but stronger bonds which prohibit cyanide flipping, have relatively weaker NTE [223, 224].

Mapping not only allows the ability to physically realise experimentally unseen phases, but also allows users to draw on theoretical work from different fields to reveal how degrees of freedom may be manipulated for targeted phase formation.

1.4.2 Tuning interaction strengths

The control of magnetic properties is of critical importance for diverse fields such as spintronics and high-temperature superconductivity [225]. Magnetic interactions tend to be dictated by the type of magnetic ion and structure of the underlying lattice. Depending on the bonding angles, a Heisenberg interaction can either lead to a antiferromagnetic or ferromagnetic state, and the underlying symmetry can dictate whether spiral like magnetic structures can be formed [176, 226]. As there are few

candidates of magnetic ions, the interactions and relative strengths are considered to be a somewhat inherent property of the material. The conditions, control, and consequences of magnetic interactions are central to the study of condensed matter physics.

Often, the formation of complex magnetic phases arises from competing interactions on different length scales due to added degrees of freedom (*e.g.* magnetic, structural, orbital) [227]. These competitions drive the formation of exotic quantum states but also inhibit controlled manipulation of interaction parameters, resulting in limited experimental confirmation of many theoretically predicted ground states [228]. Especially with increased exploration of $4f$ and $5d$ elements, which come with their own complications due to competing spin–orbit, on-site Coulomb, and crystalline electric field interactions [228]. Moreover, many interaction models rely on the true low dimensionality of a system, yet there are few magnetic systems that are strictly two-dimensional as some degree of interlayer interaction persists [229]. Therefore, phases predicted from the theory may not be spanned by their physical realisations [230].

Structural phases, however, have fewer competing interactions, and tend to have more degrees of freedom to alter, such that their interaction strengths can be manipulated with greater ease. This is especially important when considering materials whose interactions span a phase diagram where the areas of interest are rather small as in helical materials [118] and spin liquid candidates [227]. Targeting the required phase through tuning interaction strengths is key to harnessing intended properties of materials.

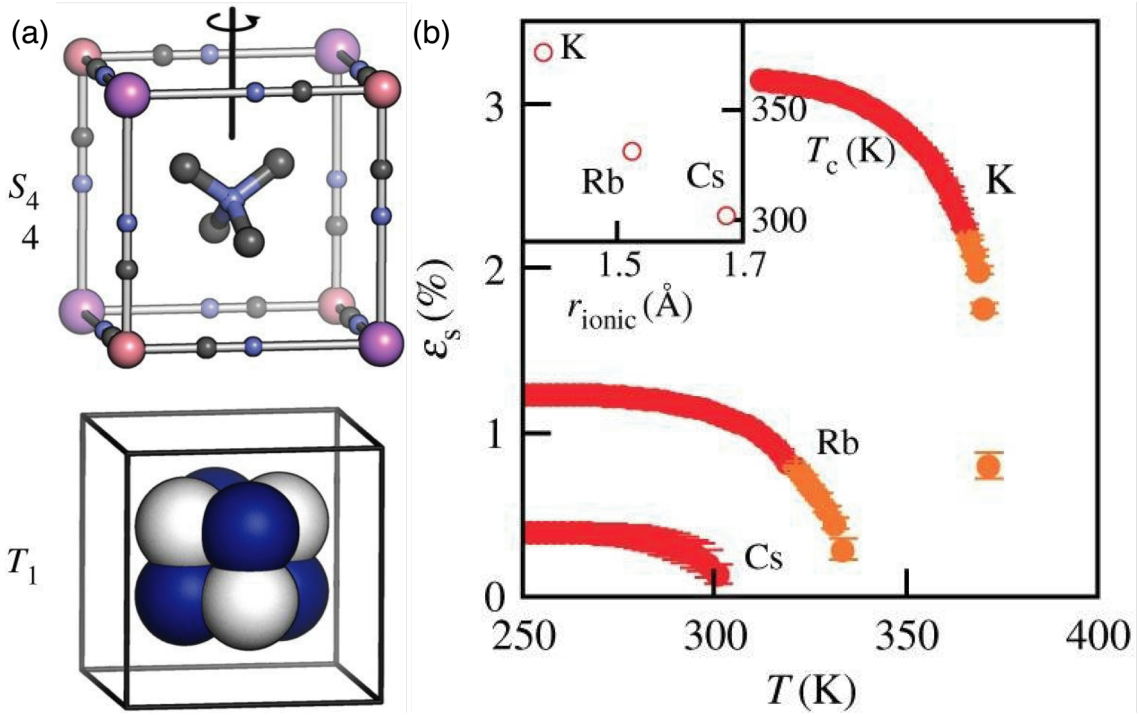

Figure 1.19: (a) A unit cell of the cyanoelpasolite molecular perovskite $[NMe_4^+]_2K[Co(CN)_6]$ where the octupolar order of NMe_4^+ ions corresponds to concerted rotations about a given $\langle 100 \rangle$ axis. Co, K, C, and N atoms are shown in pink, purple, grey, and blue respectively. H atoms are omitted for clarity. (b) Thermal evolution of the spontaneous strain for the cyanoelpasolite molecular perovskite family $[NMe_4^+]_2A[Co(CN)_6]$ where A= K, Rb, Cs with an inset of the transition temperature versus the ionic radius. Both graphs show the coupling between neighbouring octopole orientations is inversely proportional to ionic radii. Figure reproduced from Ref. [52] with permission from the Royal Society.

This is a relatively straightforward task for some structural phases. For example, in the cyanoelpasolite molecular perovskites $[NMe_4]_2A[Co(CN)_6]$ where A= K, Rb, Cs, changing the composition was shown to correspond to tuning the coupling parameter between multipolar degrees of freedom, manipulating the temperature at which the ferromultipolar order emerges [52]. In this compound, the $A[Co(CN)_6]$ units form a framework with NMe_4^+ cations occupying the pores [Fig. 1.19(a)]. For all A, the NMe_4^+ cations are orientationally disordered at high temperatures, and order to a ferrooctupolar state with decreasing temperature. The study in Ref. [52] probed the effect of changing the composition of the A site on the transition tem-

perature. They found that increasing the ionic radii inhibited the coupling between neighbouring octupole rotations and suppressed the transition [Fig. 1.19(b)] [52]. By weakening the coupling between neighbouring cations, the authors suggest that the coupling progresses from being described by the six-state Potts model when A=K to a Heisenberg regime when A=Cs [52].

1.4.3 Rationalising complex phase behaviour

Statistical mechanical models describing the interactions and energetics of magnetic materials are used extensively in condensed matter physics [118, 231]. The same models used to study magnetic phase behaviour can often be applied successfully to intepret the structural phase behaviour of other materials. The key is to find the right coarse graining. A good example is the use of the Ising model to the packing of layered materials where the shift in layer position can be represented as Ising states [232]. Through a suitable coarse graining, the close-packed stacking of materials can be described in terms of 'ferro'—cubic close-packing (CCP)—and 'anitferro'—hexagonal close-packing (HCP)—interactions [Fig. 1.20(a)-(b)] [98, 233]. Many problems in inorganic structures are described in terms of faults in the close-packed stacking of layers [234, 235], and application of the Ising model allows the problem to be quantified and explained through competing interactions.

Polytypic behaviour can sometimes be understood in a similar fashion. Polytypes are groups of crystalline materials with the same composition that vary in their structure as they are built up by stacking layers which differ in their stacking sequence. In such cases, the interactions between nearest and next-nearest neigh-

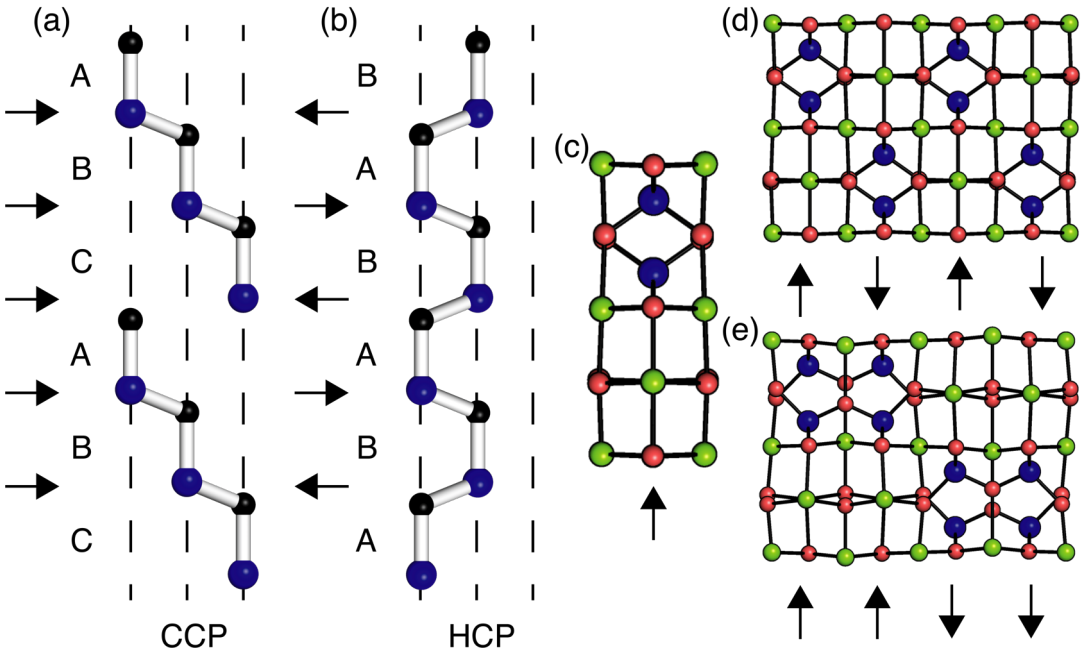

Figure 1.20: (a) Ferromagnetic and (b) antiferromagnetic mapping of interacting Ising spins onto the stacking behaviour of SiC. (c) Mapping of a basic structure unit of a spinel onto a Ising spin which can be used to explain phases of spinels formed as analogous to (d) an antiferromagnetic phase and (e) frustrated ground state, $\langle 2 \rangle$, of the ANNNI model on the β-phase of Mg_2SiO_4.

bour layers may be frustrated [236, 237], which is why the ANNNI model [Eq. 1.2] is of particular relevance to polytypic behaviour.

Polytypism is a common phenomena in materials chemistry and is not just limited to layered materials but is also exhibited in more complex materials with structurally compatible modules including pyroxenes [238], chlorites [239], and perovskites [240]. The ANNNI model was first applied to studying the phase behaviour of spinels where one structural unit of spinel (AB_2O_4) can be mapped on to one Ising spin [Fig. 1.20(c)]. For most spinels the structural units arrangement in two dimensions lead to an ordered sheet but variations occur in the packing of sheets. Examples of two packings formed by the sheets are shown in [Fig. 1.20(d)-(e)].

The phases traversed by the polytypic behaviour can be explained through the finite temperature behaviour of the ANNNI model whose phase diagram is shown schematically in Fig. 1.8(c). The ANNNI model has since been used to explain phase behavour of many other materials [240]. Similar to the relation of the Ising model to close packed structures enabling description of stacking faults as a competition between the two limiting phases, the ANNNI model has helped the formation of polytypes to be understood as a competition between first and second nearest neighbour interactions [121]. This has created a simple general description of the energetics behind modulated phases [121].

Polytypes of AB and AB_2 compounds

The ANNNI model is also known to explain the polytypic behaviour of modulated materials, denoted as the 'classical polytypes' [241]. These polytypes have AB or AB_2 stoichiometries, with planes of A atoms coordinated by B atoms and stacked in a close-packed array [242, 243]. In the case of the AB_2 compounds, this leads to $B-A-B$ 'sandwiches' in each layer of the structure. Considering the simple case of SiC, a large number of polytypes have been observed and studies have delved into explaining their thermodynamic stability [241, 244]. The ANNNI model is able to encapsulate all poltypic behaviour in SiC, even for metastable states, and explain the interactions leading to the most commonly observed phases [245].

The phase behaviour of many polytypic materials have been studied in detail, with an increasing focus on AB_2 compounds—especially the layered dichalcogenides [237, 243, 246]. Layered dichalcogenides are of particular currency for their collective properties, including superconductivity and charge density wave states [247–

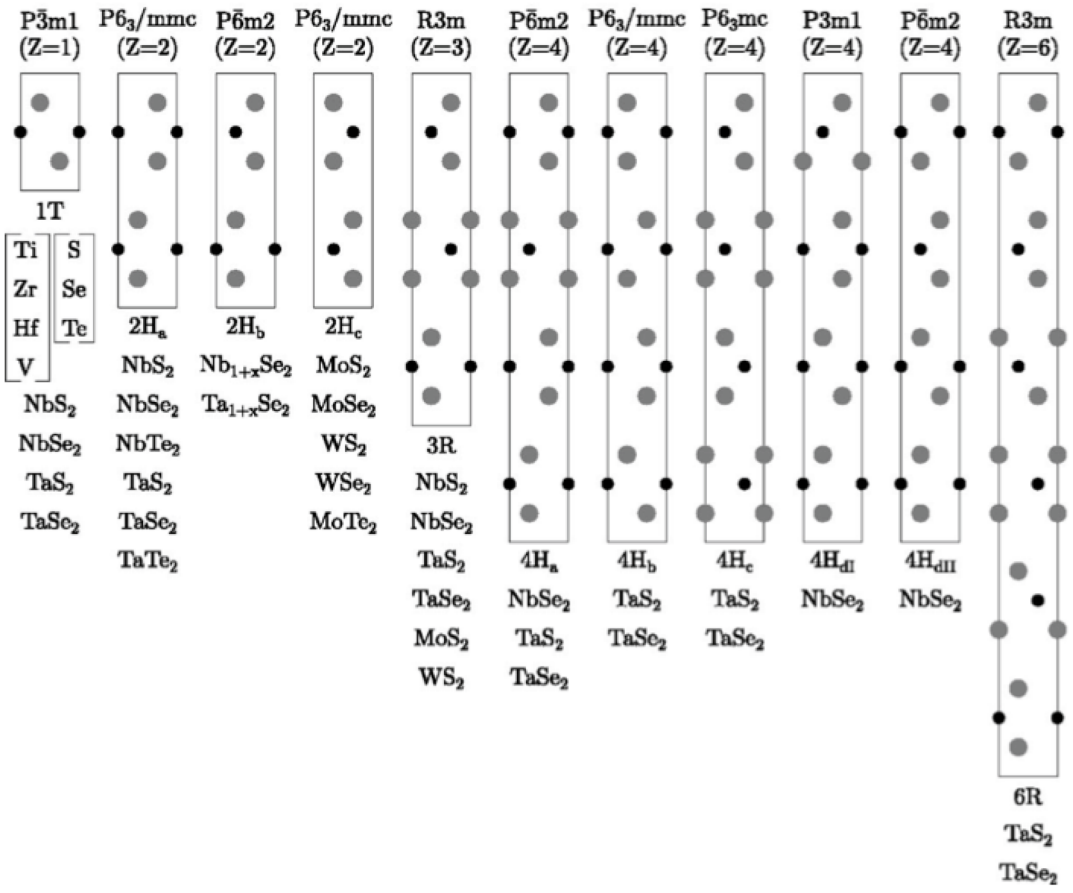

Figure 1.21: A collection of transition metal dichalcogenides polytypes shown as $(11\bar{2}0)$ projections of their hexagonal structures. The metal atoms are represented as small black circles and the chalcogenides are represented as large grey circles. Above each structure is the space group and number of AB_2 layers (Z) within each unit cell. Below each structure are the compositions known to form the different structure types. This figure has been reproduced from Ref. [37] with permission from the American Physical Society.

249]. Understanding the factors leading to the emergence of polytypes of layered dichalcogenides may allow for targeted phase formation. It can also highlight accessible routes for phase transformation based on interaction parameters of the material. In this thesis, we focus mainly on the polytypes of transition metal dichalcogenides, AB_2. An inexhaustive list of known AB_2 polytypes is shown in Fig. 1.21 which focuses on the transition metal dichalcogenides in particular.

Research into the polytypic behaviour of AB_2 compounds has been carried out

with great success. But of course this simplistic model cannot be expected to provide the whole microscopic description of all polytypes [117]. Although the ANNNI model can describe many phases through ground state or finite temperature phases, failure to rationalise all AB_2 polytypes, especially states with $\langle 13 \rangle$ modulation is unsurprising due to its simplicity, and a more involved model may be needed for more rigorous phase determination [240, 243]. Another major defect arises when drawing on the physicality of a singular 'spin flip' within the material. Taking the example of silicon carbide, the model does not accurately mirror the elementary excitations of the compound. For a 'spin flip' to occur in the ANNNI model, the corresponding SiC chain would have a line of atoms within a plane flipping all the way to the edge of the crystal which is unphysical [243, 245]. It has been suggested that the individual spin flips can instead be replaced by the average deviation of spins within a layer and as such, the small deviations throughout a plane of atoms may be caused by phonons which can stabilise long period phases [245].

The ANNNI model can also be used to explain complex phases of binary alloys that cannot be explained by the Ising model alone [245]. Although the interactions within the two state system are mostly well explained by the Ising model with short-range interactions, if the effective coupling between nearest neighbour spins is small, second nearest neighbour interactions can be important and, if antiferromagnetic, modulated phases can appear [245]. Several studies have highlighted how the ANNNI model reflects the features seen in binary alloys [250, 251]. These modulated structures are observed primarily in compounds containing noble metals [252–255] but are known to exist in other metals [256].

1.5 Thesis outline

This thesis centres on the application of statistical mechanical models to understand the driving forces behind the formation of various complex phases, with a focus on parameterising polytypic behaviour and stacking disorder in an array of materials. The concept of using models to simplify complex structures into a handful of competing interactions is key to extracting exotic behaviour and is becoming increasingly implemented in the study of materials [27]. Through appropriate mappings we seek to link complex magnetic materials to structural phases with an aim to physically realise exotic states in structural phases in order to pursue new pathways for harnessing exotic phenomena. A secondary result is the broadening of our library of materials that can be used for the fundamental study of magnetic phases and properties at less experimentally demanding conditions. To accomplish these goals, we look at sets of structural materials which differ in dimensionality and use magnetic models to explore our ability to describe their phase behaviour.

Chapter 2 outlines the methods relevant to the research undertaken during this thesis. This includes a discussion of scattering theory and techniques which, although not directly used, underpin the results within the subsequent chapters. The main techniques used for this thesis are computational with a view to model the interactions between components in the systems and analyse their phase behaviour with changing variables such as temperature, pressure, and interaction strengths. This chapter contains a discussion of the strengths and limitations of each computational technique and the power in using them in unison.

In Chapter 3 we discuss the polytypic behaviour of pseudo one-dimensional AB_2 compounds with an emphasis on the varied nomenclature in the literature. Here we suggest a new nomenclature to describe the phases which is based on their intralayer and interlayer interactions. Through this we develop a corresponding Hamiltonian which we use to reinterpret various previously identified AB_2 polytypes with complex structures.

Chapter 4 continues on the theme of layered materials by focussing on $Ni(CN)_2$—a material which contains disordered stacking arrangements [257, 258]. Here we show that the diffuse and asymmetric peaks in its diffraction pattern cannot be explained through a discrete model as predicted for most pseudo 1D materials, and instead argues that a model with continuous degrees of freedom is needed to accurately describe the phase behaviour. Moreover, the model encapsulating the structural phase behaviour can be mapped to the 1D quaternion chain, whose degrees of freedom are related to those of the quantum spin-$\frac{1}{2}$ Heisenberg XXZ model. The chapter contains a discussion of the problem of the reliability of quantum—classical analogues.

Chapter 5 moves away from layered materials, and instead focuses on the capability of realising exotic magnetic phases in less experimentally demanding systems. This chapter focuses on topological defects and more specifically on the formation of skyrmions. Instead of using magnetic dipoles as our degrees of freedom, we formulate an equivalent Hamiltonian of interacting non-magnetic quadrupoles. Here we explore the extent to which molecular orientation in chiral metal organic frameworks (MOFs) can host skyrmionic-like textures by looking at the interactions present in the candidate MOF, $[Al(N_3)_3]\cdot C_6H_6$. We show that skyrmionic phases can be

produced in chiral quadrupolar systems, and the energetics of chiral MOFs with quadrupolar hosts can be well described by the quadrupolar Hamiltonian.

The thesis ends with a discussion of the implications of the results laid out in the chapters and the questions they raise for future avenues of exploration.

Appendix A and Appendix B include preliminary experimental data and first attempt modelling results of two disordered systems. The research contained in these two appendices was conducted during the final year of the DPhil, but experimental studies were forced to be postponed due to the ongoing COVID-19 pandemic.

Chapter 2

Methods

The results reported in the main section of this thesis rely solely on computational techniques, however, both Chapters 3 and 4 draw comparisons to experimental powder diffraction patterns published elsewhere. As such, this chapter begins by outlining scattering theory and powder diffraction experiments. The remainder of the chapter focuses on the computational techniques and programs employed to analyse the structural behaviour and lattice dynamics of the systems presented in this thesis, with a discussion of their limitations.

2.1 Diffraction

The following section gives an overview of the fundamental equations and theory of diffraction. This has been constructed based on approaches developed in Ref. [55] and Ref. [4].

2.1.1 Fundamental equations

Diffraction is a fundamental technique for studying the structure of materials as elastic scattering produces information on interatomic distances within materials. Scattering occurs when a beam of radiation is incident on an atom. The radiation beam can be described in terms of its wavelength, λ, which travels in the direction of wave propagation given by the wave vector, $\mathbf{k}$, where $|\mathbf{k}| = \frac{2\pi}{\lambda}$. X-ray, electron,

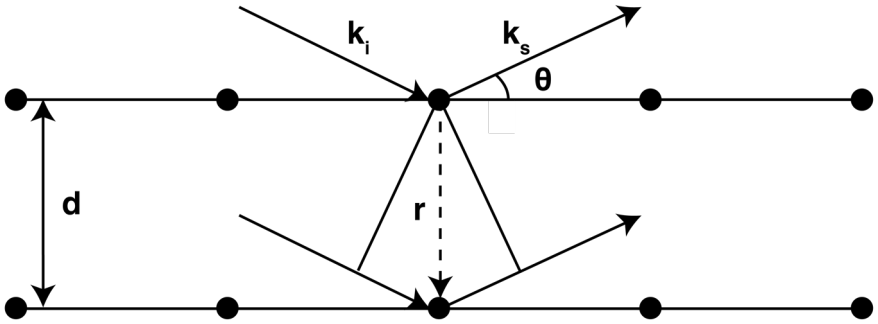

Figure 2.1: Scattering of an incident wave vector $\mathbf{k}_i$ to a scattered wave vector $\mathbf{k}_s$ by two atoms in different lattice planes, separated by a vector $\mathbf{r}$. $\mathbf{d}$ is the interplanar lattice distance.

and neutron radiation are typically used as their wavelengths are comparable to typical interatomic distances. The choice of radiation source depends highly on the material studied and the particular part of the structure being probed. In a diffraction experiment, a beam of radiation is incident on an atom with wave vector $\mathbf{k}_i$ and scattered with wave vector $\mathbf{k}_s$. This gives a change in wave vector known as the scattering vector $\mathbf{Q} = \mathbf{k}_i - \mathbf{k}_s$. The equation of a wave of radiation can be expressed as

$$\psi(\mathbf{x}) = A \exp(\mathrm{i}\mathbf{k} \cdot \mathbf{x}), \tag{2.1}$$

where $\mathbf{x}$ is the atomic position. When the beam is incident on two atoms—one at the origin and the second separated by a vector $\mathbf{r}$ [Fig. 2.1]—the scattered waves are described by the following equations:

$$\psi_1(\mathbf{x}) = \exp(\mathrm{i}\mathbf{k}_s \cdot \mathbf{x}), \tag{2.2}$$

$$\psi_2(\mathbf{x}) = \exp(\mathrm{i}\mathbf{k}_s \cdot \mathbf{x}) \exp(\mathrm{i}\mathbf{Q} \cdot \mathbf{r}). \tag{2.3}$$

with the total scattering produced from the sum of the scattered waves:

$$\psi_1(\mathbf{x}) + \psi_2(\mathbf{x}) = \exp(\mathrm{i}\mathbf{k}_s \cdot \mathbf{x})[1 + \exp(\mathrm{i}\mathbf{Q} \cdot \mathbf{r})]. \tag{2.4}$$

The modification of the amplitude of the scattered wave can be represented by the phase factor $F(\mathbf{Q})$:

$$F(\mathbf{Q}) = 1 + \exp(\mathrm{i}\mathbf{Q} \cdot \mathbf{r}), \tag{2.5}$$

with a phase shift $\mathbf{Q} \cdot \mathbf{r}$. For multiple atoms, the phase factor is summed over all the phase shifts from the scattered waves of each particle with position vectors $\mathbf{r}_j$

$$F(\mathbf{Q}) = \sum_j \exp(\mathrm{i}\mathbf{Q} \cdot \mathbf{r}_j), \tag{2.6}$$

culminating in the important result that the scattering of waves is dependent only on the change in wave vector, $\mathbf{Q}$, and not on the initial and final wave vectors themselves.

To generalise this result, the phase factor is given different weighting depending on the particles' identity:

$$F(\mathbf{Q}) = \sum_j f_j \exp(\mathrm{i}\mathbf{Q} \cdot \mathbf{r}_j). \tag{2.7}$$

In X-ray diffraction, the weighting factor f_j is proportional to the number of electrons in the atom (*i.e.* the atomic number Z) and is known as the X-ray atomic scattering

factor. For a continuous electron density distribution, the phase factor can be defined as

$$F(\mathbf{Q}) = \int \rho(\mathbf{r}) \exp(\mathrm{i}\mathbf{Q} \cdot \mathbf{r}) \mathrm{d}\mathbf{r}, \tag{2.8}$$

where $\rho(\mathbf{r})$ is the electron density at position $\mathbf{r}$. In a diffraction experiment, the phase factor itself is indeterminable, and instead the intensity of the diffracted peaks is recorded where $I(\mathbf{Q}) \propto |F(\mathbf{Q})|^2$. As a result, the information containing the phase of $F(\mathbf{Q})$ is lost and diffraction patterns tell of the distance between atoms but not their absolute positions. This is a well documented problem in crystallography known as the phase problem [259].

In solid state chemistry, many materials considered with conventional diffraction techniques consist of periodic structures made up of a regular lattice where a group of atoms (motif) is associated with each lattice point. To determine the diffraction pattern formed by periodic structures, it will be useful to first consider the Fourier transform of a lattice and motif separately. The motif can be described by Eqn. 2.7, whereas the lattice point has well defined conditions allowing for the Fourier transform to be simplified significantly.

For a regular lattice, the scattering density can be described as a periodic function where $\rho(\mathbf{r}) = \rho(\mathbf{r} + \mathbf{R}_{UVW})$ where $\mathbf{R}_{UVW} = U\mathbf{a} + V\mathbf{b} + W\mathbf{c}$ and U, V, W are integers and $\mathbf{a}, \mathbf{b}, \mathbf{c}$ are the lattice vectors. Through this, the lattice points defined by the regular repeating unit can be represented as a set of delta functions

$$L(\mathbf{r}) = \sum_{U,V,W} \delta[\mathbf{r} - (U\mathbf{a} + V\mathbf{b} + W\mathbf{c})]. \tag{2.9}$$

The Fourier transform of this lattice:

$$R(\mathbf{k}) = \int \exp(\mathrm{i}\mathbf{k}\cdot\mathbf{r}) L(\mathbf{r}) \mathrm{d}\mathbf{r}, \tag{2.10}$$

$$= \sum_{U,V,W} \int \exp(\mathrm{i}\mathbf{k}\cdot\mathbf{r}) \delta[\mathbf{r} - (U\mathbf{a} + V\mathbf{b} + W\mathbf{c})] \mathrm{d}\mathbf{r}. \tag{2.11}$$

then contains a similar delta function, which can be simplified using the sifting property of the Dirac delta function explained below [260]. Since the delta function is zero everywhere except at $\mathbf{r} = U\mathbf{a} + V\mathbf{b} + W\mathbf{c}$, the range of the integration can be changed to some infinitesimally small range, $\mathbf{r}'$, around $U\mathbf{a} + V\mathbf{b} + W\mathbf{c}$ such that

$$R(\mathbf{k}) = \sum_{U,V,W} \int_{U\mathbf{a}+V\mathbf{b}+W\mathbf{c}-\mathbf{r}'}^{U\mathbf{a}+V\mathbf{b}+W\mathbf{c}+\mathbf{r}'} \exp(\mathrm{i}\mathbf{k}\cdot\mathbf{r}) \delta[\mathbf{r} - (U\mathbf{a} + V\mathbf{b} + W\mathbf{c})] \mathrm{d}\mathbf{r}. \tag{2.12}$$

Over this very small range of $\mathbf{r}$, the function $\exp(\mathrm{i}\mathbf{k}\cdot\mathbf{r})$ is constant and can be taken out of the integral.

$$R(\mathbf{k}) = \sum_{U,V,W} \exp[\mathrm{i}\mathbf{k}\cdot(U\mathbf{a} + V\mathbf{b} + W\mathbf{c})] \int \delta[\mathbf{r} - (U\mathbf{a} + V\mathbf{b} + W\mathbf{c})] \mathrm{d}\mathbf{r}, \tag{2.13}$$

by definition, the Dirac delta function is normalised, so the Fourier transform becomes

$$R(\mathbf{k}) = \sum_{U,V,W} \exp\left[\mathrm{i}\mathbf{k} \cdot (U\mathbf{a} + V\mathbf{b} + W\mathbf{c})\right]. \tag{2.14}$$

Since all lattices are centrosymmetric, when expanding the exponential term the sine terms cancel whereas the cosine terms persist resulting in

$$R(\mathbf{k}) = \sum_{U,V,W} \cos\left[\mathbf{k} \cdot (U\mathbf{a} + V\mathbf{b} + W\mathbf{c})\right]. \tag{2.15}$$

For a general wave vector $\mathbf{k}$, some of the cosine terms are negative and some are positive. As the number of terms tends to infinity, the positive and negative terms cancel out to give an overall zero value for the Fourier transform. The only terms that do not cancel are when the argument of all the cosines are equal to an integer multiple of 2π. The cases where this is true are uniquely defined three Miller indices hkl where

$$\mathbf{k} \cdot \mathbf{r}_j = (h\mathbf{a}^* + k\mathbf{b}^* + l\mathbf{c}^*) \cdot (U\mathbf{a} + V\mathbf{b} + W\mathbf{c}) = 2\pi(hU + kV + lW), \tag{2.16}$$

and $\mathbf{a}^*$, $\mathbf{b}^*$, and $\mathbf{c}^*$ are the reciprocal lattice vectors, with the relationship to the real space lattice vectors $\mathbf{a}^* = \frac{2\pi}{V}(\mathbf{b} \times \mathbf{c})$, $\mathbf{b}^* = \frac{2\pi}{V}(\mathbf{c} \times \mathbf{a})$, and $\mathbf{c}^* = \frac{2\pi}{V}(\mathbf{a} \times \mathbf{b})$. Therefore the Fourier transform of the three-dimensional lattice is

$$R(\mathbf{k}) = \sum_{h,k,l} \delta[\mathbf{k} - (h\mathbf{a}^* + k\mathbf{b}^* + l\mathbf{c}^*)]. \tag{2.17}$$

The important result from this analysis is that a Fourier transform of a crystal lattice is itself a lattice in reciprocal space. In diffraction experiments, the change in wave vector, $\mathbf{Q}$, is measured instead of directly probing the reciprocal lattice vector, $\mathbf{k}$, so more commonly the Fourier transform of the lattice is rewritten as

$$R(\mathbf{Q}) = \sum_{h,k,l} \delta[\mathbf{Q} - (h\mathbf{a}^* + k\mathbf{b}^* + l\mathbf{c}^*)]. \tag{2.18}$$

Eqn. 2.18 requires strict conditions to be met in order to produce intensity, namely $\mathbf{Q} - (h\mathbf{a}^* + k\mathbf{b}^* + l\mathbf{c}^*) = 0$ (*i.e.* $\mathbf{Q} = \mathbf{d}^*$ where $\mathbf{d}^*$ is the reciprocal lattice vector). To determine the condition on θ [Fig. 2.1] for constructive interference to occur, we use Fig. 2.1 to derive the trigonometric consideration:

$$|\mathbf{Q}| = 2|\mathbf{k}| \sin\theta = \frac{4\pi}{\lambda} \sin\theta. \tag{2.19}$$

Combining these results with the relationship between the reciprocal and real space lattice, $|\mathbf{d}^*| = 2\pi/|\mathbf{d}|$, for intensity to occur in the diffraction pattern,

$$2d \sin\theta = \lambda, \tag{2.20}$$

which is known as Bragg's law [86].

As we have now determined the Fourier transform of both the lattice and motif,

we can combine these results to formulate the conditions required for diffraction in crystalline materials. A benefit of using Fourier transforms when studying the theory of diffraction is in the use of convolution. The convolution theorem states that if three functions, $f(x), g(x), h(x)$ are related through the convolution operation $f(x) = g(x) \circledast h(x)$, then the respective Fourier transform of $F(k)$, $G(k)$, and $H(k)$ are related by

$$F(k) = \int (g(x) \circledast h(x)) \exp(ikx) \mathrm{d}x = G(k) \times H(k), \tag{2.21}$$

As a crystal structure can be described as a convolution of a lattice and motif, the Fourier transform will simply be the product of their Fourier transforms. Combining Eqn. 2.7 and Eqn. 2.18 gives the Fourier transform of a crystal

$$\begin{aligned} \mathrm{FT(crystal)} =& R(\mathbf{Q}) \times F(\mathbf{Q}) & (2.22) \\ =& \sum_{h,k,l} \delta[\mathbf{Q} - (h\mathbf{a}^* + k\mathbf{b}^* + l\mathbf{c}^*)] \times \sum_j f_j(\mathbf{Q}) \exp(\mathrm{i}\mathbf{Q} \cdot \mathbf{r}_j). & (2.23) \end{aligned}$$

As the reciprocal lattice function is only non-zero when $\mathbf{Q} = h\mathbf{a}^* + k\mathbf{b}^* + l\mathbf{c}^*$, the Fourier transform of the crystal need only be considered at these values of $\mathbf{Q}$. Defining the position of an atom within a unit cell as $\mathbf{r}_j = x_j\mathbf{a} + y_j\mathbf{b} + z_j\mathbf{c}$,

$$\mathbf{Q} \cdot \mathbf{r}_j = (h\mathbf{a}^* + k\mathbf{b}^* + l\mathbf{c}^*) \cdot (x_j\mathbf{a} + y_j\mathbf{b} + z_j\mathbf{c}) = 2\pi(hx_j + ky_j + lz_j), \tag{2.24}$$

resulting in the structure factor

$$F(hkl) = \sum_j f_j(Q_{hkl}) \exp[2\pi \mathrm{i}(\mathrm{hx_j} + \mathrm{ky_j} + \mathrm{lz_j})]. \tag{2.25}$$

There are now well-defined interference conditions where $\mathbf{Q}$ (and thus $F(\mathbf{Q})$) are non zero when h, k, and l have integer values. If there is long-range order, the interference conditions lead to sharp peaks in the diffraction pattern known as Bragg peaks [86] whereas for disordered systems, conditions can be satisfied in non Bragg peak positions [63]. For amorphous solids or liquids, the patterns show a continuous diffuse distribution of intensity, evidencing little order. For crystals with underlying periodicity as well as partial disorder in the form of defects or correlated disorder, sharp Bragg peaks are present as well as diffuse scattering as the scattering projects the average structure [63].

2.1.2 Powder diffraction

The best technique to determine the crystal structure of a material is to perform a diffraction experiment on a single crystal sample [55]. In a well-ordered single crystal with a regular arrangement of atoms, the structure can almost always be fully determined based on Bragg scattering as a 3D reconstruction can be made from the peaks [Fig. 2.2(a)] due to well-set-out peak conditions. However, single crystals of many materials are unable to be grown to sufficient sizes, or even at all, instead forming as polycrystalline powder samples or suffering from twinning. Powder diffraction is typically used when samples are polycrystalline, prohibiting 3D reconstruction, where the radial distribution of diffraction intensity is instead rotationally averaged,

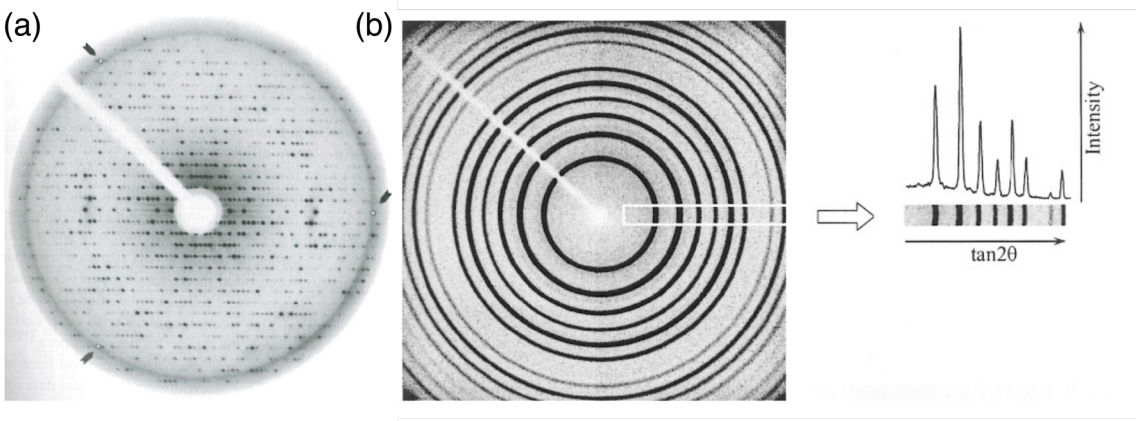

Figure 2.2: Examples of (a) single crystal and (b) powder diffraction patterns. For the powder pattern, the 3D structural information is projected onto 1D. Figures reproduced from Ref. [4] and [261].

producing a 1D powder diffraction pattern [Fig. 2.2(b)]. Predictably, information is lost when moving from three to one-dimensional data, hence structural determination from single crystal diffraction is usually more straightforward than with powder diffraction. However, powder diffraction can be more advantageous than single crystal diffraction as the powder sample preparation is simpler than single crystal growth, and the patterns are faster and easier to obtain.

Ironically, condensing information can sometimes make it easier to analyse. When diffraction intensity is spread throughout 3D reciprocal space, the signal can be very weak and concentrating this information can lead to stronger signals. Additionally, powder diffraction patterns still contain a wealth of data that allow for the identification of different phases and lattice parameter assignment. When looking at stacking disorder, which is heavily considered in this thesis, the characteristic behaviour seen in single crystal diffraction patterns produces no more insight about the form of the stacking disorder than powder patterns and powder diffraction is sufficient for the analysis of the evolution of stacking faults [Fig. 2.3]. The diffuse

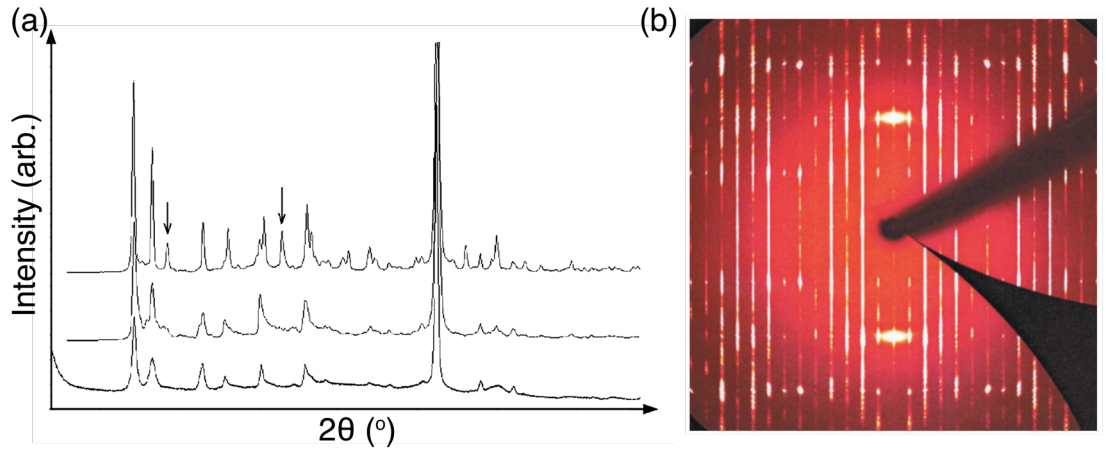

Figure 2.3: (a) Simulated (top two) and experimental (bottom) powder X-ray diffraction patterns of the $\beta-$phase of Pigment Red 170, evidencing stacking disorder due to the broad asymmetric peaks pertaining to reflections associated with the $(h00)$ planes. (b) Single crystal X-ray diffraction pattern of the same pigment where the stacking disorder is evident through the diffuse streaks parallel to $\mathbf{a}^*$. The pattern shows the reciprocal-lattice layer $(hk0), [h00]$ vertical, $[0k0]$ horizontal. Figures are reproduced from Ref. [262].

scattering arising from stacking disorder leads to signature anisotropic peak broadening in powder diffraction. Thus for the effect of composition and temperature on stacking disorder, variable-temperature powder diffraction experiments are ideal.

Analysis of powder diffraction data often assumes the polycrystalline sample contains a uniform distribution of crystallite orientations, allowing for every plane of the crystal structure to be represented in the signal [55]. A uniform distribution necessarily stipulates that the conditions for diffraction intensity set out by Bragg's law [Eqn. 2.20] will automatically be fulfilled for some crystallites. This results in quicker data collection than in single crystal experiments, as only the scattering angle needs to be varied, whereas single crystal measurements require changing the samples orientation as well [55].

In cases where the crystals are not arranged randomly, the relative intensities are skewed due to preferred orientations of the crystallites [261]. Commonly, preferential

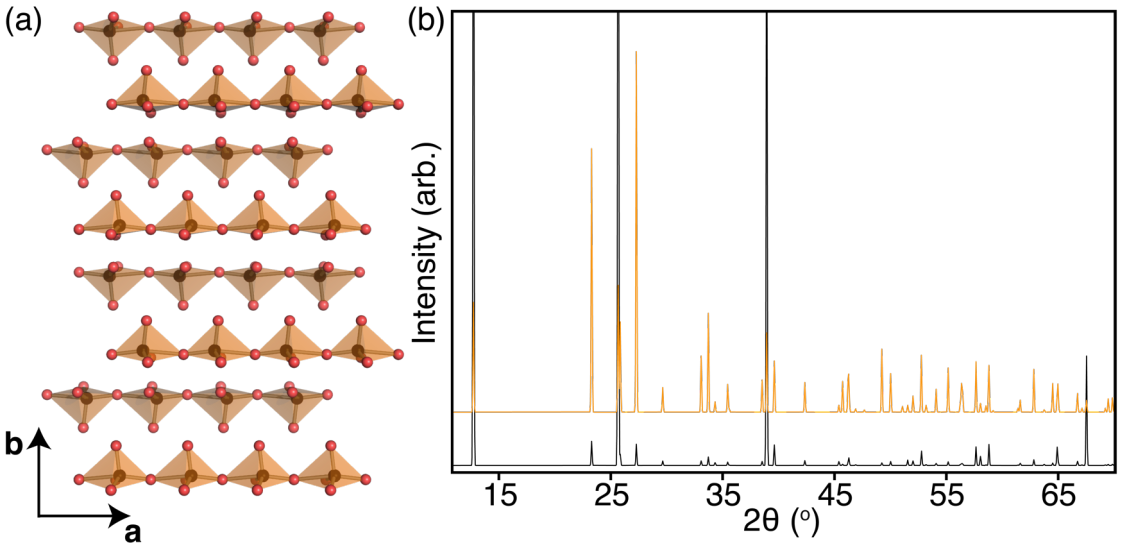

Figure 2.4: (a) Structure of MoO_3 showing layers of MoO_3 tetrahedra (orange) produced within the $\mathbf{a}, \mathbf{c}$ planes. Mo atoms are shown in black and O atoms are in red. (b) Simulated powder X-ray diffraction patterns of the structure without preferred orientations (orange) and with (black). The preferred orientations of crystallites cause larger relative intensities along (0k0) axes.

alignment occurs in layered materials as they can be easily cleaved, forming needles or plates which, when packed, prefer to coalign resulting in increased intensities of peaks corresponding to the cleavage planes. For example, MoO_3 is a layered material consisting of planes of MoO_3 tetrahedra [Fig. 2.4(a)] [263]. Comparing the diffraction pattern of a sample with randomly oriented crystallites and a sample containing preferred orientations evidence the same characteristic reflections but with vastly different intensities [Fig. 2.4(b)]. Methods have been developed to overcome this, mainly through careful sample preparation as preferred orientations can be caused when preparing the sample in the specimen holder for X-ray analysis.

2.1.3 Small-angle scattering

Bragg scattering [Eqn. 2.20] defines the fundamental relation for constructive interference of scattered beams from a radiation source, namely that the diffraction angle θ is inversely proportional to the separation of diffraction lattice planes d. For inorganic matter, the majority of observed lattice spacings are of the same order of magnitude as the wavelength of X-rays, requiring a relatively coarse θ resolution. For some materials, it is desirable to detect large lattice spacings ten or even a hundred times greater than interatomic distances. In these cases, in order to resolve separate reflections, a very fine Q-space resolution is required as the reciprocal lattice is much smaller than the X-ray's wave vector, which is maximised at small angles [264, 265]. An alternative approach is to change other variables present in Bragg's law. However, manipulating for longer wavelengths is unfeasible as long-wavelength X-rays are absorbed to a large extent in matter, complicating the diffraction experiment and means of detecting the X-rays, as well as diminishing the intensity of the diffracted beam [264].

Small-angle scattering is a well-developed technique used in a diverse set of fields from material science in the study of alloys, ceramics and composite materials [188], to biology for probing the structure of proteins and DNA [266, 267]. More common to condensed matter physics, small-angle neutron scattering (SANS) is used to look at macroscopic magnetic properties which emerge on scales greater than the interatomic distances [187]. For example, chiral magnets can produce spin textures which arise from the preference for spins to propagate in one direction and SANS is often used to characterise these phases due to their emergence on

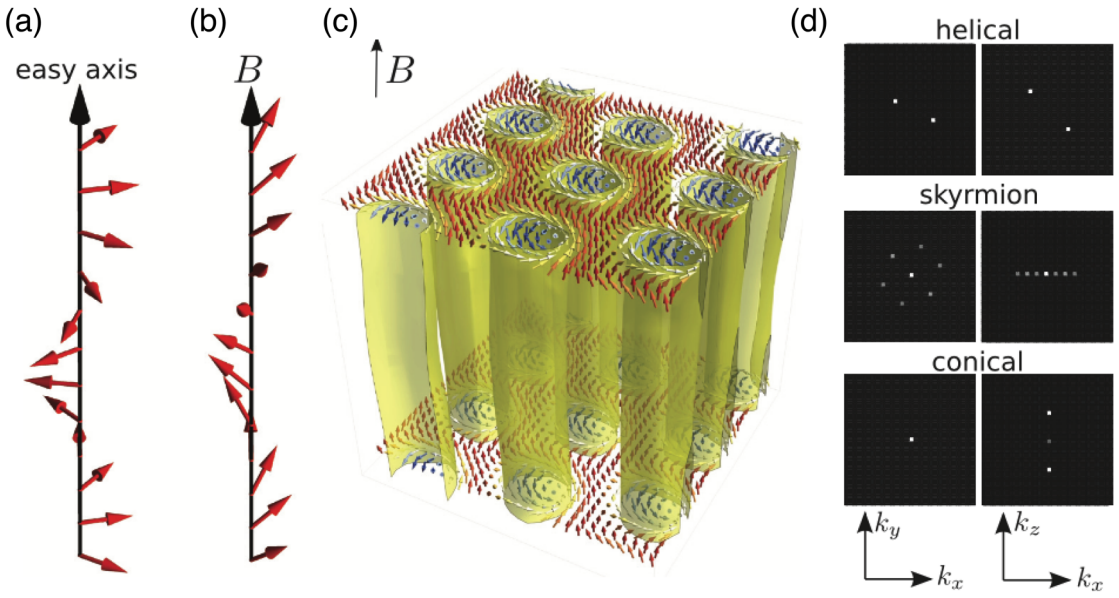

Figure 2.5: Schematic representation of (a) helical, (b) conical and, (c) skyrmionic textures produced in some chiral magnets with (d) their corresponding SANS diffraction patterns. Reproduced from Ref. [167] with permission from the American Physical Society.

the mesoscopic lengthscale [Fig. 2.5]. Magnetic SANS has played a pivotal role in progressing the field of magnetism and superconductivity [268] and is commonly used in conjunction with established methods, including neutron diffraction, for characterising and analysing the static and dynamic spin structure of nanomaterials [269]. In this thesis we simulate small-angle scattering to detect the formation of textures in simulated materials.

2.1.4 Modelling diffraction

Although analysing structures from ordered crystals is a routine procedure, analysing disordered materials is more complex [13]. There are two main approaches used to analyse disordered structures. The first uses 3D-ΔPDF maps—the Fourier transform of the diffuse scattering—to reveal the difference in atomic correlations from

the average structure in real space [102]. The second creates disordered structures by computationally generating large supercells of model systems with chemically sensible local rules and comparing the calculated diffuse scattering from them to experimental data [270, 271]. Due to finite size effects, large supercells are required when modelling disorder as, although many disordered states manifest from local deviations alone, the realisation of degenerate configurations produced in general requires several unit cells [31]. Furthermore, the granularity of the diffuse features is inversely proportional to the 'lot' size calculated [272].

As the size of the reciprocal lattice is inversely proportional to the regular lattice, if the model contains one unit cell, the reciprocal space grid will only be as fine as one reciprocal lattice unit. Unsurprisingly, only Bragg scattering can be observed. Introducing more cells in the system by creating a supercell of unit cells allows for the detection of scattering between the Bragg peaks. Diffuse scattering arising from disordered systems exists in non Bragg peak positions and tends to manifest through more continuous scattering with broad peak widths. If the simulated box size were doubled to contain a $2 \times 2 \times 2$ supercell, diffuse effects may show up in the form of superlattice reflections as the reciprocal space grid now has two points along each axis where $\mathbf{k} = 0, 0.5$. Calculating diffraction patterns on larger supercells allows for a finer grid in reciprocal space, causing the diffuse peak widths to be 'filled in' at reciprocal lattice vectors between. Therefore the larger the supercell, the more continuous the diffuse scattering is observed to be, mimicking real crystals to a higher degree [270]. There is usually a trade off in computational expense and size of the supercell as the complexity increases for a 3D system as ZN^3 where N is the

size of the supercell and Z is the number of atoms within each unit cell. There is no general rule as to how large the simulation box should be, however, it must at least exceed the correlation length of the structural ordering effects studied [273].

This thesis employs computationally generated large supercells for diffraction analysis of disordered systems. Diffraction patterns are produced either by using curated software or with custom written code. In Chapters 3, 4, and Appendix B, to determine the cause of the stacking disorder seen in experimental patterns, this thesis employs computer simulations of model systems. Using Monte Carlo models, we output configurations and use CrystalDiffract [274] to simulate scattering intensities and compare to experimental data. For Chapter 5 and Appendix A, single crystal X-ray scattering patterns are created by using a custom written code to Fourier transform the atomic positions and analyse configurations. The study in Chapter 5 focused on the small-angle scattering in particular, in depth details of which are explained within Chapter 5.

2.2 Monte Carlo simulations

For many systems, Hamiltonians can be constructed which encapsulate the energetics of the material through modelling the characteristic interactions. Analysing these models can be approached in a variety of ways, chosen based on the model in question. For some statistical mechanical models, exact solutions can be formulated [275], as is the case for the Ising spin chain [Eqn. 1.1] [154]. But in most cases, particularly for disordered structures, it is necessary to employ techniques such as mean field theory [276] or Monte Carlo (MC) simulations [277]. MC simulations are

used to tackle problems from a large variety of fields, from modelling the impact of pollution [278] to efficiently pricing seats on airplanes [279]. In solid-state chemistry, MC is a key technique as it allows examination of the behaviour and properties of materials over phase transitions [196, 280]. The most relevant use of MC simulations for the research in this thesis is its ability to generate representative atomistic models for a given interaction model: the corresponding diffraction pattern can then be calculated and compared against experiment [277].

2.2.1 Metropolis algorithm

In this thesis, the MC simulations make use of the Metropolis algorithm [281] to generate ground state configurations whose energies are defined by a given Hamiltonian. The MC process starts by generating a configuration where the initial states of the features of interest are randomly assigned. To explain the procedure, we use the example of antiferromagnetically coupled Ising spins on a square lattice where generating the configuration consists of populating the vertices of the square lattice with spins randomly assigned in the up or down state [Fig. 2.6(a)]. The configurational energy is then calculated using the predefined Hamitonian. In each Monte Carlo step, one of the states is chosen at random and a trial move is proposed (in this case spin flipping) [Fig. 2.6(b)] and accepted with a given probability based on Boltzmann statistics:

$$P = \exp\left[-\frac{\Delta E}{k_B T}\right], \tag{2.26}$$

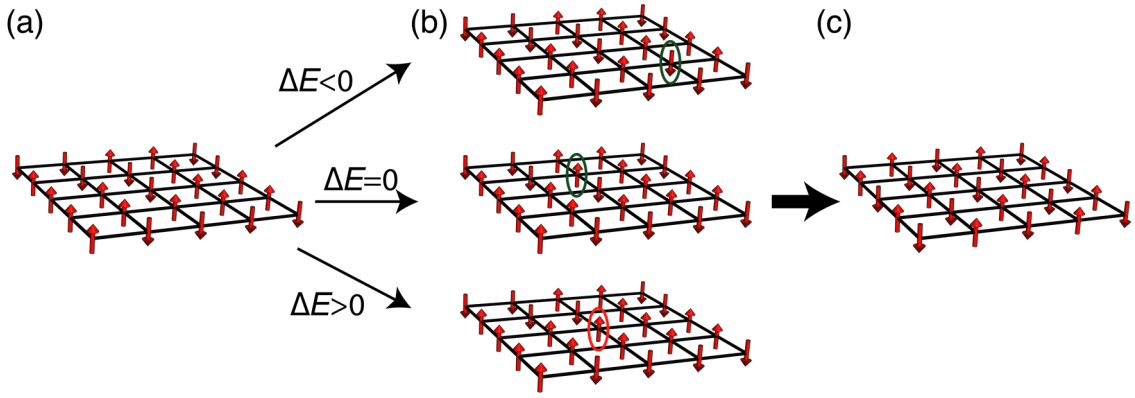

Figure 2.6: (a) Starting configuration of Ising spins on a square lattice. (b) Monte Carlo steps at sites circled that lead to a decrease in energy (top) no change in energy (middle) an increase in energy (bottom) with respect to antiferromagnetic coupling. The top and middle spin flips are circled green as they are always accepted whereas the bottom is circled red as it is only accepted when P [Eqn. 2.26] is greater than a random number n. (c) Representative ground state configuration produced from Monte Carlo simulations for antiferromangetic Ising spins on a square lattice.

where ΔE is the change in configurational energy upon the move, T is the temperature, and k_B is the Boltzmann constant. The value of P determines whether a move is accepted by comparing it to a generated random number, n, where $0 \leq n < 1$ and the move is accepted if $P > n$. This criteria stipulates that the move is always accepted when $\Delta E \leq 0$ and accepted with a given probability determined by how energetically unfavourable the move is when $\Delta E > 0$. The acceptance of unfavourable moves increases the configurational energy but lowers the risk of the simulation getting stuck in a local minima such that the process can repeat until the configurational energy reaches a stable equilibrium state [Fig. 2.6(c)]. An overview of this process is shown in Fig. 2.7.

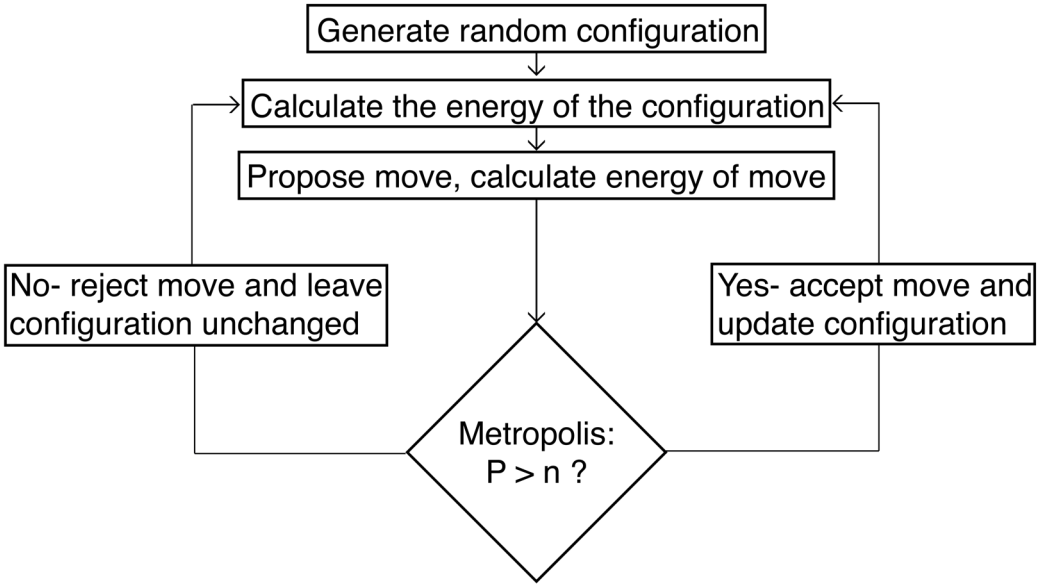

Figure 2.7: Overview of the Metropolis algorithm for Monte Carlo simulations.

2.2.2 Equilibration

In order to obtain a representative estimate of the model under study, it is imperative to ensure that one is actually sampling an equilibrium state. To ensure equilibration at each temperature step, the number of moves required for the system to become uncorrelated from its initial state is measured and 10 times this many moves are subsequently discarded. For example, if the degrees of freedom in question are magnetic spins, at each new temperature step, the initial spin states ($\mathbf{S}^s$) were recorded and at regular intervals, the scalar products of the current ($\mathbf{S}^c$) and initial spin state were sampled at each site i. When

$$\sum_i \mathbf{S}_i^s \cdot \mathbf{S}_i^c < 0, \tag{2.27}$$

then the configuration is considered to be uncorrelated from its initial state and

therefore an accurate reflection of the behaviour of the system at the given temperature [282, 283].

However, in some cases there is preferential aligning of the degrees of freedom along one of the axes (as is the case with spins in a magnetic field). For these systems, the degrees of freedom may be unable to completely decorrelate from their initial state, and instead the conditions are loosened to a minimum number of moves [176].

2.2.3 Simulated annealing

There remains a question of how quickly the system should be cooled. In practical contexts, abrupt cooling to the target temperature is not a sufficient condition for finding ground states of matter and experimentally, must be done by careful annealing [284]. If the substance is not annealed slowly, it can become non-equilibrium, leading to the formation of defects and disordered domains which are not thermodynamically stable [285]. Computationally, the procedure is very similar. Accepting rearrangements that only lower the energy is computationally equivalent to rapid quenching from high temperature to $T = 0$ and as such, it should not be surprising that the results under these conditions are metastable [286]. Thus, when trying to access accurate ground states, to avoid decreasing the temperature too quickly and circumvent entrapment in a local minima, simulations employ a process known as simulated annealing [287, 288]. The Metropolis algorithm outlined above allows iterative improvement where uphill steps can be incorporated in a controlled fashion. The repetitions of this process simulates the thermal motion of atoms at tempera-

ture T. Simulated annealing then lowers the temperature once an equilibrium state has been reached, requiring the simulation to run long enough for a steady state to be produced.

To avoid this issue, temperature changes should be done multiplicatively where $T_{i+1} = (1 - \alpha)T_i$ and i is the step in cooling. However, the rate of decrease, *i.e.* the value of α still needs to be chosen carefully as it can have a great effect on the ground state behaviour. Unfortunately there is no universal rule when picking temperature scales as it is a case-by-case basis. A good starting point is to use the interaction parameters defining the energy scale as a guide, and sample a range of temperature points with varying increments proportional to them by testing how many moves are required to become uncorrelated when decreasing temperature. If the ground state energy is known *a priori*, it is possible to raise/lower the temperature as required and exit only when the energy has the value [289]. Doing so uses MC to generate a configuration but it is not technically forming the thermodynamic product.

2.2.4 Finite size effects

The problem of finite size effects has been noted in most areas of MC simulations [290] where the size of the simulation has a pronounced effect on the calculation. It can affect the temperature of phase transitions [291] and phase formation [292] meaning great care must be taken when choosing the size of the system. It is especially important when looking at phases which exist on a greater length scale than the interatomic distance, such as textures [167]. When there are only a small number of sites within the system, the number of textures able to form will be

significantly influenced by how many sites are needed to produce each texture. For example if the material is in a helical state and has a pitch length of 7 sites, a simulation box size of $10 \times 10 \times 10$ allows only a single helix to be completed due to periodic boundary conditions. This causes the stepwise formation of textures instead of continuously—as in real systems—as only an integral number of textures can be observed [293]. To avoid finite size effects completely, an infinite box must be used; however, an increased number of variables comes with its own cost of greater computational expense and a careful balance must be struck. For textured systems, this limitation is often overcome by simulating 2D layers and subsequently extrapolating results into three dimensions [166].

Another pitfall of MC simulations occurs as the formulation of a Hamiltonian requires *a priori* knowledge of the system to accurately depict the interactions involved. Other modelling techniques such as Reverse Monte Carlo allow for refinement against experimental data with no knowledge of the interactions beforehand, but intepretation of the resulting structure can prove challenging [99, 294, 295]. Quantum calculations such as density functional theory allow for accurate analytical solutions of the ground state of materials with minimal information about the interactions involved in the phase; however, these require a good approximation to solving the Schrodinger equation for the given system which can be more complex in some materials than in others.

2.3 Density functional theory

Density functional theory (DFT) is a quantum mechanical modelling method that investigates the ground state structure of materials. It is a powerful technique that is used in many disparate areas of science from nanotechnology [296] to determining organic reaction mechanisms [297] to structure and property prediction for materials discovery in batteries [298]. For one-electron atoms, such as hydrogen, determining the electronic wavefunction is trivial as one can solve the Schrödinger equation exactly to produce an analytical answer. Most chemistry however, does not exist solely in hydrogen and when moving to many electron systems, even two electrons, the ability to solve the Schrödinger equation analytically ceases and assumptions have to be made in order to solve the equation as accurately as possible.

The breakthrough for designing an approach to analyse electronic wavefunctions of many-body systems came when Hohenberg and Kohn showed that the ground-state energy and properties of a system can be uniquely defined by the electron density [299, 300]. Expressing the energy, E, as a unique function of the electron density, the energy functional is written as the sum of two terms:

$$E[\rho(\mathbf{r})] = \int V_{ext}(\mathbf{r})\rho(\mathbf{r})\mathrm{d}\mathbf{r} + F[\rho(\mathbf{r})]. \tag{2.28}$$

The first term arises from the interaction of electrons with an external potential, typically a Coulombic interaction with the nuclei, and $F[\rho(\mathbf{r})]$ is the sum of the energy of the electrons and the contribution from interelectronic interactions [299]. When dealing with energy functionals, difficulties arise as the exact form of $F[\rho(\mathbf{r})]$

is unknown. The function is instead approximated by the sum of three terms [301]

$$F[\rho(\mathbf{r})] = E_{\mathrm{KE}}[\rho(\mathbf{r})] + E_{\mathrm{H}}[\rho(\mathbf{r})] + E_{\mathrm{XC}}[\rho(\mathbf{r})]. \tag{2.29}$$

The first two terms are well defined where $E_{\mathrm{KE}}[\rho(\mathbf{r})]$ is the kinetic energy of a system with non-interacting electrons and $E_{\mathrm{H}}[\rho(\mathbf{r})]$, the Hartree electrostatic energy, arises from classical interactions between two charge densities. The remaining term $E_{\mathrm{XC}}[\rho(\mathbf{r})]$, the exchange-correlation functional, incorporates the neglected interactions from the first two terms—many-body interactions arising from exchange, correlation, corrections to the non-interacting electron kinetic energy, and self-interaction energy of electrons—and is key to the success of DFT [299].

The assumptions taken in DFT calculations are designated by the exchange correlation functional used. There are many different levels of functionals, starting from the simplest approximation of exchange-correlation functionals: the local density approximation (LDA), to approximations including the hybrid functional exchange terms. The LDA was orginally introduced by Kohn and Sham [301], which assumes the exchange energy per electron is the identical to that of a homogeneous electron gas with the same electron density at any given value of r. This functional, although incredibly simple, is surprisingly effective at finding the ground state energy of some solid state structures. However, the functional is known to overestimate cohesive energies and underestimate band gaps in semiconductors [302].

To increase accuracy, generalised gradient approximation (GGA) functionals can be used where the functional depends on the energy density and gradient of the

density [303]. This is particularly useful when studying crystalline materials, as the electron density varies rapidly within the structure. As with most computational techniques, increased accuracy comes with a greater associated computational cost than the simpler LDA functionals. The additional degrees of freedom given by also calculating the gradient of the density mean that unlike LDA functions, there is no single approximation but instead a group of related approximations. The most common GGA functionals are PBE [304] and PW91 [305]. Although these functionals are a vast improvement on LDA functionals, they tend to over-polarise structures to have more ionic character and fail to capture dispersion interactions. To improve on these, electron exchange can be included from the Hartree Fock method to incorporate effects from static correlation, creating hybrid functionals [306]. Examples of such functionals are PBE0 [307, 308] and B3LYP [309, 310] where B3LYP is the most common choice for transition metal containing molecules [311]. Again, this increased accuracy comes with an associated computational cost as the exchange is non-local and requires calculating the Hartree Fock solution to the multi electron problem. An overview of the computational expense/accuracy for a range of different functionals is shown in Fig. 2.8.

DFT calculations are incredibly powerful for studying ordered states. However, they are less well equipped to deal with disordered states as the computational complexity substantially increases with more atoms in the unit cell, needed for accurately characterising disordered states. The periodic boundary conditions required for DFT calculations enforce a periodicity which is unlikely to be physical for any real disordered system [313]. For materials which contain correlated disorder,

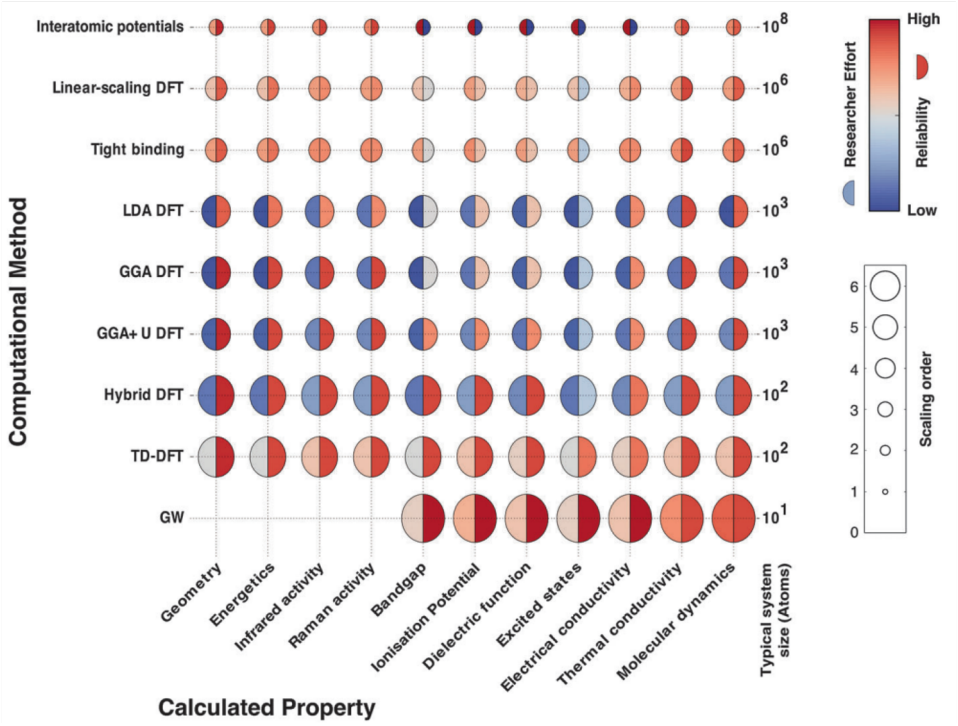

Figure 2.8: An overview of the computational and research effort for a range of calculable material properties for a set of common computational methods. The circle size corresponds to the scaling of computational effort with system size, and the shade corresponds to the effort required to use the method (left) and reliability of the results (right). Figure reproduced from Ref. [312].

DFT calculations are usually avoided as great consideration must go into selecting a suitable model and subsequently interpreting the results in the appropriate context. Moreover they are necessarily computationally expensive as they predominantly require large box sizes to sufficiently analyse ground state configurations. Although not directly relevant to this thesis, another important limitation of note is the drastic increase in computational expense and complexity of DFT calculations containing open-shelled atoms with unpaired electrons [314]. The inclusion of spin means additional interactions must be considered such as spin-orbit coupling which can be conveniently ignored in most functionals [315]. Magnetic materials are therefore notoriously difficult materials for DFT calculations, although, with

the improvement of functionals, the approximations are becoming increasingly more accurate but with considerably increased numerical efforts [316].

In this thesis, GGA appoximations are used; more specifically, the Perde, Burke, and Ernzehof (PBE) or PBE0 exchange-correlation functional [304, 317] with DZVP-GTH-PADE basis sets [318]. DFT calculations were carried out in both Chapter 5 and Appendix B using the CRYSTAL14 or CRYSTAL17 software [319]. The functional, basis set, and reciprocal space net used were determined based on procedures outlined in Ref. [320]. The functional and basis set were chosen by running calculations with a variety of both and choosing which were least computationally expensive with sufficient chemical sensibility. The shrinking factor generates the corresponding grid of k-points in reciprocal space. Choosing the granularity of the grid depends on the size of the unit cell. In general large unit cells only need to be sampled at the Γ point in order to reach convergence, whereas smaller lattice parameters require larger sampling with a typical shrinking factor chosen such that shrinking factor $\times$ lattice parameter $= 30 - 40\,\text{Å}$ [320].

Static DFT is a 0 K representation of the system, meaning it will describe only the state of lowest energy. However, at any finite temperature the atoms in a crystal are vibrating. Although analysing the ground state of materials is imperative to understand their behaviour, it may not be representative of the room temperature structure where materials are more traditionally analysed. The vibrational response of materials is fundamental when explaining their bulk properties such as phonon mediated negative thermal expansion [321, 322]. Thus multiple lattice dynamical techniques using analytical and numerical simulations are employed to analyse the

behaviour of materials with increasing temperature.

2.4 Lattice dynamical calculations

The discussion on methods used for energy minimisation in this section is constructed based on the overview given in Ref. [323].

2.4.1 General Utility Lattice Program

The General Utility Lattice Program (GULP) [324] is a classical lattice dynamics program commonly used for lattice energy minimisation and structural optimisation but has may other functionalities such as surface energy and bulk property calculations [325, 326]. The software conducts energy-minimisation using classical (or parameterised) approximations of interatomic interactions. Energy minimisation is a prerequisite for most other types of calculations such as lattice dynamics calculations [327], molecular dynamic simulations [328], and determining elastic properties [329]. To begin the process of energy minimisation, the program searches for general stationary points in the energy at which the gradients are zero. Whilst there are a number of methods used to achieve this, all of them start by using a Taylor expansion, as the energy about any given point can be expanded as a Taylor series:

$$E(x + \mathrm{d}x) = E(x) + E'(x)\mathrm{d}x + \frac{1}{2}E''(x)\mathrm{d}x^2 + \cdots . \tag{2.30}$$

Here $E'(x)$ is the vector of first derivatives at x and $E''(x)$ is the matrix of second derivatives, referred to as the Hessian matrix. Terminating the expansion at the first order, as is common for the harmonic approximation, requires the energy and

first derivatives to be calculated. These determine the direction of movement. The simplest method of steepest descents then repeats this process until convergence. This strategy is particularly inefficient as all previous information gained about the energy is ignored, but recent techniques have been developed to use the conjugate gradients algorithm [330] where subsequent steps are made orthogonal to previous search vectors.

The Newton-Raphson method for energy minimisation involves expanding the Taylor expansion to the second order term. The displacement vector, $\mathrm{d}x$, from the current point to the energy minimum becomes:

$$\mathrm{d}x = -E''(x)^{-1}E'(x). \tag{2.31}$$

If the interaction is harmonic, this vector takes the system to the local energy minimum in one step. In general, this process is done iteratively until the minimum is reached as, once the structure is close to the minimum, the energy is close to harmonic. The inverted Hessian matrix only varies slowly between each step and the process of inverting it is often computationally expensive and wasteful. To avoid this, methods can be used to update the inverse Hessian between cycles of minimisation based on the gradient, $E'(x)$, and position vectors, x, from the current and previous cycles. One of these methods is known as Broden-Fletcher-Goldfarb-Shanno (BFGS) [331] Hessian update. This process initialises the Hessian by performing an exact inversion of the second derivatives and then subsequently updates for a number of cycles.

The choice of algorithm depends on the size of the system. For small systems, the Newton-Raphson method is efficient but as the size increases, so does the computational cost for building and inverting the Hessian matrix, growing as N^3 where N is the number of atoms and as such memory requirements rapidly increase. Therefore, for large systems it is necessary to use the BFGS Hessian update and ultimately the conjugate gradients method as N continues to increase.

Typically lattice dynamical calculations require a suitable input of the crystallographic information including atomic positions, space groups, and lattice parameters. The key difference to other computational calculations such as DFT is they also include the interatomic potentials. From these input data, GULP calculates the lattice energy of the material which, in the case of electrostatic interactions in ionic structures, is carried out using Ewald summation technique, because of their long-range nature [332].

The application of GULP calculations pertaining to the research contained in this thesis is twofold. Firstly, in Chapter 4 we use electrostatic potential calculations between rigid layers of $Ni(CN)_2$ to determine the potential energy surface of slipping planes. Secondly, in Appendix A energy minimisation and structural optimisation is implemented for the analysis of outputted Monte Carlo configurations.

Lattice dynamical calculations are well suited for determining crystal properties, structural manipulation, and defect calculation as they allow relatively simple manipulation of real systems by changing parameters and are computationally inexpensive. This approach works well for systems which exhibit translational periodicity. However, many calculations within GULP require periodic systems and so difficultly

arises when modelling disordered systems. In some cases, such as phonon calculations, this issue can be combated through the use of a large supercells calculated at $\mathbf{k} = 0$, followed by supercell lattice dynamical (SCLD) analysis [11].

Having to devise a fixed model potential for lattice dynamical calculation leads to serious drawbacks. Firstly, when analysing materials behaviour over time—as is the case of molecular dynamics simulations—the electronic structure, and thus bonding, may change over the course of the simulation. Secondly, the more complex the material, the more interactions have to be parameterised between many atoms and molecules. Arriving at a set of empirical potentials that accurately capture both structure and dynamics is a complex task. To overcome these problems, *ab initio* techniques such as DFT and *ab initio* molecular dynamics are implemented instead [333].

2.5 Molecular dynamics

Molecular dynamics is a well established, powerful tool used to investigate many-body condensed matter systems. Molecular dynamics simulations can be sorted into one of two classes; classical molecular dynamics (MD) calculations, and *ab initio* molecular dynamic (AIMD) simulations. Setting up a classical MD simulation requires the approximation of interatomic interactions by breaking up them up into two, three, or many body contributions, and grouping the short and long-range terms [334]. For *ab initio* methods, the forces acting on the nuclei are computed from electronic structure (DFT) calculations as the molecular dynamics trajectory is generated. In *ab initio* techniques, the electronic variables are considered active

degrees of freedom instead of a constant quantity as in classical simulations. Thus the approximation is shifted from defining a fixed model in the classical case, to selecting an approximation for solving the Schrödinger equation [335].

2.5.1 *Ab initio* molecular dynamics

AIMD simulations are numerical techniques which allow accurate simulation of finite temperature behaviour of materials. Typically, the trajectory of a molecule is obtained by numerically solving Newton's equations of motion:

$$\mathbf{F}_I = M_I \mathbf{R}_I = -\frac{dE}{d\mathbf{R}_I} \tag{2.32}$$

which is important to assess time dependent (dynamic) observable such as vibrational behaviour of atomic diffusion [336]. AIMD has been used in many areas of research such as in the study of biological systems [337], the behaviour of phase transitions [338], and the study of chemical reactions [339]. To perform an AIMD simulation, an appropriate thermodynamic ensemble needs to be chosen. For real systems, the temperature and pressure can be controlled and accordingly the canonical (N, V, T) and (N, p, T) ensembles are commonly selected [340]. It is important to run the simulations for long enough to ensure the potential and kinetic energy have equilibrated such that the total energy has converged to give a representative sampling at a specific temperature. AIMD simulations use similar approximations to that of DFT calculations, with the added approximation that the trajectories of nuclei can be calculated classically (*i.e. via* Newton's equations of motion). Therefore, the main challenge again comes from the choice of functional.

In Chapter 5 of this thesis, we use a combination of MC, DFT, and AIMD to analyse the phase behaviour of a system and then determine the extent to which materials depend on the interactions set out by the MC model. The AIMD simulations carried out for this study were implemented using the CP2K software [341]. The PBE exchange-correlation functional [304] was used with DZVP-GTH-PADE basis sets. These were performed by first taking a geometry optimised structure from DFT calculations and then running the molecular dynamics simulation in the constant-volume (N, V, T) ensemble at a time step of 0.5 fs and run for 20000 steps to get an equilibration period of 10 ps. As the inputted configuration is the energy minimised structure at 0 K, a sufficient number of steps had to be discarded to ensure equilibration has been reached. To achieve this, the energy of the simulation was tracked as a function of simulation time and when it stabilises, the structure was considered equilibrated and sampling of data begun [Fig. 2.9]. For the AIMD simulations considered in this thesis, the first 6000 steps were discarded to ensure equilibration at each temperature.

Despite the obvious advantages of *ab initio* simulations, the calculations are necessarily computationally expensive and it is difficult to simulate processes which occur on a timescale longer than nanoseconds. Also, compared to classical MD, tracing back the properties of a simulated system to the interactions responsible is a less straight forward task. Conversely, whereas predefining and interaction model confines the system to only produce phenomena relating to those interactions, *ab initio* techniques allow for unpredicted phenomena to occur during simulations.

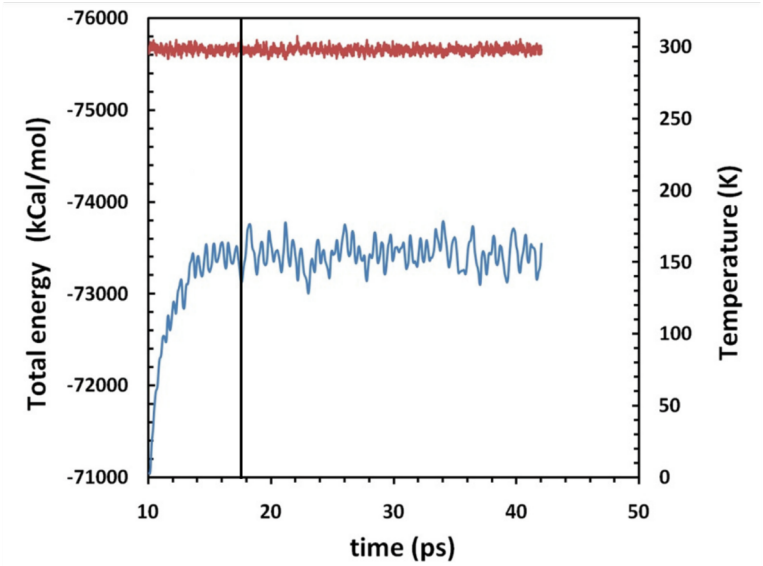

Figure 2.9: Total energy (blue) and temperature (red) against time for the molecular dynamics simulation of water-Cu nanofluids. The levelling of the plot indicated by the black line defines the equilibration time. Figure reproduced from Ref. [342].

2.6 Overview

At the heart of all the computational techniques outlined lies the question; how do we describe/approximate interatomic interactions? For techniques such as MC and classical MD, one has to know—or assume—a great deal about the material in order to create an accurate model encapsulating the interactions and degrees of freedom. If this is done successfully, the results can build a detailed phase diagram and compute predicted properties as well as assign interaction parameters to the material with relatively minimal computational cost. This can lead to easy phase determination and precise manipulation of materials to access complex phases with interesting properties.

For *ab initio* techniques, the route back to the specific interactions formulating the phases produced by simulations is much less clear. This makes it comparatively

difficult to understand how to navigate the phase space of the material and harder to target specific functionalities. However, very little detail of the material, and no interaction potentials, are needed to run the simulations. This allows structure determination and dynamic behaviour to be calculated with no assumptions of the interactions between sites. More recently, techniques have been developed to combine the two by using *ab initio* calculations to derive the necessary parameters for numerical calculations [343, 344]. These studies have the added benefit of deriving parameters entirely from first principles which can be drawn on for future studies requiring interatomic potentials.

By combining the various techniques described here, it can become possible to determine a model of the interactions in a given material and assess to what extent they are relevant to experiment. Throughout this thesis we aim to create models that can accurately represent the phase space of materials with as few parameters as possible. This is done mainly by using MC simulations but also a combination of DFT calculations and AIMD simulations are implemented to authenticate the results presented.

Chapter 3

Polytypism in layered AB_2 solids

3.1 Summary

Despite their long history and ostensible simplicity, one-dimensional statistical mechanical models continue to assume a particular importance in contemporary condensed matter physics. Naturally, much of the focus within the field has been on systems with 1D electronic and/or magnetic behaviour. Yet it has long been known that the 1D Ising model is also relevant to the polytypic behaviour of structures such as SiC [233, 345]. Not only did the mapping of statistical mechanical models onto stacking behaviour help interpret otherwise-unexpected physical properties of fundamentally-important systems, but the behaviour of the physical systems provided the motivation to develop the relevant theory [245].

An historic example is the development of the ANNNI model, which later proved pivotal in interpreting incommensurate and commensurate modulation phenomena in condensed phases [116]. Due to the numerous states formed by finite temperature simulations of the ANNNI model, 1D statistical mechanical models were able to describe structural phases with increasing complexity [240]. The ANNNI model is a powerful statistical mechanical model as it can predict the polytypic behaviour in complex phases from disparate areas of chemistry, and it is argued all fundamental aspects of polytypism can be explained qualitatively through the ANNNI model

[346]. Yet, the model is not without its limitations. Not all polytypic phases are predicted, with the inability to account for the $\langle 13 \rangle$ phase (... $\uparrow\downarrow\downarrow\uparrow\downarrow\downarrow\downarrow$ ...) particularly noteworthy [240].

Polytypic behaviour is found in materials with psuedo 1D behaviour [241]. The effect of polytypism on the properties of materials is well characterised for many systems [347, 348], with increasing attention paid to the van der Waals materials including layered dichalcogenides [349, 350]. The sustained interest in their phase behaviour stems from a rich spectrum of physical properties for a comparatively small class of chemical compositions [351]. Layered compounds provide a vast range of useful electronic, optical, mechanical, chemical, and thermal properties that can sometimes be tuned as a function of their structure [352–355]. Although the ANNNI model can explain the stability of some AB_2 phases, not all polytypes formed in practice can be accounted for [243, 246].

In this chapter we look at a new way of describing the structure of layered AB_2 compounds, translating their degrees of freedom to a 1D model of coupled Ising chains to explain the polytypic behaviour. Our analysis suggests a family of ten 'simplest' ground states, seven of which have previously been reported. Using Monte Carlo simulations, we find that other phases identified in the literature but not expected by our model, are either describable as disordered states intermediate to our limiting phases, or mischaracterised. We proceed to show that the coupled 1D Ising chains encapsulate the behaviour of solid solutions of layered AB_2 systems, with a long term aim to link the properties of these materials to the interaction parameters relevant to the model. This phase control is an important result as it

could lead to targeted design for specific properties, as structure is known to have a profound influence on materials' properties.

3.2 Background

Up until the 1960s, polytypism was believed to be a special phenomenon which was restricted to a few select compounds [243]. Extensive research over the next twenty years revealed that the phenomenon is widespread in nature and exists in a variety of crystalline substances such as silicon carbides and perovskites [356, 357]. Along with increased experimental exploration, the theory behind polytypism was developed. Polytypism tends to occur in layered materials which are thought to be psuedo 1D due to the large difference between in-plane and out-of-plane interaction strengths. Thus the theory behind polytype formation focuses on 1D statistical mechanical models with discrete degrees of freedom describing the layers' relative positions; *i.e.* the Ising model. Although there has been continued research on the structure and properties of polytypic materials through experimental techniques and *ab initio* modelling [111, 358–360], the development of theoretical models from a Hamiltonian point of view was ultimately discontinued in the late 1980s [243, 245, 246].

Compounds with the general formula AB_2 where A is a transition metal and B is a polarisable anion tend to adopt a particular type of layered structure [37]. The universal building block for all AB_2 structures in consideration is a hexagonal unit with the A cation at the vertical midpoint, sandwiched between two B anion planes [Fig. 3.1(a)]. This cell generates planes of A and B ions where the three possible positions for each plane in the cell correspond to the three possible close-

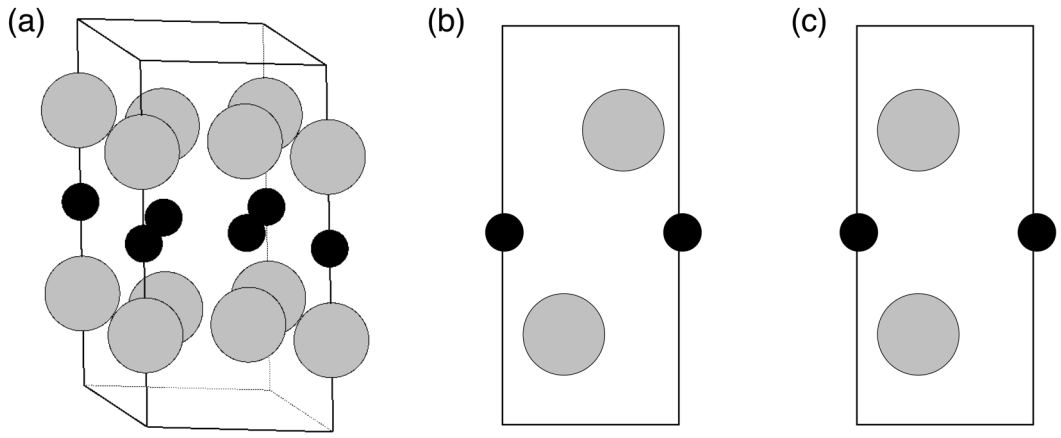

Figure 3.1: (a) The universal collapsed average structure of AB_2 structures showing all possible positions of the A cations and B anions. The hexagonal 'unit cell' contains A cations at its vertical midpoint ($z = 0.5$), sandwiched between two B anion planes ($z = 0.25, 0.75$). The interlayer space lies at $z = 0$. In reality, only $\frac{1}{3}$ of the crystallographic positions within each plane are filled, with ions in neighbouring planes sitting in different sites, leading to two possible orientations. AB_2 'unit cell' projected onto the $(\mathbf{a}, \mathbf{c})$-plane with (b) octahedral and (c) trigonal prismatic coordination. A cations are shown as small black spheres and B anions are represented by large grey spheres.

packed-plane position-types: **A** $(0, 0, z)$, **B** $(\frac{1}{3}, \frac{2}{3}, z)$, and **C** $(\frac{2}{3}, \frac{1}{3}, z)$. There are two coordinations within each cell; octahedral and trigonal prismatic. For octahedral coordination, the three ions within a unit occupy distinct position-types [Fig. 3.1(b)] whereas for trigonal prismatic coordination, the two B anions within the layer are in the same position-type, with the A cation in a different position-type [Fig. 3.1(c)]. The motif of one hexagonal unit is described as the intralayer structure, whereas the stacking behaviour due to neighbouring units is referred to as the interlayer structure. Within the intralayer structure, both the octahedral and trigonal prismatic coordination can have two different orientations. Between the layers, neighbouring B anions are always slipped with respect to one another by $\pm(\frac{1}{3}, \frac{2}{3}, z)$ which naturally lends itself to close-packed positions once again. Thus there are a variety of structures that AB_2 compounds can take due to the combination of interlayer and

intralayer arrangements.

Currently, the nomenclature surrounding AB_2 polytypes is insufficient for building the complete structure from the notation alone. Descriptors tend to focus either on the interlayer stacking, ignoring effects from intralayer behaviour, or focus on the global symmetry of the material which is often governed by the intralayer configuration. As such, a new description of the structures may be useful, containing details of the interlayer stacking behaviour as well as intralayer structure.

Here we develop a new, constructive way of describing the stacking behaviour in AB_2 compounds, resulting in a nomenclature that encapsulates the ordered stacking arrangements of the materials which allows recreation of the structure from the descriptors alone. To develop this idea, we begin by discussing the current terminology used for polytypic materials with reference to AB_2 structures, and then explain how our new constructive descriptors can be used to build up the stacking behaviour. From this new description we create the structure types that are chemically feasible within our model, and relate them to known structures in the literature. For the structures within the literature which are unable to be described by our model, we go through each in turn and suggest how they may be understood in the context of our model instead. Finally we look at the ability of our model to mimic the structure of solid solutions of AB_2 compounds, and end with an outlook of how our model may be developed and used elsewhere.

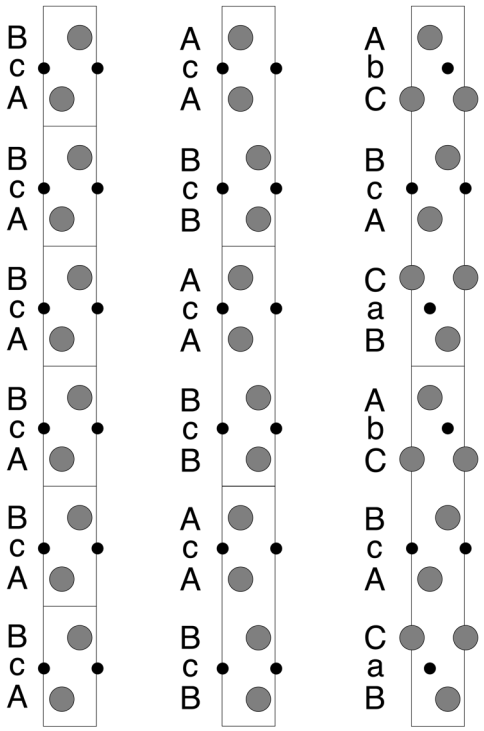

Figure 3.2: Projection onto the $(\mathbf{a}, \mathbf{c})$-plane for layers of CdI_2 (left), MoS_2 (middle), and $CdCl_2$ (right). To the left of each structure is their corresponding ABC notation. The descriptors for each structure in the different notations described in Section. 3.2.1 are represented in Table. 3.1.

3.2.1 Stacking descriptors

There have been numerous notations for the stacking behaviour of layered materials since the discovery of polytypism [361]. Each notation comes with its own benefits and limitations, leading to the use of some notations in only very specific fields whereas others are more universal. Here we give a brief overview of the most common nomenclature within the field of stacking behaviour and how each can be used to describe a few well known structures; CdI_2, MoS_2, and $CdCl_2$ [Fig. 3.2].

ABC notation

Commonly, polytypic structures are labelled by the close-packing site description using **ABCabc** where both upper and lowercase (or Greek) letters are used to distinguish between different types of atoms within a layer [Fig. 3.2] [362]. For many materials, the layers either only consist of one atom, or the intralayer atomic positions belong to the same closed packed site. In these cases, it is customary to omit the lowercase letters [362]. However, in AB_2 structures it is essential to use both lower and upper case notations to denote the metal and anion positions within each layer respectively. Although this method of notation gives a complete description, it gives no indication of the symmetry and becomes complicated for structures with large modulations [363, 364]. Moreover, the notation gives no information on whether the structure is unique due to equivalent stacking on cycling *i.e.* ABC/BCA/CAB. Even so, ABC notation is one of the more universal notations that, although not used commonly when referring to the material itself, is a useful way of explaining the structure of materials and is often used in conjunction with other notations, most commonly the Ramsdell notation [363].

Hägg notation

Instead of defining specific layering positions, Hägg notation [365] uses + and − to denote the direction of vector translation $(\frac{1}{3}, \frac{2}{3}, z)$ between neighbouring layers of close-packed structures. Using the ABC notation above, stacking between layers A-B are now denoted with a plus and B-A are denoted with a minus. Although more convenient than the ABC notation to discuss polytypism, especially with stacking

faults [366], this notation is insufficient for describing AB_2 phases due to the inability to distinguish between intralayer/interlayer stacking. Thus to use Hägg notation effectively for these phases, a starting atomic position must be given.

Zhdanov notation

The Zhdanov notation [122, 123] is the same notation used to describe the various phases in the ANNNI model explained in Section. 1.2.1 by summing the number of 'like' signs used in the Hägg notation. This is a simplification of the Hägg notation and as such is just as, if not more, convenient description for many structure types, particularly when looking at stacking faults. However, it comes with the same pitfalls as it cannot differentiate between intralayer and interlayer stacking and is insufficient for describing AB_2 structures.

Jagodzinski notation

The h-c or Jagodzinski notation [367] describes the rotations of neighbouring layers by 0 or 180 degrees using 'c' and 'h' respectively, reflecting the cubic or hexagonal symmetry. This notation has proved particularly useful when detailing the effects of faulted structures on X-ray diffraction patterns and calculating stacking fault energies [368, 369]. Again this description is concise as with the Zhdanov notation, but insufficient for describing AB_2 structures due to the inability to differentiate between the inter- and intra- layer stacking.

Ramsdell notation

The last commonly used label is the Ramsdell notation which is a shorthand notation which encapsulates the lattice type of the material by labelling the structure in three parts [364]. The main label is a letter which is related to the symmetry of the material. For the focus of layered transition metal AB_2 compounds, there are three key letters used to denote the different structures; H, T, and R which represent hexagonal, trigonal, and rhombhedral symmetries respectively. Layers of structures within the H and R categories tend to have trigonal prismatic coordination whereas layers of T structures are octahedrally coordinated.

The next most important label is a prefix containing a number associated with the number of close-packed layers in the material's unit cell. For example, in the case of CdI_2—$1T$ and MoS_2—$2H_c$ there are one and two layers per unit cell respectively [Fig. 3.2]. Lastly, for cases where there are multiple phases that can be described by the first two labels, an additional suffix is added. This suffix can be in the form of a letter, number, or prime ($'$); however the literature on AB_2 phases contains little evidence of a number being used [37]. For H phases, the suffix comes in a form of a letter which is used to differentiate between different stacking configurations that are formed from the combination of the number of layers with hexagonal symmetry. For example, in the case of $2H$ phases, there are three known structures that are formed which are labelled with a subscript letter *e.g.* a, b, or c. For differing T type structures, the suffix is in the form of a prime ($'$) usually denoting a degree of metallic bonding within the system such as $1T'$ and $1T''$. Although this can differentiate between the structures, it is sometimes misleading—as is the case for

Notation	CdI_2	MoS_2	$CdCl_2$
ABC	AcB	BcBAcA	BaCAcBCbA
Hägg	$---\!--$	$---+\!+$	$--+-\!-+$
Zhdanov	$\langle\infty\rangle$	$\langle 3\rangle$	$\langle 21\rangle$
Jagodzinski	cccc	hcchcc	chhchh
Ramsdell	$1T$	$2H_c$	—

Table 3.1: Different nomenclatures for structures represented in Fig. 3.2. The Ramsdell notation for the $CdCl_2$ is not recorded in the literature and has therefore been omitted.

$1T'$ where the structure actually contains two layers per unit cell [370]. Whilst the suffixes help highlight the existence of distinct phases, they are not sufficient to explain the form of the stacking or differences within the structure.

Evidently the field of stacking notation has been well explored in order to represent structures in a clear concise way with loss of minimal data. Yet, none of the descriptions are sufficient to fully reproduce the stacking arrangement of AB_2 compounds. For the three examples in Fig. 3.2, the Hägg, Zhdanov, and Jagodzinski notations [Table. 3.1] have no way of discriminating between intralayer and interlayer descriptors and are therefore insufficient to build up the structure. Studies have looked into removing the problem of considering interlayer and intralayer stacking separately by first considering and labelling the intralayer structure before considering the interlayer stacking. However these have focused on just the octahedral coordinated structures and are rather cumbersome [361].

The Ramsdell notation tells of the symmetry and number of layers within a unit, but nothing of the stacking behaviour itself. In some cases, as for CdI_2 ($1T$), this notation is sufficient as the label is unique. However, in most cases, as for $2H$, the label is not unique and a variety of structures can be described through the same

lattice. Adding a suffix does nothing more than highlight the existence of other phases, and cannot tell of the nature of the different stacking sequences. Moreover, there is no recorded Ramsdell notation for the $CdCl_2$ structure implying that the notation has not been developed to describe all structures. Only the ABC notation can be used to fully build up the stacking description of AB_2 structures however this becomes complicated for structures containing long-range modulations.

For complex phases, labels work best if they are constructive, by which we mean they contain sufficient information to devise the structure type. A good example is that of tilted perovskites, where the combination of rotations known as a 'tilt' system can be compactly described using Glazer notation [371]. The tilts are split into the three cubic axes, and the letters ascribed to each axis determine whether the rotation angle is the same or different. For example the $a^+a^+c^+$ tilt has a different rotation angle about the z axis than the rotation angle about the x and y axes. The superscript formalism indicates whether the rotations in adjacent layers are the same, $+$, different, $-$, or if no rotation occurs, 0. This description of tilting is constructive as it uses symbolic representations to describe all the features of the tilts (in/out of phase; distinct/equal magnitude) which, when combined, can construct a complex distortion of the perovskite structure. This formalism is not exhaustive, intentionally not including so-called 'unusual' tilts [372], and instead focuses on simple combinations *e.g.* in-phase and out-of-phase rotations. In principle more complex phases can occur, but these are rare and are not included by design. Enumerating the tilt systems in this way allows for targeted explanation of different tilt systems [373].

Here we develop a similar constructive nomenclature to represent the structures of layered AB_2 compounds. We show that there are ten simple AB_2 structure types and develop a generalised Hamiltonian that has as its ground states these ten phases at the limits of phase space. Through comparison with published diffraction patterns, we demonstrate that a number of ostensibly complex AB_2 phases can be described as points within the phase space between simple AB_2 structure types, and can be understood in terms of finite temperature states in our model.

3.3 The model

Layered AB_2 systems are constructed from AB_2 layers that stack on top of each other with strong intralayer interactions but weak, van der Waals interlayer interactions. Each layer can be in one of two configurations (octahedral or trigonal primsatic): each of these can be in one of two possible orientations; and each stacking step involves a shift in one of two directions. So, in principle, an AB_2 system with N layers has $8N$ viable arrangements. In practice, these degrees of freedom are not independent. The choice of octahedral or trigonal prismatic geometry, for example, strongly affects the electronic band structure, and so there is usually a clear electronic preference for one geometry that persists throughout the bulk [374]. Likewise, the charge density (multipolar) and dispersive interactions that govern the relative arrangements of neighbouring layers favour simple patterns where layer orientations or slipping directions are either always the same, or always alternate [375]. Much like the Glazer notation, in principle, more complex phases such as modulated periods of slipping directions could exist, but these are less likely to form

than simple patterns and are excluded from our model by design. Using these additional considerations we show that the number of distinct simple AB_2 structure types can be reduced to just ten which represent the vertices of a multidimensional phase space, and we illustrate the relationships amongst these.

For octahedral coordination, an intralayer orientation can be assigned based on the two possible permutation directions as the layer is traversed from bottom to top [Fig. 3.3(a)]. This can be assigned as clockwise—**ABC**—or anticlockwise—**ACB**—permutations. The orientation of trigonal prismatic layers can also be denoted by the same permutation as for octahedral coordinations (clockwise/anticlockwise), however the layer is spanned from the interior (A cation plane) out (B anion planes) [Fig. 3.3(a)]. Representing octahedral layers as square symbols and trigonal prismatic layers as triangles, we can depict the four possible layer types by using open symbols for orientations corresponding to clockwise permutations and filled symbols for anticlockwise permutations [Fig. 3.3(b)].

Irrespective of the individual layer types, neighbouring layers are always slipped with respect to one another. The two possible choices for this slip direction reflect the observation that a **B**-type B-anion only forms a viable interface with **A**- or **C**-types. Hence, much like the intralayer permutations, the slip direction can be mapped onto the same orientations by assigning the vacancy position accordingly. For example, the **B**/**A** and **B**/**C** interfaces may be assigned clockwise—**B**(**C**)**A**—or anticlockwise—**B**(**A**)**C**—orientations, respectively. Here the positions in brackets represent the 'missing' A-site cations between layers. We denote these slip directions by open and filled circles.

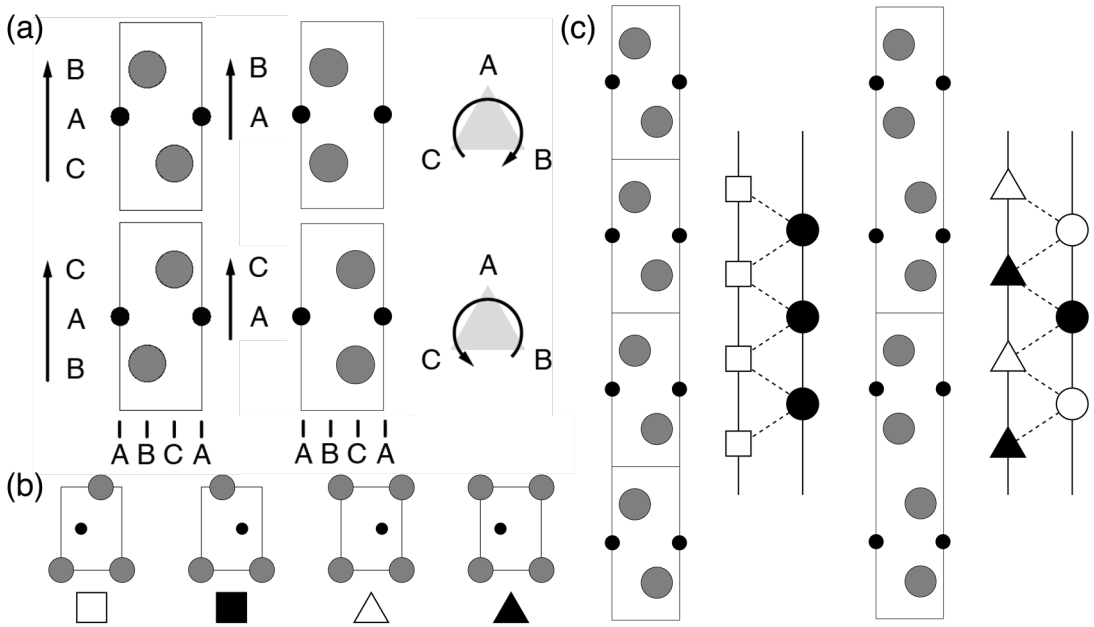

Figure 3.3: (a) Projection of AB_2 layers with octahedral (left) and trigonal prismatic (right) coordination, projected onto the (**a**,**c**)-plane where the orientation of layers are associated with two possible permutation directions in a clockwise (top) and anticlockwise (bottom) manner. (b) The four possible layer types/orientations where square symbols represent octahedral layers and triangular symbols correspond to trigonal prismatic layers. The open/closed symbols represent clockwise/anticlockwise permutations respectively. (c) $1T$ (CdI_2) (left) and $2H_c$ (MoS_2) (right) structure types with the layered structure represented as a coupled pair of 1D symbol-chains. The left chain describes the layer types and orientations and the right chain describes the interlayer slip directions. A cations are shown as small black spheres and B anions are represented by large grey spheres.

In this way, we can now represent any layered AB_2 structure by a coupled pair of 1D symbol-chains: one describing the layer types and orientations, and the other the interlayer slip directions. These chains directly map onto Ising chains and therefore the model can be described as a coupling of two 1D Ising chains. Importantly, this representation is independent of origin choice. The $1T$ (CdI_2) and $2H_c$ (MoS_2) structures correspond to the coupled 1D chains shown in Fig. 3.3(c).

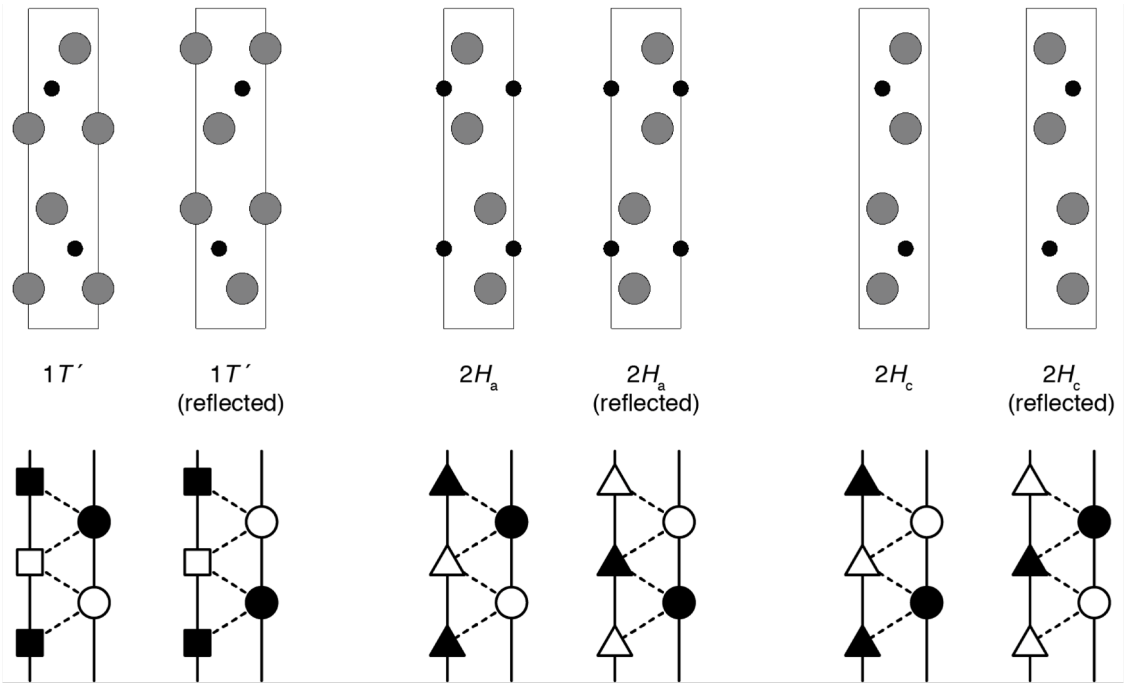

Figure 3.4: Examples of equivalent configurations due to reflections along horizontal or vertical mirror planes bisecting the projection edges and midpoints.

3.3.1 Enumerating structure types

In principle, all stacking of AB_2 layers can be represented in this way. Here we enumerate those which form from a combination of ferro/antiferro Ising states. Clearly, not all combinations will be unique as many will be equivalent under symmetry operations such as reflections in the horizontal or vertical mirror planes [Fig. 3.4]. We use the symbol '+' to denote a chain containing always-clockwise permutations, '−' for an always-anticlockwise chain, and '±'/'∓' for the two possible phases of chains with alternating permutations. We represent the pair of coupled chains by an ordered couple *e.g.* '+, −', where the first term corresponds to the layer orientations, and the second to the slip directions. Finally, we enclose this couple within square brackets for octahedral systems and angle brackets for trigonal prismatic systems.

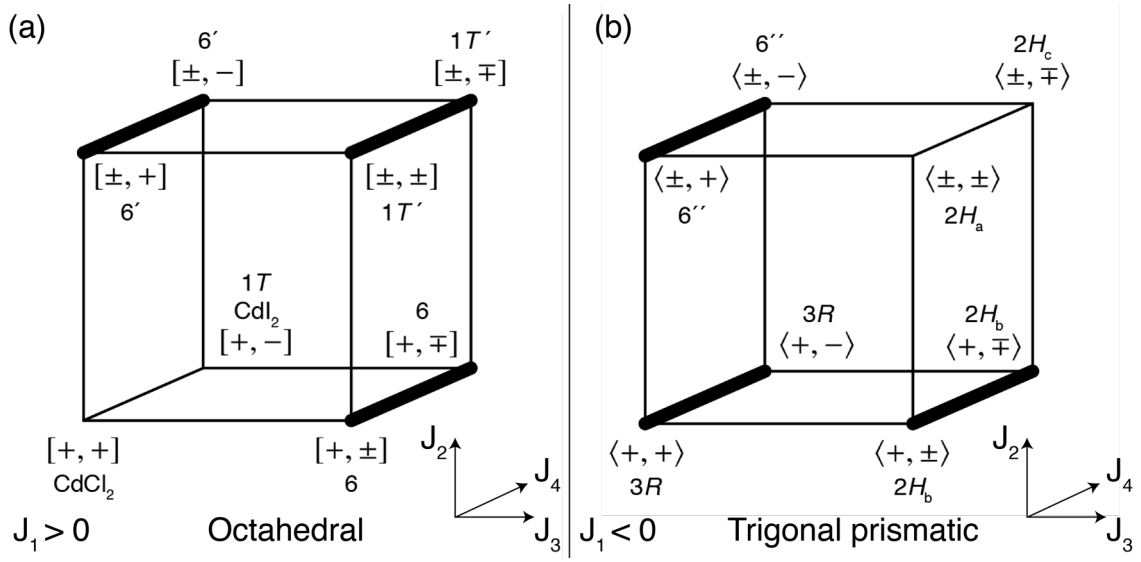

Figure 3.5: Structure types mapped out by the model described in Section. 3.3 which maps onto the Hamiltonian of coupled 1D Ising chains in Eqn. 3.1. (a) Octahedral structure types where $J_1 > 0$ and (b) trigonal prismatic structure types where $J_1 < 0$. The x, y, z axes of the cube correspond to J_3, J_4, J_2 respectively. The bold lines connect corners/symbols that give equivalent structure types

Hence $[+,-]$ and $\langle \pm, \mp \rangle$ generate the CdI_2 and MoS_2 structure types (depicted in Fig. 3.3(c)) respectively.

To enumerate all structure types that can be formed under this representation, we consider the octahedral and trigonal prismatic phases separately and begin by examining the octahedral AB_2 structures. As each term in the couple can adopt one of four states (*i.e.* $+, -, \pm, \mp$), there are in principle 16 possible combinations to test. However, as reflection about a plane that includes the c-axis inverts both orientation and slip directions, each phase has at least one duplicate; *e.g.* $[+,+]$ and $[-,-]$. Thus we consider the eight possibly-unique combinations which we can arrange at the corners of a cube [Fig. 3.5(a)]. The resulting structures, of which there are only five unique kinds, are found using FINDSYM [376]. The bold lines on the phase cubes connect corners/symbols that give equivalent structure types.

Symbol	No. of blocks in cell	Space group	Structure-type
$[+,+]$	3	$R\bar{3}m$	$CdCl_2$
$[+,-]$	1	$P\bar{3}m1$	$1T$ (CdI_2)
$[+,\pm]$	6	$R\bar{3}m$	6
$[\pm,+]$	6	$R\bar{3}m$	$6'$
$[\pm,\pm]$	2	$P6_3mc$	$1T'$
$\langle+,+\rangle$	3	$R3m$	$3R$
$\langle+,\pm\rangle$	2	$P\bar{6}m2$	$2H_b$
$\langle\pm,+\rangle$	6	$R\bar{3}m$	$6''$
$\langle\pm,\pm\rangle$	2	$P6_3/mmc$	$2H_a$
$\langle\pm,\mp\rangle$	2	$P6_3/mmc$	$2H_c$ (MoS_2)

Table 3.2: Resulting unique structure types emerging from different symbol combinations and their corresponding space groups.

The same analysis for the trigonal prismatic AB_2 structures [Fig. 3.5(b)] also results in five unique structure types. The full details of these are given in Table. 3.2 and the structure types themselves are illustrated in Fig. 3.6. Simulated diffraction patterns for representative AB_2 compounds corresponding to these structure types are found in Appendix C.1.

Clearly the cell size and space group are not by themselves capable of distinguishing all possibilities, so the bracket nomenclature may prove a more straightforward and universal label.

3.4 Hamiltonian

Using the new descriptors to illustrate the structure types, we construct a Hamiltonian to navigate the multidimensional phase space. The Hamiltonian has four terms, three pertaining to a degree of freedom mapped out in the above section, and one coupling term:

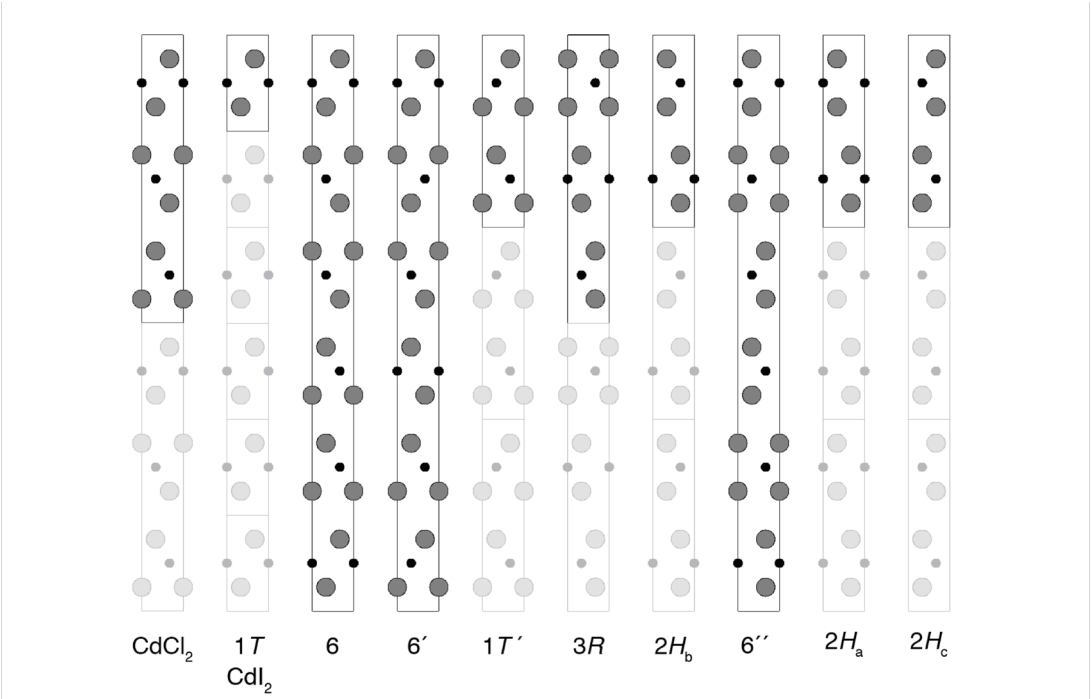

Figure 3.6: Unique phases produced by combining the degrees of freedom outlined in Section. 3.3.

$$\mathcal{H} = J_1 \sum_i \epsilon_i + J_2 \sum_i \sigma_i \sigma_{i+1} + J_3 \sum_i \zeta_i \zeta_{i+1} + J_4 \sum_i \sigma_i \zeta_i. \tag{3.1}$$

Here each variable $\epsilon_i, \sigma_i, \zeta_i = \pm 1$ where ϵ_i represents the intralayer coordination of B anions by defining whether the anions are in the same ($J_1 < 0$) or different ($J_1 > 0$) close-packed plane positions (trigonal prismatic and octahedral respectively). σ_i refers to clockwise (1) or anticlockwise (-1) directions of the permutations. Thus the sign of J_2 determines whether the permutations alternate between clockwise and anticlockwise ($J_2 > 0$) or stay in one orientation ($J_2 < 0$). ζ_i determines the direction each subsequent layer slips. Therefore the sign of J_3 dictates whether the layers slip in the same direction ($J_3 < 0$) or if the direction of slip changes with each layer ($J_3 > 0$). Finally, J_4 is a coupling parameter between the two variables

Symbol	Structure type	J_1	J_2	J_3	J_4
$[\pm,\mp]$	$1T'$	$+$	$+$	$+$	$+$
$[\pm,\pm]$	$1T'$	$+$	$+$	$+$	$-$
$[\pm,-]$	$6'$	$+$	$+$	$-$	$+$
$[\pm,+]$	$6'$	$+$	$+$	$-$	$-$
$[+,\mp]$	6	$+$	$-$	$+$	$+$
$[+,\pm]$	6	$+$	$-$	$+$	$-$
$[+,+]$	$CdCl_2$	$+$	$-$	$-$	$+$
$[+,-]$	$1T$ CdI_2	$+$	$-$	$-$	$-$
$\langle\pm,\mp\rangle$	$2H_c$	$-$	$+$	$+$	$+$
$\langle\pm,\pm\rangle$	$2H_a$	$-$	$+$	$+$	$-$
$\langle\pm,-\rangle$	$6''$	$-$	$+$	$-$	$+$
$\langle\pm,+\rangle$	$6''$	$-$	$+$	$-$	$-$
$\langle+,\mp\rangle$	$2H_b$	$-$	$-$	$+$	$+$
$\langle+,\pm\rangle$	$2H_b$	$-$	$-$	$+$	$-$
$\langle+,-\rangle$	$3R$	$-$	$-$	$-$	$+$
$\langle+,+\rangle$	$3R$	$-$	$-$	$-$	$-$

Table 3.3: Interaction parameter signs and corresponding symbols and structure types.

σ_i, ζ_i. In principle, the combination of different signs of the interaction parameters would lead to 16 phases, but much like the symbolic model, only 10 phases occur. This is a result of J_4 becoming obsolete for certain combinations of the other three parameters where one Ising chain interacts in a 'ferro' manner and couples to an 'antiferro' chain as both combinations are equivalent [Table. 3.3]. Importantly, the 10 limiting cases produced from the Hamiltonian are never frustrated, irrespective of the signs of interaction parameters.

As a side note, we wish to mention that this Hamiltonian maps onto the coupling of two 1D Ising chains where, instead of spins, the coupling occurs between layer orientations and displacements. This has conceptual parallels to ladder models, although the additional degrees of freedom pertaining to the different orientations/permutations makes it unsuitable for exact mappings [377].

Whilst this new description produces most known phases (and also highlights predicted, unrecorded phases) there are a number of structure types which are reported in the literature which are unable to be produced through the limiting cases of the phase space, highlighted in Fig. 3.7. These structure types can be split into two groups based on their intralayer configurations. The first group consists of structure types with only trigonally prismatic coordinated layers ($4H_a$ and $4H_c$) whilst the second group contains structure types with layers of alternating octahedral and trigonal prismatic coordinations ($4H_b$, $4H_{dI}$, $4H_{dII}$, and $6R$), which are excluded in our model by design. Comparatively, these phases contain longer periodic structures along the stacking direction and are less well characterised within the literature, as the main interest behind transition metal dichalogenides lies in their two-dimensional nature [248]. This directed interest may also explain why some predicted phases of our model are not recorded, as many of the undocumented phases contain six layers in their unit cell.

Our theory is that the systems reported to adopt the structure types depicted in Fig. 3.7 may in fact be equally well—or better—described in terms of disordered structures associated with the interior of the phase space spanned by our phase cubes laid out in Fig. 3.5. To test this theory we employ Monte Carlo simulations using the Hamiltonian in Eqn. 3.1, and vary the strengths of the interaction parameters to determine whether the model can accurately describe the phases as disordered. We shall analyse each structure type of Fig. 3.7 in turn, and compare the model phases to experimental data from the literature.

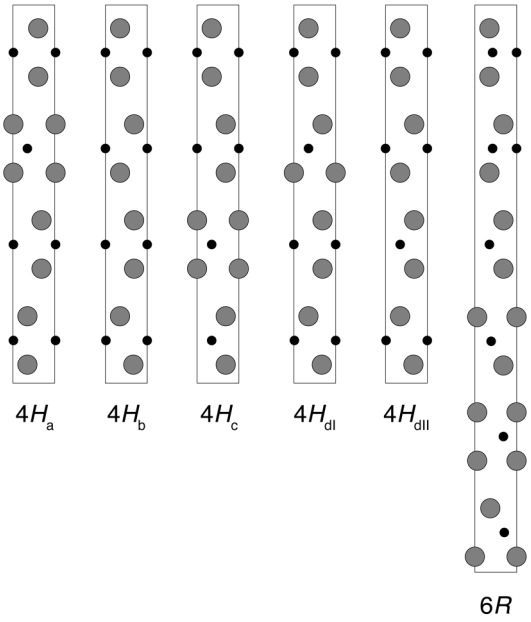

Figure 3.7: Phases recorded in the literature [37] which are unable to be described by the model outlined in Section. 3.3.

3.5 Reinterpretation of exception phases

3.5.1 $4H_b$

The $4H_b$ phase, reported for TaS_2 and $TaSe_2$ [37], is documented as containing alternating intralayer coordination between octahedral and trigonal prismatic and is thought to exist at intermediate temperatures on transitioning between the low temperature $2H_a$ and high temperature $1T$ phases [378]. The justification first came as single crystal X-ray diffraction experiments showed the a-axis dimension is between that of octahedral and trigonal planar, suggesting the polytype contains both octahedral and trigonal prismatic coordination. This is compounded by the presence of the peaks only belonging to the family of $(00l)$ reflections when $l = 4n$, where n is the number of layers in the unit cell, found in both single crystal [378] and

powder diffraction patterns [379, 380]. Through this analysis the authors suggest their results indicate it cannot be a phase-separated mixture of $2H$ or $1T$ domains [379, 380].

Although the peak reflections suggest a four layered unit cell, this does not necessarily mean the structure is formed by an ordered arrangement of alternating H and T layers. We find that the existence of only the specific $(00l)$ planes highlighted in these papers is also true for disordered states of our model and argue this is not enough alone to prove the existence of ordered alternating layer types. Moreover, alternating layer types have no well-understood chemical driving force whereas the drive for same layer types persisting through the bulk is understood through electronic considerations [374]. We theorise there may be another explanation of the stacking behaviour seen in this structure, and use simulated diffraction patterns from Monte Carlo simulations to compare our model [Eqn. 3.1] to experimental data.

Experimental diffraction patterns of compounds ascertained as $4H_b$ containing reflections other than those belonging to $(00l)$ planes (and not in list form) are sparse within the literature; however we have found two reports with good orientational averages [379, 381]. The data for TaS_2 from Ref. [379] have diffuse components and are therefore unable to be explained by the ordered $4H_b$ structure suggested, whereas the data on TaS_2 from Ref. [381] evidence a more ordered stacking sequence [Fig. 3.8].

Through MC simulations, we show these two phases can be explained by the symbol $[+,-]$ $(1T)$ instead of alternating layer types with the formation of the ordered phase from Ref. [381], and a more disordered phase from Ref. [379] when

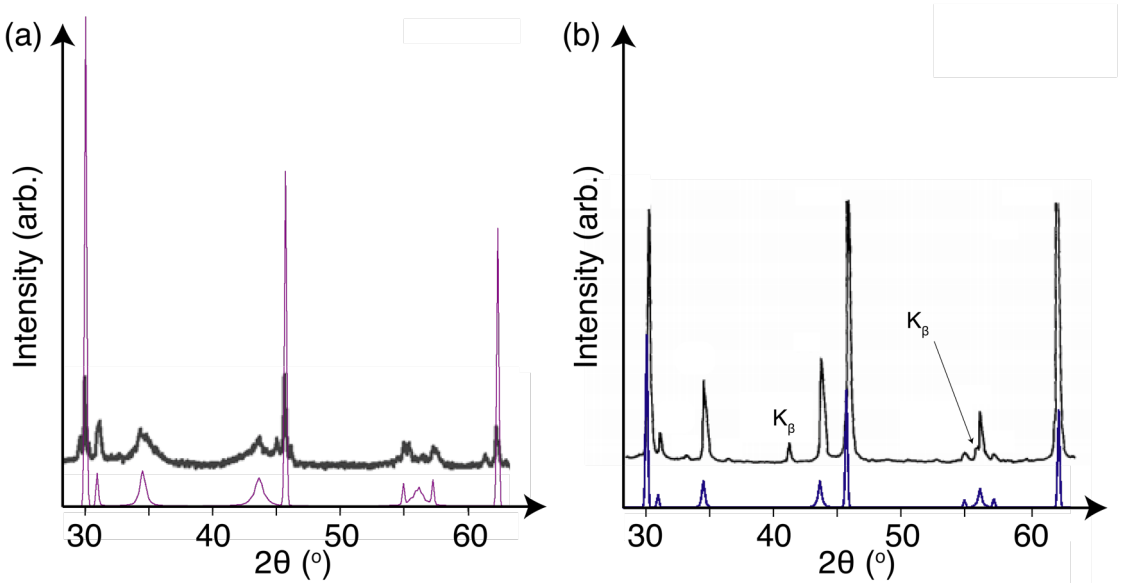

Figure 3.8: (a) Experimental diffraction pattern of TaS_2 from Ref. [379] ($\lambda = 1.5418$ Å) assigned as structure type $4H_b$ (top) and simulated diffraction pattern of the $[+,-]$ phase (bottom) produced from MC simulations where $T/J = 0.75$. (b) Experimental diffraction pattern of TaS_2 from Ref. [381] ($\lambda = 1.5406$ Å) assigned as structure type $4H_b$ (top), and simulated diffraction pattern of the $[+,-]$ phase (bottom) produced from MC simulations where $T/J = 0.3$. All simulated diffraction patterns were produced using MC simulations where $J_1 > 0$ and $J_2, J_3, J_4 < 0$. In all simulations $J = |J_1| = |J_2| = |J_3| = |J_4|$. Data from Ref. [379] and Ref. [381] adapted with permission from AIP Publishing.

there are strong/weak interaction strengths respectively [Fig. 3.8]. Although $[+,-]$ with strong interactions would only contain octahedral coordination, it is plausible that the more disordered phase contains some trigonal prismatic layers due to the weaker interaction parameters. However, our results for $J_1 = 0$ [Fig. 3.9(a)] where there is no preference for either layer coordination, show this is unlikely to be a true 50:50 mix of layer types as suggested by the $4H_b$ structure. We note that comparing the literature structure from Ref. [382] to the experimental data from Ref. [381] evidences similar reflections [Fig. 3.9(b)], but our model [Fig. 3.8(b)] provides a closer match with a structure formed from well understood chemical driving forces. Ref. [381] and Ref. [379] both focused on studying $4H_b$ due to its

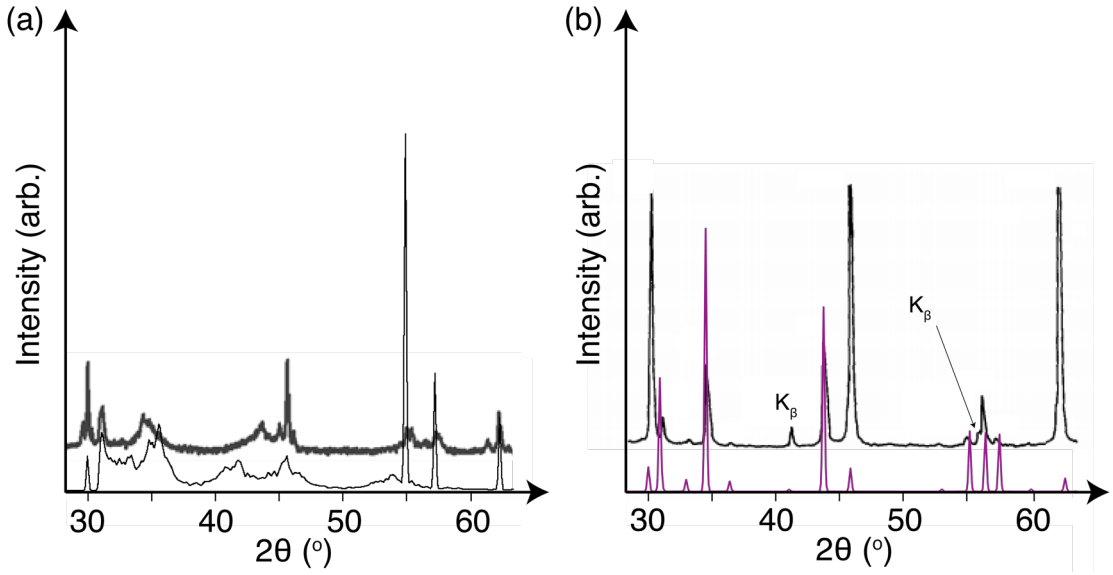

Figure 3.9: Failure of existing models to account for the scattering behaviour of TaS_2. (a) Experimental diffraction pattern of TaS_2 from Ref. [379] ($\lambda = 1.5418\,\text{Å}$) assigned as structure type $4H_b$ (top) and simulated diffraction pattern of the phase between $[+,-]$ and $\langle +,-\rangle$ (bottom) where $T/J = 0.75$, $J_1 = 0$ and $J = -J_2 = -J_3 = -J_4$, showing that a 50:50 mixture of trigonal and octahedral coordination environments produced by our model cannot produce a good match to the data. (b) Experimental diffraction pattern of TaS_2 from Ref. [381] ($\lambda = 1.5406\,\text{Å}$) assigned as structure type $4H_b$ (top) and simulated diffraction pattern of the literature structure of $4H_b$ (bottom) taken from Ref. [382]. Data from Ref. [379] and Ref. [381] adapted with permission from AIP Publishing.

superconducting properties which is consistent also with assignment of the structure to the $[+,-]$ phase, as this structure type in the same material is known to exhibit superconductivity [383].

3.5.2 $6R$

$4H_b$ is not the only structure suggested to have alternating octahedral and trigonal prismatic layers, with the $6R$ polytype also being observed in TaS_2 and $TaSe_2$ [37]. The first mention of this polytype was in Ref. [384] where the authors noticed the coexistence of this phase with $1T$ and $2H_a$ at high temperatures, and sole existence of $6R$ on increasing temperature. The rationale behind the phase's structure was

due to the unsatisfactory agreement of the rhombohedral 6 hexagonal unit cell with purely octahdeal or trigonal prismatic environments [384]. Instead they noted that the diffraction patterns had good agreement with a structure containing alternating layer types [384].

To determine whether these structures may be explained in terms of our model instead of alternating octahedral and trigonal prismatic layers, we again compared simulated results with experimentally reported data. The literature contains two different diffraction patterns; one of $TaS_{1.2}Se_{0.8}$ [385], which is fully ordered, and one of TaS_2 [386] which has diffuse features [Fig. 3.10(a)-(b)]. We first focus on matching simulated data to the ordered diffraction pattern taken from Ref. [385]. For these data, we have been unable to match the diffraction patterns with any simulated data produced from exploring the phase space spanned by our model. At first glance, this suggests that the phase may truly contain alternating octahedral and trigonal prismatic layers, however, comparing the data to the calculated diffraction pattern from the recorded structure of $6R$ TaS_2 reported in the database [384] reveals a mismatch between the characteristic peaks and those present in Ref. [385] [Fig. 3.10(a),(c)]. Thus we are unable to determine the structure from these data but can confidently conclude it is not $6R$.

Turning to data of TaS_2 in Ref. [386], the peak positions of the recorded structure of $6R$ TaS_2 match up with the experimental diffraction pattern [Fig. 3.10(b)-(c)]. Although these patterns give slightly different intensities, one cannot interpret much from the peak intensities of diffraction data of layered materials due to the strong possibility of preferred orientation. Again at first glance, it looks as though

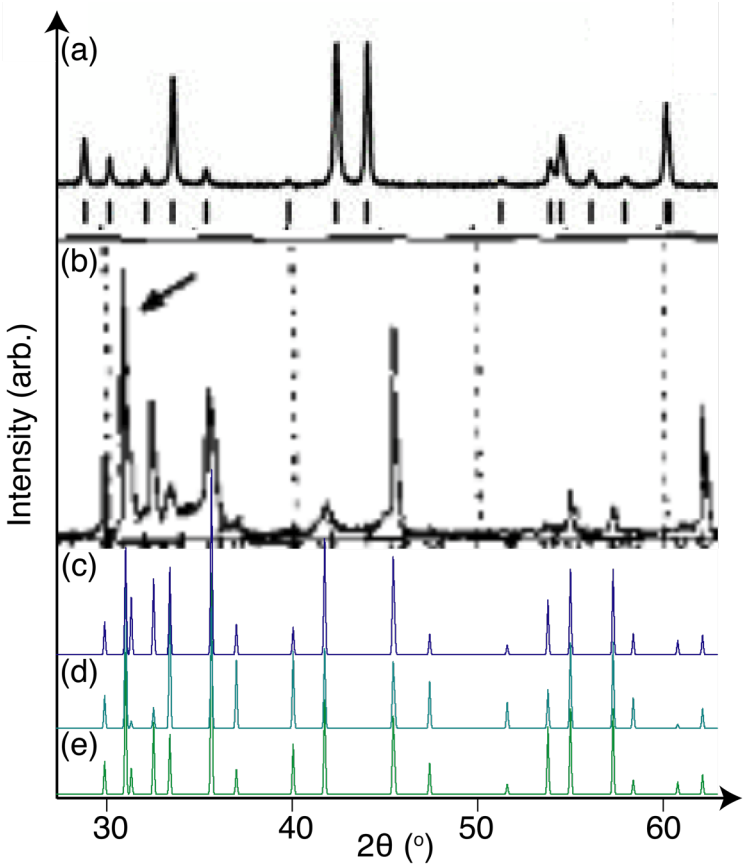

Figure 3.10: (a) Experimental diffraction pattern of $TaS_{1.2}Se_{0.8}$ from Ref. [385], ($\lambda = 1.5418\,$Å). (b) Experimental diffraction pattern of TaS_2 from Ref. [386] ($\lambda = 1.5406\,$Å). (c) Simulated diffraction pattern from the structure of $6R$ TaS_2 from the database (Ref. [384]). Simulated diffraction pattern of (d) $\langle \pm, + \rangle$ and (e) $[+, \pm]$. Data from Ref. [385] adapted with permission from AIP Publishing. Data from Ref. [386] adapted with permission from Elsevier.

the structure can be explained by alternating octahedral and trigonal prismatic layers; however, the calculated diffraction pattern from the literature structure is the same as the diffraction pattern produced from both $\langle \pm, + \rangle$ ($6''$) and $[+, \pm]$ (6) [Fig. 3.10(d)-(e)]. We suggest that perhaps, from a chemical perspective, one of these structures is a more accurate representation since neither model involves multiple coordination geometries of the same transition metal cation. Moreover, from simulated diffraction patterns using Eqn. 3.1, we show that both these phases with weaker interactions account for the diffuse scattering seen in the experimental data

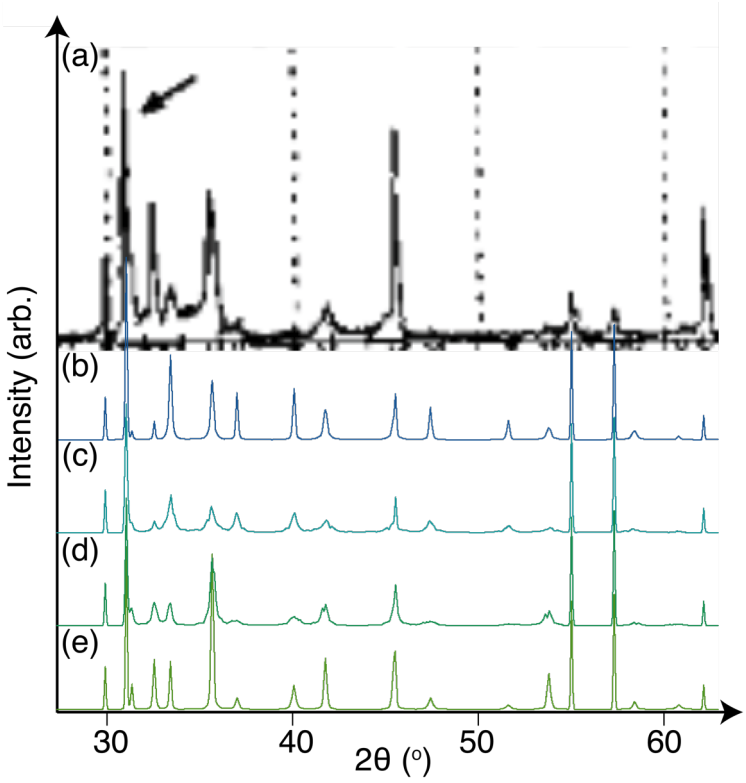

Figure 3.11: (a) Experimental diffraction pattern of TaS_2 from Ref. [386] ($\lambda = 1.5406$ Å). Simulated diffraction pattern of $\langle \pm, + \rangle$ produced from MC simulations where (b) $T/J = 0.3$ and (c) $T/J = 0.6$ ($J = -J_1 = J_2 = -J_3$, $J_4 = 0$, and $J_1 < 0$). Simulated diffraction pattern for the structure of $[+, \pm]$ produced from MC simulations where (d) $T/J = 0.6$ and (e) $T/J = 0.3$ ($J = J_1 = -J_2 = J_3$, $J_4 = 0$, and $J_1 > 0$). Data from Ref. [386] adapted with permission from Elsevier.

from Ref. [386] [Fig. 3.11]. This may allow for the presence of some hexagonal layers within the structure, although again not in the 50:50 ratio predicted by the $6R$ structure type.

3.5.3 $4H_a$ and $4H_c$

The two exception phases containing layers of only trigonal prismatic coordination are $4H_a$ and $4H_c$. $4H_a$ is found in phases of $NbSe_2$ and both $4H_a$ and $4H_c$ have been recorded in phases of TaS_2 and $TaSe_2$ at various temperatures [37, 387, 388]. $4H_a$ was first characterised in the 1960s *via* diffraction and derived from a Patterson

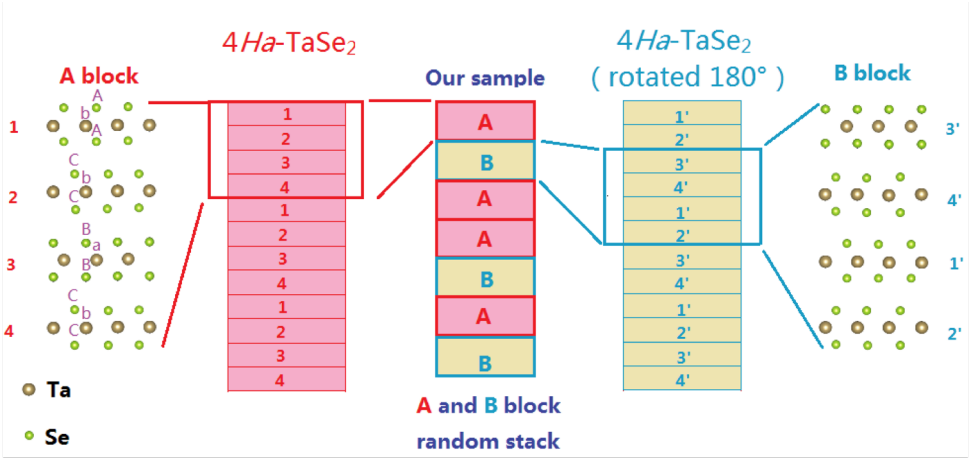

Figure 3.12: Explanation of the stacking disorder within $4H_a$ as given in Ref. [391] where the phase was characterised using direct imaging techniques. Figure reproduced from Ref. [391] with permission from IOP Publishing.

synthesis [389]. We aim to see whether we can describe the stacking behaviour of this structure through our model instead. Using the powder X-ray diffraction data poses a problem, as early works only report the reflections in the form of lists [390], and no graphical data has been published. Instead of diffraction data, we use more recent studies which use direct imaging techniques to probe the structure.

A recent study indicates that the structure of $4H_a$ in $TaSe_2$ consists of two 'blocks' of $4H_a$, one of which is rotated by 180° and these blocks are stacked randomly with the unit cell boundary changing between them. This leads to a fundamentally more disordered structure than the ordered $4H_a$ structure originally assigned [Fig. 3.12] [391]. Although this is one explanation, one block of $4H_a$ can also be described as a mixture of $2H_a$ and $2H_b$ [Fig. 3.13(a)]. Moreover, the boundaries between the 'blocks' described in Ref. [391] are themselves $2H_a$ or $2H_b$ stacking and we suggest that instead of the structure being composed of randomly stacked and oriented blocks of $4H_a$, the structure of $4H_a$ may be explained as a disordered

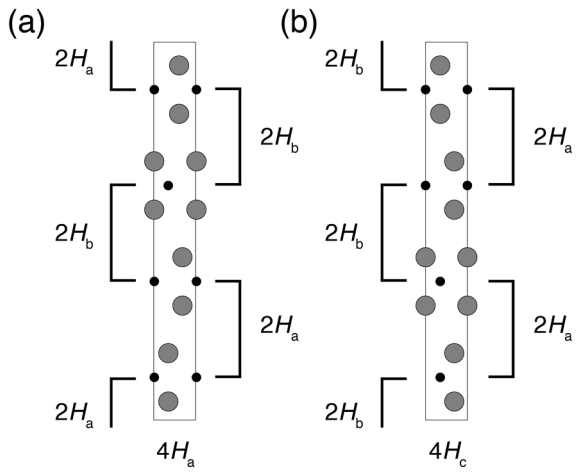

Figure 3.13: (a) $4H_a$ and (b) $4H_c$ structures which can be broken down to smaller units of $2H_a$ and $2H_b$ with different alternation of stacking between the layers.

state between $2H_a$ and $2H_b$. In our new nomenclature, this would be a phase lying between $\langle \pm, \pm \rangle$ and $\langle +, \pm \rangle$. Energetically, a transition between these two phases requires just one change in interaction parameter with the sign of J_2 going from positive to negative on transition, suggesting the energy scale of J_2 is low with respect to $k_B T$. Comparing configurations produced from MC simulations existing between the $\langle \pm, \pm \rangle$ and $\langle +, \pm \rangle$ phases to the direct images collected from Ref. [391] [Fig. 3.14] shows the disordered stacking arrangement evidenced in the high resolution transmission electron microscopy image can also be described through weak interactions, particularly in the case of J_2.

The $4H_c$ structure type is less well studied and it is harder to comment on whether this exists as a disordered state. What is reported of the structure can be explained, similarly to $4H_a$, as a mixture of $2H_a$ and $2H_b$ [Fig. 3.13(b)] [392]. Therefore we propose that instead of the ordered structure suggested, this may also exist as an intermediate phase between $2H_a$ and $2H_b$, with the average structure

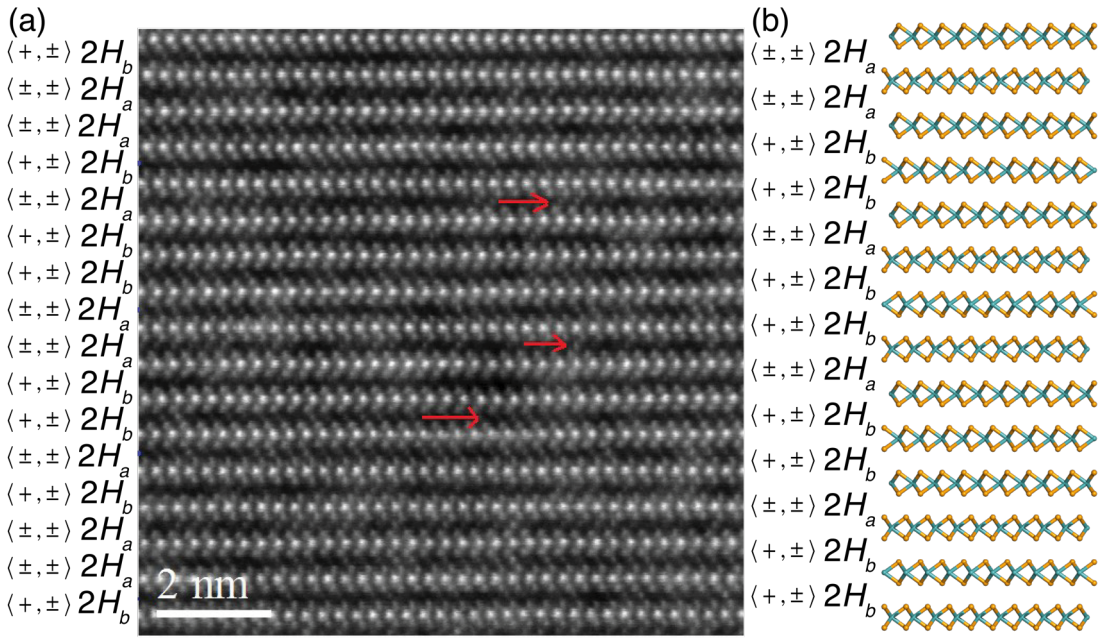

Figure 3.14: (a) Direct image comparison of a high resolution transmission electron microscopy image reproduced from Ref. [391] with permission from IOP Publishing. (b) A representative configuration from MC simulations of a mixture of $\langle \pm, \pm \rangle$ and $\langle +, \pm \rangle$ where $T/J_1 = -0.3$, $T/J_2 = -1.5$, $T/J_3 = 0.3$, $T/J_4 = -0.6$.

representing a mixture of both. Where X-ray diffraction patterns have been reported, the authors comment on the poor quality of the data and observation of peak broadening in most of the diffraction peaks [392] which may be consistent with disordered structures within our phase cubes.

The observations outlined here are consistent with the literature as the mixture of $2H_a/2H_b$ structure types used to describe both structures is common for intercalated structures where many $4H$ structures are suggested to be found [37].

3.5.4 $4H_{dI}$ and $4H_{dII}$

The last two 'exception' structure types not predicted by our simple Hamiltonian are $4H_{dI}$ and $4H_{dII}$ which are only found in $NbSe_2$ [37]. Again, the experimental diffrac-

tion patterns recorded are sparsely reported and, where they have been reported, they are in list form and the author has commented on the poor quality of the data [393]. It is hard to do much more than speculate whether these structures truly have alternating octahedral and trigonal prismatic layers or not. Ref. [393] indicates the coexistence of phases $4H_{dI}$ and $4H_{dII}$ and comments on their existence in a small temperature range between $1T$ ($[+,-]$) and $2H_a$ ($\langle\pm,\pm\rangle$) in the $NbSe_2$ compound. The authors suggest the structure contains layers of alternating octahedral and trigonal prismatic coordination due to the analogous transition found in $TaSe_2$ where the structure transitions through the $4H_b$ and $6R$ structures [389, 390]. As we have explored both these phases and found them unlikely to contain an ordered structure of alternating octahedral and trigonal prismatic layers, perhaps these phases also sit somewhere within the phase cubes with weaker interactions than limiting phases, instead of having truly alternating octahedral and trigonal prismatic layers. This argument is reinforced by the quality of the data and suggested coexistence of phases [393].

3.6 Solid solutions

Solid solutions of layered chalcogenides are widely studied as they allow tuning of physical properties such as superconductivity [394] and optical properties [395]. We explore whether the interaction strengths, J_i, for solid solutions are intermediate to the interactions for the corresponding end members.

Two examples of solid solutions from the literature include $Ru_xNb_{1-x}S_2$ and $Re_xTa_{1-x}Se_2$ [396, 397]. Both solid solutions are reported to transition from $3R$

($\langle +,+\rangle$) to $2H_b$ ($\langle +,\pm\rangle$) with increasing x where the diffraction contains diffuse scattering as a function of composition, explained through stacking faults due to different ratios of $2H_b/3R$. If our model is correct, this structure should exist on the bottom face of the phase cube [Fig. 3.5(b)] containing $\langle +,-\rangle$, $\langle +,+\rangle$, $\langle +,\pm\rangle$, and $\langle +,\mp\rangle$.

To test our theory, using the Hamiltonian set out in Eqn. 3.1, we employed Monte Carlo simulations to analyse the behaviour of the phases when transitioning from the interactions that stabilise $\langle +,+\rangle$ to those that stabilise $\langle +,\pm\rangle$. The simulations analysed the structural changes with changing interaction strength, J_3, to navigate from $\langle +,+\rangle$, where $J_1, J_2, J_3 < 0$ and $J_4 = 0$, to $\langle +,\pm\rangle$, where $J_1, J_2 < 0, J_3 > 0$, and $J_4 = 0$. Comparing the simulated diffraction patterns from the outputted configurations to experimental data, the configurations where $J_1, J_2 < 0$ and $J_3, J_4 = 0$, $\langle +,0\rangle$, have the best agreement to experimental data [Fig. 3.15]. This shows that these disordered phases exist in a regime where there is no preference for alternating (HCP) or non alternating (CCP) stacking of layers which occur at the border between the two phases [Fig. 3.16]. As the transition between these two phases is commonly found in transition metal dichalcogenides, these results suggest that the weakest interaction in the structures is the one parameterised by J_3, which is unsurprising as this parameter determines next-nearest neighbour correlations, which would be weaker than intralayer or nearest neighbour coupling interactions.

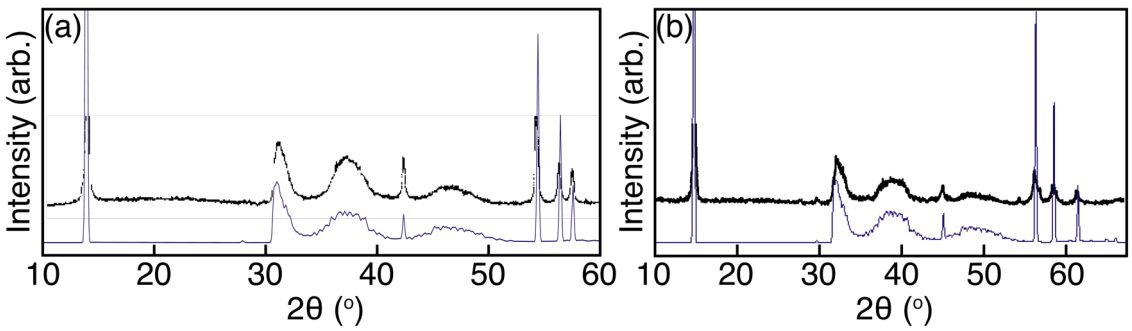

Figure 3.15: Experimental diffraction patterns of (a) $Re_{0.23}Ta_{0.77}Se_2$ from Ref. [397] and (b) $Ru_{0.2}Nb_{0.8}S_2$ from Ref. [396] with corresponding simulated diffraction patterns produced from MC simulations using the Hamiltonian in Eqn. 3.1 where $J_1, J_2 < 0$, $J_3, J_4 = 0$, $J = |J_3| = |J_4|$, and $T/J = 1.5$ which exists on the plane between $\langle +, + \rangle$ and $\langle +, \pm \rangle$ ($3R$ and $2H_b$). Data reproduced from Ref. [397] and Ref. [396] with permission from Elsevier.

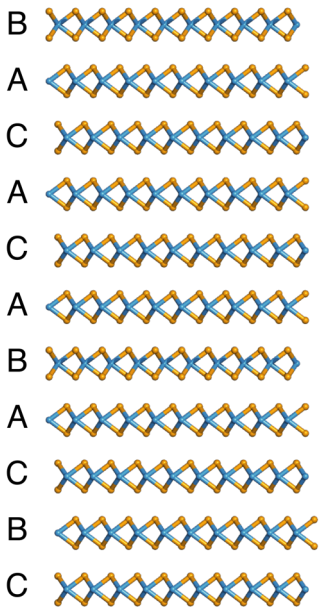

Figure 3.16: Representative structure of the intermediate phase, $\langle +, 0 \rangle$, on transition from $\langle +, + \rangle$ to $\langle +, \pm \rangle$. The ABC notation represents the position of the metal cation within each layer. The configuration shows no preference for HCP or CCP stacking of the layers and instead is randomly close-packed.

3.7 Outlook

The research carried out within this chapter highlights the need for a new nomenclature as multiple studies [379, 386, 391] assign phases containing diffuse compo-

Ramsdell notation of old phase	New descriptor
$4H_b$	$[+,-]$
$6R$	$\langle\pm,+\rangle/[+,\pm]$
$4H_a$	$\langle\pm,\pm\rangle/\langle+,\pm\rangle$
$4H_c$	more data needed
$4H_{dI}$	more data needed
$4H_{dII}$	more data needed

Table 3.4: Summary of reinterpretation of exception phases with their old Ramsdell notation and our new descriptors.

nents to an ordered structure, which is fundamentally meaningless unless the form of the disorder is explicitly described. Using a constructive approach to represent the structure allows for a clearer explanation of where the diffuse behaviour comes from through tuning interactions. This chapter has presented such a constructive nomenclature for explaining the stacking behaviour of layered AB_2 structures where the new descriptors are constructive such that no other details are needed in order to build a complete picture of the stacking behaviour of materials. Although this is already possible using the ABC notation, the stacking behaviour through our descriptors can be concisely represented using only three symbols.

Using the new nomenclature has led to the reassessment of phases that have previously been described as ordered phases. Through the use of the Hamiltonian given in Eqn. 3.1, we have been able to characterise these phases as either other known phases described by our symbol notation, or as disordered phases existing within the multidimensional phase space. These results signify the need to re-evaluate how we assign coordination geometries as they can greatly effect the electronic structure. In the case of TaS_2, this is particularly important as the material's properties (*e.g.* superconductivity) relies heavily on the electronic structure and thus geometric coor-

dination [380, 383, 386]. Through this study we were able to show that a previously characterised phase containing a mixture of coordination geometries [379, 381], was better represented as the purely octahedral phase $[+,-]$.

A summary of the phases able to be recharacterised using experimental data is given in Table. 3.4. For many of the exception phases, peaks were noted with descriptions of their intensities such as very strong or weak. As we now know, these weak peaks are indicative of diffuse scattering and a more disordered phase than perhaps characterised [389, 398]. Moreover, papers often comment on the poor quality of their data or the coexistence of phases which are a result of more complicated peaks [384, 392, 393]. The poor quality/multiple phases observed in these references could be consistent with disordered structures interpreted as ordered phases at the time.

In this regard, more experimental powder X-ray diffraction data is required for proper assessment of all phases falling in this category, namely $4H_a$, $4H_c$, $4H_{dI}$, $4H_{dII}$, and to some extent $6R$, to determine whether they can be described by our model. Direct imaging techniques of some phases already show evidence of disordered behaviour [391], though direct imaging holds limitations as one can only sample small regions, and the average structure from diffraction data would allow for more accurate characterisation of the disordered phases.

There are three key questions remaining from this study. The first concerns the highlighted undocumented phases and whether they actually exist within recorded materials and have been overlooked. Our results for $6R$ phases emphasise the importance of this question, which poses particular significance as many of these structures

share the same space group.

The second question is whether structures containing both octahedral and trigonal layers actually exist. Comparing our model to previously characterised $4H_b$ and $6R$ phases indicates that structures containing both octahedral and trigonal layers can exist, but are unlikely to have an ordered arrangement of alternating configuration types suggested by both structure types. Instead, a mixture of configurations is likely to occur when the structures are disordered at finite temperatures within our phase space. Scanning transmission electron microscopy of both the $4H_b$ and $6R$ phase of TaS_2 and $TaSe_2$ would offer some validation of whether truly alternating octahedral and trigonal layers do or do not exist. As our model can only describe instances with no preference between the two types of layers, not an ordered arrangement of alternating octahedral and trigonal layers, incorporating these structures into our model would require an additional term which gives an 'antiferro' layer type arrangement.

The third question asks what drives the behaviours of each of the variable identified in creating the model. For the configuration of each layer, this is a trivial task, as the link between octahedral/trigonal prismatic coordination and the electronic structure is clearly mapped out [374], but for the other degrees of freedom, such as the permutation and orientation of layers, the interactions leading to these variables is much less clear. However this is the case for many models, including those that are constructive such as Glazer tilts where the driving force for one tilt system over another one is rarely well understood [373].

For now we are confident that the model can describe most phases that exist

within layered AB_2 compounds. Future directions may include detailing how tuning the interaction within the structures can be used to explore the phase cubes, and relating the model to other layered materials such as AB_3 compounds or graphene bilayers. Currently, the stacking nomenclature of layered materials have different standards [399]. A uniform standard would benefit the community to describe the stacking of all structures. Perhaps this new way of describing the layers can be utilised elsewhere for other layered materials behaviour.

Chapter 4

Stacking disorder in $Ni(CN)_2$

4.1 Summary

In the previous chapter, we discussed how structural phase behaviour can be described in terms of statistical mechanical models based on discrete degrees of freedom. In this chapter, we explore whether models with continuous degrees of freedom can express particular types of unusual stacking behaviour, with a focus on the inorganic layered material $Ni(CN)_2$. Physical realisations of one-dimensional statistical mechanical models with continuous degrees of freedom describing magnetic or electronic interactions are well established in condensed matter physics [400–407]. Such systems are known to produce various deconfined exotic behaviour through their quasiparticle excitations such as deconfined orbitons and spinon continua [408]. Although structural behaviour is commonly described with continuous degrees of freedom, as with structural distortions in perovskites [409] or cation rotation in $MAPbI_3$ [410], interactions describing the stacking of layered materials are commonly explained through models containing discrete degrees of freedom. This is unsurprising as the nature of switching atomic positions and symmetry considerations lends itself naturally to discrete behaviour [411, 412]. However, stacking behaviour, especially pertaining to disorder, can be continuous, as is the basis behind the formation of different Moiré patterns in graphene and hBN nanosheets due

to rotation of pairs of sheets [40, 413].

The benefits of explaining the energetics behind phase formation has been explained in detail throughout the last few chapters. An additional benefit of mapping 1D magnetic models containing continuous degrees of freedom is that many have not been physically realised in structural states [152, 414]. Thus, devising a continuous model to explain structural phase behaviour opens up new ways of potentially accessing novel exotic 1D behaviour under ambient conditions.

In this chapter we consider the structural disorder present in the layered material $Ni(CN)_2$ and demonstrate its relevance to a 1D model of interacting anisotropic quaternions. We show that the model can both explain the form of the diffuse scattering in nickel cyanide, and be related loosely to a chain of quantum spin-$\frac{1}{2}$ Heisenberg spins. Additionally, using lattice dynamical calculations we demonstrate how the interaction parameters responsible for the stacking behaviour in $Ni(CN)_2$ may be tuned as a function of uniaxial pressure. Our results flag the possibility of studying exotic phenomena produced from spin-$\frac{1}{2}$ chains through analysing the dynamics of $Ni(CN)_2$.

This chapter is arranged as follows; we begin by discussing the motivation for this study before delving into what is known about the $Ni(CN)_2$ structure from the literature. Next we create a model of interacting $Ni(CN)_2$ layers, and use it to probe the energetics of $Ni(CN)_2$. Our approach is to use lattice dynamical calculations through GULP to determine the energetics of interlayer interactions and assign a Hamiltonian to represent the stacking energetics of the system. Subsequently, we fit an interaction parameter to the model using experimental data collected

from Ref. [415]. We then apply a topological mapping, enabling representation of the stacking arrangements as a 1D chain of interacting quaternions. From this we employ Monte Carlo simulations to determine whether interlayer interactions alone can explain the full extent of the stacking disorder, and subsequent scattering behaviour, by comparing simulated diffraction patterns to experimental data. With these results, we discuss the relevance of our Hamiltonian to known magnetic models, with a detour exploring mathematical concepts related to the topological mapping required to examine the physical implications of our model. The topological mapping formulated in this section leads to the speculation of whether our classical model may be an analogue of a spin-$\frac{1}{2}$ XXZ chain due to parallels between the degrees of freedom. Using experimental data, we go on to show how the interaction parameter can be tuned as a function of pressure. The chapter ends with an overview of the implication of the results and suggests future directions of research.

4.2 Background

1D models have a special role in condensed matter theory [118, 416, 417]. These same statistical models can also be used to explain structural behaviour of layered materials [21, 233, 240]. Stacking behaviour is a well characterised pseudo one-dimensional problem as the in- and out-of-plane interactions act on different length scales due to intralayer interactions being much stronger than interlayer interactions. For the 1D Ising model, predominately known for its relevance in modelling magnetic interactions [119], the degrees of freedom describing whether spins tend to align or anti-align are also relevant to the structural behaviour of some surpris-

ingly simple bulk phases: the best studied of these are the metals Co and Ni, which are susceptible to stacking fault disorder [418]. Mapping the degrees of freedom between the two systems provided an explanation for the preference of CCP/HCP stacking as a difference in the sign of the relevant interaction parameter, resulting in analogous ferromagnetic/antiferromagnetic interactions, respectively [21, 412]. Moreover, stacking faults and disordered states have been explained as a competition between the two limiting ground states where the interaction parameter may be small [418]. Using 1D models to analyse disorder in structural states is becoming increasingly commonplace, which has helped characterise some particularly complex phases [15, 16, 98, 116].

More recently, employing models to explore the link between magnetic materials and structural phases has led to the realisation of exotic behaviour through structural phases and dynamics [48, 152]. For example, the relation between the supramolecular assembly of inorganic polymer chains, $Ag_xAu_{1-x}CN$, to the bilinear biquaratic (BLBQ) XY model lead to the realisation of topological defects within the organisation of the polymer chains [152]. Theoretically, the phase diagram of the BLBQ triangular XY model contains two interaction parameters which span four different phases—ferromagnetic, antiferromagnetic, ferroquadrupolar, and a chiral disordered phase—depending on the relative interaction strengths and signs of the two terms [Fig. 4.1(a)] [419]. Experimentally, however, magnetic systems following this model have yet to evidence the ferroquadrupolar phase which arises due to dipolar disorder coupling with hidden ferroquadrupolar order, resulting in a complex nematic state [230]. The ferroquadrupolar phase of the BLBQ XY model is

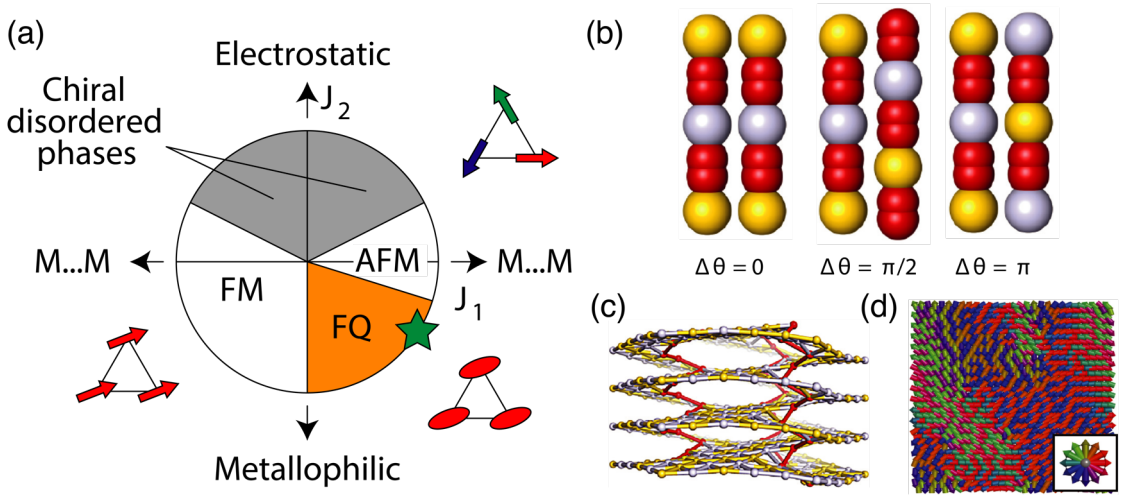

Figure 4.1: (a) Phase diagram of the bilinear biquadratic triangular XY model where the green star represents the energetically favoured phase formed in the low energy structure of $Ag_{0.5}Au_{0.5}(CN)_2$. (b) Chains of $Ag_{0.5}Au_{0.5}(CN)_2$ that differ in the relative vertical shifts which correspond to phase angles. (c) Vortex structure formed by the $Ag_{0.5}Au_{0.5}(CN)_2$ chains and (d) corresponding spin-vortex structure formed by magnetic spins. Figure adapted from Ref. [152] with permission from Springer Nature.

predicted to be thermally unstable to the formation of topological defects (vortices) which are relevant to data storage applications [165]. Relating the linear displacements of polymer chains to the phase angle in the BLBQ model [Fig. 4.1(b)] lead to targeted exploration of the solid solution and subsequent discovery of the topological defects—vortices—predicted within the phase diagram of the analogous frustrated magnet [Fig. 4.1(c)-(d)] [152]. Here we build on the idea of using mathematical mappings to find analogous emergent behaviour in systems on vastly different length-scales by analysing the stacking behaviour of $Ni(CN)_2$.

$Ni(CN)_2$ is a layered inorganic compound with strong ionic intralayer interactions and weak electrostatic interlayer interactions [258]. The structure of $Ni(CN)_2$ is complex as its X-ray powder diffraction pattern [Fig. 4.2(a)] contains a mixture of sharp, broad, and asymmetric peaks [257]. The average symmetry of the mate-

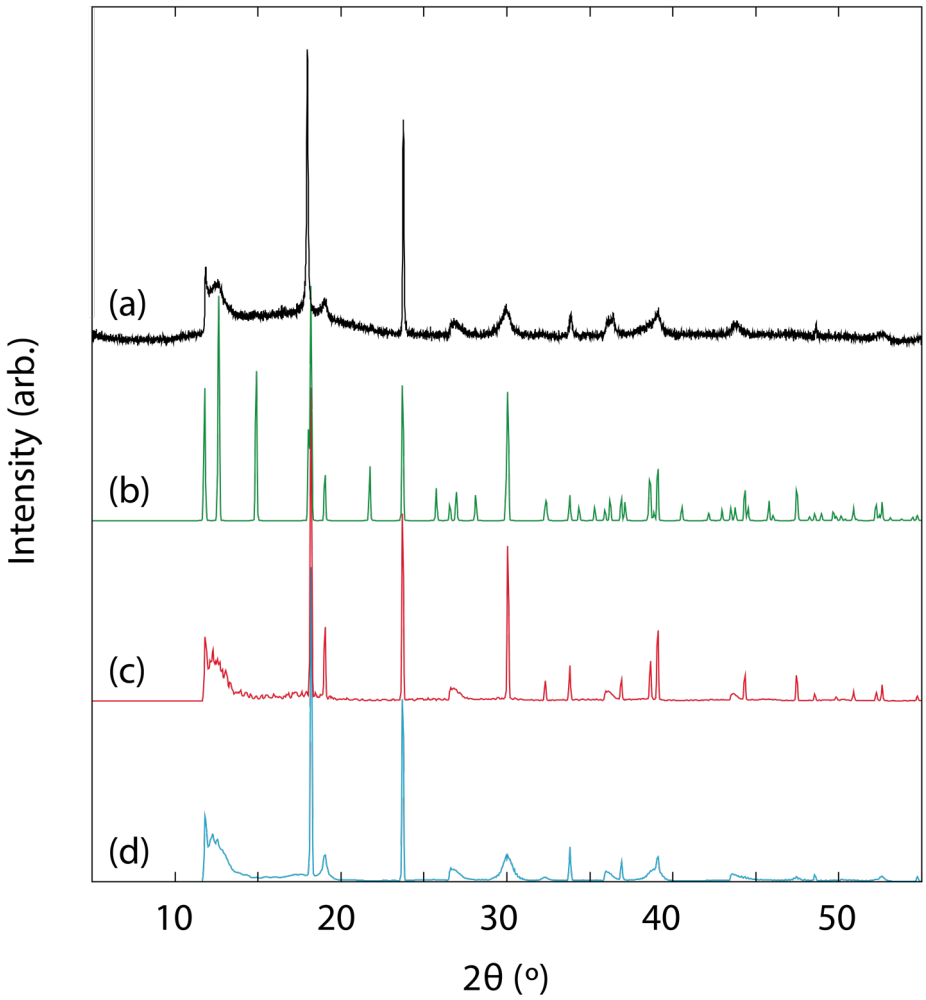

Figure 4.2: (a) Experimental X-ray diffraction pattern ($\lambda = 1.0000(1)$ Å). Calculated X-ray diffraction patterns of (b) the ordered structure of layers stacking with cyanide ions of one layer positioned directly above Ni^{2+} cations of neighbouring layers described in Ref. [257], disordered stacking model proposed by Ref. [258] where Ni^{2+} can sit on one of two equivalent sites (c) without a global shear and, (d) with a global shear. Figure is reproduced from Ref. [258] with permission from the American Physical Society.

rial has layers of periodic square planar Ni^{2+} cations coordinated to orientationally disordered CN^- anions [Fig. 4.3(a)]. Previously, it was suggested that the stacking arrangement involved an ordered arrangement where cyanide ions of one layer reside directly above Ni^{2+} cations of the neighbouring layer [257]. The resulting diffraction pattern from this structure accounts for the sharp diffraction features in reciprocal space, but is unable to reproduce the diffuse scattering and contains

too many reflections, signalling that the symmetry of the real material is higher [Fig. 4.2(b)]. The interlayer interactions in layered materials are weak and layers are notoriously easy to cleave [420]. Therefore the diffuse scattering has been previously explained through stacking faults within the structure [257]. Goodwin *et al.* built on this description and explained the previously perceived stacking faults were in fact the result of energetically equivalent stacking arrangements due to there being twice as many cyanides as Ni^{2+} ions [258]. The calculated X-ray diffraction pattern [Fig. 4.2(c)] does indeed have a better agreement with the experimental structure than its ordered counterpart, but fails to fully encapsulate all diffuse behaviour with the peaks at $2\theta \approx 19°$, 30°, and 39° being most notable. Adding shear displacements perpendicular to [001] rectifies the mismatch between the model and experimental data, fully explaining the form of the diffuse scattering [Fig. 4.2(d), Fig. 4.3(b)] [258]. Yet, the question remains of what is the driving force behind the shear. We aim to analyse the energetics of the interlayer interactions to determine whether we can explain the diffuse scattering through simple nearest neighbour considerations without the need of a global shear.

4.3 The model

Crystallographically, two things are clear: the layer spacing and the structure of individual layers are well defined, characterised by the sharp $(hk0)$ and $(00l)$ peaks, but interlayer positions in x and y are poorly defined, which we know because the (hkl) peaks are broad for $(h, k), l \neq 0$ [Fig. 4.4] [257, 421]. Therefore, the coarse graining involves treating layers as collective objects. We sought to determine the

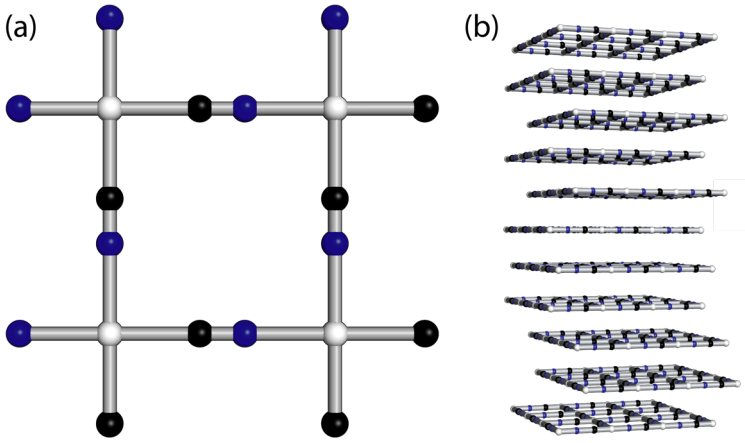

Figure 4.3: (a) Layer of periodic square planar $Ni(CN)_2$ where Ni, C, and N ions are represented as white, black, and blue spheres respectively. (b) Bulk structure of $Ni(CN)_2$.

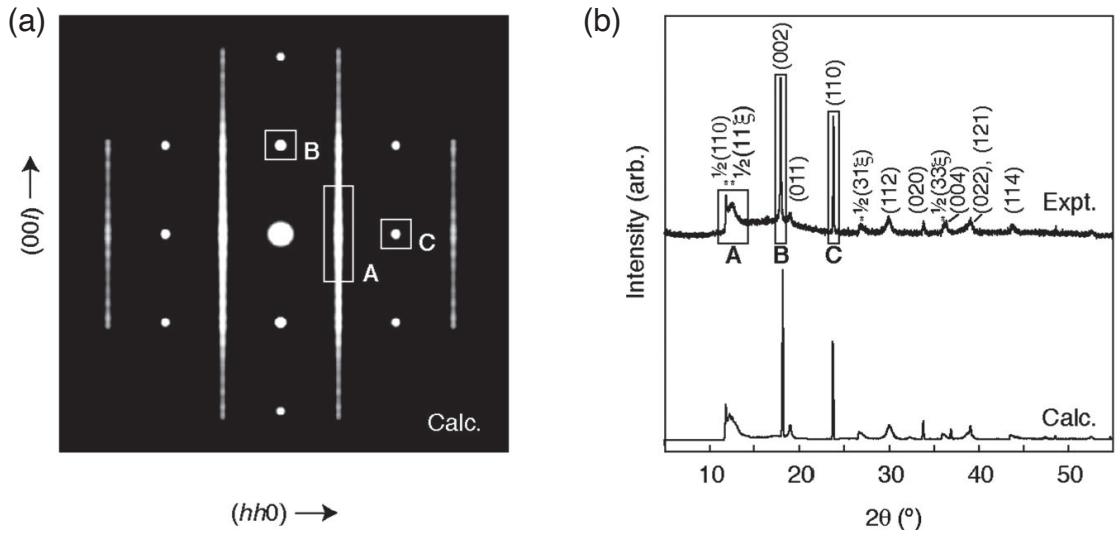

Figure 4.4: (a) Hypothetical single crystal diffraction pattern of $Ni(CN)_2$ with rods of diffuse scattering parallel to $\mathbf{c}^*$. (b) Powder diffraction pattern with labels and corresponding sections A, B, C in the single crystal diffraction pattern highlighted. Figure reproduced from Ref. [421] with permission from the Royal Society of Chemistry.

functional form of the effective interactions between $Ni(CN)_2$-type layers. To accomplish this we tracked the lattice energy as a function of the relative displacements of neighbouring layers within the $(\mathbf{a}, \mathbf{b})$ plane.

Using GULP, we created an array of input files containing a unit cell of four

layers of $Ni(CN)_2$ evenly spaced by 3.2 Å along the c-axis [Fig. 4.5(a)]. The choice of four layers was due to the two crystallographically distinct layers of $Ni(CN)_2$ both having energetically equivalent configurations [258]. The first and third layer were the same for all input files where the Ni^{2+} ions of the layer sat at $(0, 0, 0)$ and $(0.5, 0.5, 0.5)$ due to their energetic equivalence as determined in Ref. [258]. Each layer was defined as a periodic square grid with half occupancy of both carbon and nitrogen ions displaced $\frac{1}{3}$ and $\frac{2}{3}$ along each axis relative to the nickel centre. The remaining two layers were set up similarly such that the Ni^{2+} ions were at $(x, \mathrm{T}, 0.25)$ and $(0.5 + x, 0.5 + \mathrm{T}, 0.75)$. 100 input files were created where the value of x was changed by 0.01 increments. T is a translate function which is predefined and implemented by GULP. The translate function translated each layer of $Ni(CN)_2$ along the y axis in 0.01 increments during the calculations, calculating the energy of the configuration at each point. Each ion was assigned point charges and the electrostatic energy of the structure was calculated for every combination of x, y between 0 and 1. A representative input file is included in Appendix F. The energy of the outputted configurations were plotted as a function of $(\Delta x, \Delta y)$ where $(\Delta x, \Delta y)$ is the relative displacement between neighbouring layers, producing a potential energy surface [Fig. 4.5(b)-(c)].

Examining the appearance of the potential energy surface, it becomes apparent that discrete models are insufficient to describe the form of the electrostatic potential between the layers. The sinusoidal nature of the surface leads to quadratic behaviour around the minima which can only be accurately explained through a model containing continuous degrees of freedom. To determine a model that could

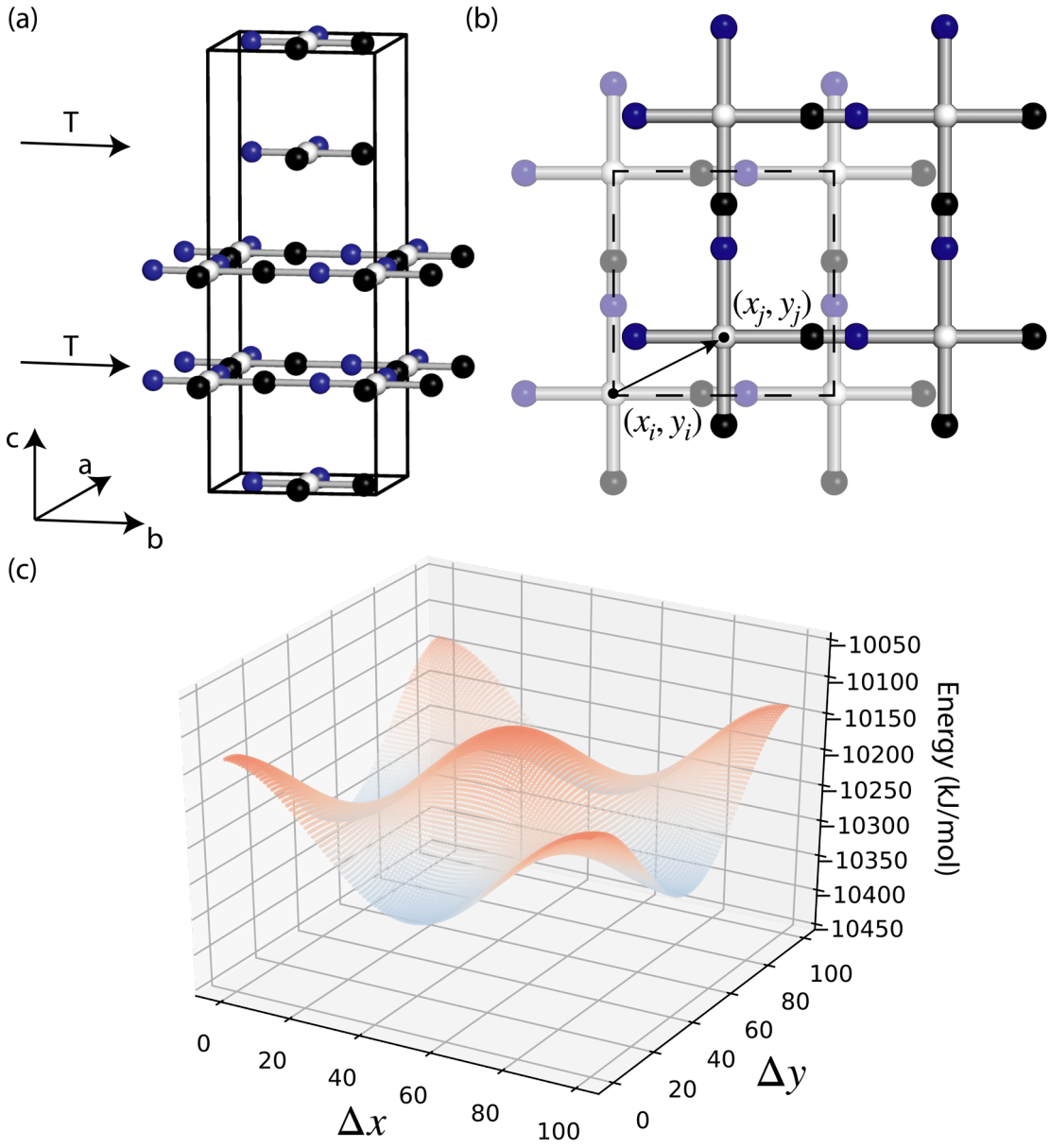

Figure 4.5: (a) Model used in electrostatic calculations for $x = 0$ with the first and third layer fixed and the translate function, T, displacing the offset second and forth layers. (b) Two layers of $Ni(CN)_2$ with their relative positions (x_i, y_i), (x_j, y_j) represented through the change in coordinates of the Ni^{2+} ion. (c) Potential energy surface of the layers displacing relative to one another as a function of $(\Delta x, \Delta y)$.

describe the energetics, we will come to parameterise the interactions in terms of the simplest Fourier components in 2D:

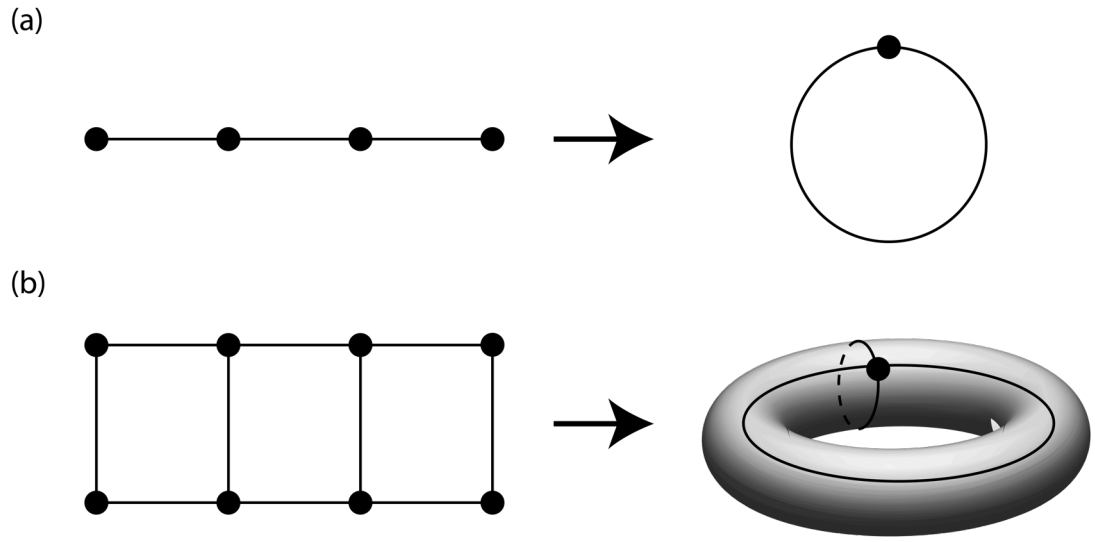

Figure 4.6: Topological mapping of (a) a periodic chain onto a circle and (b) a periodic grid onto a torus by connecting the periodic boundaries together.

$$H = J \sum_{\langle ij \rangle} \cos[2\pi(\Delta x_{ij})] \cos[2\pi(\Delta y_{ij})], \tag{4.1}$$

where (x_i, y_i) and (x_j, y_j) represent the positions of neighbouring layers of $Ni(CN)_2$ and $\Delta x_{ij} = x_i - x_j, \Delta y_{ij} = y_i - y_j$. For positive values of J, Eqn. 4.1 is minimised for those stacking arrangements of $Ni(CN)_2$ sheets where Ni^{2+} centres sit directly above CN^- ions.

4.3.1 Topological mapping

The form of Eqn. 4.1 is periodic in x and y, by design. Periodicity in functions can sometimes lead to unexpected topological mappings. For example, in the case of the polymer chains $Ag_xAu_{1-x}CN$, the periodic chains allowed the mapping of the relative displacement of the chain, Δz, onto a phase shift $\Delta\theta$ between XY spins [152]. This is the topological equivalence of mapping a periodic chain onto

a circle [Fig. 4.6(a)]. Similarly, a periodic grid can also be mapped onto phase angles, although instead of one periodic coordinate leading to an angle describing a circle, there are two periodic coordinates leading to two angles describing a pair of entangled circles. Thus from topological considerations, a periodic square grid can be mapped onto a torus [Fig. 4.6(b)]. Mapping each unit cell onto a torus converts the parameters (x, y) into two new parameters (θ, ϕ) where $\theta = 2\pi(x + y)$ and $\phi = 2\pi(x - y)$, chosen to making the following mathematical formulation more straightforward. Consequently, utilising compound angle formulae, the energetics of the stacking behaviour in $Ni(CN)_2$ can be reformulated as:

$$\begin{aligned}
H =& J \sum_{\langle ij \rangle} \cos[2\pi(x_i - x_j)] \cos[2\pi(y_i - y_j)] \\
=& J \sum_{\langle ij \rangle} \frac{1}{2} \cos\{2\pi[(x_i - x_j) + (y_i - y_j)]\} + \cos\{2\pi[(x_i - x_j) - (y_i - y_j)]\} \\
=& J \sum_{\langle ij \rangle} \frac{1}{2} \cos(\theta_i - \theta_j) + \cos(\phi_i - \phi_j) \\
=& J \sum_{\langle ij \rangle} \frac{1}{2} \cos\theta_i \cos\theta_j + \sin\theta_i \sin\theta_j + \cos\phi_i \cos\phi_j + \sin\phi_i \sin\phi_j \\
=& J \sum_{\langle ij \rangle} \mathbf{p}_i \cdot \mathbf{p}_j, \qquad (4.2)
\end{aligned}$$

where

$$\mathbf{p} = \frac{1}{\sqrt{2}} \begin{pmatrix} \cos(\theta) \\ \sin(\theta) \\ \cos(\phi) \\ \sin(\phi) \end{pmatrix}. \qquad (4.3)$$

The continuous parameters that represent the translational degrees of freedom in a layer of nickel cyanide can now be represented as a unit quaternion [Eqn. 4.3]. Hence we map the degrees of freedom in $Ni(CN)_2$ onto those of a 1D string of unit quaternions, the relevance of which will be discussed in detail later.

4.3.2 Parameterising the model

To estimate the magnitude of the interaction parameter, J, in Eqn. 4.2 relevant to $Ni(CN)_2$, we used the method of least squares refinement to fit the potential energy surface implicit in Eqn. 4.2 to that calculated using GULP [Fig. 4.5(c)]. This fit involved minimising the difference function

$$\chi^2 = \left[E_{\mathrm{GULP}}(\Delta x, \Delta y) - J\cos(2\pi\Delta x)\cos(2\pi\Delta y)\right]^2 \tag{4.4}$$

where E_{GULP} is the energy from the GULP calculations. Minimising χ^2 gives a value of $J = 83.6$ kJ/mol, typical of electrostatic supramolecular interactions [422] with $R^2 = 0.9998$, which implies our coarse graining is well justified. Using this interaction parameter, we employed Monte Carlo simulations at 300 K. These simulations contained 2000 quaternions which were mapped back onto coordinates of $Ni(CN)_2$ layers by placing regularly-spaced individual layers ($a = b = 4.857$ Å, $c = 3.2$ Å) offset in the (**a**, **b**) plane according to the Monte Carlo configuration, and simulated the diffraction pattern.

The model produced remarkably similar characteristics to experimental data [Fig. 4.7]. Much like the disordered model described in Ref. [258], it is able to account for all the reflections but, unlike the disordered model [Fig. 4.7(b)], the

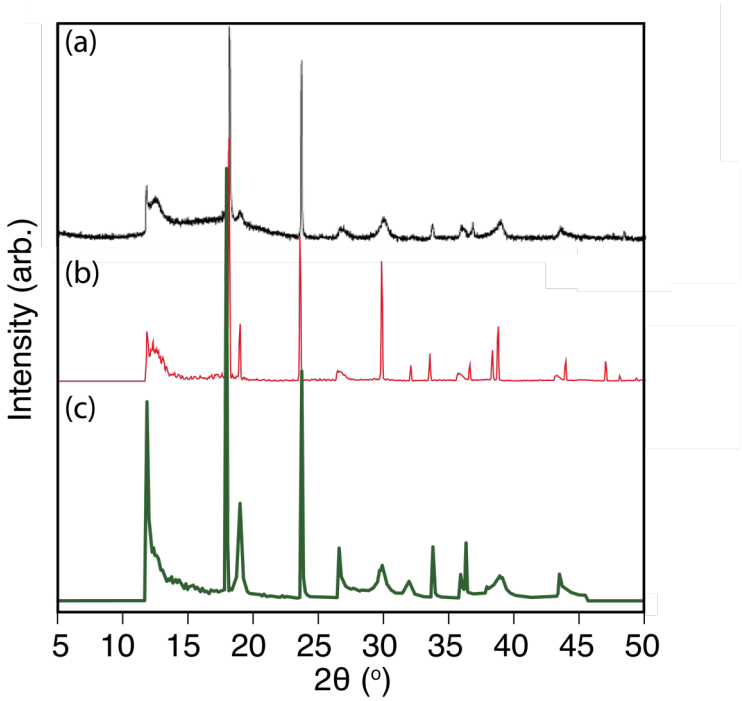

Figure 4.7: (a) Experimental diffraction pattern of $Ni(CN)_2$, adapted from Ref. [257]. Simulated diffraction patterns using (b) the disordered model described in Ref. [258] and (c) the continous model described in Eqn. 4.2.

quaternion simulation gives all the correct peak widths through local first neighbour interactions alone. Therefore these broad features can be assigned to topological features of the 1D stacking arrangement instead of a global shear to which it was originally attributed [258]. One limitation of the model is its inability to account for the diffuse peak at approximately $2\theta = 12.5°$. It is known from Ref. [258] that the shape of this broad feature arises from second-nearest neighbour interactions which, by design, our model does not take into account.

4.4 Relation to magnetic models

It is useful to be able to energetically describe the stacking behaviour of $Ni(CN)_2$, but the benefit of having a continuous model of a structural phase is the likelihood

of finding the phase elsewhere in condensed matter physics. Continuous statistical mechanical models are used extensively in 1D magnetism, here we explore the possibility of mapping our model onto magnetic degrees of freedom. In its current form, there is no obvious relationship between the energetics of $Ni(CN)_2$ and magnetic materials. However, topological mappings allow each layer to be converted into an expression more conventionally seen in the magnetic community. In this section, we describe a detailed construction of the topological mapping by using the mathematical construct of fibrations, resulting in restrictions of the quaternion in 3D space.

From topological considerations described in Section. 4.3.1, mapping the coordinates of the $Ni(CN)_2$ layers onto a torus, each layer of the bulk structure [Fig. 4.8(a)] can be represented by two vectors spanning a subset of quaternion space [Fig. 4.8(b)]. Quaternions, by construction, exist in four-dimensional space. Much like a unitary 3D vector spans the surface of a sphere with radius 1, unit quaternions can be mapped onto points on the surface of a hypersphere with radius 1. The additional constraints on θ and ϕ for our particular quaternion constrain this projection to a distinct surface in 4D space [Fig. 4.8(c)-(d)].

The following section gives an overview of the mathematical concepts required to relate our model to known magnetic models. This has been constructed based on approaches developed in Ref. [423].

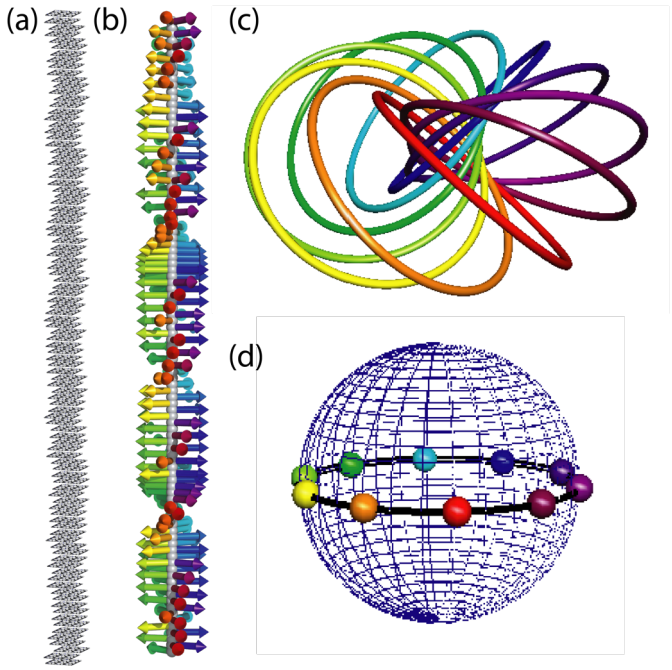

Figure 4.8: (a) Layers of $Ni(CN)_2$ and (b) corresponding quaternion chain. (c) Hopf fibration in 4D space traced by the unit quaternions set out in Eqn. 4.3 which (d) sit on the equator of the 3D sphere. Here the colours represent the phase angle.

4.4.1 Hopf projections

As we are about to embark on a voyage into 4D space, it seems pertinent to talk about how one may project higher order spaces onto subsets of that space which may be easier to view. Projections onto lower dimensional space in order to visualise data are commonplace in many areas of science including cartography. Instead of observing maps of the world in 3D, we tend to use stereographic projections which project the sphere onto a plane [Fig. 4.9]. Although the stereographic projection loses some information, obscuring relative distances in the case of maps, it preserves other important aspects of the sphere—in this case angles—and allows for easier visualisation. The same is true when projecting from 4D to 3D. In order to explain the mathematical mapping from a 4D sphere ($\mathbb{S}_3$) to 3D space ($\mathbb{R}_3$) rigorously, we

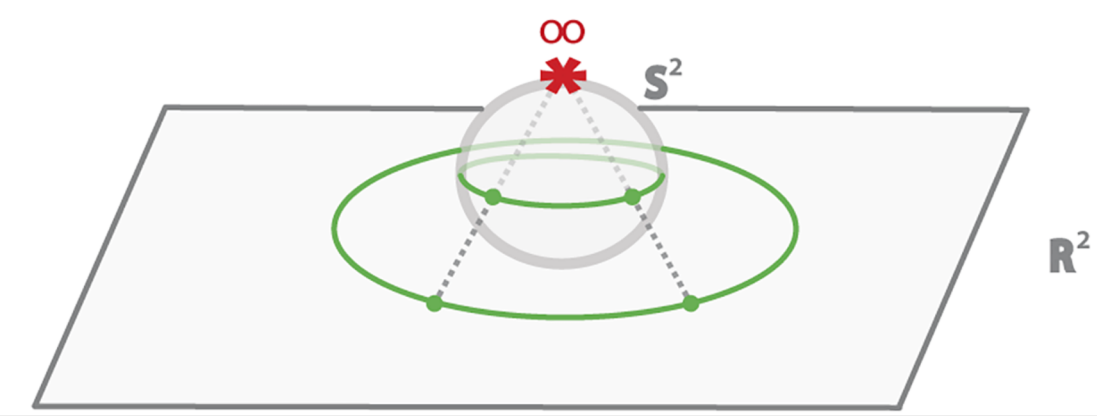

Figure 4.9: Stereographic projection of a sphere ($\mathbb{S}_2$) onto a 2D plane ($\mathbb{R}_2$), as commonly used in visualising maps. Figure reproduced from Ref. [424].

discuss the derivation of the Hopf fibration by first going through some mathematical definitions. We start with a discussion on cartesian products and fibrations with some examples, and move on to develop the mathematical construction of the Hopf fibration, with a view to the specific case of our model explained above.

A cartesian product is the set created by combining two sets, *e.g.* A and B. One common example of a cartersian product is the formulation of cartesian coordinates where the cartesian product of the coordinate x and coordinate y produces a new set of coordinates described by x, y. In this case, two one-dimensional sets are combined to form a new two-dimensional set. Cartesian products need not be formed by combining similar dimensional sets, for example, one can create a cartesian product of a unit circle in two-dimensional space ($\mathbb{S}_1$) and a one-dimensional coordinate ($\mathbb{R}_1$) to create a three-dimensional set, which in this case, spans a cylinder [Fig. 4.10(a)].

All cartesian products have projections. For example, taking the case of the cartesian coordinates above, each coordinate (x, y) can be projected onto a point contained within the set y. Similarly, starting with a projection at point y_1 in the

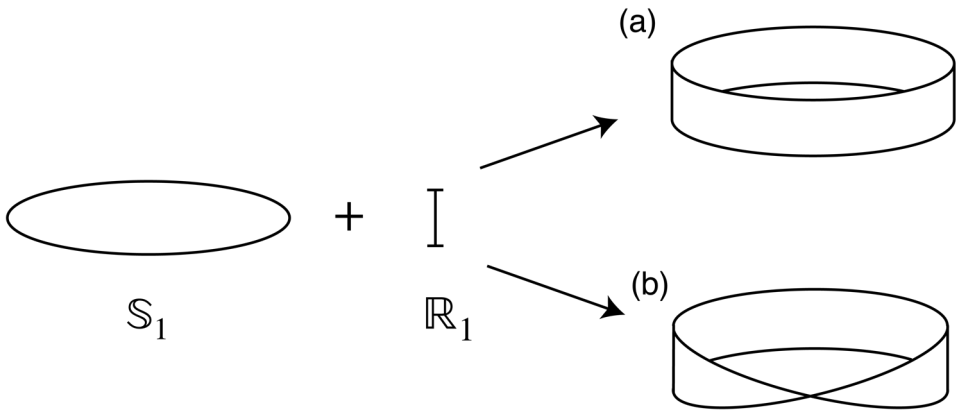

Figure 4.10: (a) Cartesian product of ($\mathbb{S}_1$) and ($\mathbb{R}_1$) forming a cylinder. (b) Fibration of ($\mathbb{S}_1$) and ($\mathbb{R}_1$) to form a mobius strip where the fibre inverts on traversing round the circle.

set of y, a set of all points that project down onto point y_1 can be recreated. In this case, it would be the set of all coordinates x, y_1, termed the fibre over y_1. Although all cartesian products are examples of fibrations, there are plenty of examples of sets created from two components which can not be described as cartesian products and this is where the construct of fibrations proves essential.

For example, taking the case of the mobius strip, a mobius strip can be projected onto a circle and the fibre can be described by a vertical line about each point on the strip [Fig. 4.10(b)]. The clear distinction here from a cartesian product is that whereas with the cartesian product you can change the projection point y_1 to another point along the y axis, y_2, and still have the same fibre of x, for the mobius strip, as the fibre moves round the $\mathbb{S}_1$, it inverts. Hence a fibration can be thought of as a 'twisted' cartesian product where the fibre retains the same dimensionality, but may invert or change orientation depending on where the projection is within the set.

With this definition in mind, we now turn to the specific example of a Hopf fibration which defines a function that projects $\mathbb{S}_3$ onto $\mathbb{S}_2$. For this we go back to our definition of a quaternion where instead of writing it in terms of a 4D vector, we can write it as the linear combination, $q = w + x\mathbf{i} + y\mathbf{j} + z\mathbf{k}$ where $\mathbf{i}$, $\mathbf{j}$, and $\mathbf{k}$ have the relationship $\mathbf{i}^2 = \mathbf{j}^2 = \mathbf{k}^2 = \mathbf{ijk} = -1$. To form a Hopf fibration we begin by defining a function η that projects q onto $\mathbb{S}_2$.

$$\eta(q) = q\mathbf{k}q^{-1}, \tag{4.5}$$

where q^{-1} is the complex conjugate of q and $\mathbf{k}$ is the imaginary number. Following the projection through algebraically results in:

$$\eta(q) = (0, 2wy + 2xz, 2yz - 2wx, w^2 + z^2 - x^2 - y^2). \tag{4.6}$$

The important result from this is the first coordinate always ends up being 0 and thus $\eta(q)$ lies in a three-dimensional subspace $\mathbb{R}_3$. Moreover, summing the squares of each coordinate gives a magnitude of 1, such that $\eta(q)$ lies in the unit sphere $\mathbb{S}_2$ resulting in a projection from $\mathbb{S}_3$ to $\mathbb{S}_2$ known as the Hopf projection [425].

For our specific quaternion $\mathbf{p}$, defined in Eqn. 4.3, this leads to some interesting properties of the projection in 3D space. Substituting $w = \cos\theta, x = \sin\theta, y = \cos\phi, z = \sin\phi$ into Eqn. 4.6 where $\theta = 2\pi(x + y), \phi = 2\pi(x - y)$ causes the $\mathbf{k}$ component $(w^2 + z^2 - x^2 - y^2)$ to vanish. Therefore, in the Hopf projection of $\mathbb{S}_3$, the trace of the quaternion defined in Eqn. 4.3 corresponds to an equator of $\mathbb{S}_2$ [Fig. 4.8(c)-(d)]. Through this mapping, $\mathbf{p}$ is shown as anisotropic as it has no z

component in the 3D projection and lies purely in the (x, y) plane.

4.4.2 Spinors

Quantum spins also have degrees of freedom that can be related to the surface of the hypersphere. These degrees of freedom are commonly represented as spinors where, for a spin-$\frac{1}{2}$ particle, the state of a particle can be written as the two component spinor,

$$\psi = \alpha|\uparrow\rangle + \beta|\downarrow\rangle = \begin{pmatrix} \alpha \\ \beta \end{pmatrix}, \quad |\alpha|^2 + |\beta|^2 = 1. \tag{4.7}$$

Quaternions are a type of spinor and our unit quaternion [Eqn. 4.3] can be represented as the spinor:

$$\psi = \frac{1}{\sqrt{2}} \begin{pmatrix} \exp(\mathrm{i}\theta) \\ \exp(\mathrm{i}\phi) \end{pmatrix}, \tag{4.8}$$

where the coefficients α, β in Eqn. 4.7 can be expressed in terms of the angles θ, ϕ: $\alpha = \frac{1}{\sqrt{2}} \exp(\mathrm{i}\theta)$ and $\beta = \frac{1}{\sqrt{2}} \exp(\mathrm{i}\phi)$. With the positions of layers now represented in spinor form, we can mathematically relate the planar displacements of $Ni(CN)_2$ to states of spin-$\frac{1}{2}$ particles. To determine the constraints set out by the spinon representation, we look at the expectation operators of S_z, S_+, and S_- for spin half spins:

$$S_z|\uparrow\rangle = \frac{\hbar}{2}|\uparrow\rangle \quad S_z|\downarrow\rangle = -\frac{\hbar}{2}|\downarrow\rangle, \tag{4.9}$$

$$S_+|\uparrow\rangle = 0 \quad S_+|\downarrow\rangle = \hbar|\uparrow\rangle, \tag{4.10}$$

$$S_-|\uparrow\rangle = \hbar|\downarrow\rangle \quad S_+|\downarrow\rangle = 0, \tag{4.11}$$

where

$$|\uparrow\rangle = \begin{bmatrix}1\\0\end{bmatrix}, |\downarrow\rangle = \begin{bmatrix}0\\1\end{bmatrix}. \tag{4.12}$$

For the case of our spinor representation in Eqn. 4.8, applying the operators and using the relations $S_x = \frac{1}{2}(S_+ + S_-)$ and $S_y = \frac{1}{2i}(S_+ - S_-)$, the expectation value for the spins in all three directions can be written as:

$$\begin{aligned}
\langle\psi|S_x|\psi\rangle =& \frac{\hbar}{2}\left(\frac{1}{2}\exp(-\mathrm{i}\theta)\exp(\mathrm{i}\phi)\langle\uparrow|\uparrow\rangle + \frac{1}{2}\exp(-\mathrm{i}\phi)\exp(\mathrm{i}\theta)\langle\downarrow|\downarrow\rangle\right) && (4.13)\\
=& \frac{\hbar}{4}\left(\exp(\mathrm{i}\phi)\exp(-\mathrm{i}\theta) + \exp(-\mathrm{i}\phi)\exp(\mathrm{i}\theta)\right),\\
\langle\psi|S_y|\psi\rangle =& \frac{\hbar}{2\mathrm{i}}\left(\frac{1}{2}\exp(-\mathrm{i}\theta)\exp(\mathrm{i}\phi)\langle\uparrow|\uparrow\rangle - \frac{1}{2}\exp(-\mathrm{i}\phi)\exp(\mathrm{i}\theta)\langle\downarrow|\downarrow\rangle\right) && (4.14)\\
=& \frac{\hbar}{4\mathrm{i}}\left(\exp(\mathrm{i}\phi)\exp(-\mathrm{i}\theta) - \exp(-\mathrm{i}\phi)\exp(\mathrm{i}\theta)\right),\\
\langle\psi|S_z|\psi\rangle =& \frac{\hbar}{2}\left(\left|\frac{1}{\sqrt{2}}\exp(\mathrm{i}\theta)\right|^2\langle\uparrow|\uparrow\rangle - \left|\frac{1}{\sqrt{2}}\exp(\mathrm{i}\phi)\right|^2\langle\downarrow|\downarrow\rangle\right) && (4.15)\\
=& \frac{\hbar}{2}\left(\frac{1}{2} - \frac{1}{2}\right) = 0.
\end{aligned}$$

Here, the important result is that the expectation value for $S_z = 0$ signifying

that the spins have equal probability of being spin up or down. Conversely, S_x and S_y both have non zero expectation values and span the same set of possible values. As already shown through the Hopf fibration, the quaternion is anisotropic and contains no component along the z axis in its projection onto 3D. In the same way, these expectation values show that the spins defined in Eqn. 4.8 have an expectation value of 0 for their z component and are equally likely to be in the up or down state.

Heisenberg spin-$\frac{1}{2}$ particles interact through the Heisenberg XYZ model:

$$\mathcal{H} = \sum_i (J_x S_i^x S_{i+1}^x + J_y S_i^y S_{i+1}^y + J_z S_i^z S_{i+1}^z), \tag{4.16}$$

and with $\langle\psi|S_z|\psi\rangle = 0$, the Hamiltonian can be simplified to that of a Heisenberg XY model:

$$\mathcal{H} = \sum_i (J_x S_i^x S_{i+1}^x + J_y S_i^y S_{i+1}^y + \Delta S_i^z S_{i+1}^z). \tag{4.17}$$

where $\Delta = 0$. As the symmetry is unbroken in the XY plane, there is no way of distinguishing between the two in-plane variables. This results in θ, ϕ spanning the same set of expectation values for both S_x and S_y. Therefore, the interaction parameter for pairwise interactions between S_x and S_y components is expected to be the same, and the Heisenberg model can be simplified further to an XX spin-$\frac{1}{2}$ chain:

$$\mathcal{H} = J \sum_i (S_i^x S_{i+1}^x + S_i^y S_{i+1}^y + \Delta S_i^z S_{i+1}^z), \tag{4.18}$$

where $\Delta = 0$. Mathematically, we have related the translational degrees of freedom of nickel cyanide layers to that of a spin-$\frac{1}{2}$ Heisenberg XX chain. Thus, just like the Ising model for anti/ferromagnetism can be related to HCP and CCP stacking, interacting Heisenberg spins may have links to the continuous stacking seen in $Ni(CN)_2$. Through this result we may be able to infer information about the exotic magnetic phase of the spin-$\frac{1}{2}$ XX chain through a greater understanding of complex structural phases.

4.4.3 Quantum and classical analogues

As noted in Section. 4.2, relating structural and magnetic models can highlight unexpected links in emerging properties between ostensibly unrelated systems. In the case of $Ag_xAu_{1-x}CN$, the mapping between the two classical systems was sufficiently robust to allow a correspondence between the topological properties of emergent objects in both systems [152]. Finding classical analogues to quantum mechanical systems is an ongoing challenge [426]. But making analogies between apparently unrelated fields is important in understanding physical concepts and the limits of applicability to different theories [426]. Analogies between classical physics and quantum mechanics in particular helps bridge the gap between disparate areas of physics. Even equations underpinning quantum mechanics such as the Schrödinger equation have been shown to have the same form as classical mechanical equations such as the Helmholtz equation, and can be reformulated using only classical tools [427, 428]. Quantum-classical analogies are becoming increasingly utilised to study quantum behaviour with classical means and analogues to purely quantum phenomena such as tunneling have been proven to exist in classical systems [429]. In

fact the deviation of spin waves from spin wave theory can sometimes highlight the importance of quantum fluctuations within the specific system [430].

Although we have shown that there are similarities in the mathematical construction of our continuous model and the 1D Heisenberg XXZ chain, the question remains of what the physical implications may be. Whilst we cannot comment on the extent to which $Ni(CN)_2$ can exhibit experimental characteristics of the XXZ Heisenberg model, mathematically the formulation shows the quaternion behaviour can be used to both describe the structure of $Ni(CN)_2$ and represent spin-$\frac{1}{2}$ particles. Spin-$\frac{1}{2}$ particles are of particular interest due to their unique excitations. Whereas classical spins form magnons, quantum spins fractionalise, forming a two-spinon continuum in their excitation spectrum [150]. The spinon continuum produced in the magnetic spectrum is a signature of the XXZ Heisenberg model and analogous phases should contain the same quasiparticle excitations. In the case of $Ni(CN)_2$, we expect the 'spinon continuum' would manifest as excitations in the lattice dynamics through phonon broadening of the low energy phonon modes due to layer slipping which could have profound effects on the materials thermal conductivity.

The phonon modes in $Ni(CN)_2$ have been studied in Ref. [431] from both an experimental and computational perspective. Computationally, the phononic behaviour of $Ni(CN)_2$ was studied through *ab initio* calculations. These calculations give no evidence of phonon broadening as *ab initio* techniques require a periodic unit cell, losing information on the behaviour expected to lead to phonon broadening. Moreover the study in Ref. [431] calculated phonons for the structure with an incorrect stacking arrangement of Ni ions of neighbouring layers reside in the same

positions within the $(\mathbf{a}, \mathbf{b})$ plane, resulting in inaccurate data.

The experimental study of Ref. [431] did not explicity address phonon broadening. Even if $Ni(CN)_2$ supported a spinon-like phonon continuum, it would be impossible to resolve from the measurements made in that study. This is a direct effect of the eigenvectors being x, y-polarised and expected 'spinons' occurring along $\mathbf{k} = [00\xi]$. Due to selection rules, the neutron scattering will only by visible for $\mathbf{Q} = \mathbf{G} + \mathbf{k}$ where $\mathbf{G}$ is a reciprocal lattice point $(hk0)$ and scattering intensity increases with large h, k. Therefore, visible phonon contribution would occur far out in reciprocal space, at which point the powder inelastic neutron scattering spectrum would contain too many overlapping modes for direct resolution and information on broadening behaviour is lost.

For accurate determination of the phonon broadening due to the materials characteristics, single crystal triple axis neutron spectroscopy is required to fully resolve the phononic behaviour. Unfortunately, single crystals of anhydrous $Ni(CN)_2$ have never been synthesised and therefore precise measurements of the low energy phonons, especially the broadening behaviour, to test this theory is a difficult task. If single crystal triple axis neutron spectroscopy evidenced a spinon-like continuum, this would provide additional evidence towards $Ni(CN)_2$ being an analogue to the Heisenberg XXZ model.

4.4.4 Manipulating interaction parameters

As highlighted throughout the thesis, one of the main advantages of mapping behaviour between magnetic and structural states rests in changing the energy scale of

exotic phenomena for easier access of novel phases. This is not the only advantage. A second benefit lies in the ability to manipulate interaction parameters of structural phases with greater ease than their magnetic analogues. In the case of $Ni(CN)_2$, the material is known to have a large uniaxial compression under pressure [431]. Here we look at how pressure might effect the interaction strength of our model by computationally monitoring the effect on the energy with increased pressure. Variable pressure studies indicate that compression of the c-axis can linearly decrease the lattice parameter by up to 12% [415]. Using GULP, we calculated potential energy surfaces for a range of interlayer separations between 3.2 Å and 2.9 Å and tracked the potential energy surface as a function of changing lattice parameter [Fig. 4.11], again optimising for goodness of fit using Eqn. 4.4. From the c lattice parameter, we can calculate the experimental pressure using the following equations, and data given in Ref. [415]:

$$c(p) = c(0)[1 + e(p)], \tag{4.19}$$

where $e(p)$ is the strain response along the c-axis given by:

$$e(p) = \epsilon_0 - \lambda p^v. \tag{4.20}$$

The empirical parameters ϵ_0, λ, v were produced by fitting the lattice parameter data from Ref. [415] [Appendix D.1] in the program *PASC*al [432].

Combining the two equations with the c lattice parameters used to calculate the potential energy surface, we can collect data on how the interaction parameter, J,

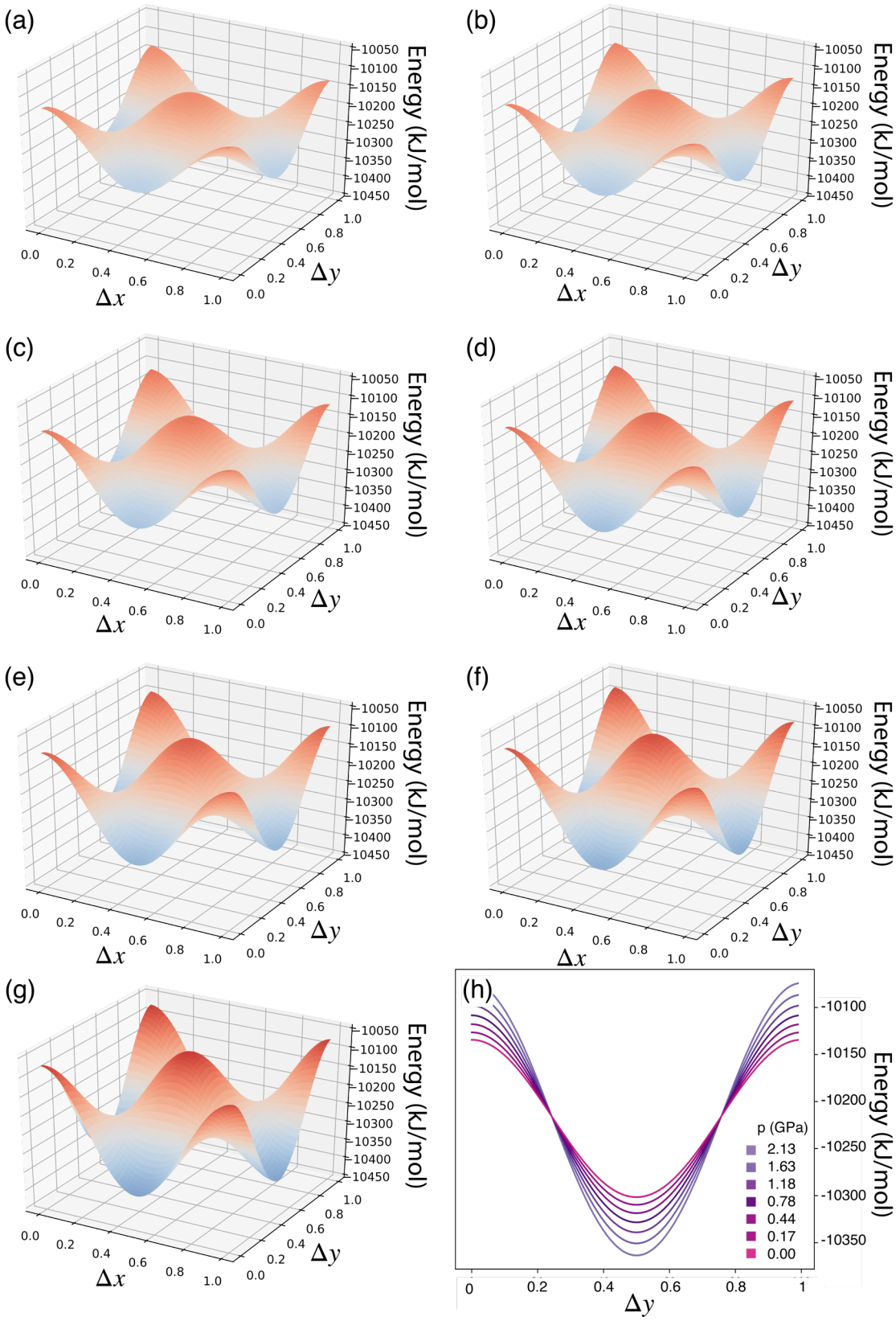

Figure 4.11: The potential energy surface of relative displacements of layers of $Ni(CN)_2$ under different pressures where $p(\mathrm{GPa}) =$ (a) 0.00, (b) 0.17, (c) 0.44, (d) 0.78, (e) 1.18, (f) 1.63, and (g) 2.13. (h) Cuts of the potential energy surface at each pressure for $\Delta x = 0$.

c (Å)	p (GPa)	J (kJ/mol)
3.20	0.01	86.64
3.15	0.17	91.26
3.10	0.44	98.80
3.05	0.78	108.35
3.00	1.18	119.56
2.95	1.63	132.20
2.90	2.13	146.12

Table 4.1: Data from potential energy surface calculations fitted to Eqn. 4.2, giving the variation of the interaction parameter with changing pressure and lattice parameter, graphically depicted in Fig. 4.12.

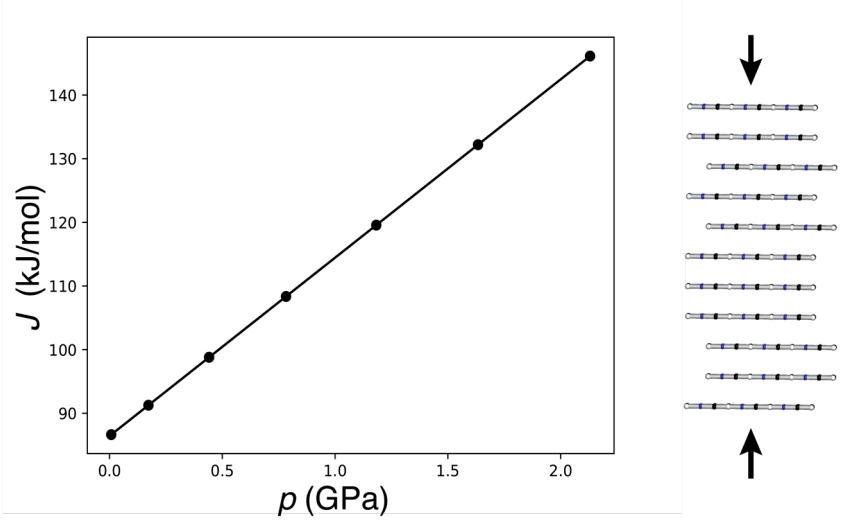

Figure 4.12: Interaction parameter vs uniaxial pressure, compressing along the c-axis. These data were collected from fitting the Hamiltonian in Eqn. 4.2 to GULP calculations of the potential energy surface at different pressures. Relationships between the pressure and lattice parameters were taken from Ref. [415].

varies with pressure [Table. 4.1]. Fig. 4.12 evidences a linear relationship between the interaction parameter and pressure such that pressure can be used to manipulate the energy scale of the interaction. This gives $\mathrm{d}J/(k_B\mathrm{d}p) = 3.4\,\mathrm{K/GPa}$ which is a much larger response than for known magnetic systems acting with Heisenberg XXZ interactions, $\mathrm{d}J/(k_B\mathrm{d}p) = 0.25\,\mathrm{K/GPa}$ [433], highlighting the greater difficulty in manipulating interaction parameters between magnetic degrees of freedom.

4.5 Outlook

In this chapter we have shown an example of stacking behaviour in a layered material which can be described through continuous degrees of freedom. As this investigation has indicated a possible mathematical link to phases with exotic dynamics, the study highlights avenues for further exploration of the underlying relationship between disorder and dynamics which is becoming increasingly more studied [48, 70, 152, 434]. Although the link between $Ni(CN)_2$ layers and anisotropic quaternions may not lead to a true analogue of a quantum Heisenberg chain, it is nonetheless a useful analogy to make.

In order to test the validity of this route, we suggest future work of mapping the quasiparticle phenomena of these two, ostensibly different systems. In the case of a spin-$\frac{1}{2}$ XX chain, this is well documented as a spinon continuum in the excitation spectrum [150]. For $Ni(CN)_2$ however, the expected low energy phonon broadening due to the interaction between neighbouring layers have not been measured and may hold the key to this classical/quantum crossover.

The model suggested is not unique to $Ni(CN)_2$, and can easily be generalised to any similar structured material. Layered phases such as graphite are known to slip and disorder into turbostratic carbon [435]. A continuous model describing the variation in the stacking behaviour may be used to describe this transformation and could explain phases that exist between the two extremes. Evidence of continuous behaviour has also been noted in the stacking behaviour of the layered polymer melon where similar asymmetric diffuse peaks are observed and the relative layer

displacements produce a very flat energy profile [436, 437]. The examples selected are by no means an exhaustive list of systems which may be described by more continuous models. Creating these links informs our understanding of the interactions involved in layered materials and can lead to novel mappings of other continuous magnetic models and physical realisations of exotic phases.

Chapter 5

Skyrmion lattices in chiral metal organic frameworks

5.1 Summary

Throughout this thesis we have explored mappings of magnetic models to allow us to understand the structural behaviour of known compounds. In the last chapter we saw how finding physical realisations of complex magnetic phases with different, less experimentally demanding, energy scales can increase our capability of phase exploration which may shed further light on the underlying physics of spin chains. In this chapter we instead identify complex magnetic phenomena, and devise an analogous model to determine the propensity for phases to exist in a structural form. In particular, we determine the extent to which topologically protected magnetic phases can be emulated in structural analogues through mapping spin degrees of freedom of magnetic ions within a chiral lattice onto the orientations of guest molecules within the pores of chiral frameworks.

Topologically protected states are ideal candidates for memory storage applications due to the preservation of information contained in their topological charge in the absence of external pertubations [171, 438]. A particular interest has been in magnetic topologically protected phases as they are easily manipulated with a

magnetic field [439]. However, accessing these states for industrial applications can prove challenging as the temperatures required for the formation of spin textures typically occur below $\sim 30\,\mathrm{K}$ [165] and topological charges only manifest within a small regime of $\sim 2-3\,\mathrm{K}$ within this range [440]. This low energy scale poses severe challenges for experimental studies and practical applications of magnetic textures.

In this chapter, we explore the degree to which topologically protected states conceptually related to spin textures can be formed in chiral metal organic frameworks (MOFs). We begin by adapting the magnetic Hamiltonian of interacting dipoles on a chiral lattice to a non-magnetic Hamiltonian of interacting quadrupoles within a chiral framework. Through Monte Carlo simulations, we examine the phase behaviour of the quadrupolar Hamiltonian, providing evidence of topologically protected phases. To determine the extent that real materials might exhibit the thermodynamic behaviour produced by our Hamiltonian, we employ a mixture of density functional theory calculations and *ab initio* molecular dynamics simulations on a candidate MOF and track the energetics of the structure as a function of strain and temperature. To set the context, this chapter starts with a brief overview of topologically protected spin systems and the Hamiltonians driving their formation, as well as a discussion on candidate materials for hosting non-magnetic skyrmions.

5.2 Background

Magnetic textures arise in materials with competing microscopic interactions, leading to emerging order on the mesoscopic scale [165]. The interest in studying magnetic textures stems from their ability to form non-trivial topological structures

which, due to their stability and small size, may find application as data storage and low-energy spintronic devices [163]. Such states were first predicted in 1961 [162] and since their experimental realisation as skyrmions [165], hopfions [441], and more recently merons [174] the emergence of topological states in spin textures has become an increasing area of interest in condensed matter physics.

Typically, magnetic skyrmions arise from a combination of the three interactions in the following Hamiltonian

$$\hat{\mathcal{H}} = -J \sum_{ij} \mathbf{S}_i \cdot \mathbf{S}_j - K \sum_{ij} (\mathbf{S}_i \times \mathbf{S}_j) \cdot \mathbf{r}_{ij} - \mathbf{B} \cdot \sum_i \mathbf{S}_i. \tag{5.1}$$

Here $\mathbf{S}_i$ is the spin orientation, $\mathbf{r}_{ij}$ is the vector between neighbouring magnetic ions, J the strength of symmetric (ferromagnetic) interaction, K that of an antisymmetric (Dzyaloshinskii-Moriya) interaction arising from the underlying chirality of the lattice, and $\mathbf{B}$ an applied magnetic field. Three magnetic textures are generated from a combination of these interactions with changing temperature and magnetic field [Fig. 5.1] [167].

Although the interactions leading to skyrmionic phases are well characterised, the number of chemical families known to support magnetic skyrmionic textures remains remarkably small due to the difficulty of engineering antisymmetric interactions [166, 169]. However, mesoscopic textures do not exist solely within magnetic materials and nematic liquid crystals have been known to host vortex-like defects [215, 442, 443] which have been shown to be rigorously skyrmionic and thermodynamically stable in model systems when placed under confinement [Fig. 5.2] [202].

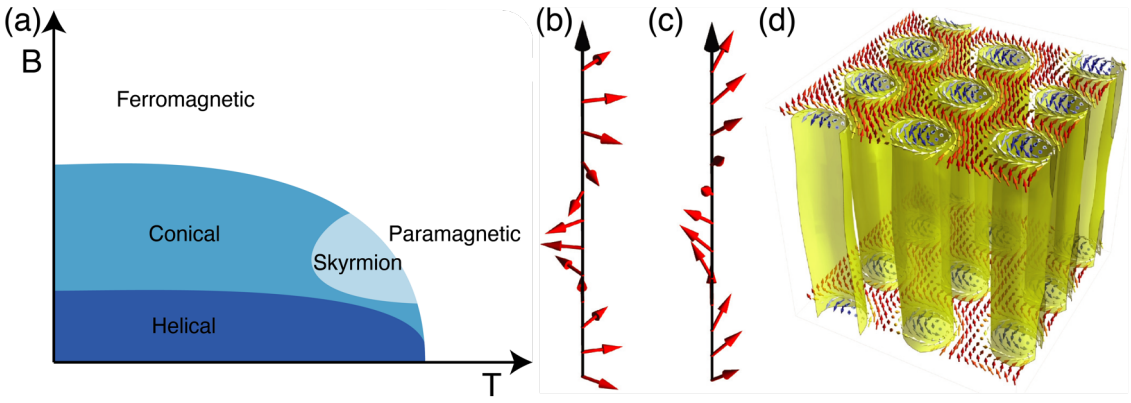

Figure 5.1: (a) Schematic representation of a typical phase diagram for a chiral magnet which hosts skyrmions, and corresponding (b) helical, (c) conical, and (d) skyrmionic phases. Figure adapted from Ref. [167] with permission from the American Physical Society.

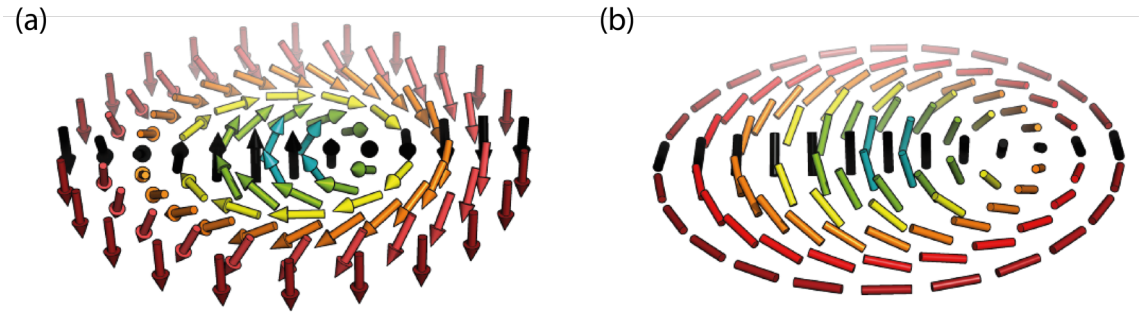

Figure 5.2: (a) A magnetic skyrmion is a topological object where the magnetic spins wind around a singularity, shown here as vectors coloured according to orientation. The path coloured black involves a rotation of the magnetisation by 360°. (b) Nematic liquid crystals containing quadrupolar degrees of freedom show similar states, except winding around the singularity now involves an 180° rotation as the quadrupolar directors are unchanged under inversion.

Generating new routes to produce topologically protected states is imperative for the development of materials for industrial applications. Although skyrmions have been reported at room temperature [444], most topological states require extreme conditions such as low temperatures or high magnetic fields. Finding more experimentally accessible phases increases our understanding of how they may be manipulated, and opens potential pathways to producing low energy spintronics.

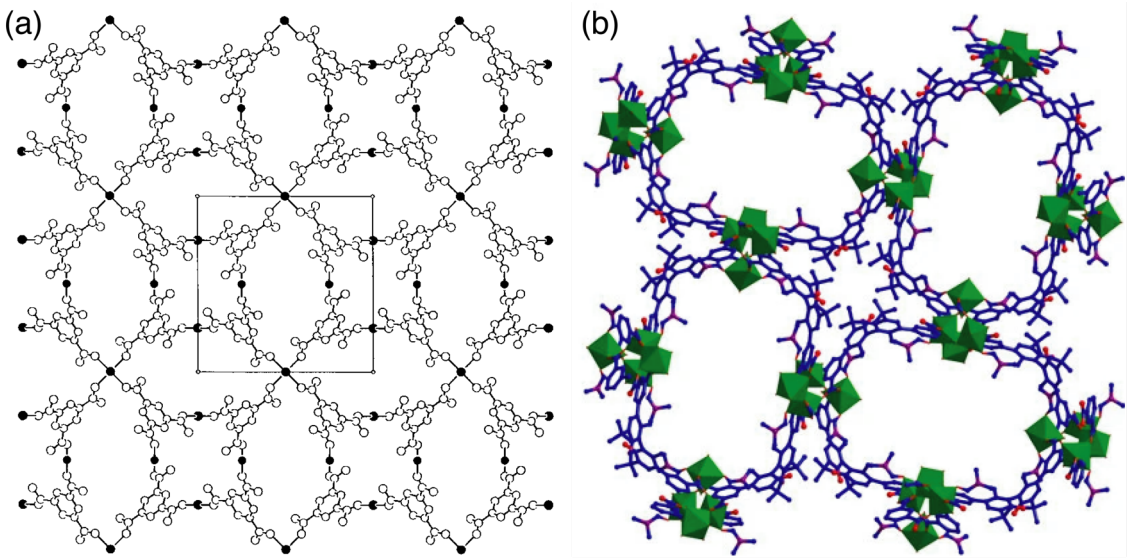

Figure 5.3: Examples of chiral MOFs within the literature. (a) Axial projection of the chiral metal organic framework $Ni_3(btc)_2(py)_6(eg)_6 \cdot xeg\cdot y H_2O$ (space group $P4_232$) adapted from Ref. [445] with permission from Springer Nature. (b) View of a three-dimensional porous structure (space group $P4_12_12$) along the c-axis, (metal ions shown as coordinated within green polyhedra; O, red; N, purple; C, blue). Figure adapted from Ref. [446] with permission from the Royal Society of Chemistry.

One important task is finding materials which could potentially harbour the interactions present in Eqn. 5.1. This is a non-trivial task as, for example, in the case of MnSi, the nonvanishing Dzyaloshinskii-Moriya interaction relies on a peculiar combination of spin-orbit coupling and chirality of its B20 lattice type [165]. Consequently there is much to be gained by diversifying the chemical space accessible for topological materials design.

Although chirality is rare amongst ferromagnetic metals, it is commonplace amongst MOFs [Fig. 5.3] [445, 447, 448]. MOFs are porous materials consisting of metal clusters bridged by multidentate organic ligands, forming 3D structures which can harbour guest molecules. Manipulating MOF topoplogy is routine in structural chemistry to modify pore sizes [449] and adapt the structure for various

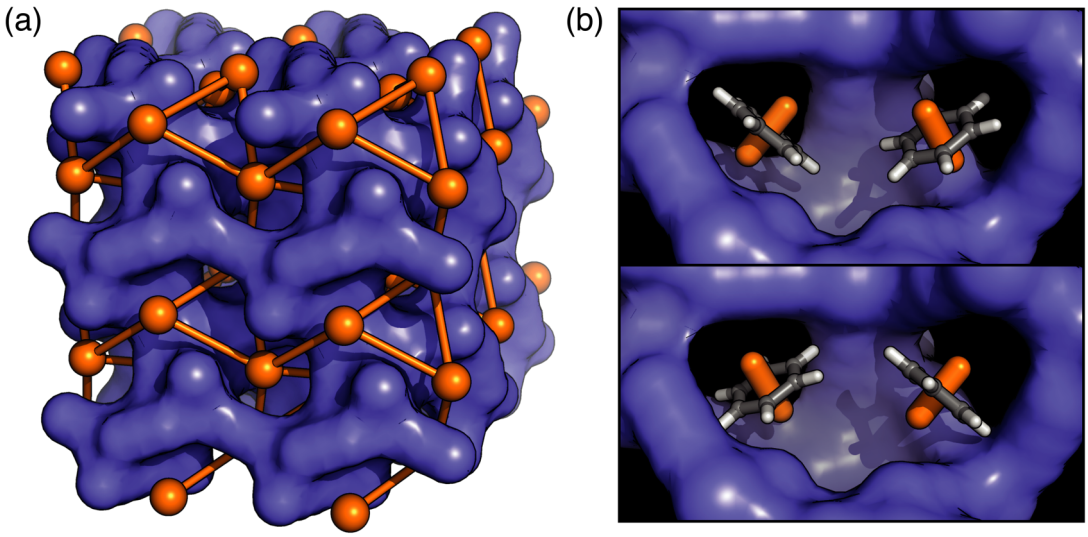

Figure 5.4: (a) A MOF framework represented as a purple surface and the corresponding pore network (orange). (b) Orientations of benzene molecules within the pores which are free to fluctuate and can also be represented by a quadrupolar moment (orange).

applications such as gas separation [450], gas storage [451], and catalysis [452]. In fact there are now a number of well-established strategies for synthesising chiral MOFs, including many that use achiral reagents [453], or involve only host-guest interactions, such as adsorption of achiral molecules [454]. Although magnetic interactions are notoriously weak in MOFs [455], the intermolecular interaction between molecules within pores can be strong—such is the basis of the 'crystalline sponge' concept [456, 457]. Here, framework materials known as crystalline sponges can be used as scaffolding to selectively absorb molecules from solution [458] and allow isolation of molecules for characterisation which otherwise would be near impossible to isolate, purify, and recrystallise [459].

MOFs can harbour a large number of different molecules whose orientations can fluctuate within the pores [Fig. 5.4], while the MOF framework—due to external stimuli and chemical interactions—can mediate their molecular organisation. The

chiral nature of frameworks could facilitate a Dzyaloshinskii-Moriya type interaction, thus creating an ideal architecture for skyrmions. In this chapter we will explore how such interactions can potentially stabilise topologically protected phases predicted to exist in liquid crystals [202]. This is conceptually different to topological phases of liquid crystal as the framework builds in translational confinement of the molecules.

To assess whether MOFs can host orientational skyrmions, we approach the problem in three stages. First, we establish an interaction model by replacing magnetic dipoles with non-magnetic quadrupoles, which will come to relate the orientational order in MOFs to magnetic order within chiral magnets. The focus on quadrupoles rather than dipoles stems from the tendency of dipole moments to be small and long-ranged interactions; by contrast effective quadrupolar interactions have $J \approx 100\,\mathrm{K}$ and are short-ranged [52]. Second, we must perform a series of MC simulations in order to establish the phase behaviour of the model. Through this we identify a number of accessible topologically non-trivial phases, including that of a skyrmion crystal. For the third stage, we use *ab initio* molecular dynamics (AIMD) simulations to establish the relevance of our simple microscopic model to the thermodynamic behaviour of a representative chiral MOF. We argue on this basis that MOFs are viable hosts for emergent topological objects, and we conclude by discussing some of the challenges and opportunities associated with realising, characterising, and exploiting skyrmionic MOFs. The key result is the production of topologically protected phases using the quadrupolar Hamiltonian whose interactions are shown to exist within chiral MOFs. This opens up the field to new ways of creating non-trivial topological textures that could potentially be less restrictive

than chiral magnets.

5.3 The model

For the first stage, we require a mapping between the magnetic interactions seen in MnSi to quadrupolar degrees of freedom [161]. This process must be undertaken with great care as the degrees of freedom in the two systems are ostensibly different. The key difference here is that instead of ferro- (0°) or antiferro- (180°) magnetic coupling between spins, there is a ferro- (0°) or antiferro- (90°) quadrupolar coupling between quadrupoles. Similarly, for magnetic spins, the Dzyaloshinskii-Moriya interaction—importantly the cross product—is minimised when the spins are perpendicular (90°), whereas an analogous 'quadrupolar cross product' would require minimisation for the quadrupole orientations at 45°.

We begin by mathematically defining the quadrupolar orientations. Whereas, the dipolar magnetic spins are represented as vectors $\mathbf{S}_i = (s_{ix}, s_{iy}, s_{iz})$, the quadrupole orientations are represented by the symmetric tensor:

$$\mathbf{Q}_i = \begin{pmatrix} s_{ix}^2 & s_{ix}s_{iy} & s_{ix}s_{iz} \\ s_{iy}s_{ix} & s_{iy}^2 & s_{iy}s_{iz} \\ s_{iz}s_{ix} & s_{iz}s_{iy} & s_{iz}^2 \end{pmatrix} \tag{5.2}$$

where we denote the orientation of molecule i parallel (if rodlike) or normal (if planar) to an axis defined by $\pm(s_{ix}, s_{iy}, s_{iz})$. We note that, conventionally, nematic order parameters are represented as the traceless tensor:

$$\mathbf{n}_i = \begin{pmatrix} s_{ix}^2 - \frac{1}{3} & s_{ix}s_{iy} & s_{ix}s_{iz} \\ s_{iy}s_{ix} & s_{iy}^2 - \frac{1}{3} & s_{iy}s_{iz} \\ s_{iz}s_{ix} & s_{iz}s_{iy} & s_{iz}^2 - \frac{1}{3} \end{pmatrix} \tag{5.3}$$

which is related to our tensor through $\mathbf{n}_i = \mathbf{Q}_i - \frac{1}{3}\mathbf{I}$ where $\mathbf{I}$ is the 3×3 identity matrix [460].

The magnetic domains that form topologically protected states exist on the mesoscopic level but emerge purely from microscopic interactions [167], thus only local interactions need to be considered. We begin by subjecting quadrupoles to analogous interactions too those laid out in Eqn. 5.1 for chiral magnets, forming a chiral quadrupolar system:

$$\hat{\mathcal{H}} = -\hat{J}\sum_{ij} \mathbf{Q}_i : \mathbf{Q}_j - \hat{K}\sum_{ij} (\mathbf{Q}_i * \mathbf{Q}_j) \cdot \mathbf{r}_{ij} + \hat{A}\mathbf{E} : \sum_i \mathbf{Q}_i, \tag{5.4}$$

where $\mathbf{r}_{ij}$ is the vector between the two neighbouring sites i, j, $\hat{J}$ is the strength of symmetric interaction, $\hat{K}$ is the strength of the antisymmetric interaction arising from the underlying chirality of the lattice, and $\hat{A}$ is the strength of the applied strain field $\mathbf{E}$. Below we describe each of the terms in Eqn. 5.4.

Instead of a Heisenberg interaction between neighbouring spins, there is a quadrupolar coupling defined by the inner product:

$$\mathbf{Q}_i : \mathbf{Q}_j = \mathrm{Tr}(\mathbf{Q}_i \mathbf{Q}_j^{\mathrm{T}}). \tag{5.5}$$

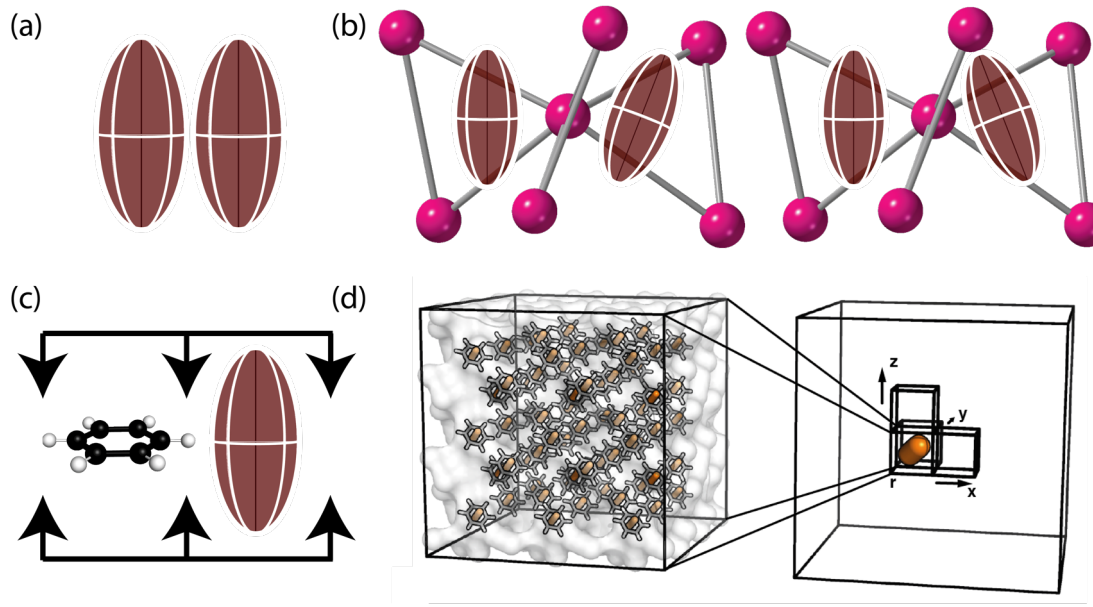

Figure 5.5: Quadrupolar interactions analogous to those seen in magnetic skyrmions with the brown oval representing the quadrupolar moment of a molecule. (a) Ferroquadrupolar interaction in a low energy configuration. (b) Low (left) and high (right) energy configurations of the antisymmetric interactions mediated by the chiral framework. (c) Quadrupolar coupling of a benzene ring to a strain field represented by the black arrows. (d) Coarse graining of the configurations by mapping the average orientation of guest molecules within a finite volume onto a single degree of freedom represented by an orange bar on the right. Hence any emerging textures from our coarse grained simulations involve lengthscales that are orders of magnitude greater than the distances between neighbouring guest molecules.

As our quadrupolar tensors are symmetric, the inner product is also symmetric where

$$\mathbf{Q}_i : \mathbf{Q}_j = \mathbf{Q}_j : \mathbf{Q}_i. \tag{5.6}$$

Therefore, this term represents symmetric exchange and if $\hat{J} > 0$ then the quadrupoles preferentially align (ferroquadrupolar), reaching an energy maximum when the quadrupoles lie perpendicular to one another (antiferroquadrupolar) [Fig. 5.5(a)].

The second term is an antisymmetric term analogous to the Dzyaloshinskii-Moriya interaction and was derived to give a 'quadrupole cross product' by defining

a new function, $\mathbf{u} = \mathbf{Q}_i * \mathbf{Q}_j$. The key mathematical requirements of this function are that $\mathbf{u} = \mathbf{Q}_i * \mathbf{Q}_j = -\mathbf{Q}_j * \mathbf{Q}_i$, $\mathbf{u}$ is a vector which describes the angle between the quadrupoles orientations, and $\mathbf{Q}_i * \mathbf{Q}_j$ is invariant under inversion of $\mathbf{S}_i$ or $\mathbf{S}_j$. The elements of the vector $\mathbf{u}$ are given explicitly as

$$u_\alpha = \sum_{\beta=1}^{3} (Q_{i\alpha'\beta} Q_{j\alpha''\beta} - Q_{i\alpha''\beta} Q_{j\alpha'\beta}) \tag{5.7}$$

where $\alpha \in \{1, 2, 3\}$, and $\alpha = 1 \implies \alpha' = 2, \alpha'' = 3$, *etc.* Expanding this quadrupolar cross product in terms of the underlying vector spin components $s_{i\alpha}$, we have

$$\mathbf{u} = \begin{bmatrix} u_x \\ u_y \\ u_z \end{bmatrix} = \begin{bmatrix} s_{ix}s_{iy}s_{jx}s_{jz} + s_{iy}^2 s_{jy}s_{jz} + s_{iy}s_{iz}s_{jz}^2 - s_{ix}s_{iz}s_{jx}s_{jy} - s_{iy}s_{iz}s_{jy}^2 - s_{iz}^2 s_{jy}s_{jz} \\ s_{ix}s_{iz}s_{jx}^2 + s_{iy}s_{iz}s_{jx}s_{jy} + s_{iz}^2 s_{jx}s_{jz} - s_{ix}^2 s_{jx}s_{jz} - s_{ix}s_{iy}s_{jy}s_{jz} - s_{ix}s_{iz}s_{jz}^2 \\ s_{ix}^2 s_{jx}s_{jy} + s_{ix}s_{iy}s_{jy}^2 + s_{ix}s_{iz}s_{jy}s_{jz} - s_{ix}s_{iy}s_{jx}^2 - s_{iy}^2 s_{jx}s_{jy} - s_{iy}s_{iz}s_{jx}s_{jz} \end{bmatrix}, \tag{5.8}$$

giving the relationship

$$\mathbf{Q}_i * \mathbf{Q}_j = \mathbf{S}_i \cdot \mathbf{S}_j (\mathbf{S}_i \times \mathbf{S}_j). \tag{5.9}$$

This term encompasses the chirality of the system as $\mathbf{Q}_i * \mathbf{Q}_j = -\mathbf{Q}_j * \mathbf{Q}_i$ and is invariant under pseudospin inversion $\mathbf{S}_i \to -\mathbf{S}_i, \mathbf{S}_j \to -\mathbf{S}_j$ as required. If $\hat{K} > 0$, then the overall energy decreases when the quadrupole at site j is rotated in one direction relative to its neighbour at site i but increases when it is rotated in the opposite direction [Fig. 5.5(b)]. Whereas the Dzyaloshinsky-Moriya interaction is minimised by a 90° clockwise rotation around the axis between the two sites i, j, this term is minimised when the quadrupole at site j is rotated 45° from the neighbouring

quadrupole at site i in a clockwise direction.

The last term in Eqn. 5.4 represents the coupling to an external field. For magnetic spins, the degrees of freedom couple to a magnetic field whereas the molecular orientations are unaffected by a magnetic field. Instead, the quadrupolar moments represented couple to a strain field:

$$\mathbf{E} = \begin{pmatrix} +\frac{\epsilon}{2} & 0 & 0 \\ 0 & +\frac{\epsilon}{2} & 0 \\ 0 & 0 & -\epsilon \end{pmatrix}, \tag{5.10}$$

as it is a conjugate field and quadrupoles arise from physical shape, hence the mechanical interaction. This results in the molecules aligning or anti-aligning to the field depending on the shape of the molecule [Fig. 5.5(c)].

Due to skyrmions emerging on a lengthscale fundamentally removed from that of the underlying microscopic interactions, the convention is to coarse-grain to the Hamiltonian by assuming a slow variation in the textures [166, 167]:

$$\begin{aligned} \hat{\mathcal{H}} = & - J \sum_{\mathbf{r}} \mathbf{Q}_r : (\mathbf{Q}_{\mathbf{r}+\mathbf{x}} + \mathbf{Q}_{\mathbf{r}+\mathbf{y}} + \mathbf{Q}_{\mathbf{r}+\mathbf{z}}) \\ & - K \sum_{\mathbf{r}} [(\mathbf{Q}_r * \mathbf{Q}_{\mathbf{r}+\mathbf{x}}) \cdot \mathbf{x} + (\mathbf{Q}_r * \mathbf{Q}_{\mathbf{r}+\mathbf{y}}) \cdot \mathbf{y} + (\mathbf{Q}_r * \mathbf{Q}_{\mathbf{r}+\mathbf{z}}) \cdot \mathbf{z}] \\ & + A\mathbf{E} : \sum_{\mathbf{r}} \mathbf{Q}_r, \end{aligned} \tag{5.11}$$

thereby allowing us to use a lattice Hamiltonian instead of accounting specifically

for the geometry of the chiral system. Here $\mathbf{Q}_r$ represents the average quadrupolar moment of a section of the underlying structure [Fig. 5.5(d)]. Through this, the exact details of the underlying symmetry of the material become unimportant, as long as they are chiral. The values used in the lattice Hamiltonian, J, K, and A are directly proportional to $\hat{J}$, $\hat{K}$, and $\hat{A}$ [167]. To account for anisotropic contributions caused by coarse graining to the lattice Hamiltonian, second nearest neighbour interactions must be considered to give a better approximation of the continuum field theory [167] such that:

$$\hat{\mathcal{H}}_{MC} = \hat{\mathcal{H}} + \hat{\mathcal{H}}_2 \tag{5.12}$$

where

$$\begin{aligned}\hat{\mathcal{H}}_2 =& J_2 \sum_{\mathbf{r}} \mathbf{Q}_r : (\mathbf{Q}_{\mathbf{r}+2\mathbf{x}} + \mathbf{Q}_{\mathbf{r}+2\mathbf{y}} + \mathbf{Q}_{\mathbf{r}+2\mathbf{z}}) \\ &+ K_2 \sum_{\mathbf{r}} [(\mathbf{Q}_r * \mathbf{Q}_{\mathbf{r}+2\mathbf{x}}) \cdot \mathbf{x} + (\mathbf{Q}_r * \mathbf{Q}_{\mathbf{r}+2\mathbf{y}}) \cdot \mathbf{y} + (\mathbf{Q}_r * \mathbf{Q}_{\mathbf{r}+2\mathbf{z}}) \cdot \mathbf{z}]\end{aligned} \tag{5.13}$$

Here $J_2 = J/16$, $K_2 = K/8$ [167], so as to cancel out the second order momentum terms which are determined by Taylor expansion resulting in even powers for J (as the symmetric term is cosinusodial) and odd powers for K (as the antisymmetric term is sinusodial).

5.4 Monte Carlo simulations

So far we have set up a classical Hamiltonian governing the interactions between quadrupoles that contains the ingredients thought to generate non-trivial textures. Now we aim to test our theory by determining the phase behaviour of the Hamiltonian [Eqn. 5.12] using MC simulations to produce representative configurations as a function of the three interaction parameters and temperature. A custom MC code was used to generate the quadrupole orientations of a coarse grained chiral MOF with quadrupolar guests. Simulations were performed using a $10 \times 10 \times 10$ supercell of the simple cubic lattice with one quadrupole—where each quadrupole represented the collective orientation of a volume of multiple MOF unit cells—per unit cell (*i.e.* 1000 quadrupoles per configuration) with periodic boundary conditions applied. Simulations were started at $T_i = 0.7$ and cooled by $T_{i+1} = T - 0.02$ until $T_f = 0.02$ for constant K' and A' where $K' = K/J$, $A' = A\epsilon/J$. These simulations showed no significant variation with temperature and thus a two-dimensional phase map is sufficient to encapsulate the phase behaviour [Fig. 5.6(a)].

Each MC move involved a random reorientation of a randomly chosen quadrupole, and was accepted or rejected according to the standard Metropolis criterion. The number of MC steps required to reach equilibration was determined by an autocorrelation function where we discarded ten times as many moves as were required for the system to become uncorrelated from its initial state. At very low temperatures, and high strains, equilibration became difficult and instead configurations were collected after a suitably large number of moves. By analogy to the simulations performed in

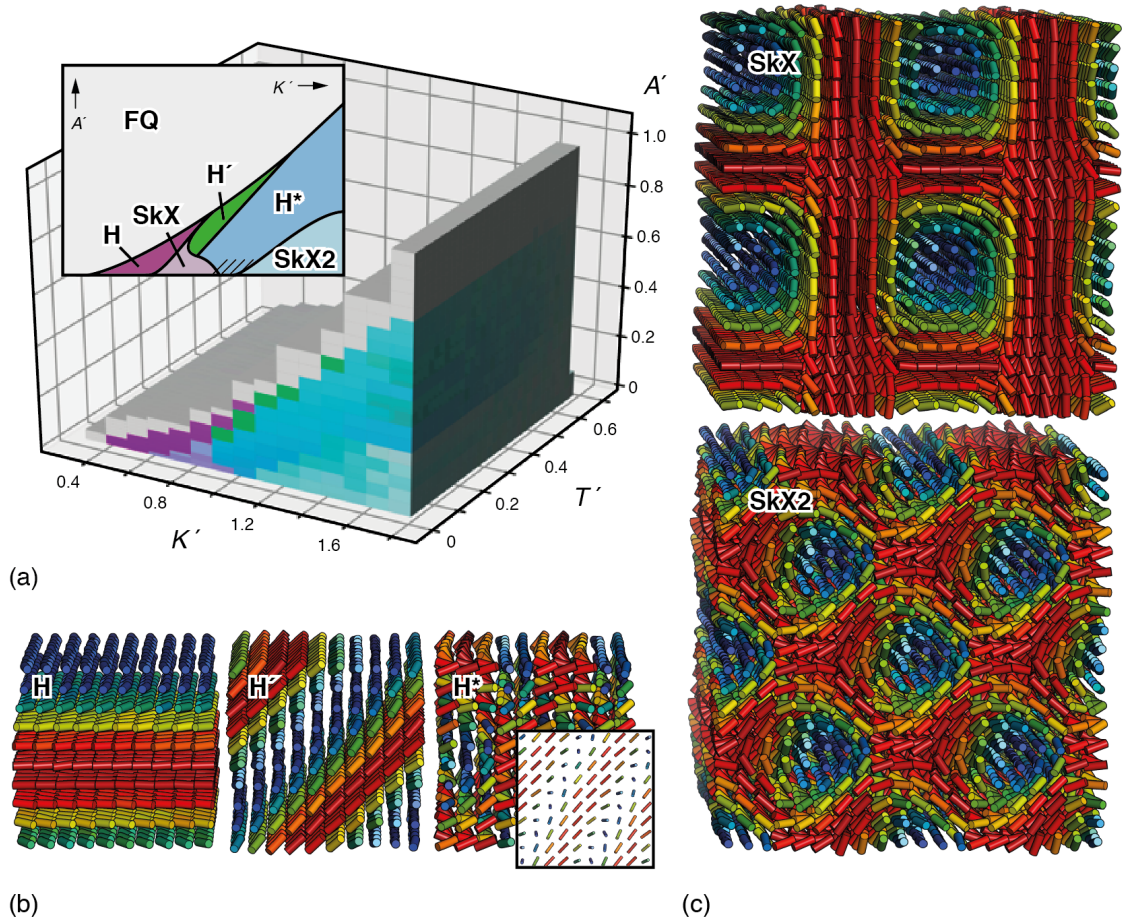

Figure 5.6: (a) Phase diagram as a function of relative antisymmetric interaction strength (K'), applied strain (A'), and simulation temperature (T'). The RGB values in the phase diagram were determined through the small angle scattering of the resulting MC simulations. The phase behaviour has very little effect with temperature and so a 2D representation of low temperature behaviour encapsulates the Hamiltonian phases (inset). (b) View along the c-axis of the three helical phases which differ due to their axes of propagation. (c) The two skyrmion crystal phases which differ in their density of skyrmions. Here we have shown a $2 \times 2 \times 2$ supercell of the simulation cell to highlight the square lattice on which the skyrmion cores sit. The colour of the quadrupoles in each configuration is determined by their orientation.

Ref. [167], we also carried out MC simulations at constant K' and T' with varying A' but equilibration was substantially more difficult in this case [Appendix E.1].

5.4.1 Phase determination

By using Fourier transforms, we were able to identify six different phases from their small angle scattering [Fig. 5.7], as shown in Figure. 5.6. At high strains or low K', the system is ferroquadrupolar as there is a collective alignment of all molecular orientations along the strain direction (for rod molecules) or perpendicular to the strain direction (for planar molecules). Below a critical line in A', K'-space the phase behaviour is dominated by helical states where the quadrupole precesses around a single propagation vector $\mathbf{k} \in \langle 100 \rangle^*$ (H), $\langle 110 \rangle^*$ (H$'$) or a pair of propagation vectors $\mathbf{k}_1, \mathbf{k}_2 \in \langle 210 \rangle^*$ that alternate along [001] (H*). These helical states are closely related to those found in a variety of chiral magnets [176, 185] where the different helical phases are accessed by tuning the anisotropy of the interaction strengths whereas here we can access these states by isotropically changing K' and A'.

The main results from the simulations lie in the behaviour at low A' with varying K', where two topologically non-trivial phases containing skyrmions exist: SkX and SkX2. The key difference between these two phases is their skyrmion density where SkX (SkX2) has one (two) skyrmion(s) per MC box. In our simulations, both phases form square lattices instead of the typical hexagonal lattice seen in magnetic skyrmions [165]. This is likely due to the limiting box size of our simulations as one/two cores per unit cell have no choice but to form a square lattice, and larger box sizes may show a continuous evolution of skyrmion density and accommodate other lattice geometries like triangular packing. Larger box sizes ($20 \times 20 \times 20$ and $30 \times 30 \times 30$) were simulated, however the energies per unit cell were much larger than that for the $10 \times 10 \times 10$ system and we concluded that equilibration was unable

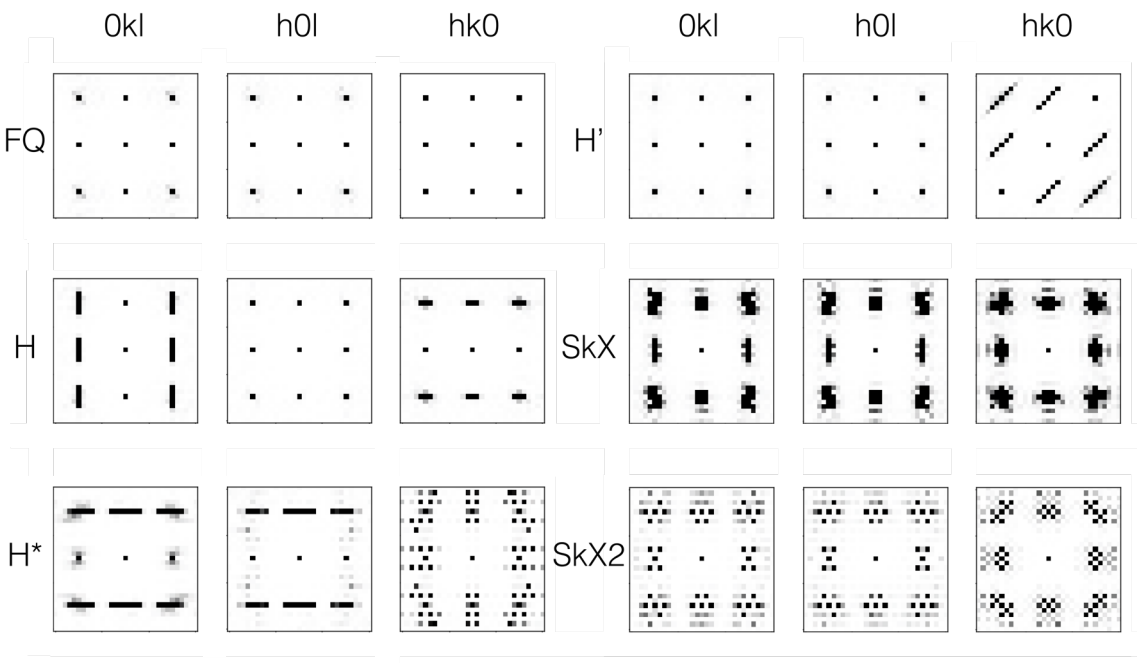

Figure 5.7: Representative small-angle scattering planes of the $I(\mathbf{q})$ function from the six different phases. The field of view corresponds to the regions of reciprocal space $-1.5 \leq h, k, l \leq 1.5$.

to be properly reached.

To identify the various phases, the outputted configurations from MC simulations were converted to Crystallographic Information Files (CIFs) which contained five identical scattering objects evenly distributed along the quadrupole axis. The Fourier transform of the resulting configurational data were then taken, generating a small-angle scattering function $I(\mathbf{q})$ which was reduced to three two-dimensional scattering cuts perpendicular to each of the crystal axes [Fig. 5.7]. These scattering data were averaged over the first Brillouin zone and normalised such that:

$$I_{\mathbf{m}}(\mathbf{k}) = \alpha \sum_{\mathbf{G}} I(\mathbf{G} + \mathbf{k}) \tag{5.14}$$

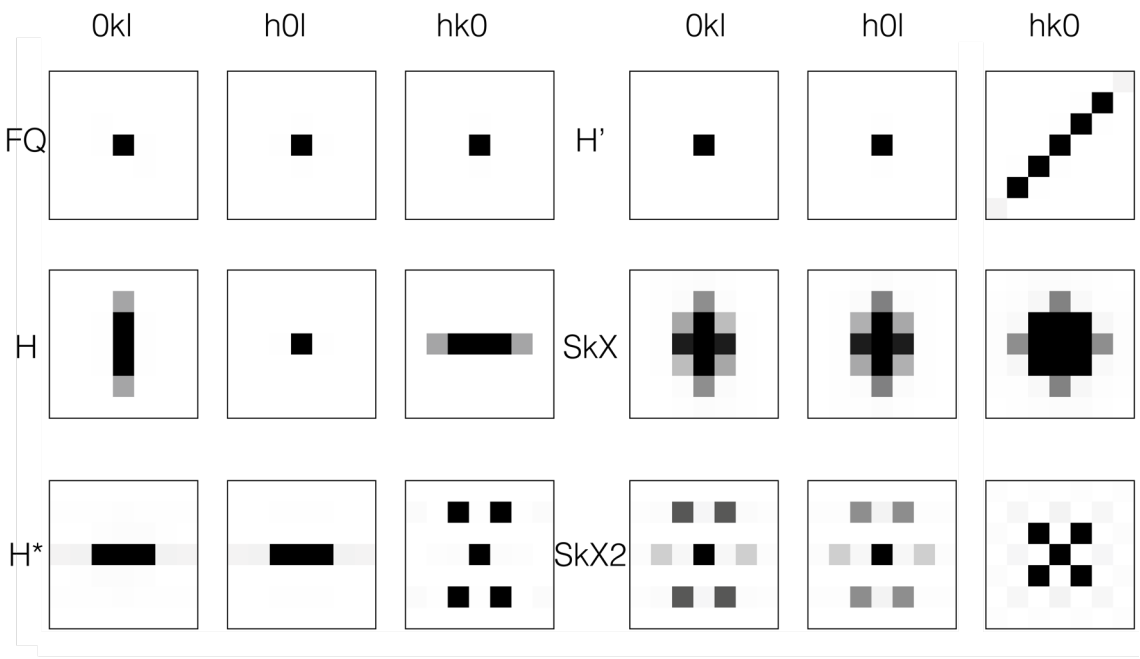

Figure 5.8: The averaged scattering planes as defined by $I_{\mathbf{m}}(\mathbf{k})$ for the six different phases. The field of view corresponds to the regions of reciprocal space $-0.5 \leq h, k, l \leq 0.5$.

where $\mathbf{m} = \mathbf{a}, \mathbf{b}, \mathbf{c}$ and $\mathbf{G}$ is a reciprocal lattice vector lying in the relevant plane of reciprocal space ($\in \{(0,-1,-1)^*, ..., (0,1,1)^*\}, \{(-1,0,-1)^*, ..., (1,0,1)^*\}$, $\{(-1,-1,0)^*, ..., (1,1,0)^*\}$. Here, α is a scaling factor chosen such that the maximum value of $I_{\mathbf{m}} = 1$ and $\mathbf{k} \perp \mathbf{m}$ is a scattering vector contained within the first Brillouin zone. These functions were evaluated across a 7×7 grid in reciprocal space with the central pixel corresponding to the centre of the Brillouin zone [Fig. 5.8]. These scattering values informed the colour of the phases set in the phase diagram [Fig. 5.6(a)] by splitting the scattering data into sections dependent on the on-axis and off-axis components. For each function, the on-axis scattering was contained within the 13 pixels corresponding to $\mathbf{k}$-values parallel to at least one unit cell vector [Fig. 5.9(a)]. Due to the scaling by $\max(I_{\mathbf{m}})$, the central pixel ($\mathbf{k} = 0$) always has unit intensity and the remaining 12 pixels were split into two parts, corresponding to

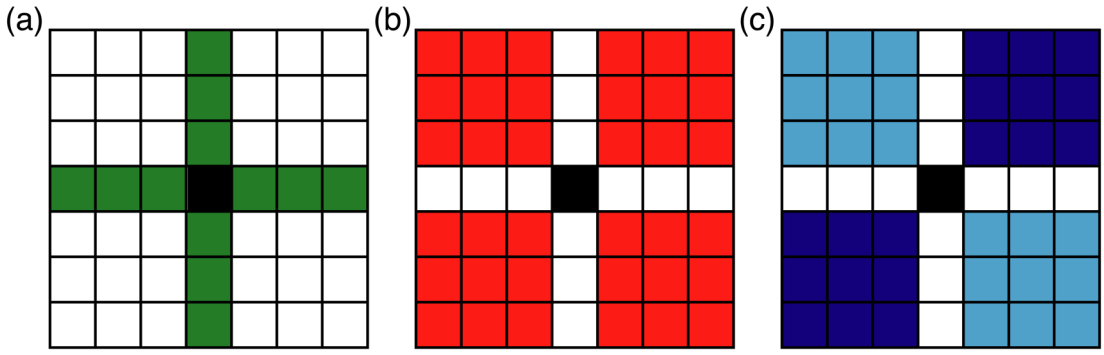

Figure 5.9: Scattering data split into three different components. Pixels which make up (a) I_{on} which informs the green component, (b) I_{off} which informs the red component, (c) I_{off}^{+} (dark blue) and I_{off}^{-} (light blue) which inform the blue component of the colour of the phases. The central pixel at $\mathbf{k} = 0$ is shown in black.

the two reciprocal axes, and summed. I_{on} is set as the maximum on-axis scattering across the six summed values from three mutually perpendicular scattering plane with two directions each [Fig. 5.9(a)], and I_{off} as the maximum off-axis scattering [Fig. 5.9(b)]. The off-axis scattering was subdivided into two component I_{off}^{+} and I_{off}^{-} corresponding to the scattering contained within the two sets of diagonal fields (*e.g.* $k_x k_y > 0, k_x k_y < 0$) [Fig. 5.9(c)]. The red (r), green (g), and blue (b) values were then produced by:

$$r = 1 - 3I_{\text{off}} \tag{5.15}$$

$$g = 1 - 2I_{\text{on}} \tag{5.16}$$

$$b = 1 - \frac{3}{2}|I_{\text{off}}^{+} - I_{\text{off}}^{-}|. \tag{5.17}$$

This novel approach was designed for automatic phase determination and representative small-angle scattering planes of the six different phases are shown in Fig. 5.8.

5.5 *Ab initio* techniques

Through the results presented so far, we have shown a MOF governed by Eqn. 5.12 can in principle host SkX phases. The question now is whether the Hamiltonian [Eqn. 5.12] is at all relevant to MOFs. With this in mind, it is important to identify candidate materials that could host these phases. In using the Hamiltonian set out in Eqn. 5.11, we have already created criteria the material must follow; the MOF must have a chiral architecture and contain quadrupolar guests. In absence of a MOF known experimentally to support skyrmions, we chose to study a model system that at once captures the key flavours of our anticipated design rules, whilst also allowing AIMD simulations to be computationally tractable (small unit cell, high symmetry, closed-shell configuration). For these reasons we have focused on the hypothetical, but chemically sensible, analogue of $Na[Mn(HCOO)_3]$ in which the open-shell Mn^{2+} ion is replaced by closed-shell Al^{3+}, the formate linker replaced by the slightly-extended azide anion (N_3^-) to open up the pore network [461], and the guest Na^+ ions replaced by planar benzene molecules that now fit in the larger pores. Hence our model system has the formula $[Al(N_3)_3]\cdot C_6H_6$ [Fig. 5.10] and is characterised by the same chiral space group symmetry ($P2_13$) as $Na[Mn(HCOO)_3]$ and MnSi.

5.5.1 DFT calculations

Quantum chemical calculations were performed to confirm the stability and monitor the behaviour of $[Al(N_3)_3]\cdot C_6H_6$ under strain. DFT calculations were used first to optimise geometry, and then calculate its elastic tensor at 0 K which was inputted

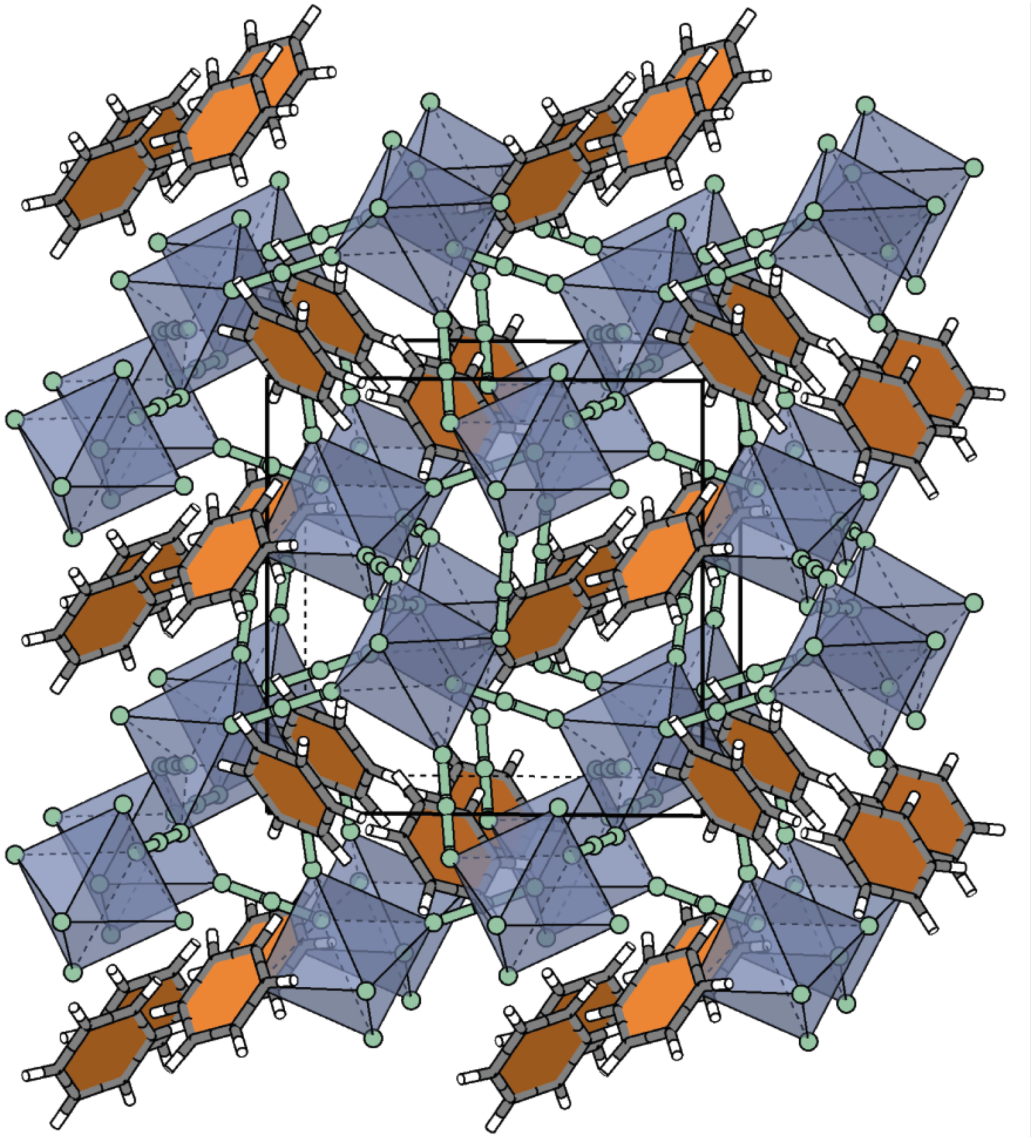

Figure 5.10: Representation of the relaxed structure of $[Al(N_3)_3]\cdot C_6H_6$ determined using DFT. Al co-ordination polyhedra shown in blue, azide links in green, and benzene molecules in grey, white and orange.

into ELATE [462] to determine the elastic properties [Table. 5.1]. All calculations were performed with the CRYSTAL14 software [319] using the PBE exchange correlation functional [304] and double-ζ plus polarization basis sets were used for all atoms. A modified Broyden [463] scheme was implemented as laid out in the CRYSTAL17 manual [464] to help with convergence by using Fock matrix mixing. The convergence criteria for geometry optimisation were the default values set

Averaging scheme	Bulk modulus (GPa)	Young's modulus (GPa)	Shear modulus (GPa)	Poisson's ratio
Voigt	28.587	24.570	9.0548	0.35675
Reuss	28.587	23.527	8.6317	0.36283
Hill	28.587	24.050	8.8432	0.35979

Table 5.1: Elastic properties determined from DFT results for the relaxed structure of $[Al(N_3)_3]\cdot C_6H_6$.

out by CRYSTAL17 (Maximum gradient 0.0045a.u., root mean squared gradient of 0.0030a.u., maximum displacement 0.0018a.u., and root mean squared displacement of 0.0012a.u.) and reciprocal space was sampled with a $3 \times 3 \times 3$ **k**-point mesh.

A representative input file that includes all relevant control parameters, together with the crystallographic details of the relaxed structure are provided in Appendix F and Appendix E.1 respectively and shown in Fig. 5.10. These calculations show the relaxed structure is energetically and mechanically stable, even when subjected to large strains.

5.5.2 *Ab initio* molecular dynamics simulations

The behaviour of the $[Al(N_3)_3]\cdot C_6H_6$ framework as a function of temperature and strain was studied by means of DFT based MD simulations with the CP2K software package [341]. Starting from the geometry optimised structure, we carried out AIMD simulations by employing the hybrid Gaussian and plane-wave method GPW as implemented in the Quickstep module in CP2K. Again, the PBE exchange correlation functional [304] was used, along with DZVP-GTH-PADE basis sets. The simulations were performed in the constant-volume (N, V, T) ensemble with fixed size and shape of the unit cell, and with periodic boundary conditions. A timestep

of 0.5 fs was used, and the AIMD simulations consisted of an equilibration period of 10 ps (20000 steps) to determine the energy as a function of temperature and strain. We chose the plane-wave cut-off for the electronic density to be 750 Ry and a relative cut-off of 60 Ry for high accuracy, after checking that the energy converged at these values. A representative input file is provided in Appendix F.

Our AIMD simulations were carried out for a range of temperatures $10 - 300\,\mathrm{K}$ and uniaxial strains $0 - 7\%$ using a single $P2_13$ $[Al(N_3)_3]{\cdot}C_6H_6$ unit cell (containing four formula units) with periodic boundary conditions applied. From analysing the energy of the outputted configurations, equilibrium was determined to be reached after 3 ps (6000 steps) and post-equilibrium configurations were analysed using tensors to determine the four benzenes quadrupolar orientations [Fig. 5.11]. Custom code was implemented to map the coordinates of each outputted configuration onto the quadrupole orientations.

For each of the four benzene molecules per unit cell, the centre of the molecule was determined by averaging the positions of the carbons within the ring. To generate the quadrupole orientation, we took the normalised cross product of two carbon-centre vectors that define the plane containing the benzene molecules, producing $\mathbf{S}_i$. From this we were able to generate the quadrupolar tensor $\mathbf{Q}_i$, given in equation Eqn. 5.2, and therefore track the quadrupolar moment from the benzene molecule's orientation with the AIMD simulations. The orientations were shown to fluctuate more strongly at high temperatures and align more strongly with the field at larger strains, as expected [Fig. 5.12]. From the configurations, we calculated corresponding pair-wise interactions of $\sum_{ij} \mathbf{Q}_i : \mathbf{Q}_j$, $\sum_{ij} (\mathbf{Q}_i * \mathbf{Q}_j) \cdot \mathbf{r}_{ij}$, and $\mathbf{E} : \sum_i \mathbf{Q}_i$ for the four

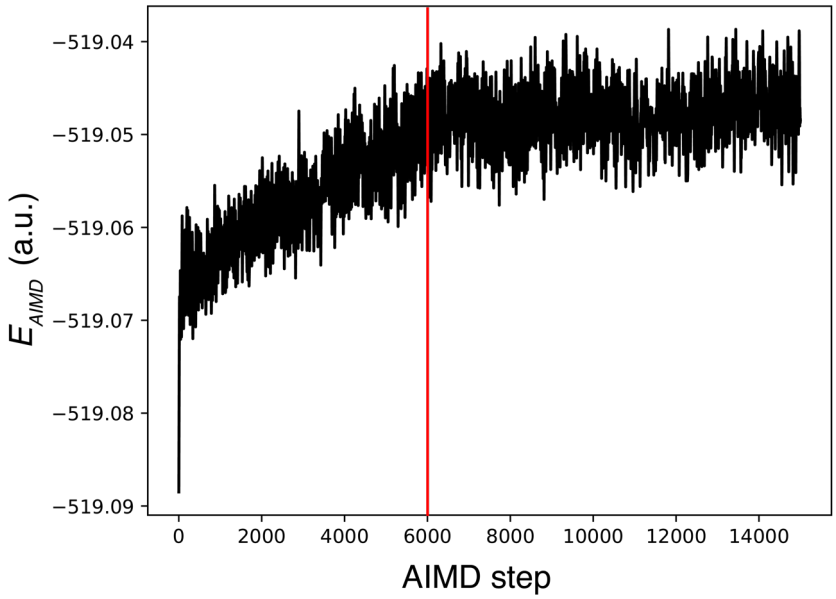

Figure 5.11: Total energy against time for 15000 steps of the AIMD simulation where $T = 100\,\mathrm{K}$ with no strain field. The red line indicated the time allowed for equilibration, after which the system was considered equilibrated and used in the averaging measurements.

benzene molecules and calculated E_{CG}:

$$E_{CG} = E_0 - \hat{J}\sum_{ij}\mathbf{Q}_i : \mathbf{Q}_j - \hat{K}\sum_{ij}(\mathbf{Q}_i * \mathbf{Q}_j)\cdot\mathbf{r}_{ij} + \hat{A}\mathbf{E} : \sum_i \mathbf{Q}_i. \tag{5.18}$$

given a set of $\hat{J}, \hat{K}, \hat{A}$.

From the post-equilibrium AIMD configurations, at each temperature and strain, we used a linear least squares minimisation to identify the values of the interaction parameters outlined in Eqn. 5.18, corresponding to our fictitious MOF $[Al(N_3)_3]\cdot C_6H_6$. This minimisation optimised the goodness of fit:

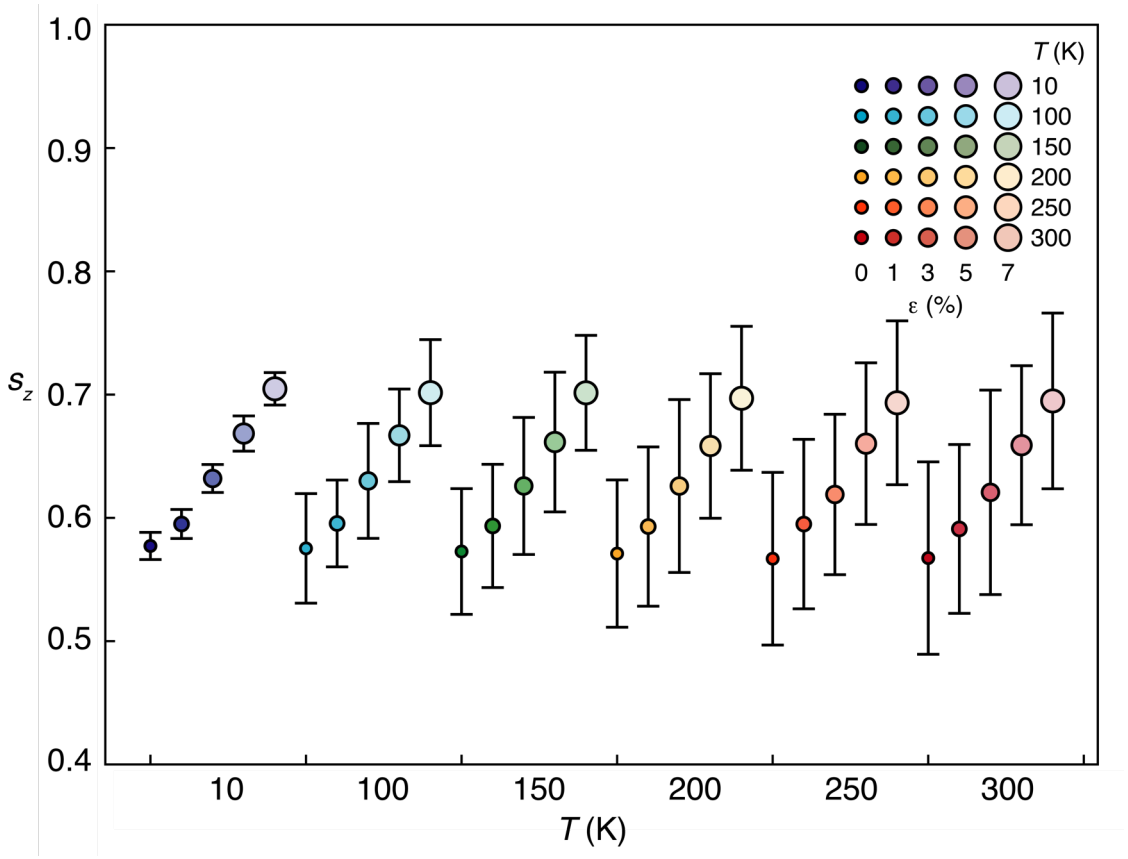

Figure 5.12: Fluctuation of s_z, where each quadrupole is defined by the axis $\pm(s_x, s_y, s_z)$, at different temperatures and strains evidencing more fluctuation of the molecular orientation with increasing temperature. With increasing strain the molecules orientation aligns stronger with the field (strain field being along the z axis) evidenced by the larger value of s_z.

$$\chi^2 = \sum_{T,\epsilon} \left[\frac{\langle E_{AIMD} \rangle (T,\epsilon) - \langle E_{CG} \rangle (T,\epsilon)}{\sigma(T,\epsilon)} \right]^2 \tag{5.19}$$

where the averages were taken for all equilibrium configurations at constant T, ϵ and the uncertainty σ is given by the corresponding standard deviation in energy. The interactions can therefore be parameterised as the energy of the Hamiltonian is monitored. This gave $\hat{J} = -584.16$kJ/mol, $\hat{Kr} = 66.264$kJ/mol, $\hat{A} = 5477.9$kJ/mol for the energy of one asymmetric unit (*i.e.* one benzene molecule in a pore) with $R^2 = 0.6175$. These interaction strengths are larger than for benzene molecules

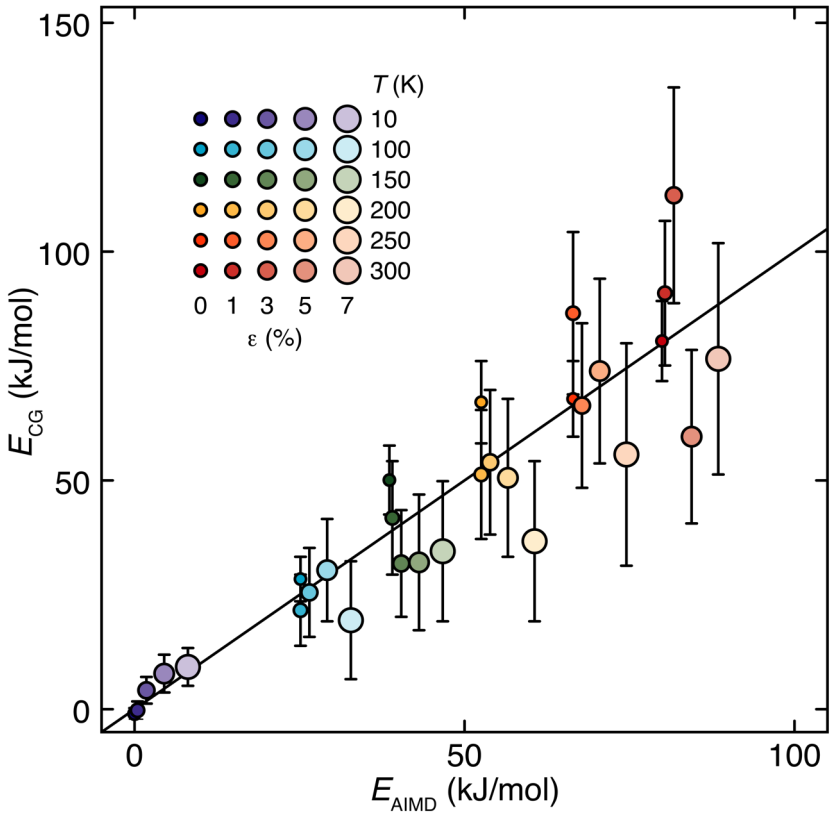

Figure 5.13: Match between coarse-grained and AIMD configurational energies as a function of simulation temperature (symbol colour) and applied strain (symbol size). The solid line shows the relation $E_{CG} = E_{AIMD}$. The key result is that our data cluster around the line, reflecting the ability of the coarse grained Hamiltonian (Eqn. 5.11) to capture the key thermodynamics of this representative phase at low temperatures and small applied strains.

alone, which is to be expected due to the mediation of the host framework [465]. $\hat{K}r$ is the smallest value as expected as it is a measure of the coupling of the benzene rings to the framework [422], $\hat{J}$ is a degree of magnitude larger due to the distortion of bonds within the framework required for the reorientation of benzene rings [466], and finally $\hat{A}$ is the largest as it is essentially a measure of how easy it is to compress the entire crystal, expected to require a lot of energy [467].

The match between calculated and AIMD simulation energies relative to the ground state energy are shown in Fig. 5.13 and the corresponding data for the four

T (K)	ϵ (%)	E_{AIMD} (kJ/mol)	E_{CG} (kJ/mol)
10	0	0.00(2)	1.0(11)
100	0	24.69(15)	29(5)
150	0	38.5(2)	50(7)
200	0	52.2(3)	67(9)
250	0	66.0(4)	68(8)
300	0	79.7(4)	80(9)
10	1	0.17(2)	0(2)
100	1	24.93(16)	22(8)
150	1	38.8(2)	42(12)
200	1	52.4(3)	51(14)
250	1	66.2(4)	87(18)
300	1	79.9(4)	90(16)
10	3	1.51(2)	4(3)
100	3	26.23(16)	25(10)
150	3	40.0(2)	32(12)
200	3	53.7(3)	54(16)
250	3	67.6(4)	66(18)
300	3	81.2(4)	112(24)
10	5	4.12(2)	8(4)
100	5	28.97(17)	30(11)
150	5	42.6(2)	32(15)
200	5	56.3(3)	51(17)
250	5	70.1(4)	74(20)
300	5	84.1(4)	59(19)
10	7	7.94(2)	9(4)
100	7	32.67(15)	19(13)
150	7	46.5(2)	34(15)
200	7	60.2(3)	37(18)
250	7	74.1(4)	56(24)
300	7	88.0(4)	76(25)

Table 5.2: Data graphically depicted in Fig. 5.13 of the energy of $[Al(N_3)_3]\cdot C_6H_6$, relative to the lowest energy configuration, during from molecular dynamics simulations (E_{AIMD}) with changing temperature and strain, compared to calculated energy (E_{CG}) from the corresponding AIMD configurations.

benzenes within a unit cell is given in Table. 5.2. Although R^2 is slightly low, the agreement is still remarkable as the coarse graining maps the $3N-3 = 261$ positional degrees of freedom from the simulation onto just eight from the orientation of each of the four quadrupoles and so is more of an approximation than for $Ni(CN)_2$ in

Chapter 4. Also, as anticipated, the fit gets worst with increasing temperature and strain as more degrees of freedom are activated, not accounted for by our model. The key take away point is that the Hamiltonian is a good first order representation of the thermodynamic behaviour of this model MOF system. This result implies that the host framework imposes a non-trivial antisymmetric coupling between neighbouring guests and, as such, MOFs may have the potential to harbour complex topological phases.

5.6 Outlook

In this chapter we have shown the capacity of chiral MOFs to host skyrmions. MC simulations show that quadrupolar interactions can lead to topologically protected structures and AIMD simulations have identified a MOF system whose energetics can be described *via* the terms in the Hamiltonian. Unfortunately, our model system $[Al(N_3)_3]\cdot(C_6H_6)$ is unlikely to host skyrmions as, were it able to be synthesised, our molecular dynamics simulations show that the symmetric interaction parameter, $\hat{J}$, is negative, leading to antiferroquadrupolar order which cannot lead to a skyrmionic texture. However, there are a whole host of chiral frameworks, not limited to MOFs alone, which could host quadrupolar molecules that contain ferroquadrupolar interactions. For example, in some MOFs the balance between ferro- and antiferro-quadrupolar order can be changed simply though varying the ionic radius [454] and thus this is an avenue worth exploring. Moreover, the chemical aptitude of other porous materials with chiral architecture have yet to be explored, including covalent organic frameworks [468] and zeolites [469, 470].

This study highlights the benefits of analysing small-angle scattering data of chiral frameworks with quadrupolar guests. In some cases, the skyrmion may even emerge on a periodicity commensurate with visible light and optical Bragg scattering may be visible, as in liquid crystals [471]. If so, a colour change would be direct experimental evidence of skyrmion formation and may form the basis for sensing materials, whereas magnetic skyrmions tend to form on the lengthscale of 100 nm to 1 μm [164]. The physical realisation of skyrmionic textures within chiral frameworks could lead to new pathways for data storage at less experimentally demanding temperatures. The problem here is figuring out how best to manipulate individual skyrmions—a challenge also found in the magnetic community [171].

From a theoretical perspective, our model may prove too simplistic, especially when considering increasingly complex chiral systems. No long-range terms or other short-range interactions have been taken into account, which may prove unavoidable when applying the theory to real systems. We can also not rule out the substantial effect that finite size effects may play in our simulations. Although we expect size effects to not alter the existence of the phases, they may persist in a substantially smaller area of phase space, leading to issues when using our model for targeted phase exploration. In this respect, there is plenty of scope for further refinement of the model, but our results nonetheless suggest that topological textures may exist in a broad class of materials not normally associated with emergent phenomena.

Chapter 6

Conclusions and future outlook

The research contained in this thesis highlights the importance of using statistical mechanical models to develop the link between magnetic and structural degrees of freedom. Mappings reported throughout the thesis have not only increased our understanding of potentially industrially important materials, but have also laid the pathway for the discovery of emergent phenomena in new materials.

In Chapter 3 we showed that by using simple statistical mechanical models, we can explain complicated polytypic behaviour of functional materials. This allows us to describe, and more importantly predict, phases spanned by solid solutions of $A_xM_{1-x}B_yX_{2-y}$ by relating the compositions of end members to interaction parameters, and navigating the phase space between them. Now that we have identified the key interactions responsible for phases, the goal is to link these interactions to the unique properties of the AB_2 compounds, creating clear design rules for property manipulation. The advent of the new nomenclature may also prove fruitful in explaining polytypic behaviour in other disparate materials, as a way to fully encapsulate the phase behaviour, and also predict phase stability and aid characterisation.

In Chapter 4 we classified stacking within a material with continuous structural degrees of freedom and explored the significance of classical analogues of quantum models for classical materials. This result may not be unique to $Ni(CN)_2$ and other disordered layered materials such as graphene or $(BN)_x$ may draw on other contin-

uous 1D statistical mechanical models to describe their stacking. Layered materials could provide a whole host of classical analogues to quantum models.

Chapter 5 highlights the potential existence of analogues to topological magnetic phases in structural materials. Additionally, the formation of topological defects in these systems may have increased functionality due to their difference in length scale, with sensing applications found in cholesteric liquid crystal phases being the most apparent.

The ubiquity of statistical mechanical models in condensed matter physics underpins our theoretical understanding of magnetic phases. The theory from this area of condensed matter physics is rich and drawing from it to explain structural behaviour can lead to the unearthing of a vast array of emergent phenomena which may otherwise remain unexplored. Other exotic phases such as charge density waves arising from electronic degrees of freedom may also have analogues in structural phases through degrees of freedom such as occupational density.

From a crystallographic point of view, many of the phases discussed will appear disordered but, as highlighted throughout the thesis, there could be a wealth of physics hidden within these phases. It is feasible that many already synthesised materials may contain interesting underlying physics but have been overlooked due to the relative difficulty of understanding and characterising disorder. We hope the work outlined in this thesis truly highlights the importance of creating these mappings, not just as means for increased scientific understanding, but also to create new avenues of exploration for functional properties and to inform guides to signatures of disorder produced by exotic phases.

Although fundamental research into the origin of interactions is important to improve our understanding about how complex phases form, the main goal in developing an understanding of key interactions stems from drawing on this knowledge to design new functional materials. Finding the right materials to embody set interactions is a future challenge, but the art of tuning the chemistry of materials is becoming more refined with increased experimental manipulation. Through the work outlined in Chapter 5, we highlighted how *ab initio* techniques can be used to determine whether interactions within statistical mechanical models can accurately explain the energetics of specific materials, as well as the interaction strengths. A more generalised approach to this would allow for mass testing on many different materials in order to select subjects containing the interactions of interest. Moreover, for frustrated interactions such as those outlined in Chapter 5, high throughput techniques could lead to a targeted approach for interaction strengths in the ratios of interest. Drawing on Chapter 5 as an example, there is a vast database of framework materials for which high throughput *ab initio* techniques could be employed to determine their dependence on the quadrupolar Hamiltonian for skymrionic interactions. Combing these calculations with a machine learning approach could inform the design of new materials by specifying new framework materials to target.

The specific test case in Chapter 5 may not be a suitable starting point as the requirement of both the host framework and a quadrupolar molecule to form the complex phases leads to computationally expensive simulations which are inappropriate for high throughput calculations. However, there are much simpler models which can be used to inform phase formation. Although not discussed explicitly

during this thesis, research conducted during my Masters and finished at the start of my DPhil investigated the interactions required to produce a ferroelectric response in proper ferroelectrics [97]. This highlighted two fundamental interactions required to induce a ferroelectric response which may be found in comparatively simpler systems than the ones needed to form non-magnetic skyrmions. Using a machine learning approach to search for interactions outlined in Ref. [97] may be a better 'proof of concept' starting point to determine how statistical mechanical models, machine learning, and high throughput calculations could inform the design of new generation materials.

Bibliography

[1] J. D. Bernal, R. H. Fowler, *J. Chem. Phys.* **1**, 515 (1933).

[2] L. Pauling, *J. Am. Chem. Soc.* **57**, 2680 (1935).

[3] A. R. West, *Solid state chemistry and its applications* (John Wiley & Sons, 2014).

[4] C. Giacovazzo, H. L. Monaco, D. Viterbo, F. Scordari, G. Gilli, G. Zanotti, M. Catti, *Fundamentals of crystallography* (Oxford University Press, Oxford, 2002).

[5] N. W. Ashcroft, N. D. Mermin, *Solid state physics* (Holt, Rinehart and Winston, 1976).

[6] F. Yonezawa, T. Ninomiya, *Topological disorder in condensed matter* (Springer-Verlag, Berlin, 1983).

[7] K. Zhao, H. Lin, X. Xiao, W. Huang, W. Yao, M. Yan, Y. Xing, Q. Zhang, Z.-X. Li, S. Hoshino, J. Wang, S. Zhou, L. Gu, M. S. Bahramy, H. Yao, N. Nagaosa, Q.-K. Xue, K. T. Law, X. Chen, S.-H. Ji, *Nat. Phys.* **15**, 904 (2019).

[8] M. N. Gastiasoro, B. M. Andersen, *Phys. Rev. B* **98**, 184510 (2018).

[9] Z. Xue, K. Liu, Q. Liu, Y. Li, M. Li, C.-Y. Su, N. Ogiwara, H. Kobayashi, H. Kitagawa, M. Liu, G. Li, *Nat. Commun.* **10**, 5048 (2019).

[10] L. Levi, M. Rechtsman, B. Freedman, T. Schwartz, O. Manela, M. Segev, *Science* **332**, 1541 (2011).

[11] A. R. Overy, A. Simonov, P. A. Chater, M. G. Tucker, A. L. Goodwin, *Phys. Status Solidi B* **254**, 1600586 (2017).

[12] D. A. Keen, A. L. Goodwin, *Nature* **521**, 303 (2015).

[13] T. R. Welberry, D. J. Goossens, *Acta Crystallogr. A* **64**, 23 (2008).

[14] M. Šimenas, S. Balčiūnas, M. Mączka, J. Banys, E. E. Tornau, *Phys. Chem. Chem. Phys.* **18**, 18528 (2016).

[15] J. M. Ziman, *Models of disorder* (Cambridge University Press, Cambridge, 1979).

[16] A. Simonov, A. L. Goodwin, *Nat. Rev. Chem.* **4**, 657 (2020).

[17] P. F. Damasceno, M. Engel, S. C. Glotzer, *Science* **337**, 453 (2012).

[18] E. H. Lieb, *Phys. Rev.* **162**, 162 (1967).

[19] P. J. Camp, A. Fuertes, J. P. Attfield, *J. Am. Chem. Soc.* **134**, 6762 (2012).

[20] V. E. Fairbank, A. L. Thompson, R. I. Cooper, A. L. Goodwin, *Phys. Rev. B* **86**, 104113 (2012).

[21] N. G. Parsonage, L. A. K. Staveley, *Disorder in crystals* (Oxford University Press, Oxford, 1978).

[22] E. Dagotto, *Science* **309**, 257 (2005).

[23] K. Huang, *Statistical mechanics* (John Wiley & Sons, 1963).

[24] A. Bienenstock, J. Lewis, *Phys. Rev.* **160**, 393 (1967).

[25] H. Johnston, A. P. Black, P. Kayser, J. Oró-Solé, D. A. Keen, A. Fuertes, J. P. Attfield, *Chem. Commun.* **54**, 5245 (2018).

[26] D. Chernyshov, A. Bosak, *Phase Transit.* **83**, 115 (2010).

[27] A. Simonov, T. De Baerdemaeker, H. L. B. Boström, M. L. Ríos Gómez, H. J. Gray, D. Chernyshov, A. Bosak, H.-B. Bürgi, A. L. Goodwin, *Nature* **578**, 256 (2020).

[28] G. Shirane, J. D. Axe, J. Harada, J. P. Remeika, *Phys. Rev. B* **2**, 155 (1970).

[29] G. Shirane, B. C. Frazer, V. J. Minkiewicz, J. A. Leake, A. Linz, *Phys. Rev. Lett.* **19**, 234 (1967).

[30] R. Comès, M. Lambert, A. Guinier, *Acta Crystallogr. A* **26**, 244 (1970).

[31] M. T. Dove, *Am. Mineral.* **82**, 213 (1997).

[32] B. K. Mani, C.-M. Chang, I. Ponomareva, *Phys. Rev. B* **88**, 064306 (2013).

[33] R. Comes, M. Lambert, A. Guinier, *Solid State Commun.* **6**, 715 (1968).

[34] H. D. Megaw, J. D. Bernal, *Proc. R. Soc. A* **189**, 261 (1947).

[35] M. S. Senn, D. A. Keen, T. C. A. Lucas, J. A. Hriljac, A. L. Goodwin, *Phys. Rev. Lett.* **116**, 207602 (2016).

[36] G. H. Kwei, A. C. Lawson, S. J. L. Billinge, S. W. Cheong, *J. Phys. Chem.* **97**, 2368 (1993).

[37] H. Katzke, P. Tolédano, W. Depmeier, *Phys. Rev. B* **69** (2004).

[38] B. E. Warren, *Phys. Rev.* **59**, 693 (1941).

[39] H. Li, C. Yang, F. Liu, *Sci. China, Ser. B: Chem.* **52**, 174 (2009).

[40] J. H. Warner, M. H. Rümmeli, T. Gemming, B. Büchner, G. A. D. Briggs, *Nano Lett.* **9**, 102 (2009).

[41] I. D. Seymour, D. S. Middlemiss, D. M. Halat, N. M. Trease, A. J. Pell, C. P. Grey, *J. Am. Chem. Soc.* **138**, 9405 (2016).

[42] J. Bréger, M. Jiang, N. Dupré, Y. S. Meng, Y. Shao-Horn, G. Ceder, C. P. Grey, *J. Solid State Chem.* **178**, 2575 (2005).

[43] R. Shunmugasundaram, R. S. Arumugam, J. R. Dahn, *J. Electrochem. Soc.* **163**, A1394 (2016).

[44] H. Y. Playford, T. F. Whale, B. J. Murray, M. G. Tucker, C. G. Salzmann, *J. Appl. Crystallogr.* **51**, 1211 (2018).

[45] S. Califano, V. Schettino, N. Neto, *Lattice dynamics of molecular crystals*, vol. 26 (Springer Science & Business Media, 2012).

[46] G. Cai, A. E. Phillips, D. A. Keen, M. G. Tucker, M. T. Dove, *J. Phys. Commun.* **4**, 023001 (2020).

[47] I. E. Collings, A. B. Cairns, A. L. Thompson, J. E. Parker, C. C. Tang, M. G. Tucker, J. Catafesta, C. Levelut, J. Haines, V. Dmitriev, P. Pattison, A. L. Goodwin, *J. Am. Chem. Soc.* **135**, 7610 (2013).

[48] C. S. Coates, M. Baise, A. Simonov, J. W. Makepeace, A. G. Seel, R. I. Smith, H. Y. Playford, D. A. Keen, R. Siegel, A. Schmutzler, J. Senker, B. Slater, A. L. Goodwin, *arxiv:1904.05749* (2019).

[49] P. J. W. Debye, *Polar molecules* (Chemical Catalog Company, Incorporated, 1929).

[50] J. Frenkel, *Acta phys.-chim. URSS.* **3**, 913 (1935).

[51] H. D. Duncan, E. O. R. Beake, H. Y. Playford, M. T. Dove, A. E. Phillips, *CrystEngComm* **19**, 7316 (2017).

[52] C. S. Coates, H. J. Gray, J. M. Bulled, H. L. B. Boström, A. Simonov, A. L. Goodwin, *Phil. Trans. R. Soc. Lond. A* **377**, 20180219 (2019).

[53] J. Timmermans, *J. Phys. Chem. Solids* **18**, 1 (1961).

[54] L. A. K. Staveley, *Annu. Rev. Phys. Chem.* **13**, 351 (1962).

[55] M. T. Dove, *Mater. Today* **6**, 59 (2003).

[56] T. D. Bennett, A. L. Goodwin, M. T. Dove, D. A. Keen, M. G. Tucker, E. R. Barney, A. K. Soper, E. G. Bithell, J.-C. Tan, A. K. Cheetham, *Phys. Rev. Lett.* **104**, 115503 (2010).

[57] N. Yamada, E. Ohno, K. Nishiuchi, N. Akahira, M. Takao, *J. Appl. Phys.* **69**, 2849 (1991).

[58] J. Hegedüs, S. R. Elliott, *Nat. Mater.* **7**, 399 (2008).

[59] K. A. Graeser, J. E. Patterson, J. A. Zeitler, T. Rades, *Pharmaceutics* **2**, 224 (2010).

[60] J. Haines, C. Levelut, A. Isambert, P. Hébert, S. Kohara, D. A. Keen, T. Hammouda, D. Andrault, *J. Am. Chem. Soc.* **131**, 12333 (2009).

[61] M. Baise, P. M. Maffettone, F. Trousselet, N. P. Funnell, F.-X. Coudert, A. L. Goodwin, *Phys. Rev. Lett.* **120**, 265501 (2018).

[62] M. Von Laue, *Ann. Phys.* **361**, 497 (1918).

[63] T. R. Welberry, B. D. Butler, *Chem. Rev.* **95**, 2369 (1995).

[64] F. Frey, *Eur. J. Mineral.* **9**, 693 (1997).

[65] V. M. Nield, D. A. Keen, *Diffuse neutron scattering from crystalline materials*, vol. 14 (Oxford University Press, Oxford, 2001).

[66] S. Rosenkranz, R. Osborn, *Neutron News* **15**, 21 (2004).

[67] T. R. Welberry, T. Weber, *Crystallogr. Rev.* **22**, 2 (2016).

[68] C. A. Young, A. L. Goodwin, *J. Mater. Chem.* **21**, 6464 (2011).

[69] J. E. Harries, S. S. Hasnain, J. S. Shah, *Calcif. Tissue Int.* **41**, 346 (1987).

[70] M. J. Cliffe, W. Wan, X. Zou, P. A. Chater, A. K. Kleppe, M. G. Tucker, H. Wilhelm, N. P. Funnell, F.-X. Coudert, A. L. Goodwin, *Nat. Commun.* **5**, 4176 (2014).

[71] L. Liu, Z. Chen, J. Wang, D. Zhang, Y. Zhu, S. Ling, K.-W. Huang, Y. Belmabkhout, K. Adil, Y. Zhang, B. Slater, M. Eddaoudi, Y. Han, *Nat. Chem.* **11**, 622 (2019).

[72] T. Matsunaga, P. Fons, A. V. Kolobov, J. Tominaga, N. Yamada, *Appl. Phys. Lett.* **99**, 231907 (2011).

[73] S. J. L. Billinge, M. G. Kanatzidis, *Chem. Commun.* **7**, 749 (2004).

[74] X. Qiu, J. W. Thompson, S. J. L. Billinge, *J. Appl. Crystallogr.* **37**, 678 (2004).

[75] C. L. Farrow, P. Juhas, J. W. Liu, D. Bryndin, E. S. Božin, J. Bloch, T. Proffen, S. J. L. Billinge, *J. Phys. Condens. Matter* **19**, 335219 (2007).

[76] L. Palatinus, G. Chapuis, *J. Appl. Crystallogr.* **40**, 786 (2007).

[77] G. M. Sheldrick, *Acta Crystallogr. A* **71**, 3 (2015).

[78] O. V. Dolomanov, L. J. Bourhis, R. J. Gildea, J. A. K. Howard, H. Puschmann, *J. Appl. Crystallogr.* **42**, 339 (2009).

[79] P. Debye, *Annalen der Physik* **348**, 49 (1913).

[80] B. E. Warren, B. L. Averbach, B. W. Roberts, *Journal of Applied Physics* **22**, 1493 (1951).

[81] F. Frey, *Acta Crystallogr. B* **51**, 592 (1995).

[82] M. Hayakawa, J. B. Cohen, *Acta Crystallogr. A* **31**, 635 (1975).

[83] T. Welberry, E. Chan, D. Goossens, A. Heerdegen, *Phase Transit.* **83**, 80 (2010).

[84] D. J. Goossens, *Adv. Condens. Matter Phys.* **2015**, 878463 (2015).

[85] R. L. McGreevy, L. Pusztai, *Mol. Simulat.* **1**, 359 (1988).

[86] W. H. Bragg, W. L. Bragg, *P. Roy. Soc. Lond. A. Mat.* **88**, 428 (1913).

[87] A. Guinier, *X-ray diffraction in crystals, imperfect crystals, and amorphous bodies* (Courier Corporation, 1994).

[88] G. Harburn, C. Taylor, T. Welberry, *Atlas of optical transforms* (Cornell University Press, 1975).

[89] S. T. Bramwell, M. J. P. Gingras, *Science* **294**, 1495 (2001).

[90] B. J. Palmer, D. M. Pfund, J. L. Fulton, *J. Phys. Chem.* **100**, 13393 (1996).

[91] F. Mauri, B. G. Pfrommer, S. G. Louie, *Phys. Rev. Lett.* **77**, 5300 (1996).

[92] A. Bosak, D. Chernyshov, S. Vakhrushev, M. Krisch, *arxiv:1101.0490* (2011).

[93] R. Ali, M. Yashima, Y. Matsushita, H. Yoshioka, K. Ohoyama, F. Izumi, *Chem. Mater.* **20**, 5203 (2008).

[94] B. Key, R. Bhattacharyya, M. Morcrette, V. Seznéc, J.-M. Tarascon, C. P. Grey, *J. Am. Chem. Soc.* **131**, 9239 (2009).

[95] D. A. Keen, *J. Phys. Condens. Matter* **14**, R819 (2002).

[96] S. Hull, S. T. Norberg, M. G. Tucker, S. G. Eriksson, C. E. Mohn, S. Stølen, *Dalton Trans.* **2009**, 8737 (2009).

[97] E. H. Wolpert, A. R. Overy, P. M. M. Thygesen, A. Simonov, M. S. Senn, A. L. Goodwin, *Phys. Rev. B* **97**, 134106 (2018).

[98] T. R. Welberry, *Rep. Prog. Phys.* **48**, 1543 (1985).

[99] R. L. McGreevy, *J. Phys. Condens. Matter* **13**, 877 (2001).

[100] P. Biswas, R. Atta-Fynn, D. A. Drabold, *Phys. Rev. B* **69**, 195207 (2004).

[101] N. Yamakawa, M. Jiang, B. Key, C. P. Grey, *J. Am. Chem. Soc.* **131**, 10525 (2009).

[102] A. Simonov, T. Weber, W. Steurer, *J. Appl. Crystallogr.* **47**, 1146 (2014).

[103] T. Weber, A. Simonov, *Z. Kristallogr. Cryst. Mater* **227**, 238 (2012).

[104] M. Kobas, T. Weber, W. Steurer, *Phys. Rev. B* **71**, 224205 (2005).

[105] M. Kobas, T. Weber, W. Steurer, *Phys. Rev. B* **71**, 224206 (2005).

[106] T. Keiber, F. Bridges, B. C. Sales, *Phys. Rev. Lett.* **111**, 095504 (2013).

[107] A. F. Sapnik, H. S. Geddes, E. M. Reynolds, H. H.-M. Yeung, A. L. Goodwin, *Chem. Commun.* **54**, 9651 (2018).

[108] Z. Liu, Y.-Y. Hu, M. T. Dunstan, H. Huo, X. Hao, H. Zou, G. Zhong, Y. Yang, C. P. Grey, *Chem. Mater.* **26**, 2513 (2014).

[109] S. Elliott, *J. Non Cryst. Solids* **123**, 149 (1990).

[110] E. A. Donlan, H. L. B. Boström, H. S. Geddes, E. M. Reynolds, A. L. Goodwin, *Chem. Commun.* **53**, 11233 (2017).

[111] A. M. Mio, P. M. Konze, A. Meledin, M. Küpers, M. Pohlmann, M. Kaminski, R. Dronskowski, J. Mayer, M. Wuttig, *Adv. Funct. Mater.* **29**, 1902332 (2019).

[112] M. O. Blunt, J. C. Russell, M. d. C. Giménez-López, J. P. Garrahan, X. Lin, M. Schröder, N. R. Champness, P. H. Beton, *Science* **322**, 1077 (2008).

[113] B. G. Mendis, M. D. Shannon, M. C. Goodman, J. D. Major, R. Claridge, D. P. Halliday, K. Durose, *Prog. Photovoltaics* **22**, 24 (2014).

[114] E. Estévez-Rams, J. Fidler, A. Pentón, J. Téllez-Blanco, R. Turtelli, R. Grössinger, *J. Alloys Compd.* **283**, 327 (1999).

[115] D. Zhang, Y. Zhu, L. Liu, X. Ying, C.-E. Hsiung, R. Sougrat, K. Li, Y. Han, *Science* **359**, 675 (2018).

[116] P. Bak, *Rep. Prog. Phys.* **45**, 587 (1982).

[117] W. Selke, *Phys. Rep.* **170**, 213 (1988).

[118] S. Blundell, *Magnetism in condensed matter* (Oxford University Press, Oxford, 2001).

[119] E. Ising, *Z. Phys.* **31**, 253 (1925).

[120] R. J. Elliott, *Phys. Rev.* **124**, 346 (1961).

[121] M. E. Fisher, W. Selke, *Phys. Rev. Lett.* **44**, 1502 (1980).

[122] G. S. Zhdanov, Z. V. Minervina, *C. R. Acad. Sci. URSS* **48**, 182 (1945).

[123] G. S. Zhdanov, Z. V. Minervina, *J. Phys. USSR* **10**, 422 (1946).

[124] C. Lacroix, P. Mendels, F. Mila, *Introduction to frustrated magnetism: materials, experiments, theory*, vol. 164 (Springer, Berlin, 2011).

[125] G. H. Wannier, *Phys. Rev.* **79**, 357 (1950).

[126] B. Rasche, A. Isaeva, M. Ruck, S. Borisenko, V. Zabolotnyy, B. Büchner, K. Koepernik, C. Ortix, M. Richter, J. van den Brink, *Nat. Mater.* **12**, 422 (2013).

[127] A. Simonov, T. Weber, W. Steurer, *J. Appl. Crystallogr.* **47**, 2011 (2014).

[128] S. Nakatsuji, K. Kuga, K. Kimura, R. Satake, N. Katayama, E. Nishibori, H. Sawa, R. Ishii, M. Hagiwara, F. Bridges, T. U. Ito, W. Higemoto, Y. Karaki, M. Halim, A. A. Nugroho, J. A. Rodriguez-Rivera, M. A. Green, C. Broholm, *Science* **336**, 559 (2012).

[129] C. L. Henley, *Annu. Rev. Condens. Matter Phys.* **1**, 179 (2010).

[130] S. W. H. Bragg, *Proc. Phys. Soc.* **34**, 98 (1921).

[131] D. M. Dennison, *Phys. Rev.* **17**, 20 (1921).

[132] W. H. Barnes, W. H. Bragg, *P. Roy. Soc. A. Mat. Phy.* **125**, 670 (1929).

[133] W. F. Giauque, M. F. Ashley, *Phys. Rev.* **43**, 81 (1933).

[134] R. Petrenko, V. & Whitworth, *Physics of ice* (Oxford University Press, Oxford, 2002).

[135] T. Fennell, P. P. Deen, A. R. Wildes, K. Schmalzl, D. Prabhakaran, A. T. Boothroyd, R. J. Aldus, D. F. McMorrow, S. T. Bramwell, *Science* **326**, 415 (2009).

[136] T. Fennell, M. J. Harris, S. Calder, M. Ruminy, M. Boehm, P. Steffens, M. H. Lemée-Cailleau, O. Zaharko, A. Cervellino, S. T. Bramwell, *Nat. Phys.* **15**, 60 (2019).

[137] P. W. Anderson, *Phys. Rev.* **102**, 1008 (1956).

[138] M. J. Harris, S. T. Bramwell, D. F. McMorrow, T. Zeiske, K. W. Godfrey, *Phys. Rev. Lett.* **79**, 2554 (1997).

[139] P. M. M. Thygesen, J. A. M. Paddison, R. Zhang, K. A. Beyer, K. W. Chapman, H. Y. Playford, M. G. Tucker, D. A. Keen, M. A. Hayward, A. L. Goodwin, *Phys. Rev. Lett.* **118**, 067201 (2017).

[140] B. F. Hoskins, R. Robson, *J. Am. Chem. Soc.* **112**, 1546 (1990).

[141] R. B. Potts, *Math. Proc. Camb. Philos. Soc.* **48**, 106 (1952).

[142] F. Y. Wu, *Rev. Mod. Phys.* **54**, 235 (1982).

[143] L. Sun, Y. F. Chang, X. Cai, *Int. J. Mod. Phys. B* **18**, 2651 (2004).

[144] D. Louis, D. Lacour, M. Hehn, V. Lomakin, T. Hauet, F. Montaigne, *Nat. Mater.* **17**, 1076 (2018).

[145] B. Barbara, M. F. Rossignol, P. Bak, *J. Phys. C* **11**, L183 (1978).

[146] A. Aharony, K. A. Müller, W. Berlinger, *Phys. Rev. Lett.* **38**, 33 (1977).

[147] V. Vaks, A. Larkin, *Soviet Phys. JETP* **22**, 678 (1966).

[148] M. E. Gouvea, F. G. Mertens, A. R. Bishop, G. M. Wysin, *J. Phys. Condens. Matter* **2**, 1853 (1990).

[149] M. Gibertini, M. Koperski, A. F. Morpurgo, K. S. Novoselov, *Nat. Nanotechnol.* **14**, 408 (2019).

[150] H.-J. Mikeska, A. K. Kolezhuk, *One-dimensional magnetism* (Springer Berlin Heidelberg, Berlin, Heidelberg, 2004), pp. 1–83.

[151] M. Elahy, M. Shayegan, K. Szeto, G. Dresselhaus, *Synth. Met.* **8**, 35 (1983).

[152] A. B. Cairns, M. J. Cliffe, J. A. M. Paddison, D. Daisenberger, M. G. Tucker, F.-X. Coudert, A. L. Goodwin, *Nat. Chem.* **8**, 442 (2016).

[153] W. Heisenberg, *Z. Phys.* **49**, 619 (1928).

[154] L. de Jongh, A. Miedema, *Adv. Phys.* **23**, 1 (1974).

[155] T. Yavors'kii, M. Enjalran, M. J. P. Gingras, *Phys. Rev. Lett.* **97**, 267203 (2006).

[156] N. P. Raju, M. Dion, M. J. P. Gingras, T. E. Mason, J. E. Greedan, *Phys. Rev. B* **59**, 14489 (1999).

[157] S. E. Palmer, J. T. Chalker, *Phys. Rev. B* **62**, 488 (2000).

[158] A. L. Wysocki, K. D. Belashchenko, V. P. Antropov, *Nat. Phys.* **7**, 485 (2011).

[159] I. Dzyaloshinsky, *J. Phys. Chem. Solids* **4**, 241 (1958).

[160] T. Moriya, *Phys. Rev.* **120**, 91 (1960).

[161] P. Bak, M. H. Jensen, *J Phys. C: Solid State Phys.* **13**, L881 (1980).

[162] T. H. Skryme, *Proc. R. Soc. Lond. A* **260**, 127 (1961).

[163] A. Fert, N. Reyren, V. Cros, *Nat. Rev. Mater.* **2**, 17031 (2017).

[164] N. Nagaosa, Y. Tokura, *Nat. Nanotech.* **8**, 899 (2013).

[165] S. Mühlbauer, B. Binz, F. Jonietz, C. Pfleiderer, A. Rosch, A. Neubauer, R. Georgii, P. Böni, *Science* **323**, 915 (2009).

[166] S. D. Yi, S. Onoda, N. Nagaosa, J. H. Han, *Phys. Rev. B* **80**, 054416 (2009).

[167] S. Burhandt, L. Fritz, *Phys. Rev. B* **88**, 195137 (2013).

[168] X. Z. Yu, Y. Onose, N. Kanazawa, J. H. Park, J. H. Han, Y. Matsui, N. Nagaosa, Y. Tokura, *Nature* **465**, 901 (2010).

[169] U. K. Rößler, A. N. Bogdanov, C. Pfleiderer, *Nature* **442**, 797 (2006).

[170] S. X. Huang, C. L. Chien, *Phys. Rev. Lett.* **108**, 267201 (2012).

[171] N. Romming, C. Hanneken, M. Menzel, J. E. Bickel, B. Wolter, K. von Bergmann, A. Kubetzka, R. Wiesendanger, *Science* **341**, 636 (2013).

[172] A. O. Leonov, M. Mostovoy, *Nat. Commun.* **6**, 8275 (2015).

[173] S. Gao, O. Zaharko, V. Tsurkan, Y. Su, J. S. White, G. S. Tucker, B. Roessli, F. Bourdarot, R. Sibille, D. Chernyshov, T. Fennell, A. Loidl, C. Rüegg, *Nat. Phys.* **13**, 157 (2017).

[174] X. Z. Yu, W. Koshibae, Y. Tokunaga, K. Shibata, Y. Taguchi, N. Nagaosa, Y. Tokura, *Nature* **564**, 95 (2018).

[175] C. Castelnovo, R. Moessner, S. L. Sondhi, *Nature* **451**, 42 (2008).

[176] J. Chen, W. P. Cai, M. H. Qin, S. Dong, X. B. Lu, X. S. Gao, J.-M. Liu, *Sci. Rep.* **7**, 7392 (2017).

[177] J. M. Kosterlitz, D. J. Thouless, *J. Phys. C* **6**, 1181 (1973).

[178] G. Tatara, A. Takeuchi, N. Nakabayashi, K. Taguchi, *J. Korean Phys. Soc.* **61**, 1331 (2012).

[179] D. I. Khomskii, *Nat. Commun.* **3**, 904 (2012).

[180] S. R. Giblin, S. T. Bramwell, P. C. W. Holdsworth, D. Prabhakaran, I. Terry, *Nat. Phys.* **7**, 252 (2011).

[181] S. R. Nagel, *Rev. Mod. Phys.* **89**, 025002 (2017).

[182] M. M. Salomaa, G. E. Volovik, *Rev. Mod. Phys.* **59**, 533 (1987).

[183] R. L. Davis, *Phys. Rev. D* **35**, 3705 (1987).

[184] P. M. Chaikin, T. C. Lubensky, *Topological defects* (Cambridge University Press, Cambridge, 1995).

[185] K. Karube, J. S. White, D. Morikawa, C. D. Dewhurst, R. Cubitt, A. Kikkawa, X. Yu, Y. Tokunaga, T.-H. Arima, H. M. Rønnow, Y. Tokura, Y. Taguchi, *Sci. Adv.* **4**, 7043 (2018).

[186] S. D. Hudson, E. L. Thomas, *Phys. Rev. Lett.* **62**, 1993 (1989).

[187] S. Mühlbauer, D. Honecker, E. A. Périgo, F. Bergner, S. Disch, A. Heinemann, S. Erokhin, D. Berkov, C. Leighton, M. R. Eskildsen, A. Michels, *Rev. Mod. Phys.* **91**, 015004 (2019).

[188] P. Fratzl, *J. Appl. Crystallogr.* **36**, 397 (2003).

[189] T. Ohzono, K. Katoh, C. Wang, A. Fukazawa, S. Yamaguchi, J.-I. Fukuda, *Sci. Rep.* **7**, 16814 (2017).

[190] J. Prakash, A. Chandran, A. M. Biradar, *Rep. Prog. Phys.* **80**, 016601 (2016).

[191] J. Nehring, A. Saupe, *J. Chem. Soc., Faraday Trans. 2* **68**, 1 (1972).

[192] T. Fennell, S. T. Bramwell, D. F. McMorrow, P. Manuel, A. R. Wildes, *Nat. Phys.* **3**, 566 (2007).

[193] O. Benton, L. Jaubert, H. Yan, N. Shannon, *Nat. Commun.* **7** (2016).

[194] P. A. M. Dirac, *P. Roy. Soc. A. Mat. Phy.* **133**, 60 (1931).

[195] D. J. P. Morris, D. A. Tennant, S. A. Grigera, B. Klemke, C. Castelnovo, R. Moessner, C. Czternasty, M. Meissner, K. C. Rule, J.-U. Hoffmann, K. Kiefer, S. Gerischer, D. Slobinsky, R. S. Perry, *Science* **326**, 411 (2009).

[196] A. P. Ramirez, A. Hayashi, R. J. Cava, R. Siddharthan, B. S. Shastry, *Nature* **399**, 333 (1999).

[197] E. B. Sirota, X. Z. Wu, *J. Chem. Phys.* **105**, 7763 (1996).

[198] Q. N. Meier, M. Lilienblum, S. M. Griffin, K. Conder, E. Pomjakushina, Z. Yan, E. Bourret, D. Meier, F. Lichtenberg, E. K. H. Salje, N. A. Spaldin, M. Fiebig, A. Cano, *Phys. Rev. X* **7**, 041014 (2017).

[199] A. Abrikosov, *J. Phys. Chem. Solids* **2**, 199 (1957).

[200] K. Epstein, A. M. Goldman, A. M. Kadin, *Phys. Rev. Lett.* **47**, 534 (1981).

[201] S. Chandrasekhar, *Liquid crystals* (Cambridge University Press, Cambridge, 1992), second edn.

[202] J.-I. Fukuda, S. Žumer, *Nat. Commun.* **2**, 246 (2011).

[203] I. Chuang, R. Durrer, N. Turok, B. Yurke, *Science* **251**, 1336 (1991).

[204] M. J. Bowick, L. Chandar, E. A. Schiff, A. M. Srivastava, *Science* **263**, 943 (1994).

[205] J. P. F. Lagerwall, F. Giesselmann, *ChemPhysChem* **7**, 20 (2006).

[206] J. Goodby, *Structures and properties of smectic liquid crystals* (American Cancer Society, 2014).

[207] S. Masubuchi, T. Akahane, K. Nakao, T. Tako, *Mol. Cryst. Liq. Cryst.* **35**, 135 (1976).

[208] N. Popov, L. W. Honaker, M. Popova, N. Usol'tseva, E. K. Mann, A. Jákli, P. Popov, *Materials* **11** (2018).

[209] M. F. Moreira, I. C. S. Carvalho, W. Cao, C. Bailey, B. Taheri, P. Palffy-Muhoray, *Appl. Phys. Lett.* **85**, 2691 (2004).

[210] M. D. A. Rahman, S. M. Said, S. Balamurugan, *Sci. Technol. Adv. Mat.* **16**, 033501 (2015).

[211] S. Meiboom, M. Sammon, *Phys. Rev. Lett.* **44**, 882 (1980).

[212] M. V. Kurik, O. D. Lavrentovich, *Mol. Cryst. Liq. Cryst.* **72**, 239 (1982).

[213] J. A. Martínez-González, X. Li, M. Sadati, Y. Zhou, R. Zhang, P. F. Nealey, J. J. de Pablo, *Nat. Commun.* **8**, 15854 (2017).

[214] I. I. Smalyukh, Y. Lansac, N. A. Clark, R. P. Trivedi, *Nat. Mater.* **9**, 139 (2010).

[215] P. J. Ackerman, R. P. Trivedi, B. Senyuk, J. van de Lagemaat, I. I. Smalyukh, *Phys. Rev. E* **90**, 012505 (2014).

[216] A. Duzgun, J. V. Selinger, A. Saxena, *Phys. Rev. E* **97**, 062706 (2018).

[217] K. Harth, R. Stannarius, *Front. Phys.* **8**, 112 (2020).

[218] J. L. Finney, *Acta Crystallogr. B* **51**, 447 (1995).

[219] C. S. Coates, Spin-ice physics and phase transitions in cadmium cyanide, Ph.D. thesis, University of Oxford (2019).

[220] T. Fennell, O. A. Petrenko, B. Fåk, S. T. Bramwell, M. Enjalran, T. Yavors'kii, M. J. P. Gingras, R. G. Melko, G. Balakrishnan, *Phys. Rev. B* **70**, 134408 (2004).

[221] S. T. Bramwell, M. J. Harris, *J. Phys. Condens. Matter* **32**, 374010 (2020).

[222] P. Ding, E. J. Liang, Y. Jia, Z. Y. Du, *J. Phys. Condens. Matter* **20**, 275224 (2008).

[223] A. G. Sharpe, *The chemistry of cyano complexes of the transition metals* (Academic Press Inc., London, 1976).

[224] A. L. Goodwin, C. J. Kepert, *Phys. Rev. B* **71**, 140301 (2005).

[225] M. F. Collins, *Magnetic critical scattering* (Oxford University Press, Oxford, 1989).

[226] J. B. Goodenough, *Magnetism and the chemical bond*, vol. 1 (Interscience publishers, 1963).

[227] S. M. Winter, Y. Li, H. O. Jeschke, R. Valentí, *Phys. Rev. B* **93**, 214431 (2016).

[228] G. Cao, P. Schlottmann, *Rep. Prog. Phys.* **81**, 042502 (2018).

[229] S. Nakatsuji, Y. Nambu, H. Tonomura, O. Sakai, S. Jonas, C. Broholm, H. Tsunetsugu, Y. Qiu, Y. Maeno, *Science* **309**, 1697 (2005).

[230] M. F. Collins, O. A. Petrenko, *Can. J. Phys.* **75**, 605 (1997).

[231] R. Skomski, *Simple models of magnetism* (Oxford University Press, Oxford, 2008).

[232] S. G. BRUSH, *Rev. Mod. Phys.* **39**, 883 (1967).

[233] J. J. A. Shaw, V. Heine, *J. Phys. Condens. Matter* **2**, 4351 (1990).

[234] R. L. Smith, M. Vickers, M. Rosillo-Lopez, C. G. Salzmann, *Cryst. Growth Des.* **19**, 2131 (2019).

[235] D. Quigley, *J. Chem. Phys.* **141**, 121101 (2014).

[236] G. D. Price, *Phys. Chem. Miner.* **10**, 77 (1983).

[237] M. L. Plumer, K. Hood, A. Caille, *J. Phys. C* **21**, 4189 (1988).

[238] M. Nespolo, M. I. Aroyo, *Eur. J. Mineral.* **28**, 189 (2016).

[239] B. E. Brown, S. W. Bailey, *Am. Mineral.* **47**, 819 (1962).

[240] G. D. Price, J. Yeomans, *Acta Crystallogr. B* **40**, 448 (1984).

[241] D. Pandey, P. Krishna, *Prog. Cryst. Growth Charact. Mater.* **7**, 213 (1983).

[242] J. Terhell, *Prog. Cryst. Growth Charact. Mater.* **7**, 55 (1983).

[243] G. C. Trigunayat, *Phase Transit.* **16**, 509 (1989).

[244] N. Jepps, T. Page, *Prog. Cryst. Growth Charact. Mater.* **7**, 259 (1983).

[245] J. Yeomans, *The theory and application of axial Ising models*, vol. 41 of *Solid State Physics* (Academic Press, Orlando, 1988).

[246] S. Ramasesha, C. N. R. Rao, *Phil. Mag.* **36**, 827 (1977).

[247] J. Wilson, F. D. Salvo, S. Mahajan, *Adv. Phys.* **24**, 117 (1975).

[248] A. H. Castro Neto, *Phys. Rev. Lett.* **86**, 4382 (2001).

[249] Y.-T. Hsu, A. Vaezi, M. H. Fischer, E.-A. Kim, *Nat. Commun.* **8**, 14985 (2017).

[250] D. de Fontaine, J. Kulik, *Acta Metall.* **33**, 145 (1985).

[251] A. Loiseau, G. Van Tendeloo, R. Portier, F. Ducastelle, *J. Phys. France* **46**, 595 (1985).

[252] J. Kulik, S. Takeda, D. de Fontaine, *Acta Metall. Mater.* **35**, 1137 (1987).

[253] R. Portier, D. Gratias, M. Guymont, W. M. Stobbs, *Acta Crystallogr. A* **36**, 190 (1980).

[254] M. Guymont, D. Gratias, *Acta Crystallogr. A* **35**, 181 (1979).

[255] G. van Tendeloo, S. Amelinckx, *Phys. Status Solidi A* **43**, 553 (1977).

[256] D. Broddin, G. V. Tendeloo, J. V. Landuyt, S. Amelinckx, R. Portier, M. Guymont, A. Loiseau, *Philos. Mag. A* **54**, 395 (1986).

[257] S. Hibble, A. Chippindale, A. Pohl, A. Hannon, *Angew. Chem. Int. Ed.* **46**, 7116 (2007).

[258] A. L. Goodwin, M. T. Dove, A. M. Chippindale, S. J. Hibble, A. H. Pohl, A. C. Hannon, *Phys. Rev. B* **80**, 054101 (2009).

[259] D. Sayre, *Struct. Chem.* **13**, 81 (2002).

[260] C. Mack, *Appendix C: the Dirac delta function* (John Wiley & Sons, Ltd, 2007), pp. 495–500.

[261] V. Pecharsky, P. Zavalij, *Fundamentals of powder diffraction and structural characterization of materials* (Springer Science & Business Media, 2008).

[262] J. L. Teteruk, J. Glinnemann, T. E. Gorelik, A. Linden, M. U. Schmidt, *Acta Crystallogr. B* **70**, 296 (2014).

[263] Y. Song, J. Zhao, Y. Zhao, Z. Huang, Y. Li, G. Wu, *CrystEngComm* **18**, 6502 (2016).

[264] A. Guinier, G. Fournet, K. L. Yudowitch, *Small-angle scattering of X-rays* (Wiley New York, 1955).

[265] L. Feigin, D. I. Svergun, *Structure analysis by small-angle X-ray and neutron scattering*, vol. 1 (Springer, 1987).

[266] B. Jacrot, *Rep. Prog. Phys.* **39**, 911 (1976).

[267] D. Franke, M. V. Petoukhov, P. V. Konarev, A. Panjkovich, A. Tuukkanen, H. D. T. Mertens, A. G. Kikhney, N. R. Hajizadeh, J. M. Franklin, C. M. Jeffries, D. I. Svergun, *J. Appl. Crystallogr.* **50**, 1212 (2017).

[268] S. D. Bader, *Rev. Mod. Phys.* **78**, 1 (2006).

[269] T. Chatterji, *Neutron scattering from magnetic materials* (Elsevier, 2005).

[270] T. Neder, R. B. & Proffen, *Diffuse scattering and defect structure simulations: a cook book using the program DISCUS* (Oxford University Press, Oxford, 2008).

[271] M. Paściak, T. Welberry, A. Heerdegen, V. Laguta, T. Ostapchuk, S. Leoni, J. Hlinka, *Phase Transit.* **88**, 273 (2015).

[272] J. A. M. Paddison, *Acta Crystallogr. A* **75**, 14 (2019).

[273] J. O. Thomas, M. A. Zendejas, *J. Comput. Aided Mol. Des.* **3**, 311 (1989).

[274] CrystalDiffract, *A powder diffraction program for Mac and Windows. CrystalMaker Software Ltd* (Oxford, England).

[275] R. J. Baxter, *Exactly solved models in statistical mechanics* (Elsevier, 1982).

[276] V. Dobrosavljevic, N. Trivedi, J. M. Valles, *Conductor insulator quantum phase transitions* (Oxford University Press, Oxford, 2012).

[277] W. Schweika, *Disordered alloys*, vol. 141 (Springer-Verlag Berlin Heidelberg, 1998).

[278] L. Int Panis, L. De Nocker, I. De Vlieger, R. Torfs, *Int. J. Vechicle Des.* **27**, 183 (2001).

[279] D. Teodorović, E. KrćmarNožić, G. Stojković, *Transport. Plan. Techn.* **17**, 219 (1993).

[280] P. A. Flinn, G. M. McManus, *Phys. Rev.* **124**, 54 (1961).

[281] N. Metropolis, A. W. Rosenbluth, M. N. Rosenbluth, A. H. Teller, E. Teller, *J. Chem. Phys.* **21**, 1087 (1953).

[282] M. Newman, G. Barkema, *Monte Carlo methods in statistical physics*, vol. 24 (Oxford University Press, New York, USA, 1999).

[283] N. C. Karayiannis, A. E. Giannousaki, V. G. Mavrantzas, *J. Chem. Phys.* **118**, 2451 (2003).

[284] F. J. Humphreys, M. Hatherly, *Recrystallization and related annealing phenomena* (Elsevier, 2012).

[285] A. Sinha, B. Giessen, D. Polk, *Metastable phases produced by rapid wuenching from the vapor and the liquid, treatise on solid state chemistry* (Springer, 1976).

[286] P. J. Van Laarhoven, E. H. Aarts, *Simulated annealing* (Springer, 1987).

[287] S. Kirkpatrick, C. D. J. Gelatt, M. P. Vecchi, *Science* **220**, 671 (1983).

[288] S. V. Semenovskaya, K. A. Khachaturyan, A. G. Khachaturyan, *Acta Crystallogr. A* **41**, 268 (1985).

[289] A. R. Overy, Structure and properties of states containing strongly-correlated disorder, Ph.D. thesis, University of Oxford (2018).

[290] E. Egenter, T. Lux, D. Stauffer, *Physica A* **268**, 250 (1999).

[291] F. Falo, L. M. Floria, R. Navarro, *J. Phys. Condens. Matter* **1**, 5139 (1989).

[292] S. Dussi, M. Chiappini, M. Dijkstra, *Mol. Phys.* **116**, 2792 (2018).

[293] H. D. Rosales, D. C. Cabra, P. Pujol, *Phys. Rev. B* **92**, 214439 (2015).

[294] M. G. Tucker, M. P. Squires, M. T. Dove, D. A. Keen, *J. Phys. Condens. Matter* **13**, 403 (2000).

[295] D. A. Keen, R. L. McGreevy, *Nature* **344**, 423 (1990).

[296] D. Srivastava, S. Atluri, *CMES Comput. Model. Eng. Sci.* **3**, 531 (2002).

[297] K. N. Rankin, J. W. Gauld, R. J. Boyd, *J. Phys. Chem. A* **106**, 5155 (2002).

[298] A. F. Harper, M. L. Evans, J. P. Darby, B. Karasulu, C. P. Koçer, J. R. Nelson, A. J. Morris, *Johnson Matthey Technol. Rev.* **64**, 103 (2020).

[299] A. R. Leach, *Molecular modelling: principles and applications* (Pearson education, 2001).

[300] P. Hohenberg, W. Kohn, *Phys. Rev.* **136**, B864 (1964).

[301] W. Kohn, L. J. Sham, *Phys. Rev.* **140**, A1133 (1965).

[302] C. Stampfl, W. Mannstadt, R. Asahi, A. J. Freeman, *Phys. Rev. B* **63**, 155106 (2001).

[303] D. C. Langreth, M. J. Mehl, *Phys. Rev. B* **28**, 1809 (1983).

[304] J. P. Perdew, K. Burke, M. Ernzerhof, *Phys. Rev. Lett.* **77**, 3865 (1996).

[305] J. P. Perdew, *Electronic structure of solids* (Akademie Verlag, Berlin, 1991).

[306] A. D. Becke, *J. Chem. Phys.* **98**, 1372 (1993).

[307] J. P. Perdew, M. Ernzerhof, K. Burke, *J. Chem. Phys.* **105**, 9982 (1996).

[308] C. Adamo, V. Barone, *J. Chem. Phys.* **110**, 6158 (1999).

[309] A. D. Becke, *Phys. Rev. A* **38**, 3098 (1988).

[310] C. Lee, W. Yang, R. G. Parr, *Phys. Rev. B* **37**, 785 (1988).

[311] P. E. M. Siegbahn, *Q. Rev. Biophys.* **36**, 91 (2003).

[312] K. T. Butler, J. M. Frost, J. M. Skelton, K. L. Svane, A. Walsh, *Chem. Soc. Rev.* **45**, 6138 (2016).

[313] L. E. Ratcliff, S. Mohr, G. Huhs, T. Deutsch, M. Masella, L. Genovese, *Wiley Interdiscip. Rev. Comput. Mol. Sci.* **7**, e1290 (2017).

[314] F. Illas, I. de P. R. Moreira, J. M. Bofill, M. Filatov, *Phys. Rev. B* **70**, 132414 (2004).

[315] G. Bihlmayer, *Density functional theory for magnetism and magnetic anisotropy* (Springer International Publishing, 2018).

[316] F. G. Eich, E. K. U. Gross, *Phys. Rev. Lett.* **111**, 156401 (2013).

[317] J. P. Perdew, K. Burke, M. Ernzerhof, *Phys. Rev. Lett.* **80**, 891 (1998).

[318] J. VandeVondele, J. Hutter, *J. Chem. Phys.* **127**, 114105 (2007).

[319] R. Dovesi, R. Orlando, B. Civalleri, C. Roetti, V. R. Saunders, C. M. Zicovich-Wilson, *Z. Kristallogr. Cryst. Mater.* **220**, 571 (2005).

[320] J. D. Evans, G. Fraux, R. Gaillac, D. Kohen, F. Trousselet, J.-M. Vanson, F.-X. Coudert, *Chem. Mater.* **29**, 199 (2016).

[321] M. T. Dove, H. Fang, *Rep. Prog. Phys.* **79**, 066503 (2016).

[322] R. Mittal, M. Gupta, S. Chaplot, *Prog. Mater. Sci.* **92**, 360 (2018).

[323] J. D. Gale, *GULP manual* (1998).

[324] J. D. Gale, *J. Chem. Soc., Faraday Trans.* **93**, 629 (1997).

[325] D. J. Henry, C. A. Lukey, E. Evans, I. Yarovsky, *Mol. Simulat.* **31**, 449 (2005).

[326] J. D. Gale, *Z. Kristallogr. Cryst. Mater.* **220**, 552 (2005).

[327] X. Zhang, H. Xie, M. Hu, H. Bao, S. Yue, G. Qin, G. Su, *Phys. Rev. B* **89**, 054310 (2014).

[328] R. Maranganti, P. Sharma, *Phys. Rev. Lett.* **98**, 195504 (2007).

[329] A.-L. Auzende, R. J.-M. Pellenq, B. Devouard, A. Baronnet, O. Grauby, *Phys. Chem. Miner.* **33**, 266 (2006).

[330] W. H. Press, *Numerical recipes* (Cambridge University Press, Cambridge, 1992).

[331] D. F. Shanno, *Math. Comp.* **24**, 647 (1970).

[332] P. P. Ewald, *Ann. Phys.* **369**, 253 (1921).

[333] D. Marx, J. Hutter, *Setting the stage: why ab initio molecular dynamics?* (Cambridge University Press, Cambridge, 2009), pp. 1–8.

[334] A. Stone, *The theory of intermolecular forces* (Oxford University Press, Oxford, 2013).

[335] D. Marx, J. Hutter, *Modern methods and algorithms of quantum chemistry* (NIC, 2000).

[336] S. Elliott, *The physics and chemistry of solids* (John Wiley & Sons, Ltd, 1998).

[337] P. Carloni, U. Rothlisberger, M. Parrinello, *Acc. Chem. Res.* **35**, 455 (2002).

[338] L. M. Ghiringhelli, E. J. Meijer, *J. Chem. Phys.* **122**, 184510 (2005).

[339] V. Speybroeck, R. Meier, *Chem. Soc. Rev.* **32**, 151 (2003).

[340] E. Braun, J. Gilmer, H. B. Mayes, D. L. Mobley, J. I. Monroe, S. Prasad, D. M. Zuckerman, *Living Journal of Computational Molecular Science* **1**, 5957 (2018).

[341] J. Hutter, M. Iannuzzi, F. Schiffmann, J. VandeVondele, *Wiley Interdiscip. Rev. Comput. Mol. Sci.* **4**, 15 (2014).

[342] A. Rajabpour, F. Y. Akizi, M. M. Heyhat, K. Gordiz, *Int. Nano Lett.* **3**, 58 (2013).

[343] M. Tafipolsky, R. Schmid, *J. Phys. Chem. B* **113**, 1341 (2009).

[344] M. Tafipolsky, S. Amirjalayer, R. Schmid, *J. Phys. Chem. C* **114**, 14402 (2010).

[345] C. Cheng, R. J. Needs, V. Heine, I. L. Jones, *Phase Transit.* **16**, 263 (1989).

[346] S. Ramasesha, *Pramana - J. Phys.* **23**, 745 (1984).

[347] A. M. Fernandez, O. N. Srivastava, *J. Appl. Crystallogr.* **8**, 645 (1975).

[348] M. Rao, O. N. Srivastava, *J. Phys. D Appl. Phys.* **11**, 919 (1978).

[349] S. Manzeli, D. Ovchinnikov, D. Pasquier, O. V. Yazyev, A. Kis, *Nat. Rev. Mater.* **2**, 17033 (2017).

[350] D. L. Duong, S. J. Yun, Y. H. Lee, *ACS Nano* **11**, 11803 (2017).

[351] Q. H. Wang, K. Kalantar-Zadeh, A. Kis, J. N. Coleman, M. S. Strano, *Nat. Nanotech.* **7**, 699 (2012).

[352] J. Wilson, A. Yoffe, *Adv. Phys.* **18**, 193 (1969).

[353] A. D. Yoffe, *Annu. Rev. Mater. Sci.* **3**, 147 (1973).

[354] A. D. Yoffe, *Adv. Phys.* **42**, 173 (1993).

[355] K. Motizuki, *Structural phase transitions in layered transition metal compounds* (Springer Netherlands, 1986).

[356] Y. M. Tairov, *Crystal growth and polytypism in silicon carbide* (Springer, Boston, MA, 1986).

[357] C. Rao, *Perovskites* (Academic Press, New York, 2003).

[358] Y. Lee, T. Lee, A. Soon, *J. Phys. Chem. C* **122**, 21644 (2018).

[359] S. S. Coutinho, M. S. Tavares, C. A. Barboza, N. F. Frazão, E. Moreira, D. L. Azevedo, *J. Phys. Chem. Solids* **111**, 25 (2017).

[360] R. M. Arif Khalil, F. Hussain, A. Manzoor Rana, M. Imran, G. Murtaza, *Physica E Low Dimens. Syst. Nanostruct.* **106**, 338 (2019).

[361] B. Palosz, *Z. Kristallogr.* **153**, 51 (1980).

[362] P. D. Ownby, X. Yang, J. Liu, *J. Am. Ceram. Soc.* **75**, 1876 (1992).

[363] G. C. Trigunayat, G. K. Chadha, *Phys. Status Solidi* **4**, 9 (1971).

[364] M. De Graef, M. E. McHenry, *Structure of materials: an introduction to crystallography, diffraction and symmetry* (Cambridge University Press, Cambridge, 2012).

[365] G. Hägg, *Arkiv. Kemi. Mineral. Geol. B* **16**, 1 (1943).

[366] W. J. Choyke, H. Matsunami, G. Pensl, *Silicon carbide: recent major advances* (Springer Science & Business Media, 2013).

[367] H. Jagodzinski, *Acta Crystallogr.* **2**, 201 (1949).

[368] D. Pandey, P. Krishna, *Mater. Sci. Eng.* **20**, 243 (1975).

[369] D. Pandey, P. Krishna, *Mater. Sci. Eng.* **26**, 53 (1976).

[370] B. E. Brown, *Acta Crystallogr.* **20**, 268 (1966).

[371] A. M. Glazer, *Acta Crystallogr. B* **28**, 3384 (1972).

[372] C. J. Howard, R. L. Withers, K. S. Knight, Z. Zhang, *Journal of Physics: Condensed Matter* **20**, 135202 (2008).

[373] P. M. Woodward, *Acta Crystallogr. B* **53**, 44 (1997).

[374] M. Kertesz, R. Hoffmann, *J. Am. Chem. Soc.* **105**, 3453 (1984).

[375] T. H. K. Barron, C. Domb, *Proc. R. Soc. A* **227**, 447 (1955).

[376] H. T. Stokes, D. M. Hatch, *J. Appl. Crystallogr.* **38**, 237 (2005).

[377] M. Troyer, H. Tsunetsugu, D. Würtz, *Phys. Rev. B* **50**, 13515 (1994).

[378] F. Di Salvo, B. Bagley, J. Voorhoeve, J. Waszczak, *J. Phys. Chem. Solids* **34**, 1357 (1973).

[379] Y. Liu, L. J. Li, W. J. Lu, R. Ang, X. Z. Liu, Y. P. Sun, *J. Appl. Phys.* **115**, 043915 (2014).

[380] A. Ribak, R. M. Skiff, M. Mograbi, P. K. Rout, M. H. Fischer, J. Ruhman, K. Chashka, Y. Dagan, A. Kanigel, *Sci. Adv.* **6** (2020).

[381] S. F. Meyer, R. E. Howard, G. R. Stewart, J. V. Acrivos, T. H. Geballe, *J. Chem. Phys.* **62**, 4411 (1975).

[382] J. Lüdecke, S. van Smaalen, A. Spijkerman, J. L. de Boer, G. A. Wiegers, *Phys. Rev. B* **59**, 6063 (1999).

[383] B. Sipos, A. F. Kusmartseva, A. Akrap, H. Berger, L. Forró, E. Tutiš, *Nat. Mater.* **7**, 960 (2008).

[384] F. Jellinek, *J. Less Common Met.* **4**, 9 (1962).

[385] Y. Liu, W. J. Lu, L. J. Li, X. D. Zhu, W. H. Song, R. Ang, L. S. Ling, X. Z. Liu, Y. P. Sun, *J. Appl. Phys.* **117**, 163912 (2015).

[386] E. Figueroa, Y.-K. Kuo, A. Olinger, M. Lloyd, L. Bastin, S. Petrotsatos, Q. Chen, B. Dobbs, S. Dev, J. Selegue, L. DeLong, C. Brock, J. Brill, *J. Solid State Chem.* **114**, 486 (1995).

[387] F. Jellinek, G. Brauer, H. Müller, *Nature* **185**, 376 (1960).

[388] F. Lévy, *Intercalated layered materials* (Springer Netherlands, 1979).

[389] R. H. F. Kadijk, F. Jellinek, *Rec. Two. Chim.* **83** (1964).

[390] B. E. Brown, D. J. Beerntsen, *Acta Crystallogr.* **18**, 31 (1965).

[391] H. Bai, M. Wang, X. Yang, Y. Li, J. Ma, X. Sun, Q. Tao, L. Li, Z.-A. Xu, *J. Phys. Condens. Matter* **30**, 095703 (2018).

[392] R. Huisman, F. Jellinek, *J. Less Common Met.* **17**, 111 (1969).

[393] F. Kadijk, F. Jellinek, *J. Less Common Met.* **23**, 437 (1971).

[394] H. Luo, W. Xie, J. Tao, H. Inoue, A. Gyenis, J. W. Krizan, A. Yazdani, Y. Zhu, R. J. Cava, *Proc. Natl. Acad. Sci.* **112**, E1174 (2015).

[395] J. A. Benda, *Phys. Rev. B* **10**, 1409 (1974).

[396] K. Hayashi, S. Fukuoka, S. Iba, N. Maeda, *J. Alloys Compd.* **383**, 69 (2004).

[397] K. Hayashi, T. Ikeuchi, H. Takeuchi, M. Shimakawa, *J. Alloys Compd.* **219**, 161 (1995).

[398] E. Bjerkelund, A. Kjekshus, *Acta Chem. Scand.* **21**, 2 (1967).

[399] S. Carr, S. Fang, E. Kaxiras, *Nat. Rev. Mater.* **5**, 748 (2020).

[400] J. Schlappa, U. Kumar, K. J. Zhou, S. Singh, M. Mourigal, V. N. Strocov, A. Revcolevschi, L. Patthey, H. M. Rønnow, S. Johnston, T. Schmitt, *Nat. Commun.* **9**, 5394 (2018).

[401] D. A. Tennant, T. G. Perring, R. A. Cowley, S. E. Nagler, *Phys. Rev. Lett.* **70**, 4003 (1993).

[402] M. Mourigal, M. Enderle, A. Klöpperpieper, J.-S. Caux, A. Stunault, H. M. Rønnow, *Nat. Phys.* **9**, 435 (2013).

[403] S. Glawion, J. Heidler, M. W. Haverkort, L. C. Duda, T. Schmitt, V. N. Strocov, C. Monney, K. J. Zhou, A. Ruff, M. Sing, R. Claessen, *Phys. Rev. Lett.* **107**, 107402 (2011).

[404] A. Nocera, N. D. Patel, J. Fernandez-Baca, E. Dagotto, G. Alvarez, *Phys. Rev. B* **94**, 205145 (2016).

[405] J. Schlappa, T. Schmitt, F. Vernay, V. N. Strocov, V. Ilakovac, B. Thielemann, H. M. Rønnow, S. Vanishri, A. Piazzalunga, X. Wang, L. Braicovich, G. Ghiringhelli, C. Marin, J. Mesot, B. Delley, L. Patthey, *Phys. Rev. Lett.* **103**, 047401 (2009).

[406] S. Johnston, C. Monney, V. Bisogni, K.-J. Zhou, R. Kraus, G. Behr, V. N. Strocov, J. Málek, S.-L. Drechsler, J. Geck, T. Schmitt, J. van den Brink, *Nat. Commun.* **7**, 10563 (2016).

[407] C. Monney, V. Bisogni, K.-J. Zhou, R. Kraus, V. N. Strocov, G. Behr, J. c. v. Málek, R. Kuzian, S.-L. Drechsler, S. Johnston, A. Revcolevschi, B. Büchner, H. M. Rønnow, J. van den Brink, J. Geck, T. Schmitt, *Phys. Rev. Lett.* **110**, 087403 (2013).

[408] J. Schlappa, K. Wohlfeld, K. J. Zhou, M. Mourigal, M. W. Haverkort, V. N. Strocov, L. Hozoi, C. Monney, S. Nishimoto, S. Singh, A. Revcolevschi, J. S. Caux, L. Patthey, H. M. Rønnow, J. van den Brink, T. Schmitt, *Nature* **485**, 82 (2012).

[409] K. S. Aleksandrov, J. Bartolomé, *Phase Transit.* **74**, 255 (2001).

[410] P. S. Whitfield, N. Herron, W. E. Guise, K. Page, Y. Q. Cheng, I. Milas, M. K. Crawford, *Sci. Rep.* **6**, 35685 (2016).

[411] C. Cheng, R. J. Needs, V. Heine, *J. Phys. C* **21**, 1049 (1988).

[412] Q.-M. Hu, R. Yang, *Acta Mater.* **61**, 1136 (2013).

[413] A. Singh, C. Dickinson, K. M. Ryan, *ACS Nano* **6**, 3339 (2012).

[414] A. Taroni, *Nat. Mater.* **13**, 915 (2014).

[415] J. Adamson, T. Lucas, A. Cairns, N. Funnell, M. Tucker, A. Kleppe, J. Hriljac, A. Goodwin, *Physica B: Condens. Matter* **479**, 35 (2015).

[416] T. Giamarchi, *Comptes Rendus Physique* **17**, 322 (2016).

[417] C. Di Castro, R. Raimondi, *Statistical mechanics and applications in condensed matter* (Cambridge University Press, Cambridge, Cambridge, 2015).

[418] B. E. Warren, *X-ray diffraction* (Courier Corporation, 1990).

[419] M. Žukovič, T. Idogaki, *Physica B Condens. Matter* **329-333**, 1055 (2003).

[420] C. Gong, K. Hu, X. Wang, P. Wangyang, C. Yan, J. Chu, M. Liao, L. Dai, T. Zhai, C. Wang, L. Li, J. Xiong, *Adv. Funct. Mater.* **28**, 1706559 (2018).

[421] A. B. Cairns, A. L. Goodwin, *Chem. Soc. Rev.* **42**, 4881 (2013).

[422] C. Faul, M. Antonietti, *Adv. Mater.* **15**, 673 (2003).

[423] D. W. Lyons, *Math. Mag.* **76**, 87 (2003).

[424] S. Antoniou, S. Lambropoulou, *PLoS one* **12**, 1 (2017).

[425] H. Hopf, *Math. Annal.* **104**, 637 (1931).

[426] D. Dragoman, M. Dragoman, *Quantum-Classical Analogies* (Springer-Verlag Berlin Heidelberg, 2004).

[427] C. Tzanakis, *Eur. J. Phys.* **19**, 69 (1998).

[428] L. Fritsche, M. Haugk, *Ann. Phys.* **12**, 371 (2003).

[429] A. Carati, L. Galgani, *Found. Phys.* **31**, 69 (2001).

[430] M. Grüninger, D. van der Marel, A. Damascelli, A. Erb, T. Nunner, T. Kopp, *Phys. Rev. B* **62**, 12422 (2000).

[431] R. Mittal, M. Zbiri, H. Schober, E. Marelli, S. J. Hibble, A. M. Chippindale, S. L. Chaplot, *Phys. Rev. B* **83**, 024301 (2011).

[432] M. J. Cliffe, A. L. Goodwin, *J. Appl. Crystallogr.* **45**, 1321 (2012).

[433] O. Breunig, M. Garst, A. Klümper, J. Rohrkamp, M. M. Turnbull, T. Lorenz, *Sci. Adv.* **3** (2017).

[434] M. J. Cliffe, J. A. Hill, C. A. Murray, F.-X. Coudert, A. L. Goodwin, *Phys. Chem. Chem. Phys.* **17**, 11586 (2015).

[435] Z. Li, C. Lu, Z. Xia, Y. Zhou, Z. Luo, *Carbon* **45**, 1686 (2007).

[436] L. Seyfarth, J. Seyfarth, B. V. Lotsch, W. Schnick, J. Senker, *Phys. Chem. Chem. Phys.* **12**, 2227 (2010).

[437] B. Lotsch, M. Döblinger, J. Sehnert, L. Seyfarth, J. Senker, O. Oeckler, W. Schnick, *Chem. Eur. J.* **13**, 4969 (2007).

[438] F. Jonietz, S. Mühlbauer, C. Pfleiderer, A. Neubauer, W. Münzer, A. Bauer, T. Adams, R. Georgii, P. Böni, R. A. Duine, K. Everschor, M. Garst, A. Rosch, *Science* **330**, 1648 (2010).

[439] A. Casiraghi, H. Corte-León, M. Vafaee, F. Garcia-Sanchez, G. Durin, M. Pasquale, G. Jakob, M. Kläui, O. Kazakova, *Commun. Phys.* **2**, 145 (2019).

[440] T. Nakajima, H. Oike, A. Kikkawa, E. P. Gilbert, N. Booth, K. Kakurai, Y. Taguchi, Y. Tokura, F. Kagawa, T. Arima, *Sci. Adv.* **3** (2017).

[441] A. B. Borisov, F. N. Rybakov, *JETP Lett.* **90**, 544 (2009).

[442] A. O. Leonov, I. E. Dragunov, U. K. Rößler, A. N. Bogdanov, *Phys. Rev. E* **90**, 042502 (2014).

[443] L. Cattaneo, Z. Kos, M. Savoini, P. Kouwer, A. Rowan, M. Ravnik, I. Musevic, T. Rasing, *Soft Matter* **12**, 853 (2016).

[444] W. Jiang, P. Upadhyaya, W. Zhang, G. Yu, M. B. Jungfleisch, F. Y. Fradin, J. E. Pearson, Y. Tserkovnyak, K. L. Wang, O. Heinonen, S. G. E. te Velthuis, A. Hoffmann, *Science* **349**, 283 (2015).

[445] C. J. Kepert, M. J. Rosseinsky, *Chem. Commun.* **1**, 31 (1998).

[446] Y. Peng, T. Gong, K. Zhang, X. Lin, Y. Liu, J. Jiang, Y. Cui, *Nat. Commun.* **5**, 4406 (2014).

[447] Z. Han, W. Shi, P. Cheng, *Chinese Chem. Lett.* **29**, 819 (2018).

[448] L. Ma, C. Abney, W. Lin, *Chem. Soc. Rev.* **38**, 1248 (2009).

[449] V. V. Butova, M. A. Soldatov, A. A. Guda, K. A. Lomachenko, C. Lamberti, *Russ. Chem. Rev.* **85**, 280 (2016).

[450] S. Shimomura, M. Higuchi, R. Matsuda, K. Yoneda, Y. Hijikata, Y. Kubota, Y. Mita, J. Kim, M. Takata, S. Kitagawa, *Nat. Chem.* **2**, 633 (2010).

[451] R. B. Getman, Y.-S. Bae, C. E. Wilmer, R. Q. Snurr, *Chem. Rev.* **112**, 703 (2012).

[452] J. Liu, L. Chen, H. Cui, J. Zhang, L. Zhang, C.-Y. Su, *Chem. Soc. Rev.* **43**, 6011 (2014).

[453] R. E. Morris, X. Bu, *Nat. Chem.* **2**, 353 (2010).

[454] N. L. Evans, P. M. M. Thygesen, H. L. B. Boström, E. M. Reynolds, I. E. Collings, A. E. Phillips, A. L. Goodwin, *J. Am. Chem. Soc.* **138**, 9393 (2016).

[455] E. Eikeland, N. Lock, M. Filsø, M. Stingaciu, Y. Shen, J. Overgaard, B. B. Iversen, *Inorg. Chem.* **53**, 10178 (2014).

[456] T. Kawamichi, T. Haneda, M. Kawano, M. Fujita, *Nature* **461**, 633 (2009).

[457] Y. Inokuma, S. Yoshioka, J. Ariyoshi, T. Arai, Y. Hitora, K. Takada, S. Matsunaga, K. Rissanen, M. Fujita, *Nature* **495**, 461 (2013).

[458] Y. Inokuma, T. Arai, M. Fujita, *Nat. Chem.* **2**, 780 (2010).

[459] Y. Inokuma, M. Kawano, M. Fujita, *Nat. Chem.* **3**, 349 (2011).

[460] D. Andrienko, *J. Mol. Liq.* **267**, 520 (2018).

[461] Z.-Y. Du, Y.-P. Zhao, C.-T. He, B.-Y. Wang, W. Xue, H.-L. Zhou, J. Bai, B. Huang, W.-X. Zhang, X.-M. Chen, *Cryst. Growth Des.* **14**, 3903 (2014).

[462] R. Gaillac, P. Pullumbi, F.-X. Coudert, *J. Phys. Condens. Matter* **28**, 275201 (2016).

[463] C. G. Broyden, *Math. Comput.* **19**, 577 (1965).

[464] R. Dovesi, V. R. Saunders, C. Roetti, R. Orlando, C. M. Zicovich-Wilson, F. Pascale, B. Civalleri, K. Doll, N. M. Harrison, I. J. Bush, *CRYSTAL17 manual* (2017).

[465] A. R. Albunia, C. Gaeta, P. Neri, A. Grassi, G. Milano, *J. Phys. Chem. B* **110**, 19207 (2006).

[466] K. I. Hadjiivanov, D. A. Panayotov, M. Y. Mihaylov, E. Z. Ivanova, K. K. Chakarova, S. M. Andonova, N. L. Drenchev, *Chem. Rev.* (2020).

[467] M. Wahiduzzaman, N. Reimer, J.-P. Itié, N. Stock, G. Maurin, P. G. Yot, *Polyhedron* **155**, 144 (2018).

[468] A. P. Côté, A. I. Benin, N. W. Ockwig, M. O'Keeffe, A. J. Matzger, O. M. Yaghi, *Science* **310**, 1166 (2005).

[469] B. M. Weckhuysen, J. Yu, *Chem. Soc. Rev.* **44**, 7022 (2015).

[470] J. Li, A. Corma, J. Yu, *Chem. Soc. Rev.* **44**, 7112 (2015).

[471] H. Kikuchi, M. Yokota, Y. Hisakado, H. Yang, T. Kajiyama, *Nat. Mater.* **1**, 64 (2002).

[472] A. Sequeira, R. Chidambaram, *Acta Crystallogr.* **20**, 910 (1966).

[473] CrysAlisPRO, *Yarnton, England* .

[474] E. C. O'Quinn, J. Shamblin, B. Perlov, R. C. Ewing, J. Neuefeind, M. Feygenson, I. Gussev, M. Lang, *J. Am. Chem. Soc.* **139**, 10395 (2017).

[475] P. N. Gerlach, B. M. Powell, *J. Chem. Phys.* **85**, 6004 (1986).

[476] D. Voneshen, M. C. Hatnean, T. Perring, H. Walker, K. Refson, G. Balakrishnan, J. Goff, *arxiv:1809.06265* (2018).

[477] A. R. Overy, A. B. Cairns, M. J. Cliffe, A. Simonov, M. G. Tucker, A. L. Goodwin, *Nat. Commun.* **7**, 10445 (2016).

[478] A. Rosenzweig, D. T. Cromer, *Acta Crystallogr.* **12**, 709 (1959).

[479] J. L. Hoard, *Z. Kristallogr. Cryst. Mater.* **84**, 231 (1933).

[480] J. Li, Y. Xie, C. Zhang, K. Ma, F. Liu, W. Ao, Y. Li, C. Zhang, *ACS Appl. Mater. Interfaces* **11**, 20064 (2019).

[481] S. H. Lapidus, G. J. Halder, P. J. Chupas, K. W. Chapman, *J. Am. Chem. Soc.* **135**, 7621 (2013).

[482] D. Goldberger, E. Evlyukhin, P. Cifligu, Y. Wang, M. Pravica, *J. Phys. Chem. A* **121**, 7108 (2017).

[483] V. Kiryukhin, D. Casa, J. P. Hill, B. Keimer, A. Vigliante, Y. Tomioka, Y. Tokura, *Nature* **386**, 813 (1997).

[484] S. Grimme, J. Antony, S. Ehrlich, H. Krieg, *J. Chem. Phys.* **132**, 154104 (2010).

[485] K. Doll, P. Pyykkö, H. Stoll, *J. Chem. Phys.* **109**, 2339 (1998).

[486] K.-J. Range, S. Kühnel, M. Zabel, *Acta Crystallogr. C* **45**, 1419 (1989).

[487] J. C. F. Colis, C. Larochelle, R. Staples, R. Herbst-Irmer, H. Patterson, *Dalton Trans.* **4**, 675 (2005).

Appendix A: Ice like disorder in $KRbZn(CN)_4$

The results outlined in this Appendix are from work pertaining to my DPhil which unfortunately had to be put on hold due to the ongoing COVID-19 pandemic. Preliminary results are included in this thesis for completeness, but concrete conclusions are unable to be drawn due to the limited data collected.

A.1 Summary

This study investigates the effects of temperature and composition on the average and local structure of the cyanospinel $Rb_xK_{2-x}[Zn(CN)_4]$. The structure of $K_2[Zn(CN)_4]$ is well characterised, with the potassium ions forming a pyrochlore sublattice [Fig. A.1] [472]. Our goal is to determine how compositional disorder manifests within the structure, with a further aim to examine how compositional disorder effects the phononic behaviour. We hypothesise that the disorder introduced by changing the occupation may lead to interesting properties due to selective phonon broadening, in this case potentially manifesting themselves through thermal conductivity. This study will ultimately play into a broader role of establishing dis-

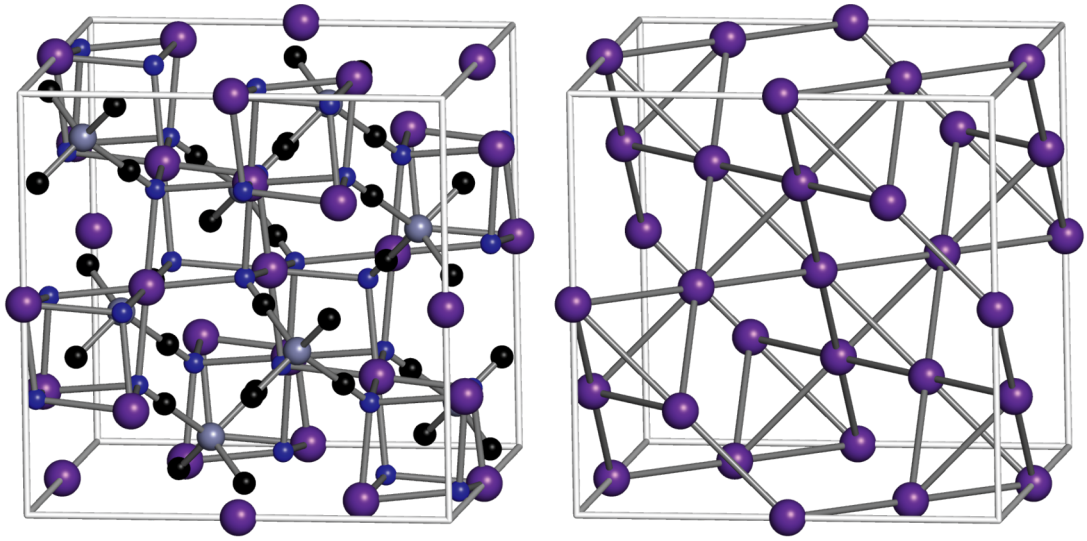

Figure A.1: Unit cell of $K_2[Zn(CN)_4]$, space group $Fd\bar{3}m$, (left) with the underlying pyrochlore sublattice of potassium ions (right).

order/property relationships. The results presented in this Appendix evidence correlated disorder within the system which order with decreasing temperature. The models presented to explain the disorder give an overview of how different forms of disorder may affect the diffuse scattering. Further work is required to correctly identify the precise form of disorder within the system.

A.2 Synthesis and experiment

All members of the solid solution $Rb_xK_{2-x}[Zn(CN)_4]$ were synthesised by dissolving different ratios of $K_2[Zn(CN)_4]$ and $Rb_2[Zn(CN)_4]$ separately in 10mL of distilled water. The two solutions were combined at room temperature, stirred until dissolved (approximately 10 minutes), and left to crystallise in a watchglass covered with a crystallising dish until crystals formed. The mass of $K_2[Zn(CN)_4]$ and $Rb_2[Zn(CN)_4]$ used to form each member of the solid solution is shown in Table A.1.

x	$K_2[Zn(CN)_4]$ (g)	$Rb_2[Zn(CN)_4]$ (g)
0	0	0.1737
0.2	0.0126	0.1564
0.6	0.0378	0.1216
1.0	0.0631	0.0869
1.4	0.0884	0.0521
1.8	0.1136	0.0173
2.0	0.1262	0

Table A.1: Mass of $K_2[Zn(CN)_4]$ and $Rb_2[Zn(CN)_4]$ used for the synthesis of different members of the solid solution $Rb_xK_{2-x}[Zn(CN)_4]$.

$K_2[Zn(CN)_4]$ was purchased as used and $Rb_2[Zn(CN)_4]$ was synthesised via ion-exchange of an aqueous solution of $K_2[Zn(CN)_4]$ with a concentrated solution of 2M RbOH. The ion-exchange column was loaded with 100g of Dowex 50W $\times$4 hydrogen form ion exchange resin and rinsed thoroughly with distilled water. The column was then saturated with RbOH, replacing the H^+ ions with Rb^+ ions. 2.03g of $K_2[Zn(CN)_4]$ was dissolved in 50mL of water and added to the ion exchange column. This solution was then run through the column with distilled water and the filtrate was rotary evaporated. The column was regenerated by washing through a solution of 2M RbOH before repeating the process twice with the filtrate solution. The resulting filtrate was left to crystallise in a watchglass covered with a crystallising dish until crystals formed.

For structural determination, in-house powder X-ray diffraction measurements (PXRD) were carried out on all members of the solid solution using a Bruker D8 instrument operating in Bragg-Brentano geometry with $Cu_{K_{\alpha1}/K_{\alpha2}}$ radiation (λ = 1.5406 Å). Patterns were collected for 20 minutes in the $(7-96)^\circ$ 2θ range. The samples were prepared by finely grinding the crystals using a pestle and mortar and loaded onto a flat plate zero background Si single crystal sample holder.

Single crystal X-ray diffraction (SCXRD) measurements were performed by Dr. Arkadiy Simonov for the $x = 1$ ($KRb[Zn(CN)_4]$) sample at I19, Diamond Light source, Didcot, Oxfordshire. A charge coupled device detector and a four-circle κ goniometer were used. Measurements were collected at 100 and 300 K. Data integration and reduction from these experiments were carried out using the CrysAlisPro [473] package. The radiation source had a wavelength of $\lambda = 0.6889$ Å and low temperature measurements were performed with an Oxford Cryosystems HeliX openflow helium cryostat. Samples were prepared by harvesting single crystals by hand.

A.3 Experimental results

From considering the in-house PXRD measurements, the symmetry of the material seems to be lowered with increased Rb concentration, excluding the end member, due to the formation of extra peaks on increasing x [Fig. A.2]. These peaks are unable to be characterised by the space group $Fd\bar{3}m$ which accurately represents both end members [Fig. A.3], albeit $K_2[Zn(CN)_4]$ may not be as pure as expected due to the inaccuracy of the intensity matching from Pawley refinements, especially with the first peak [Fig. A.3(a)]. Although PXRD data evidences symmetry lowering due to the unresolved peaks from the Pawley refinements [Fig. A.3(b)], this symmetry lowering is absent in the preliminary $x = 1$ SCXRD measurements [Fig. A.4]. Moreover, looking at the sample through a microscope, multiple crystallites formed in a variety of shapes, suggesting more than one phase formed. These observations indicate the additional peaks seen in the diffraction pattern are related to the formation of a side phase rather than symmetry lowering. Future work will examine

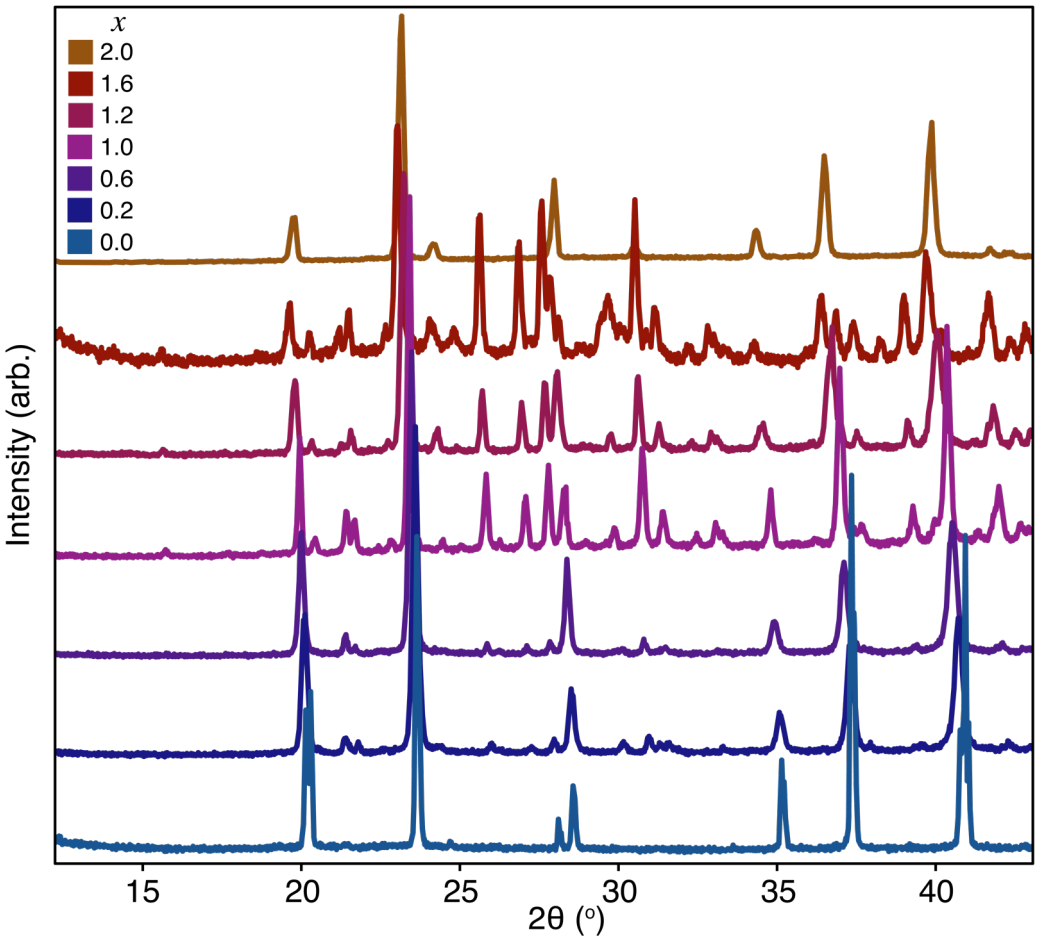

Figure A.2: PXRD patterns of the solid solution of $Rb_xK_{2-x}Zn(CN)_4$ where $x = 0$ at the bottom and $x = 2$ at the top, evidencing the linear change in lattice parameter with the uptake of Rb^+ ions, with the exception of the end member. $\lambda = 1.5406$ Å.

the impurity phases, however single crystal analysis does not require knowledge of the other phases formed. As such, understanding the other phases is beyond the scope of the current work and is unnecessary for the results presented. Assuming the extra peaks are indeed a side phase, the average structure of the end members is face-centered cubic (space group $Fd\bar{3}m$) with a linearly changing lattice parameter with composition [Fig. A.5].

Initial SCXRD measurements evidence structured diffuse scattering present in the $x = 1$ phase (*i.e.* $KRb[Zn(CN)_4]$) with the space group $Fd\bar{3}m$, signalling short-

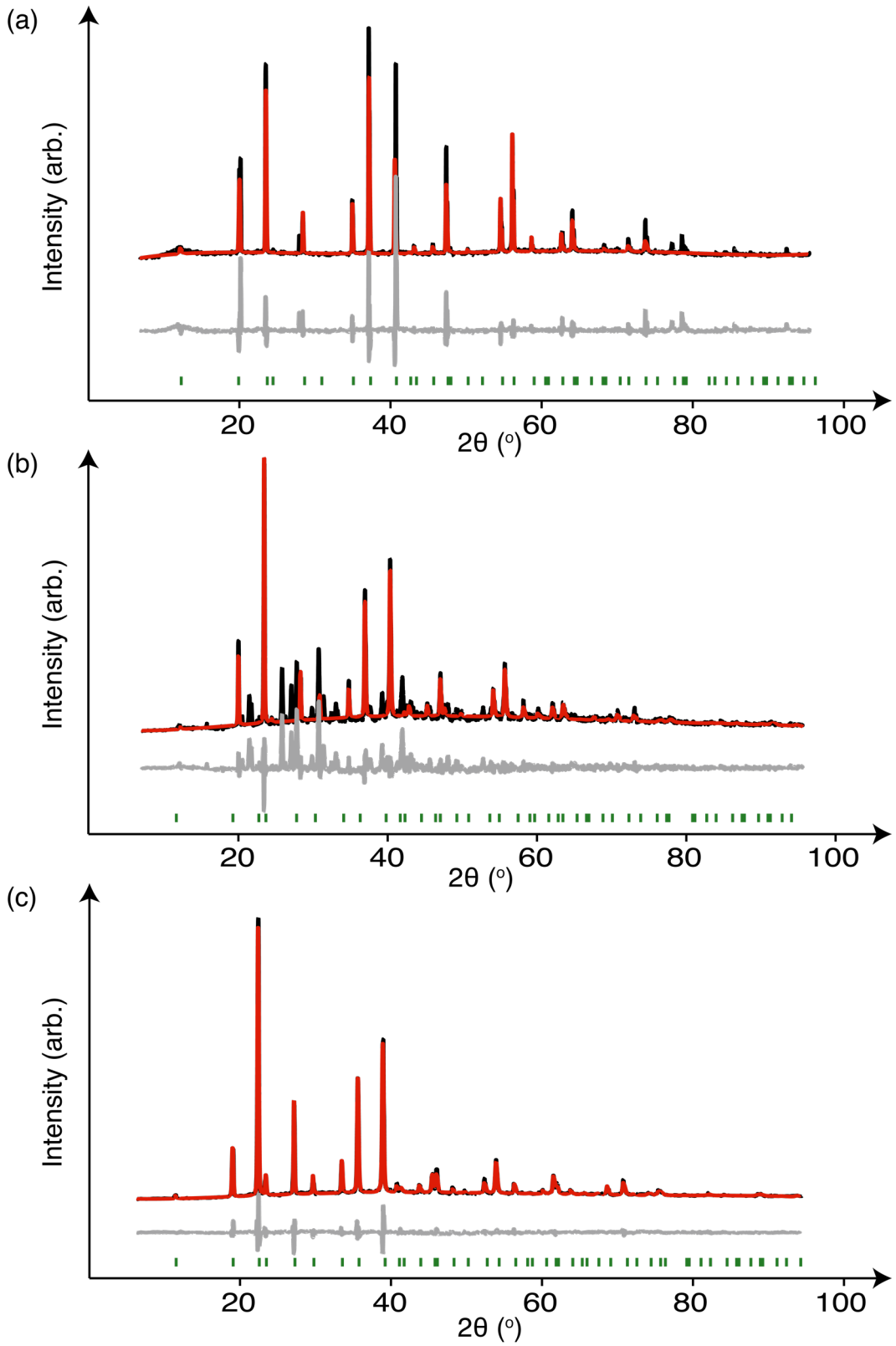

Figure A.3: Powder X-ray diffraction pattern for (a) $K_2[Zn(CN)_4]$, (b) $RbK[Zn(CN)_4]$, and (c) $Rb_2[Zn(CN)_4]$ measured at ambient temperatures (black line) and Pawley fit (red line) to the space group $Fd\bar{3}m$, with difference (data – fit) shown in grey. Representation of the crystallographic model is shown in Fig. A.1.

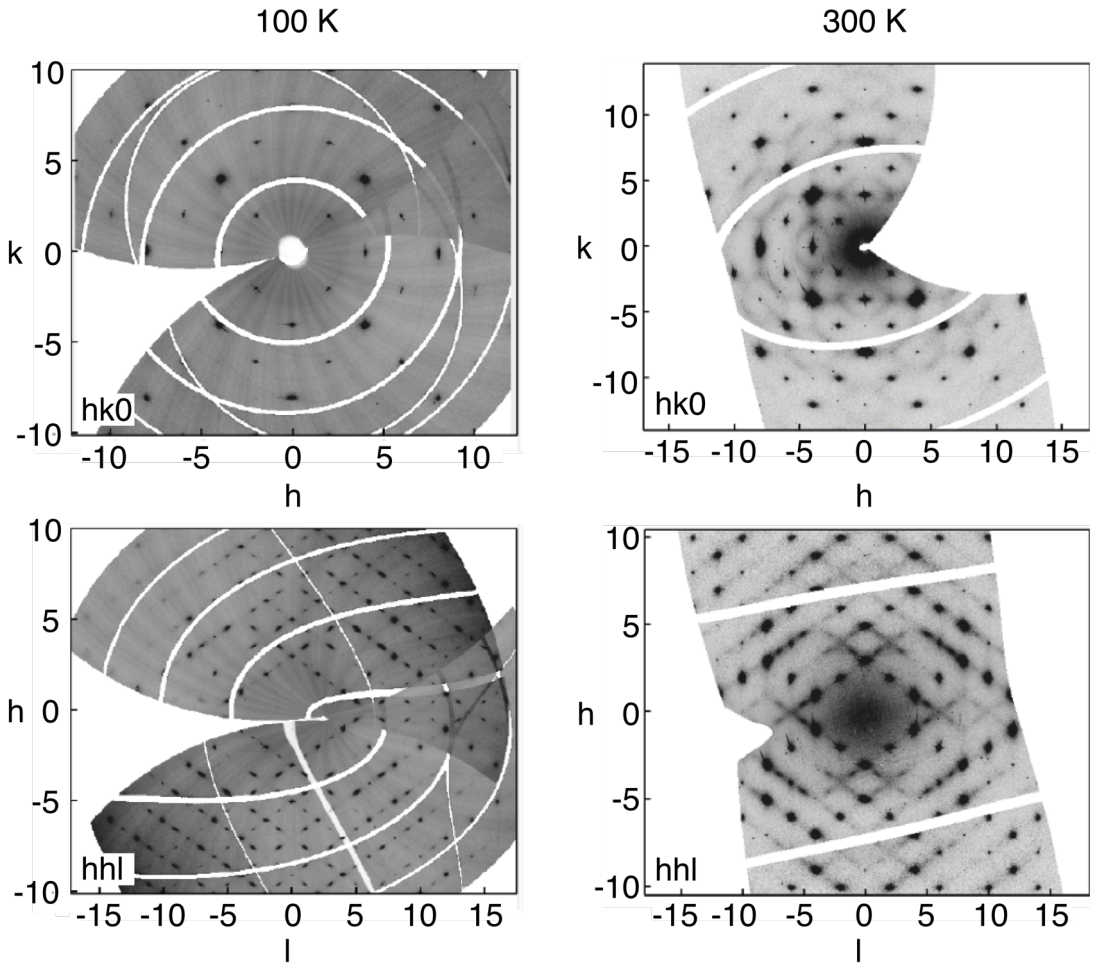

Figure A.4: SCXRD patterns of $KRb[Zn(CN)_4]$ at low temperature (left) and room temperature (right) showing the formation of satellite peaks in the (hhl) plane with decreasing temperature.

range order but long-range disorder caused by local interactions between the ions competing on the two sites [Fig. A.4]. Moreover, there is a pronounced effect of temperature on the structured diffuse scattering.

As the potassium and rubidium ions have different ionic radii (0.133 nm and 0.148 nm respectively), we expect that replacing half the potassium ions with rubidium ions, as is the case where $x = 1$, would lead to compositional ice-like disorder on the pyrochlore lattice [Fig. A.6], seen in similar systems such as the spinel

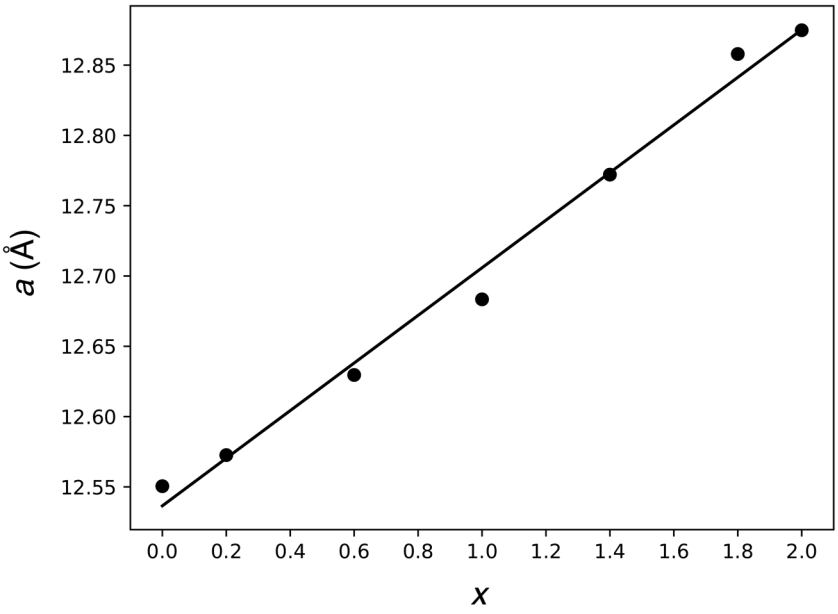

Figure A.5: Cubic lattice parameter, a, as a function of Rb composition x as determined by Pawley refinements in space group $Fd\bar{3}m$.

$Mg_{1-x}Ni_xAl_2O_4$ [474]. As a side note, ice-like disorder would not lead to a lowering of symmetry as it is a short-range ordering effect that usually leads to long-range disorder, leaving the average symmetry unchanged. These single crystal data show a stark difference from the characteristic pinch points expected for ice-like disorder [135, 136]. Instead, the diffuse scattering is more structured at ambient conditions which disappears at lower temperatures, condensing out to peaks in the (hhl) plane [Fig. A.4]. This study aims to use statistical mechanical models to understand the composition and temperature dependence of the diffuse scattering. The preliminary results presented in this Appendix focus on the ambient temperature data.

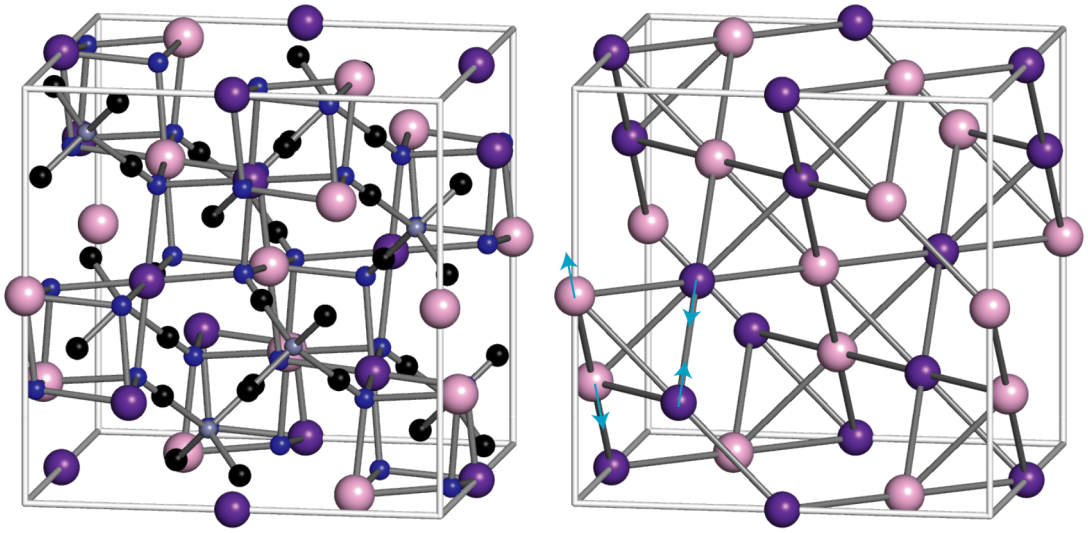

Figure A.6: Predicted unit cell for KRb[Zn(CN)$_4$] (left), space group $Fd\bar{3}m$, with half the potassium ions replaced with rubidium ions which could lead to ice-like compositional disorder on the pyrochlore lattice (right). Blue arrows on one of the tetrahedra represent the displacement which may occur due to the difference in ionic radius between the two ions.

A.4 Models

To determine the driving force of the disorder, we used a combination of Monte Carlo simulations and lattice dynamical calculations with a range of chemically sensible models to analyse the effects of different types of disorder on the diffuse scattering. The models we employed contained a variety of forms of disorder, outlined below.

(i) Compositional disorder in the form of ice rules

(ii) Positional disorder due to displacements from the underlying ice rules

(iii) Positional disorder cause by rigid unit mode activation of the kagome layers perpendicular to the ⟨111⟩ axes.

Compositional disorder manifesting as ice rules has long been known to form on pyrochlore lattices such as the inverse spinel Fe_3O_4 [137] and the displacement of the associated ions within this system is a natural conclusion due to the large difference in ionic radii between the two ions [Fig. A.6]. Including the rigid unit mode (RUM) activation is born out of phenomena observed in a similar system, $K_2[Hg(CN)_4]$. Here the compound has the same cubic symmetry at high temperature ($Fd\bar{3}m$), but on decreasing temperature, the structure transitions to the rhombohedral space group ($R\bar{3}c$) [Fig. A.7(a)-(b)] [475]. This is consistent with rotations of the $Hg(CN)_4$ tetrahedron as well as activation of the rigid unit modes—lattice vibrations where the network can rotate/translate without distorting—of the kagome layer formed by the face of the K^+ tetrahedra perpendicular to the $\langle 111 \rangle$ axis [Fig. A.7(c)-(d)]. We suggest that the differing ion sizes in our system may activate the RUMs around each of the 4 $\langle 111 \rangle$ axes, leading to distortions of the tetrahedra. The interplay of the degrees of freedom outlined above informed our four test models:

(i) Rigid unit mode activation

(ii) Ice rules

(iii) Ice rules and ion displacements

(iv) Ice rules, rigid unit mode activation, and ion displacement.

Ice rules were implemented by running Monte Carlo simulations where each vertex of the tetrahedra was decorated with a variable, S_i, where $S_i = \pm 1$ and the energy was minimised when $\sum_i S_i = 0$ for each tetrahedra. Outputted configurations characterised $S = 1/-1$ as K^+/Rb^+ ions respectively. For models

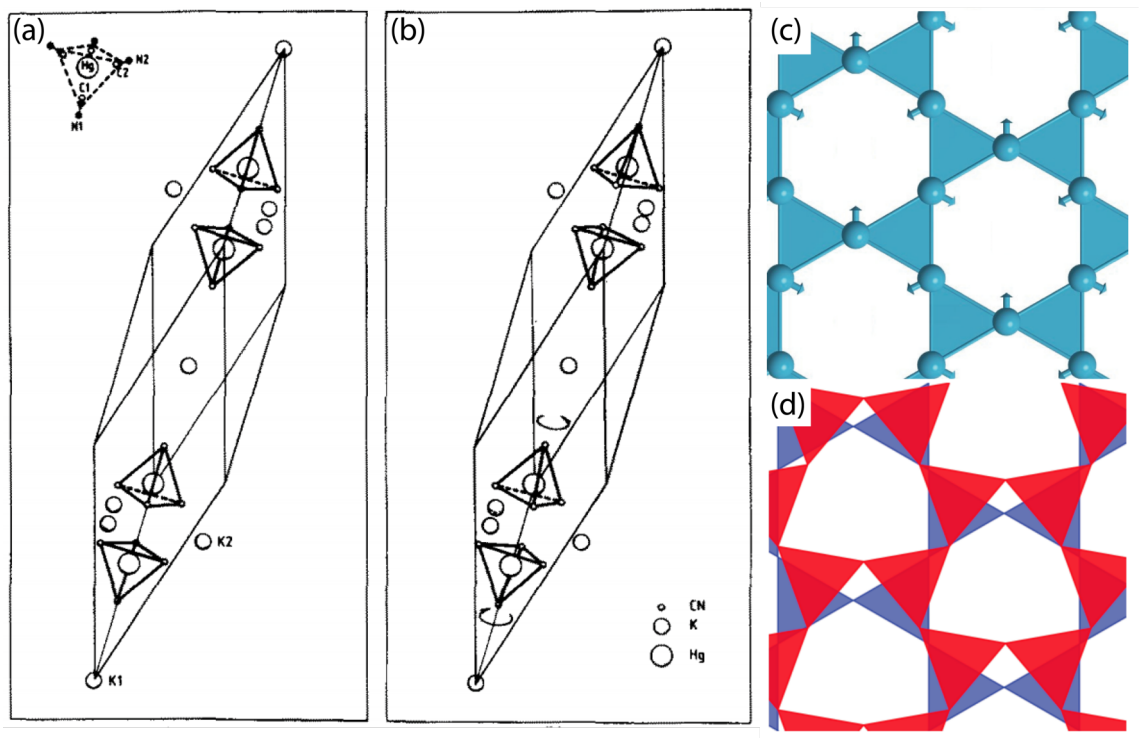

Figure A.7: Representation of the crystal structure of $K_2[Hg(CN)_4]$. (a) High temperature spinel (space group $Fd\bar{3}m$) and (b) low temperature trigonal phase showing the antiphase rotation of $Hg(CN)_4$ (space group $R\bar{3}c$) with the rhombohedral unit cell outlined. Figures adapted from Ref. [475] with permission from AIP Publishing. (c) Kagome structure with vectors representing displacements corresponding to low energy vibrations activating the RUMs. (d) Structure of the Kagome lattice after RUM displacement. Figure adapted from Ref. [476].

containing ion displacements, the Monte Carlo simulations used the same implementation as for ice rules but outputted the configurations with ionic displacements of neighbouring $S = 1$ variables towards one another and $S = -1$ variables away from one another. These configurations were inputted into GULP calculations with strong/medium/weak harmonic potentials between the K-K/Rb-K/Rb-Rb ions respectively. Lattice dynamical calculations were also used to activate the rigid unit modes by defining the equilibrium ion distance to be larger than allowed by the unit cell, activating the low energy vibrational modes. The lattice dynamical calculations then allowed the system to relax to equilibrium ionic separations for the different

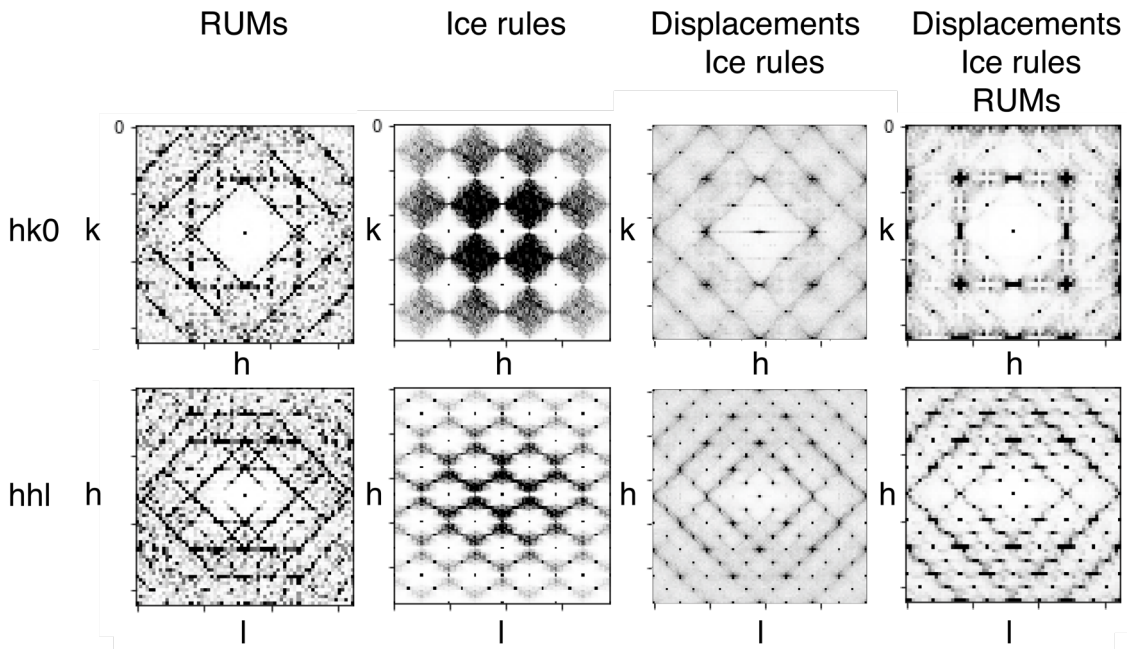

Figure A.8: Simulated SCXRD patterns with different forms of disorder in the $(hk0)$ and (hhl) planes. Left to right, $4 \times 4 \times 4$ supercell of $K_2[Zn(CN)_4]$ with rigid unit mode activation, $6 \times 6 \times 6$ supercell of $KRb[Zn(CN)_4]$ with compositional ice-like disorder, $6 \times 6 \times 6$ supercell of $KRb[Zn(CN)_4]$ with compositional ice-like disorder and displacements of K^+/Rb^+ ions within the same tetrahedra towards/away from each other, $4 \times 4 \times 4$ supercell of $KRb[Zn(CN)_4]$ with compositional ice-like disorder and displacements of K^+/Rb^+ ions within the same tetrahedra towards/away from each other and rigid unit mode activation. The field of view corresponds to the regions of reciprocal space $-16 \leq h, k, l \leq 16$.

disordered structures. Representative input files for the respective lattice dynamical calculations are included in Appendix F.

Simulated scattering planes were produced in a similar way to the process described in Chapter 5, although over a larger q range due to our interest in a larger area of reciprocal space rather than small angle scattering. Representative simulated scattering planes for each of the four models are shown in Fig. A.8. These simulations were carried out with varying supercell sizes due to the computational expense of different simulations, namely incorporating rigid unit cell activation. The scattering results from each model was averaged over 20 different configurations to

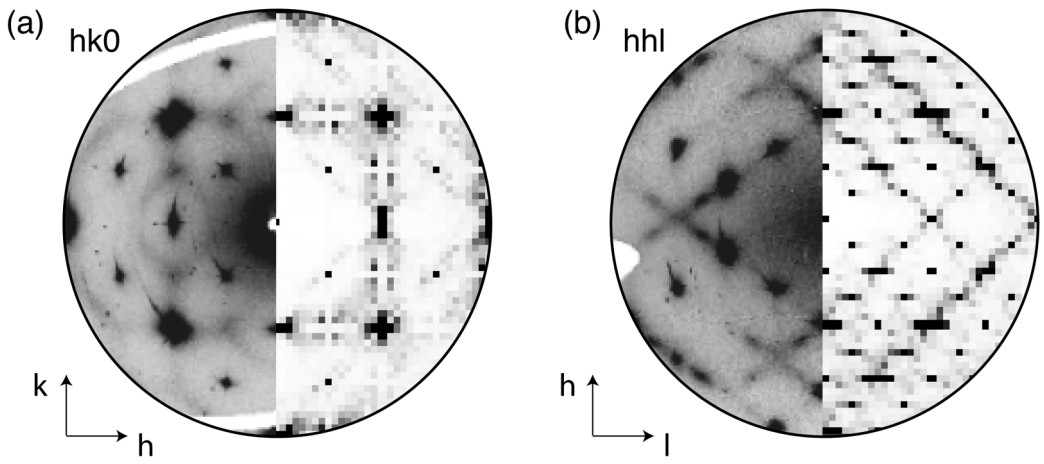

Figure A.9: Comparison of simulated and experimental SCXRD patterns of $KRb[Zn(CN)_4]$ at room temperature looking at the (a) $(hk0)$ and (b) (hhl) planes.

remove anomalies due to the small supercells. The model which best matches the data combines a number different sources of disorder including ice-like composition disorder, displacement of the compositionally disordered ions to form shorter K-K separations and longer Rb-Rb separations, and the activation of rigid unit modes within the kagome layers perpendicular to each of the $\langle 111 \rangle$ axes. The comparison to the experimental data is shown in Fig. A.9.

A.5 Outlook

This solid solution is more complex than simple compositional ice-like disorder as naively expected. Although the simulated data are able to emulate many of the diffuse features [Fig. A.8], they fail to capture some fundamental features of the structured diffuse scattering. Moreover the model is unable to account for the formation of satellite peaks seen with decreasing temperature. Due to the temperature dependence, our analysis has raised the question of whether disorder (and subse-

quent diffuse scattering) is present in all members of the solid solution, including the end members. Without single crystal measurements of all samples, particularly the end members, we cannot rule out the possibility of temperature dependent rigid unit mode activation occurring in all members. Therefore it is not yet possible to determine the extent to which the disorder seen is caused by composition alone.

Thus, increased analysis of the structural behaviour as a function of temperature and composition is required to fully characterise and measure the extent of compositional disorder. When synchrotrons allow external users on site, we plan on measuring variable temperature SCXRD patterns for all members of the solid solution. Currently, the scattering behaviour as a function of composition is unknown, but there is evidence of pronounced changes with varying temperature. Collecting data at regular increments will give a better overview of how the disorder changes with temperature, and allow for more accurate phase depiction.

For now we plan on using 3D-ΔPDF to refine our model as much as possible in order to describe the disorder seen in the room temperature $x = 1$ crystal. Once an accurate model is found, the goal here is to model its effects on the phononic behaviour of the material using super cell lattice dynamics [11, 477] with an aim to see how disorder might selectively broaden phonons, changing the thermoconductivity within the material.

Appendix B: Stacking disorder in $\mathbf{KAg}_x\mathbf{Au}_{1-x}\mathbf{(CN)}_2$

The results outlined in this Appendix are from work pertaining to my DPhil which unfortunately had to be put on hold due to the ongoing COVID-19 pandemic. Preliminary results are included in this thesis for completeness, but concrete conclusions are unable to be drawn due to the limited data collected.

B.1 Summary

The solid solution $K[Ag_xAu_{1-x}(CN)_2]$ adopts a variety of layer stacking sequences, including many surprisingly complex disordered states. The ambient-temperature structures of $K[Ag(CN)_2]$ and $K[Au(CN)_2]$ have been known for decades [478, 479]: both comprise alternating dicyanometallate $[M(CN)_2]^-$ (M = Ag, Au) and K^+ layers. Within an individual $[M(CN)_2]^-$ layer, the M^+ cations occupy the nodes of a kagome lattice. What differs between the M = Au and Ag systems is the relative position of these kagome layers from one to the next: the former adopts a CCP-like ABCABC... sequence (space group $R\bar{3}$), and the latter an HCP-like ABAB... sequence (space group $P\bar{3}1c$) [Fig. B.1(a)-(b)].

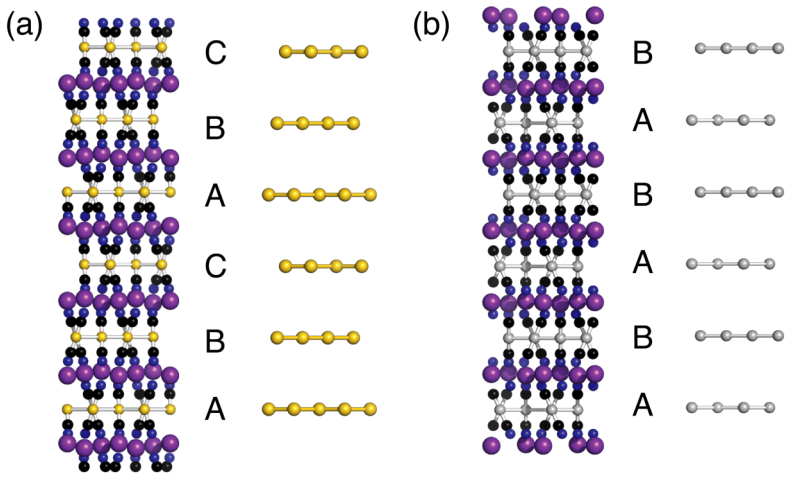

Figure B.1: (a) Representation of the ambient-temperature $R\bar{3}$ structure of K[Au(CN)$_2$]. The kagome layers of Au atoms are shown in gold, and the corresponding stacking sequence identified (here CCP-like) [478]. (b) The ambient-temperature $P\bar{3}1c$ of K[Ag(CN)2] is similar but with an HCP-like stacking arrangement [479].

In this study we show these stacking arrangements can be varied with composition and temperature, with all samples showing at least one first-order reconstructive transition near room temperature. As such, the family as a whole is an attractive system with which to explore mechanisms of chemical and thermal control over stacking complexity, such as that being explored in the development of next-generation thermoelectrics [480].

B.2 Synthesis and experiment

The synthesis of the compounds studied in this Appendix formed part of a project carried out by a summer student, Madeline Smith, under my supervision.

Members of the solid solution K[Ag$_x$Au$_{1-x}$(CN)$_2$] were synthesised by dissolving different ratios of K[Ag(CN)$_2$] and K[Au(CN)$_2$] separately in 10mL of distilled water. The two solutions were combined at room temperature, stirred until dissolved

x	$K[Ag(CN)_2]$ (g)	$K[Au(CN)_2]$ (g)
0	0	0.1
0.2	0.0146	0.0853
0.4	0.0313	0.0685
0.5	0.0411	0.0589
0.6	0.0511	0.0492
0.8	0.0735	0.0266
1.0	0.1	0

Table B.1: Mass of $K[Ag(CN)_2]$ and $K[Au(CN)_2]$ used for the synthesis of different members of the solid solution $K[Ag_xAu_{1-x}(CN)_2]$.

(approximately 10 minutes), and left to dry at room temperature until a mixture of crystals and white powder formed. The mass of $K[Ag(CN)_2]$ and $K[Au(CN)_2]$ used to form each member of the solid solution is shown in Table B.1.

For structural determination, all members of the solid solution were taken to the high-resolution powder diffraction beamline, I11 at Diamond Light Source in Didcot, Oxfordshire. The samples were prepared by finely grinding the powders using a pestle and mortar and loaded into borosilicate capillaries with diameters of 0.5 mm. The measurements make use of position-sensitive Mythen2 detectors; two measurements offset by 0.25° were made for each diffraction pattern, which were summed together to account for gaps in the detector. Heating and cooling between 100 and 500 K were performed using an Oxford Cryostreams cryostream (ramp rate 360K/h). For all measurements $\lambda = 0.826$ Å and four second measurements were taken. Data were collected at 100 and 300 K for all members of the solid solution, and variable temperature data between 100 and 500 K were collected for the three samples $x = 0, 0.5, 1$.

For the variable temperature measurements, data on both end members were

collected using two different capillaries of each sample to avoid potential radiation damage which can affect the structure and functionality of some inorganic materials [481–483]. The first capillary was placed on the instrument then heated directly to 500 K by moving the cryostream set to 500 K directly into position. After a couple of minutes to allow the sample to stabilise, a four second collection was taken. The sample was then cooled down by 25 K and the capillary was moved along the beam by 2.5 mm such that a new region of sample was in the beam and the sample was measured again. This was continued down to 325 K, then the capillary was changed to the second sample. The second capillary was measured at 300 K and then cooled down by 25 K and moved by 2.5 mm in the same fashion down to 100 K.

For the sample where $x = 0.5$, the data were collected slightly differently. Again two different capillaries of each sample were used to avoid any radiation damage effects, but for this member, the first capillary was placed on the instrument then cooled directly to 100 K by moving the cryostream set to 100 K directly into position. After a couple of minutes for the sample to stabilise, the first pattern was taken and the sample was measured on warming in 25 K steps to 275 K with a new part of the sample exposed each time. Then at 300 K the next capillary was mounted and measured on heating to 500 K.

B.3 Structural dependence on the composition of $\mathbf{K[Ag}_x\mathbf{Au}_{1-x}\mathbf{(CN)}_2\mathbf{]}$

At low temperatures (150 K), as expected, the structures of both end members are well explained by the phases recorded in the literature [Fig. B.2]. When $x = 0$,

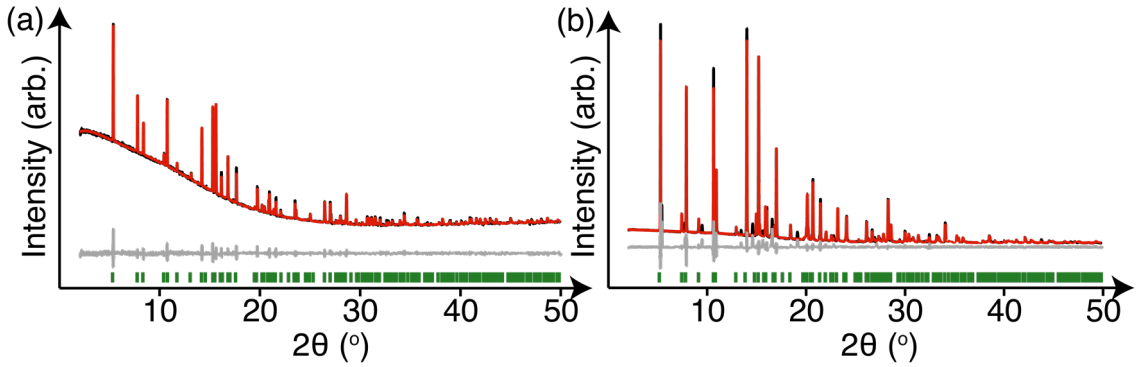

Figure B.2: Powder X-ray diffraction pattern for (a) $K[Au(CN)_2]$ and (b) $K[Ag(CN)_2]$ measured at 150 K (black line) and Pawley fit (red line), with difference (data – fit) to the space group (a) $R\bar{3}$ (b) $P\bar{3}1c$ shown in grey. Representations of the crystallographic models for both materials are shown in Fig. B.1.

($K[Au(CN)_2]$), the structure can be described by the space group $R\bar{3}$ where the kagome layers are stacked in an CCP arrangement. On increasing x, the diffraction patterns remain unchanged and the structures can still be described as CCP until $x = 0.5$ [Fig. B.3]. At this point, the peaks related to stacking within the CCP structure broaden in conjunction with the formation of of new peaks related to the HCP stacking arrangement. On further increasing Ag content, x, the new peaks increase in intensity and the broadened peaks disappear. When $x = 1$, there is no observed diffuse scattering and instead the structure can be described by the space group $P\bar{3}1c$ containing an HCP stacking arrangement of kagome layers as predicted from the literature.

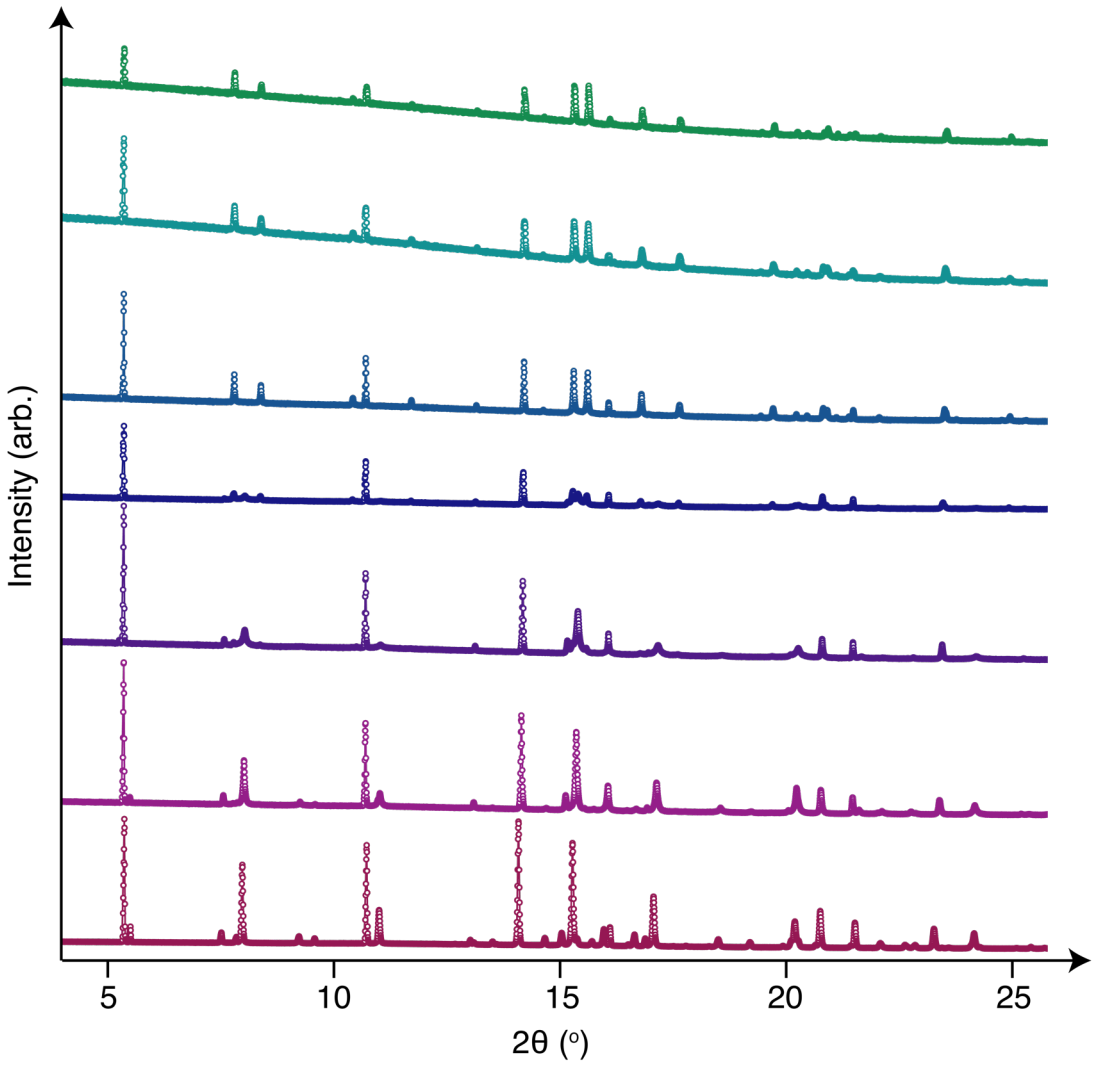

Figure B.3: PXRD patterns (measured with $\lambda = 0.826$ Å) for T= 100 K (apart from the gold end member which is shown at T= 150 K due to measuring difficulties) for members of the solid solution $K[Ag_xAu_{1-x}(CN)_2]$ where from top to bottom, $x = 0, 0.2, 0.4, 0.5, 0.6, 0.8, 1$. Intensities here are scaled in order to more easily compare the different diffraction patterns.

B.4 Temperature dependence of the structure of $K[Ag_xAu_{1-x}(CN)_2]$

When examining the ambient phase behaviour of the solid solution with changing composition, the room-temperature PXRD traces for both series end members are

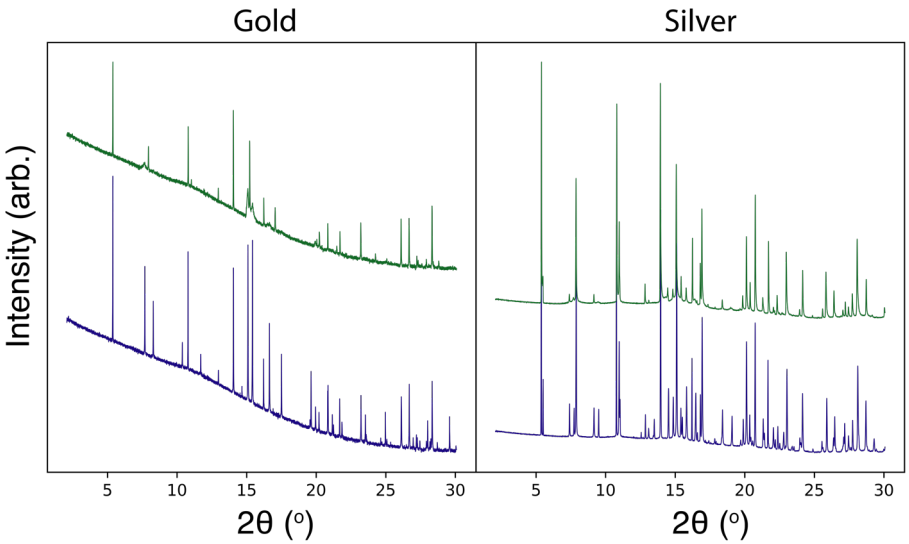

Figure B.4: PXRD patterns for $K[Au(CN)_2]$ (left) and $K[Ag(CN)_2]$ (right) at ambient temperature measured for as-made samples (blue traces) and after heating to 500 K then returning the sample to room temperature (green traces). The difference implies a history-dependence which we attribute to hysteresis.

different for as-made samples and for samples cooled from heating to 500 K [Fig. B.4]. This implies a hysteresis effect, which the data collected so far do not properly explore, owing to the non-continuous temperature history employed in the measurement sequences described in Section B.2. The limited availability of beamtime due to the ongoing pandemic has not allowed for exploratory temperature-dependent measurements for us to draw any specific conclusions from these observations, other than the obvious suggestion that we are seeing the effects of hysteresis.

On further examination of the structural temperature dependence, our preliminary PXRD measurements have shown that both end members undergo reconstructive transitions on heating from room temperature [Fig. B.5]. The M = Au system changes from CCP- to HCP-type stacking, and the M = Ag system changes from its HCP stacking to a disordered stacking arrangement at higher temperatures. Inter-

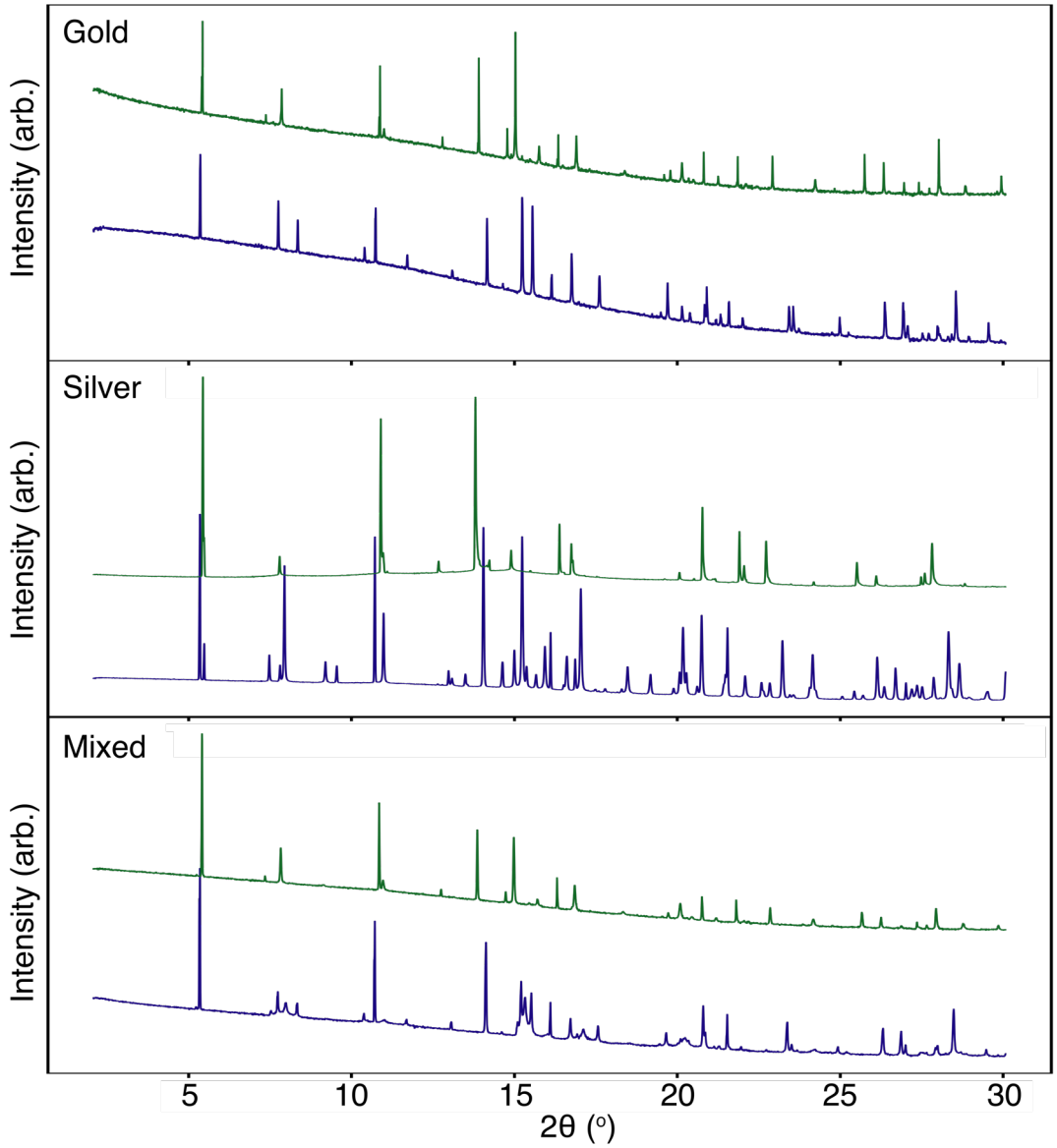

Figure B.5: PXRD patterns collected for three K[$Ag_xAu_{1-x}(CN)_2$] samples ($x = 0, 1, 0.5$, top to bottom) at temperatures above (475 K, green traces) and below (175 K, blue traces) their respective phase transitions ($\lambda = 0.826$ Å). The Warren line shapes characteristic of complex layer ordering are particularly clear for the $x = 0.5$ sample measured at 175 K.

mediate compositions such as M = $Ag_{0.5}Au_{0.5}$ adopt complex stacking arrangements intermediate to both HCP and CCP under ambient conditions, and transition to HCP-type arrangements on heating [Fig. B.5].

Historically, problems of polytypism have been interpreted in the context of one-dimensional Ising models, such as the ANNNI model [240, 411]. It is well known that the finite-temperature phase behaviour of ANNNI systems is a remarkably sensitive function of temperature and the J_1/J_2 ratio. We aim to interpret the thermodynamic phase behaviour of the $K[Ag_xAu_{1-x}(CN)_2]$ family using an ANNNI model (or similar), effectively establishing how the J_i values vary with composition x. The importance here is obvious: complex phases of particular interest—*e.g.* in a thermoelectric context—can then in principle be dialled up by choosing x accordingly.

B.5 Model and phase behaviour

Here we aim to investigate the extent to which the ANNNI model can describe the phases within our material. However, the ANNNI model gives rise to thermodynamic phase behaviour and our PXRD patterns indicate non-equilibrium behaviour, limiting the applicability of our analysis. Even so, it is useful to get an overview of where phases of our solid solution lie within the ANNNI model and how composition and temperature may enable us to navigate these phases.

The model describing the phase behaviour must incorporate two main effects. Firstly, the variation with the value of x, which on increasing Ag content gives a phase transition from CCP to HCP stacking. Secondly, the variation with temperature, which on increase causes the Au CCP stacked lattice and mixed Ag-Au phases to transition to an ordered HCP arrangement, and the Ag HCP stacked lattice to transition to a non close-packed arrangement with in-plane distortions. For the end members, the first observation is well accounted for by describing the stacking be-

haviour through the Ising model [Eqn. 1.1] where the interactions are "ferro" when M=Au and "antiferro" when M=Ag. However, a simple linear transition between the two interaction parameters is insufficient to explain the phase behaviour when $x = 0.5$, which will be discussed in more detail later.

Explaining the second observation is an even less trivial task. To analyse the relation between the ANNNI model and the solid solutions temperature dependence in more detail, we focus on the three compositions with variable temperature diffraction data $x = 0, 0.5, 1$. In referring to the stacking behaviour, we make use of the Zhandov notation explained in detail in Section 1.2.1. Here the variable describes the shift direction between neighbouring layers such that $\langle 2 \rangle$ = ABCABC *i.e.* CCP and $\langle 1 \rangle$ = ABAB *i.e.* HCP.

$K[Au(CN)_2]$ transitions from an ordered CCP arrangement to an ordered HCP structure with increasing temperature. On this transition, the PXRD patterns evidence diffuse behaviour through the broadening of diffraction peaks relating to planes involving the *c*-axis which we can attribute to some form of disordered stacking arrangement [Fig. B.6]. More specifically, this diffuse behaviour can be described as a disordered mixture of 2 (ABC) and 3 (ABCA) period modulations, where the modulation period decreases with temperature. Our data suggests these phases are not entirely a thermodynamic product, namely due to the hysteresis of the transition, but also as the mid-range temperatures cannot be sufficiently described by phases within the ANNNI model, nor by the addition of stacking faults within known phases. For example, the data collected at 375 K can be well described as a 'random' mixture of blocks of 2 and 3 period modulations but does not fit any of the

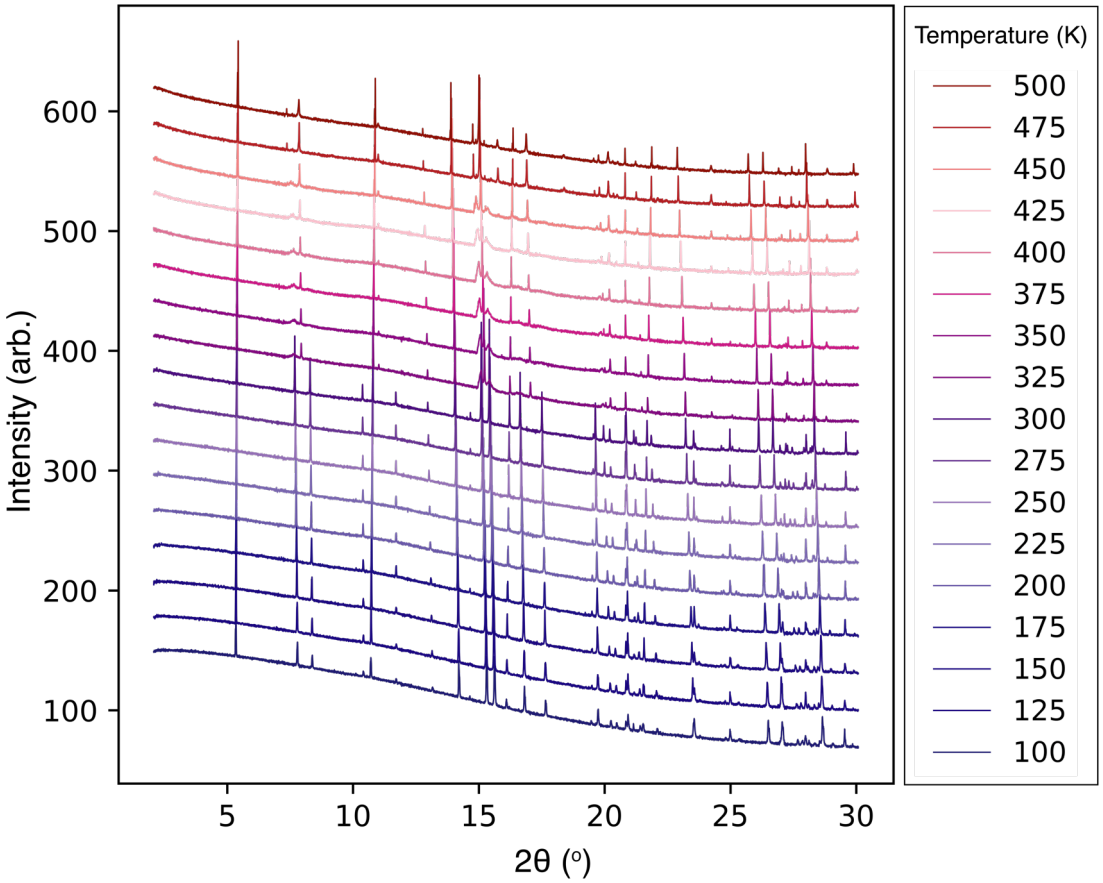

Figure B.6: Variable temperature PXRD patterns ($\lambda = 0.826$ Å) for K[Au(CN)$_2$] from 100 K to 500 K in 25 K increments.

ordered long period modulated phases of the finite temperature phase behaviour seen in the ANNNI model [Fig. B.7]. On increasing temperature, the structure can be attributed to phases within the ANNNI phase diagram, for example at 450 K the structure is well described by the frustrated $\langle 2 \rangle$ structure type with stacking faults [Fig. B.7]. Increasing the temperature further to 500 K leads to a transition to the ordered $\langle 1 \rangle$ phase. Therefore the series of phase transitions for the K[Au(CN)$_2$] structure loosely follow $\langle \infty \rangle \rightarrow \langle 2/3 \rangle \rightarrow \langle 2 \rangle \rightarrow \langle 1 \rangle$ with increasing temperature.

For $x = 0.5$, K[Au$_{0.5}$Ag$_{0.5}$(CN)$_2$], the low temperature diffraction patterns evidence a disordered HCP/CCP arrangement as they contain characteristic diffrac-

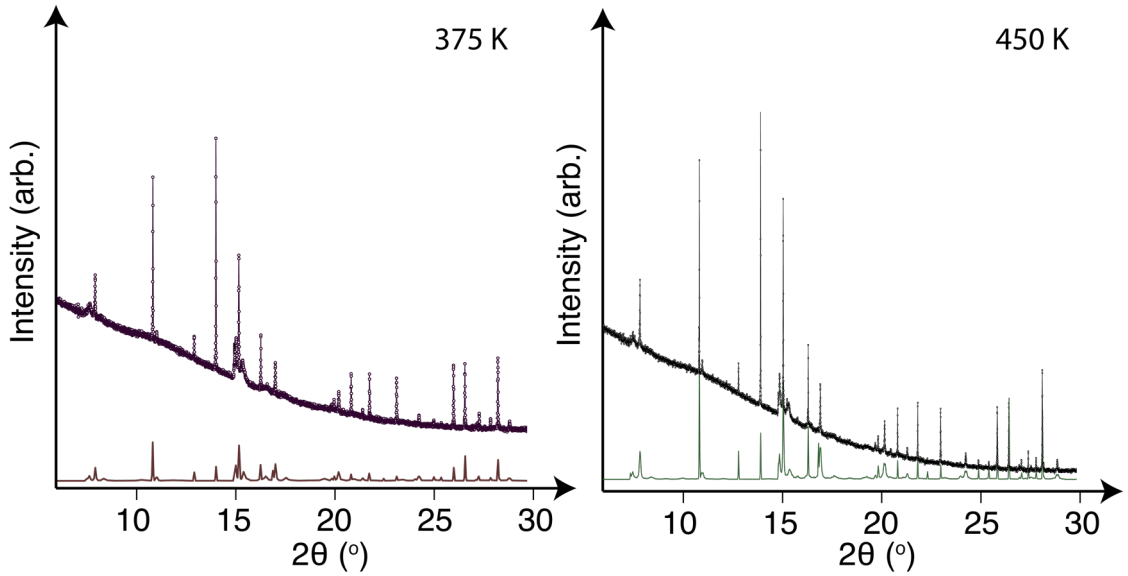

Figure B.7: Simulated (bottom) and experimental (top) diffraction patterns of $K[Au(CN)_2]$ at 375 K (left) and 450 K (right). The simulated patterns are for a random mixture of 2 and 3 modulated periods for 375 K, and a high temperature $\langle 2 \rangle$ phase (*i.e.* containing some stacking faults) at 450 K.

tion peaks of both phases [Fig. B.8]. Given the structural behaviour of the end members existing at two limiting phases of the Ising/ANNNI model (antiferro- and ferro-magnetic), the logical conclusion is for this structure to either be a completely disordered stacking arrangement between the two, or exist somewhere on the Ising model spectrum. However, Monte Carlo simulations of the ANNNI model with changing J_1 (and $J_2 > 0$) show the disordered HCP/CCP phase actually leads to one broad peak in the two characteristic areas $2\theta = 8°$ and $2\theta = 16°$ and any deviations away from $J_1 = 0$ result in either characteristic peaks of HCP or CCP, but never both [Fig. B.9]. Instead, the phase behaviour can only be explained through a non-uniform distribution of the crystallite composition in the sample. The diffraction data do not show any discernible peak-splitting driven by the sample, meaning that any compositional non-uniformity is subtle and probably a Gaussian distribu-

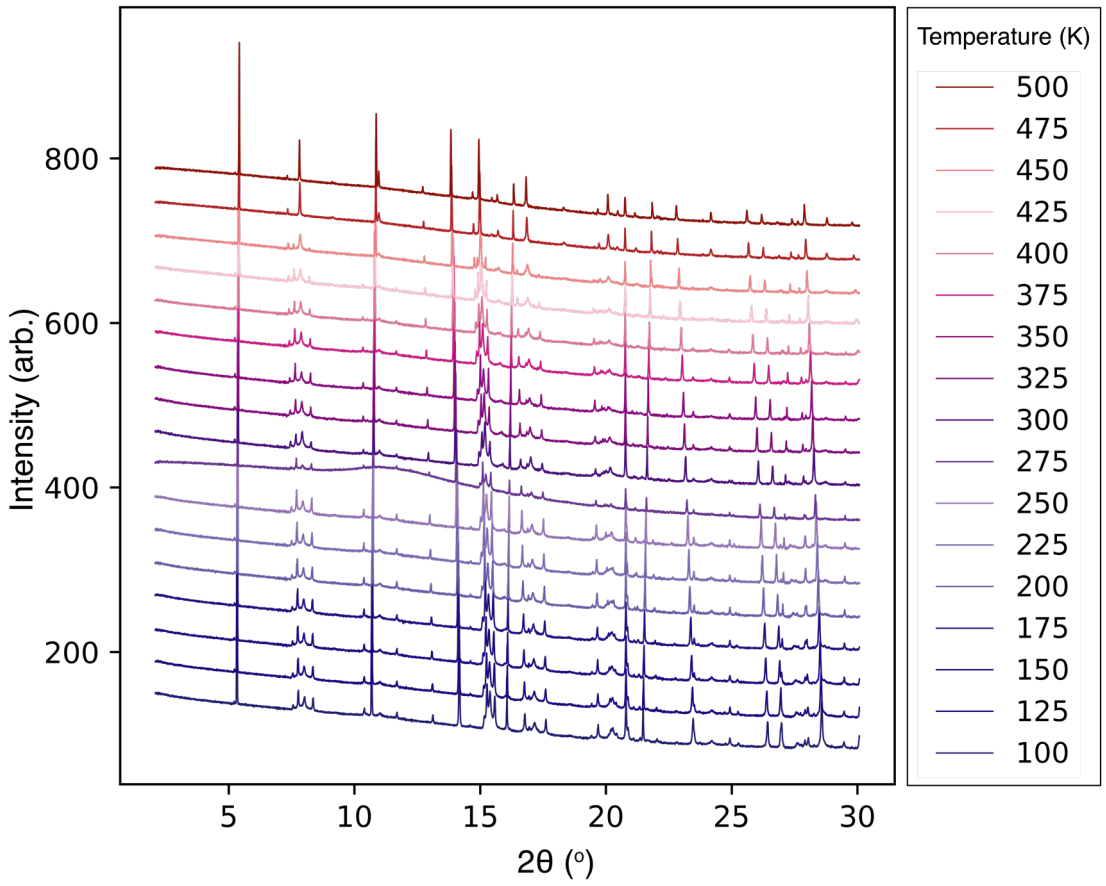

Figure B.8: Variable temperature PXRD patterns ($\lambda = 0.826\,\text{Å}$) for $K[Ag_{0.5}Au_{0.5}(CN)_2]$ from 100 K to 500 K in 25 K increments.

tion centred about the target composition, thus accounted for by the peakshape model [Fig. B.9]. This non-uniformity makes it hard to create any quantitative conclusions; however, it evidences similar behaviour to the gold end member of an CCP to HCP transition with increasing temperature through the loss/gain of peak intensity attributed to the CCP/HCP structure [Fig. B.8]. This transition to fully HCP stacking occurs at a lower temperature than for the gold end member, indicating that perhaps all members of the solid solution follow similar transitions but the transition may occur at different temperatures depending on the composition.

Lastly, we focus on the stacking behaviour of $K[Ag(CN)_2]$. Here the material

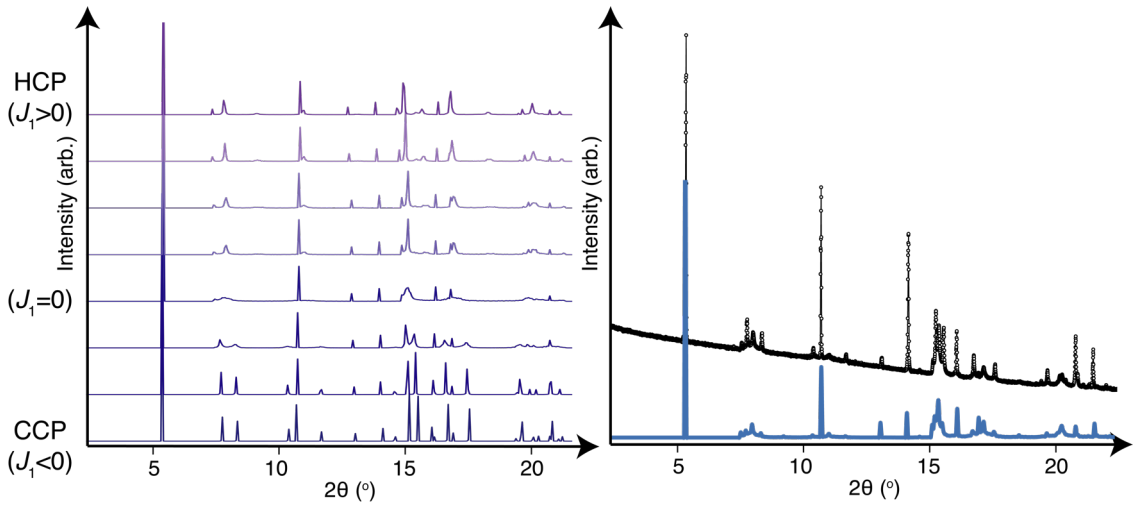

Figure B.9: Left, simulated diffraction patterns $K[Ag_{0.5}Au_{0.5}(CN)_2]$ following the Ising model with different interaction strengths going from CCP (bottom) to HCP (top). Right, simulated (bottom) and experimental (top) diffraction patterns of $K[Ag_{0.5}Au_{0.5}(CN)_2]$ at 125 K. This simulated diffraction pattern was prodcued by taking a Gaussian distribution of the diffraction patterns on the left hand side and combining them, evidencing the potential of non-uniform behaviour due to samples containing a variety of crystallite compositions.

transitions from an ordered HCP arrangement ($\langle 1 \rangle$) at low temperature to a substantially more disordered stacking arrangement than observed in the other two samples [Fig. B.10]. Here the stacking arrangement of the high temperature phase can be described as completely disordered where neighbouring metal layers have no preference for close-packing sites and can even sit in equivalent sites (*i.e.* stack AA) as evidenced by the complete depletion of characteristic HCP peaks relating to planes containing the *c*-axis. Moreover, the diffraction patterns indicate further structural changes with temperature due to loss in peak intensities attributed to in-plane reflections, signifying a structural transition within the stacking layers. This effect is not accounted for in 1D models of stacking behaviour by design. Thus to accurately describe the stacking arrangement in all phases, the ANNNI model is insufficient as it only allows for close-packed arrangements and instead we suggest

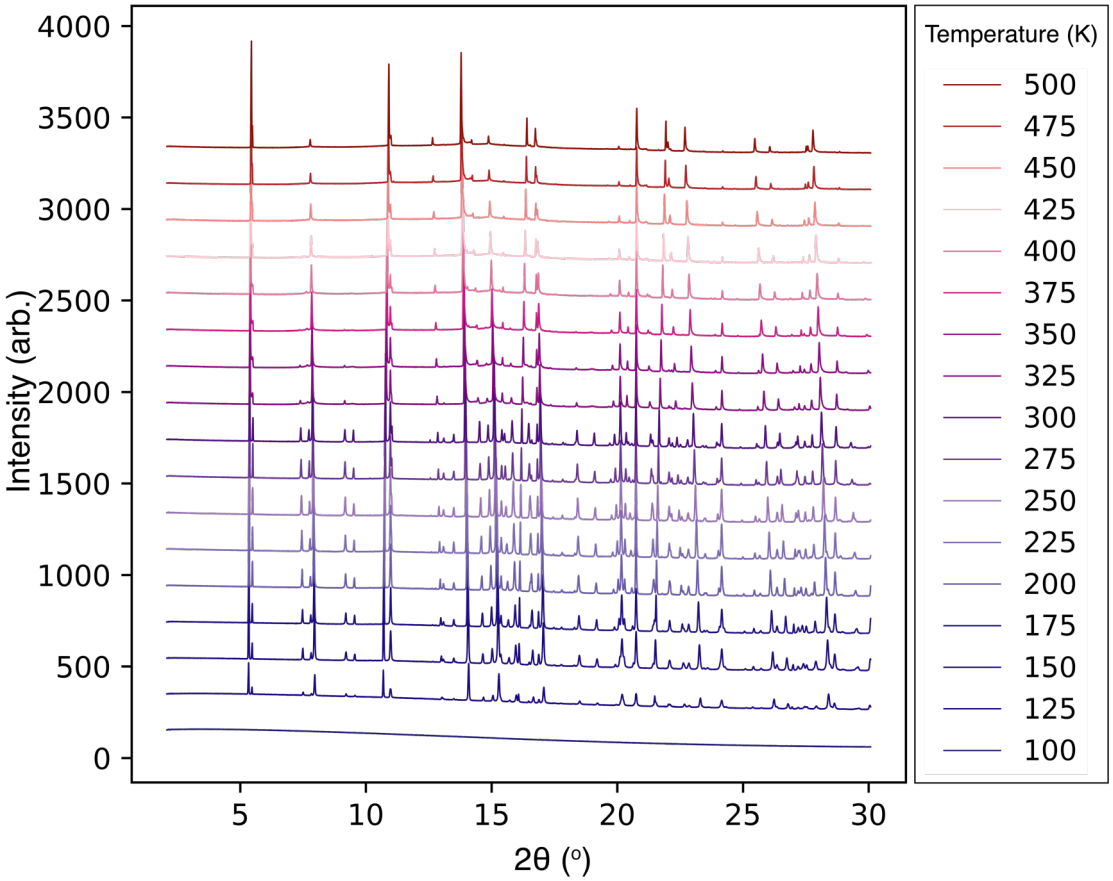

Figure B.10: Variable temperature PXRD patterns ($\lambda = 0.826\,\text{Å}$) for $K[Ag(CN)_2]$ from 100 K to 500 K in 25 K increments.

that perhaps a Potts model is required for more accurate representation of the phase behaviour.

B.6 DFT

Through this study, one of our aims was to determine the driving force responsible for the CCP to HCP transition on increasing temperature. To facilitate this transition under the ANNNI regime, the sign of the interaction parameter between nearest neighbours must be flipped. Understanding the change in stacking arrangement due to composition is a trivial task as it is well known that distinct ions can lead to

different stacking behaviour and thus changing the sign of the interaction parameter as a function of composition is chemically feasible [396]. However, temperature is less well known to affect the sign/strength of the interaction parameter without a thermal driving force such as thermal expansion. Therefore, we investigated the effect of thermal expansion on the energy of the two stacking arrangements by employing DFT calculations to determine the stability of the two end member structures with changing lattice parameters.

All calculations were performed with the CRYSTAL17 software [319] using the PBE-D3 exchange correlation functional [484] to account for dispersion effects from the gold ions, and double-ζ plus polarization basis sets were used where possible. For gold atoms, basis sets from Ref. [485] were used instead. The convergence criteria for geometry optimisation were the default values set out by CRYSTAL17 (Maximum gradient 0.0045 a.u., root mean squared gradient of 0.0030 a.u., maximum displacement 0.0018 a.u., root mean squared displacement of 0.0012 a.u.) and reciprocal space was sampled with a $5 \times 5 \times 5$ k-point mesh. A representative input file is included in Appendix F.

To understand how thermal expansion may effect the relative energy of the two structures, the calculations were run on unit cells of $K[Au(CN)_2]$ with both $R\bar{3}$ (CCP) and $P\bar{3}1c$ (HCP) space groups. First each structure was relaxed using the parameters set out above, and then subsequent calculations were performed to determine the energy as a function of the interlayer spacing between 6.7-7.6 Å by changing the c lattice parameter with constant a, b. The results from these calculations show there are no meaningful energy difference between the two structures and therefore

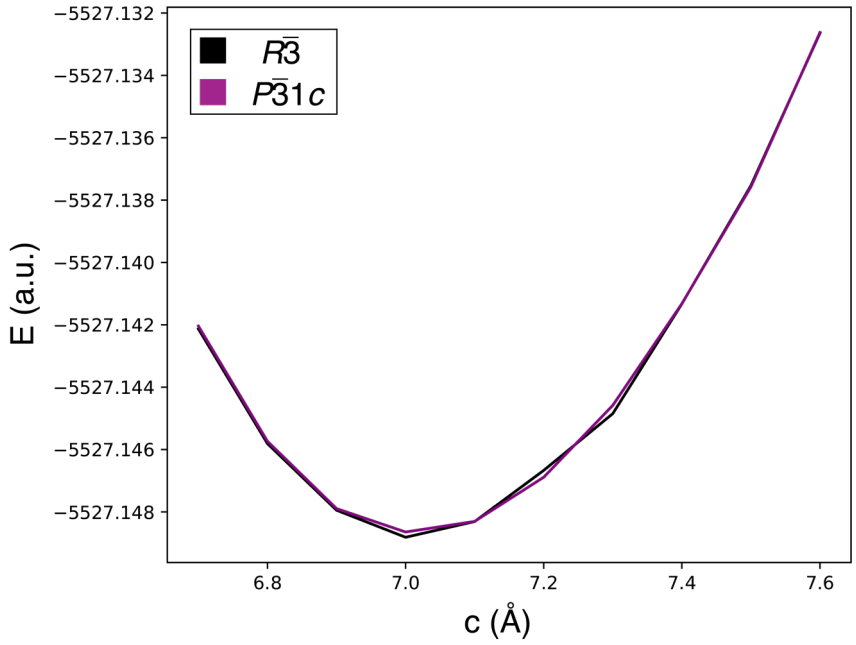

Figure B.11: Lattice energy of $K[Au(CN)_2]$ against the interlayer layer separation for the two different structure types $R\bar{3}$ (black) and $P\bar{3}1c$ (purple) produced from DFT calculations.

thermal expansion is unlikely to be responsible for the transition seen [Fig. B.11].

B.7 Outlook

Our preliminary measurements have established an overview of the phase behaviour of the family and have identified a strong history-dependence of the phase transitions we observe—as might be expected for a first-order transition. Although the structure is deceptively simple, there is obviously a profound effect of the atom type and temperature on the stacking behaviour. An overview of the phase behaviour seen from our data and where the transitions may occur in reference to the finite temperature ANNNI phase diagram is shown in Fig. B.12. For now, the driving forces behind some of the transitions still remains an unsolved question. Further measurements into the hysteretic behaviour will allow us to perfect our model in

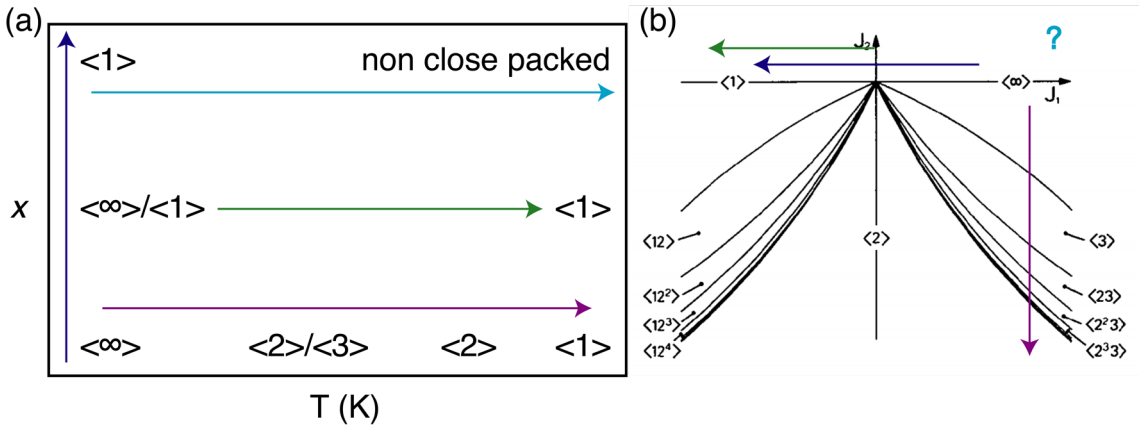

Figure B.12: (a) Schematic representation of a phase diagram of composition vs temperature for the different phases of $K[Ag_xAu_{1-x}(CN)_2]$. The coloured arrows represent the different transitions explained in the results section. (b) Finite temperature ANNNI phase diagram with arrows representing where the corresponding phase transition may sit. We note that some of the observations are unable to be fully described as laid out on the phase diagram (for example the gold phase transition—purple arrow—would not explain the observation of the high temperature $\langle 1 \rangle$ phase). The phase transition for the silver member (light blue) is represented as a question mark as the ANNNI model can not account for the observation of neighbouring layers in same close-packed sites. Figure adapted from Ref. [240].

order to fully represent the structural phase behaviour and may give further insight into the driving force of the CCP to HCP transition seen on increasing temperature.

Our aim now is to carry out a systematic investigation of the phase behaviour of key family members ($x = 0, 0.5, 1$) as a function of both temperature and heating/cooling rates. This will allow us to determine both the thermodynamics and kinetics of phase formation in this family. We will aim to interpret the thermodynamic phase behaviour of the $K[Ag_xAu_{1-x}(CN)_2]$ family using statistical mechanical models, effectively establishing how the J_i values vary with composition x. Arrhenius analysis of the rate-dependence of the hysteresis widths will allow us to determine an effective barrier height $\Delta(x)$ to layer rearrangement, and its compositional dependence. Taken together, these parameters will tell us how to choose composition and sample history to control layer stacking complexity in this family.

In the longer term, we wish to understand the connection between complex layer stacking arrangements and the vibrational properties of layered materials: ultimately it is the disorder-driven dampening of phonon lifetimes that is exploited in thermoelectric materials design. We will use harmonic supercell lattice-dynamical calculations [11, 477] to determine the effect of the stacking sequences identified on the corresponding phonon dispersion. In due course we hope to correlate these calculations with experimental measurements of the vibrational density of states.

There is a rich spectrum of chemical and physical properties yet to be explored in this seemingly simple family. Additionally, other $M[Ag/Au(CN)_2]$ compounds are known to have different stacking arrangements [486, 487]. This opens up an avenue of exploration into how the M^+ cation also affects the stacking behaviour. Moreover, the silver and gold ions sit within a kagome lattice, so the $x = 0.5$ sample may draw conceptual parallels between compositional disorder and the triangular Ising antiferromagnet.

Appendix C: Supplementary information for Chapter 3

C1 Simulated diffraction patterns of the limiting phases

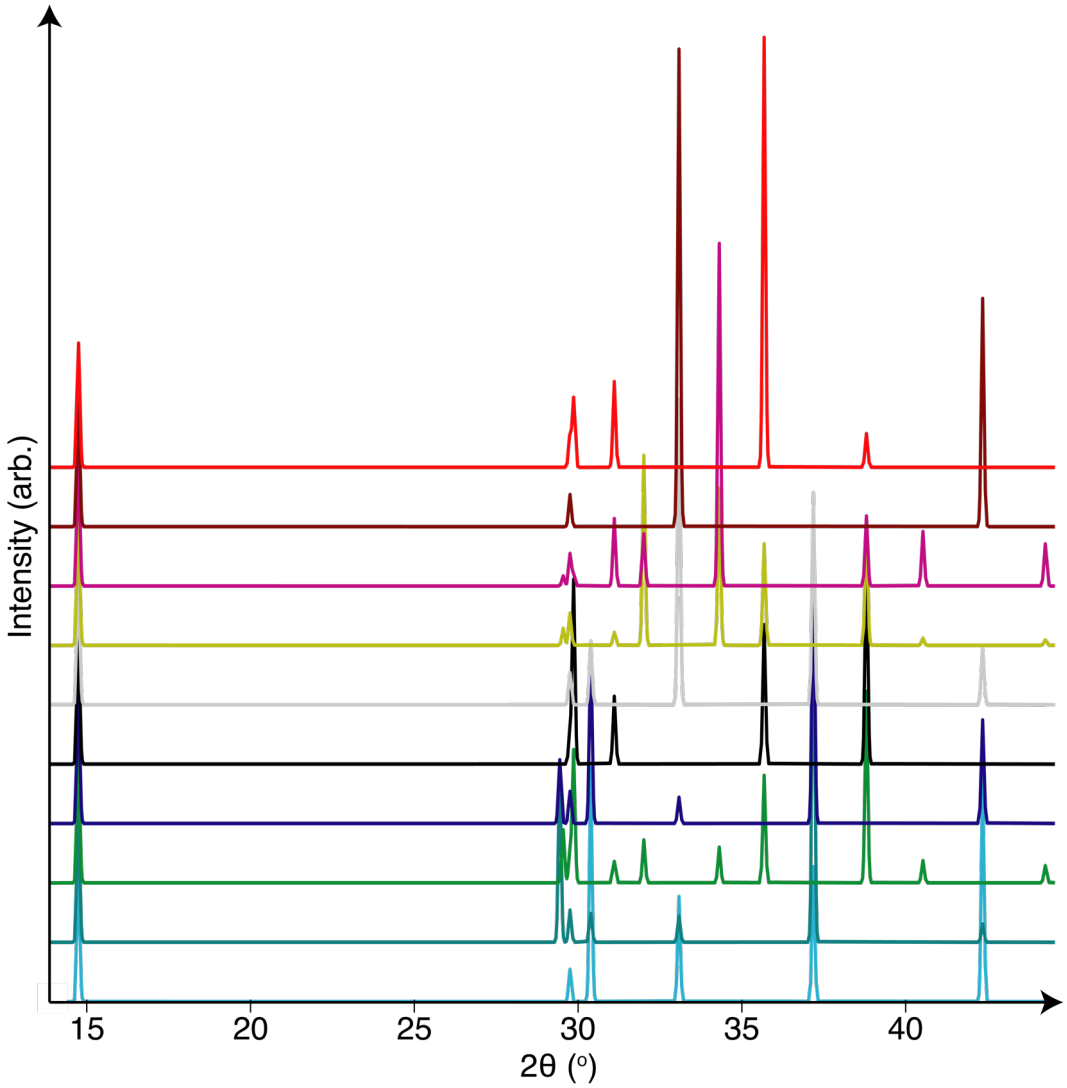

Figure C.1: Powder X-ray diffraction patterns of the limiting phases of the stacking model for layered dichalcogenides described in Chapter 3. From top to bottom the phases are $[+,+],[+,-],[+,\pm],[\pm,+],[\pm,\pm],\langle+,+\rangle,\langle+,\pm\rangle,\langle\pm,+\rangle,\langle\pm,\pm\rangle$, and $\langle\pm,\pm\rangle$. The diffraction patterns are coloured as per their interaction terms laid out in Table. 3.3 where the red value is a function of J_1 (negative 0, positive 1), green a function of J_2 (negative 0, positive 1), blue a function of J_3 (negative 0, positive 1), and J_4 determines the scaling factor of the values such that $J_4 < 0, (rgb) \times 0.5$, $J_4 > 0, (rgb) \times 1$, and for cases where J_4 can take on either sign, $(rgb) \times 0.75$.

Appendix D: Supplementary information for Chapter 4

D1 Lattice parameter data for pressure calculations

p/GPa	σ_p	a/Å	b/Å	c/Å	α°	β°	γ°
0	1	4.858000	4.858000	12.803944	90	90	90
0.18	1	4.856558	4.856558	12.620506	90	90	90
0.28	1	4.853440	4.853440	12.516216	90	90	90
0.38	1	4.853593	4.853593	12.453226	90	90	90
0.49	1	4.852365	4.852365	12.385188	90	90	90
0.54	1	4.852216	4.852216	12.337592	90	90	90
0.65	1	4.850148	4.850148	12.279814	90	90	90
0.78	1	4.850307	4.850307	12.196228	90	90	90
0.2	1	4.855418	4.855418	12.621802	90	90	90
0.58	1	4.850360	4.850360	12.271802	90	90	90
1	1	4.846975	4.846975	12.087802	90	90	90
1.53	1	4.843988	4.843988	11.874802	90	90	90
2.4	1	4.840513	4.840513	11.513802	90	90	90

Table D.1: Table containing the data used for calculating the empirical parameters using *PASC*al.

Appendix E: Supplementary information for Chapter 5

E1 Phase diagram for Monte Carlo simulations with constant A'

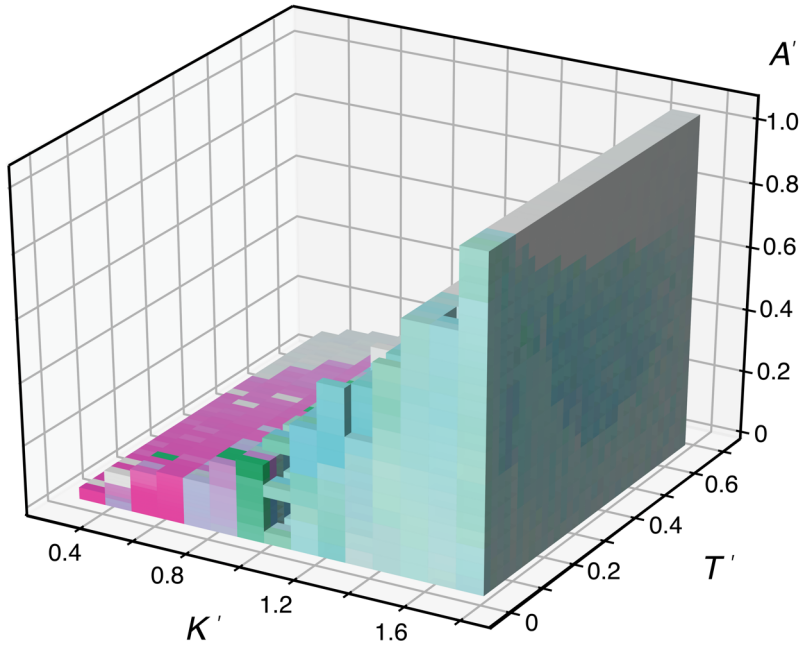

Figure E.1: Phase diagram created with simulations at constant K', T' with varying A'. Here A' was slowly increased on each MC step which changed as a function of K'. Equilibration here was especially difficult at low T and configurations tended to be trapped in their initial state. The RGB values in the phase diagram were determined through the small angle scattering of the resulting MC simulations.

E2 DFT geometry optimised structure of $[Al(N_3)_3]\cdot C_6H_6$

The crystallographic details for the DFT-optimised structure of $[Al(N_3)_3]\cdot C_6H_6$ are given in Table E.1. The corresponding CIF is included in the zip appendix.

Crystal class	Cubic		
Space group	$P2_13$		
a(Å)	9.94363		
V(Å^3)	983.185		
Z	4		
Atom	x	y	z
Al	0.137	0.137	0.137
N1	0.292	0.243	0.072
N2	0.404	0.268	0.039
N3	0.517	0.299	0.011
C1	0.450	0.482	0.295
C2	0.523	0.368	0.336
H1	0.482	0.540	0.207
H2	0.612	0.337	0.279

Table E.1: Crystallographic details for the DFT relaxed structure of $[Al(N_3)_3]\cdot C_6H_6$

Appendix F: Contents of zip appendix

F1 Contents of zip file

The following files may be found in the zip file uploaded with the thesis.

- Representative input GULP file for electrostatic energy calculations of $Ni(CN)_2$
- Representative input GULP file for electrostatic energy calculations of $Ni(CN)_2$ with different pressure (changing c lattice parameter)
- Representative input DFT file for geometry optimisation of $[Al(N_3)_3]\cdot C_6H_6$
- Representative input AIMD file for $[Al(N_3)_3]\cdot C_6H_6$
- CIF of DFT geometry optimised structure of $[Al(N_3)_3]\cdot C_6H_6$
- Representative input GULP file for the geometry optimisation of a $6 \times 6 \times 6$ supercell of $KRb[Zn(CN)_4]$ with ice rules and displacements
- Representative input GULP file for the geometry optimisation of a $4 \times 4 \times 4$ supercell of $K_2[Zn(CN)_4]$ with rigid unit mode activation

- Representative input DFT file for the geometry optimisation of $K[Au(CN)_2]$